NEAR-REGION MODIFICATION OF TOTAL PRESSURE FLUCTUATIONS BY A NORMAL SHOCK WAVE IN A LOW-DENSITY HYPERSONIC WIND TUNNEL

A Dissertation

by

CHI LUONG NHAT MAI

Submitted to the Office of Graduate and Professional Studies of
Texas A&M University
in partial fulfillment of the requirements for the degree of

DOCTOR OF PHILOSOPHY

Chair of Committee,	Rodney D. W. Bowersox
Committee Members,	Diego A. Donzis
	Simon W. North
	Edward B. White
Head of Department,	Rodney D. W. Bowersox

May 2014

Major Subject: Aerospace Engineering

ABSTRACT

Scientific understanding of the modifications to turbulence due to a normal shock wave at hypersonic speeds is lacking. The overarching research objective of this study was to characterize the effects of a hypersonic shock wave on the structure of locally homogeneous turbulence. The current study, believed to be the first hypersonic shock-turbulence interaction experiments conducted, examined in the near-region of a normal shock wave the effect on the total pressure fluctuations in a low-density hypersonic wind tunnel. Measurements were obtained with a fast-response Pitot pressure probe traversing in the freestream direction. The tunnel freestream noise level was characterized and served as the inflow/upstream condition to the interaction with the normal shock, which was a Mach stem created by the prescribed Mach reflection of two oblique shock waves. Measurements were made downstream of the Mach stem and results (noise values, autocorrelation coefficient functions, integral scales, and power spectral density estimates) were compared with the freestream measurements.

Overall, it was observed that amplification factors for the noise, time scales, and power spectral density estimates content were higher for the lower Re/m condition (i.e., lower freestream noise) than for the higher Re/m condition (i.e., higher freestream noise). In addition, the amplification factors across the range of unit Reynolds numbers were higher at 4.4 mm downstream from the Mach stem than for 2.4 mm downstream, indicating that the turbulent structures perhaps took time to grow after crossing the shock wave. Amplification was observed to be greater for higher frequencies.

DEDICATION

To my grandmother who was my first teacher

and provided me with proper initial conditions.

To all of the teachers, instructors, and mentors that I have had.

To my wife, with whom I will now be spending more time.

ACKNOWLEDGMENTS

I acknowledge and thank the DOD SMART program (and ASEE for administering the program) for my personal funding throughout my post-baccalaureate career, for the summer internship opportunities, and for gainful employment in the service of our nation. I also acknowledge the AFOSR BRI grant (grant FA9550-12-1-0168) that funded this study and thank the funding program manager, Dr. John D. Schmisseur.

I would very much like to thank and acknowledge my advisor, Dr. Rodney D. W. Bowersox for taking me on board as an undergraduate and then as a graduate student. I very much appreciate his willing guidance, patience, and (very) mild temper. I am grateful for the hours upon hours of discussions we have had the past seven years over a range of topics, both professional and personal. I look forward to more of these discussions over the years.

Acknowledgments also go out to Dr. Diego A. Donzis and Dr. Simon W. North for their joint proposal with Dr. Bowersox that provided the funding for this project among many others. Special thanks to Dr. North for his willing collaboration that introduced me to chemistry concepts and laser-based diagnostic techniques. I wish that I had been able to apply the techniques that have recently been developed and bridge that connection between AERO and CHEM that Dr. Bowersox and you have desired for so long to forge among the students. In the meantime, I thank you for putting up with the aerospace engineers and allowing us access to the chemistry machine shop.

I thank Dr. Edward B. White, the last member of my committee, for his encouragement and geniality throughout my undergraduate and graduate studies and for continuing the cordial relationship between the “High Speed Wind Tunnel” and the LSWT.

Much gratitude goes to my TAMU NAL colleagues, especially Dr. Michael T. Semper, Dr. Jerrod W. Hofferth, Dr. Rodrigo Sánchez-González, and Evan K. Marcotte for being close (and willing) collaborators and for the massive amount of extra effort exerted to develop the laboratory.

Gratitude also goes out to my current TAMU NAL colleagues: S. Alexander Craig, Ian T. Neel, Andrew N. Leidy, Wade D. Eveland, Niclas A. West, Brianne T. McManamen, Christopher W. Russo, and William T. Rogers. I especially thank Ian and Andrew for being willing to come up to the laboratory late at night on numerous occasions as a second operator for the tunnel runs. Matthew S. Kuester is also acknowledged for assistance with tunnel runs.

I would like to thank and recognize past NAL colleagues I have worked with: Dr. Ravichandra Srinivasan, Dr. Nicole R. Mendoza, Dr. Dipankar Sahoo, Dr. Nicole S. Sharp, Dr. Andrea G. Hsu Schouten, Dr. Scott J. Peltier, Dr. Ray A. Humble, Dr. Nathan R. Tichenor, Dr. Timothy J. Fuller, Brandon J. Pruski, David C. Taylor, B. Levi English, Rachel R. Vannelli, and Timothy O. Guenthner.

I want and need to recognize the exemplary work and effort of the administrative and technical staff in AERO and CHEM to keep our research programs operating. I have had the wonderful pleasure of knowing and conversing with Colleen Leatherman, Cecil

Rhodes, Rebecca Marianno, and Monica Gonzales. Cecil, I'm glad I have the experience of working with you in renovating the venerable compressor building so that we could get "back in the game."

I have taken for granted the capabilities and perks that come from being co-located with the Oran W. Nicks LSWT. I would like to acknowledge all of the LSWT personnel, past and present, with whom I have made acquaintances (and have not already acknowledged): Jorge Martinez, John Kochan, Christopher Adcock, Dave Shelby, Zahir Udovicic, Todd Williams, Ross Flach, Michael Sperry, D. Ric Warren, Byron Cotsonis, Kyle Brooks, Brian Rodgers, Rick O'Neill, John Lindeman, Teena Jeanes, and Walter Glover.

I have certainly taken for granted the willingness and outstanding workmanship of the personnel in the CHEM machine shop. William Seward (formerly of LSWT), Ronald Page (formerly of physics), and Carl Johnson (now of biomedical engineering) have made countless new parts and modifications, including the most of the parts in this study, for me over the years. And yes, I know, my parts are sharp.

Going back to my undergraduate summers, I have had the pleasure of knowing and working with Nicole Mendoza and Elizabeth Jesse in my first summer at the laboratory. Bradley Horn, Andrew White, and Christian Paul, I often think of our time together in the summer of 2008. Luke Gudgel, I am glad I got to know you before you left for Colorado. I hope all of you are doing well in wherever life has taken you, and I am proud of the work we did to set up the laboratory.

To all of the professors and personnel in the AERO department, thank you for making TAMU AERO one of the best aerospace engineering programs. Thank you for all of your dedication to educate and train the people that come through the program.

I have been very fortunate to have had friends and other couples with whom to share the burden of graduate studies. First and foremost, Matt Kuester, thank you for being there for me whenever I needed it. We went through the program our separate ways in undergraduate and graduate studies, but I have always revered and respected your dedication and demeanor. I wish you and Allie all of the best in your future, and I sincerely hope we always stay in touch wherever we may be. Alex Craig, I still remember the first time we met in the loft and how we bumped chairs for the first couple of years. I admire how you have set your goals for your time here, and I hope others follow your example. Andrea Craig, thank you for your frequent visits with my wife Jessica and being the closest person that my daughter Audra has to an aunt.

I want to recognize my family for setting high goals for me and expecting that I always do my best. I thank the Pope family for welcoming me into their family and for supporting Jessica, Audra, and me whenever and however we needed it.

Lastly, and most certainly not least, I express my appreciation and indebtedness to my wife, Jessica. You have kept me on track and focused on what I needed to get done. You have made a lot of sacrifices and waited as I went through this long program. This last year has been a whirlwind with Audra, and with me largely occupied with research, I know I have not always been there when you needed me. I cannot wait to (hopefully) spend our first entire summer together and start the next chapter of our lives.

NOMENCLATURE

Roman Letters

A	Area / Hot-Wire Calibration Coefficient
B	Hot-Wire Calibration Coefficient
E	Voltage
G	Gain
K	Shock Wave Thickness Normalized by Kolmogorov Length Scale
L	Integral Length Scale
M	Mach Number
N	Number of Points in Windowed Segment
R	Specific Gas Constant
Re	Reynolds Number
Re/m	Unit Reynolds Number (in m^{-1})
T	Temperature / Time Period
a	Speed of Sound
f	Autocorrelation Function / Frequency / Mass Flux Sensitivity
g	Wedge Separation Distance (Mouton and Hornung)
h	Enthalpy / Height
n	Filter Order
p	Pressure
t	Integral Time Scale / Time / Time Lag

u	Velocity
w	Leading Wedge Length (Mouton and Hornung)
x	Distance

Greek Letters

γ	Specific Heat Ratio (Adiabatic Index)
δ	Wedge Deflection Angle / Shock Wave Thickness
η	Kolmogorov Length Scale / Recovery Factor
θ	Oblique Shock Wave Angle
κ	Wavenumber
μ	Dynamic Viscosity / Mach Wave Angle
ρ	Density
τ	Temperature Loading Factor
ω	Angular Frequency

Subscripts

MS	Mach Stem Conditions
anem	Anemometer
avg	Average
c	Cutoff
e	Equilibrium Conditions
l	Laminar
max	Maximum

min	Minimum
norm	Normalized
o	Total/Stagnation Conditions
off	Offset
rms	Root Mean Square
s	Shock Conditions
t	Total Conditions / Turbulent / Throat
TOB	Top of Bridge
w	Wire Conditions
λ	Taylor Microscale
1	Upstream / Freestream Conditions / Initial Shock Wave
2	Downstream / Post-Mach Stem Conditions / Reflected Shock Wave
11	Autocorrelated in Freestream Direction

Modifiers

$\overline{(\ )}$	Time-Averaged Mean
$(\ )$	Mass-Weighted-Averaged Mean
$(\ )'$	Time-Averaged Fluctuation
$(\ )''$	Mass-Weighted-Averaged Fluctuation
$(\ )^+$	Nondimensionalized by w (Mouton and Hornung)

Acronyms and Abbreviations

AC	Alternating Current
ACE	Adjustable Contoured Expansion / Actively Controlled Expansion
AERO	Aerospace Engineering
AFOSR	Air Force Office of Scientific Research
AIAA	American Institute of Aeronautics and Astronautics
ASEE	American Society for Engineering Education
AVI	Audio Video Interleave
BFSL	Best-Fit Straight Line
BRI	Basic Research Initiative
CFD	Computational Fluid Dynamics
CHEM	Chemistry
CSV	Comma-Separated Values
CTA	Constant-Temperature Anemometry
DAQ	Data Acquisition
DC	Direct Current
DNS	Direct Numerical Simulation
DOD	Department of Defense
DSLR	Digital Single-Lens Reflex
EDM	Electrical Discharge Machining
FFT	Fast Fourier Transform
FPS	Frames per Second

FS	Freestream / Full-Scale
FSO	Full-Scale Output
FWHM	Full-Width Half-Maximum
KSWT	Klebanoff-Saric Wind Tunnel
LabVIEW	Laboratory Virtual Instrument Engineering Workbench
LDV	Laser Doppler Velocimetry
LED	Light-Emitting Diode
LIA	Linear Interaction Analysis
LINE	Laser-Induced Nonequilibrium (Turbulence)
LSWT	Low-Speed Wind Tunnel
M6QT	Mach 6 Quiet Tunnel
MATLAB	Matrix Laboratory
MOV	Quick-Time Movie File
MS	Mach Stem / Megasample
MTV	Molecular Tagging Velocimetry
NACA	National Advisory Committee for Aeronautics
NAL	National Aerothermochemistry Laboratory
NASA	National Aeronautics and Space Administration
NI	National Instruments
NIH	National Institutes of Health
NO	Nitric Oxide
NO_2	Nitrogen Dioxide

PC	Personal Computer
PLIF	Planar Laser-Induced Fluorescence
PNG	Portable Network Graphics
PSD	Power Spectral Density
PSFA	Pounds per Square Foot (Absolute)
PSIA	Pounds per Square Inch (Absolute)
PSIG	Pounds per Square Inch (Gauge)
RDT	Rapid Distortion Theory
RMS	Root Mean Square
RTV	Room-Temperature Vulcanizing
RW	Regular Wall
SMART	Science, Mathematics, and Research for Transformation
TAMU	Texas A&M University
TBD	To Be Determined
TDMS	Technical Data Management Streaming
TI	Texas Instruments
TKE	Turbulent Kinetic Energy
USB	Universal Serial Bus
VENOM	Vibrationally-Excited Nitric Oxide Monitoring
VI	Virtual Instrument

TABLE OF CONTENTS

Page

LIST OF FIGURES

LIST OF TABLES

INTRODUCTION

Hypersonic flight (commonly designated as a flight Mach number greater than 5) is currently of interest for applications to national security and for lower cost-of-access to low-Earth orbit. When flying at Mach 6, a hypersonic body can travel anywhere in the world in about three hours. Numerous fluid dynamic challenges encumber the design and development of hypersonic flight vehicles, some of which are notionally depicted in Figure 1.

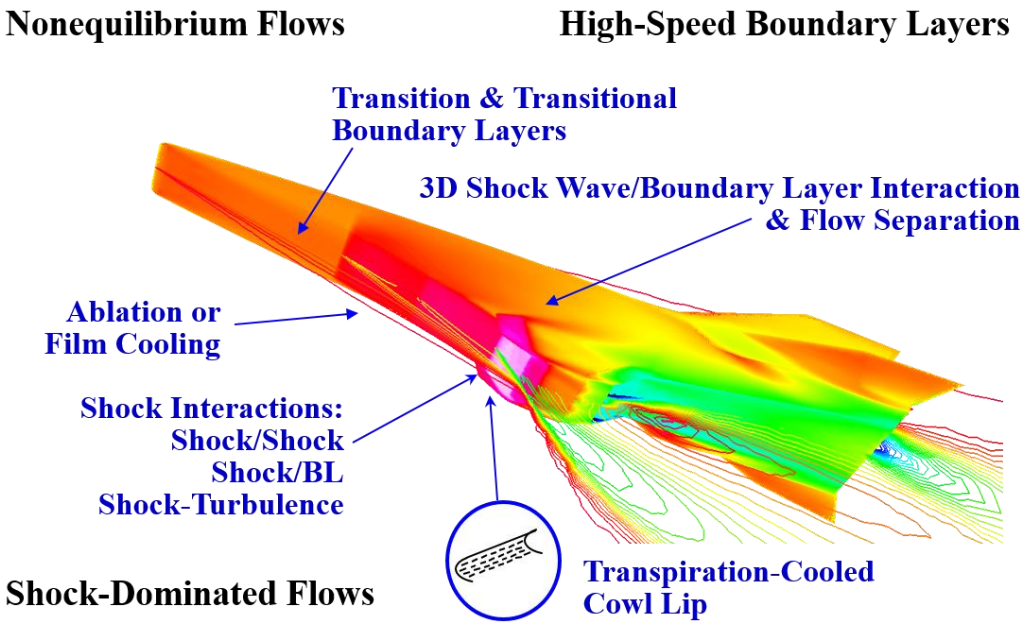

Figure 1. Hypersonic vehicle (NASA X-43) with flow physics indicated.
(credit: adapted from K. Lau [Boeing] and J. D. Schmisseur [AFOSR])

One set of fluid dynamic challenges in high-speed flow is nonequilibrium effects on turbulence behavior. Nonequilibrium can be considered in three modes: mechanical,

thermal, and chemical. Mechanical nonequilibrium consists of pressure gradient effects; shock waves are an example of a type of almost-discontinuous mechanical nonequilibrium. Real-world shock-turbulence interaction includes complicating factors such as ablation, surface curvature and surface roughness, molecular and thermal nonequilibrium, and flow separation. With so many compounding factors, it seems prudent to attempt to isolate interactions and study the fundamentals so that mechanisms can be realized and exploited among the different types of interactions to achieve the desired effects that will enable the efficient and intelligent design of hypersonic vehicles.

For shock-turbulence interaction, turbulence interacting with a normal shock wave is a canonical study. The study detailed in this dissertation was part of an interdisciplinary project to examine the role of shock waves, a strong mechanical effect, in altering the structure and energy distribution of turbulence in hypersonic, thermal nonequilibrium flows.

Current Study

This particular study contributed the beginning of a hypersonic, thermal equilibrium baseline data set for comparison to planned future thermal nonequilibrium experiments conducted as part of an interdisciplinary project. The data set also enables planned comparisons to DNS conducted as part of the overall study. In addition, this was the first known experimental study of turbulence interacting with a normal shock wave in hypersonic flow. Whereas previous experimental studies have utilized hot-wire anemometry to obtain data on rapid mass flux and velocity fluctuations, this study used a

robust, flush-mounted, fast-response pressure transducer to measure total (Pitot) pressure fluctuations. Hot-wire anemometry measurements have begun; initial freestream characterization data are presented in Appendix H.

Research Questions

The specific research questions answered as part of this study of the interaction of a normal shock wave with freestream noise in a hypersonic flow were:

- How were the *total pressure fluctuation* (noise) amplitudes modified across the normal shock wave?
- How were the *time scales* of the noise modified across the normal shock wave?
- How were the *power spectral density* content of the noise modified across the shock wave?

Research Approach and Planned Experiments

The research approach and planned experiments followed three phases:

- *Characterization of the wind tunnel freestream noise*, which served as the upstream/inflow condition to this study of shock-turbulence interaction.
- *Characterization of the wedge models that generate oblique shock waves that intersect in a Mach reflection*, creating a Mach stem that served as the normal shock in this study of shock-turbulence interaction.
- *Characterization of the post-Mach stem near-region noise*, which is the downstream/outflow condition in this study of shock-turbulence interaction.

Expected Contributions

The results of this experimental study extended the current state of knowledge of shock-turbulence interaction to include:

- First experiments of fluctuations interacting with a normal shock wave at a hypersonic Mach number. The specific fluctuations measured are total pressure fluctuations.

- The current study's focus was mechanical nonequilibrium (shock wave) effects on turbulence (i.e., thermal equilibrium baseline) for comparisons to DNS, thermal equilibrium experiments in a new pulsed facility, and thermal nonequilibrium experiments.

Shock-Turbulence Interaction

Another hypersonic vehicle design challenge is heat transfer to the vehicle surface. It is known that the heat transfer rate for a turbulent boundary layer is higher than the rate for a laminar boundary layer ([1]-[2]). There are major research efforts to understand, predict, and possibly control the state of turbulence, especially in interactions with other flow phenomena, such as shock waves. Surveys of such efforts can be found in Adamson and Messiter [3], Anyiwo and Bushnell [4], Délery [5], Lele [6], Andreopoulos, Agui, and Briassulis [7], Dolling [8], Babinsky and Harvey [9], and Clemens and Narayanaswamy [10].

Previous research has shown that shock waves alter the turbulent state by amplifying some turbulent quantities and attenuating other turbulent quantities. An understanding of this process is imperative because of its implications on surface heat transfer (a key quantity of vehicle durability) and fluid mixing (a key quantity in combustion efficiency). The phenomenon of shock-turbulence interaction is also applicable to supersonic inlet design, turbomachinery design, boundary-layer receptivity, and the field of astrophysics ([7], [11]).

In “real-world” situations, shock-turbulence interaction is complicated by wall effects (such as surface roughness), effects due to surface curvature, molecular and chemical nonequilibrium, and/or unsteady separation ([7], [11]). Figure 2 shows multiple images demonstrating shock-turbulence interaction. The top panel is a schlieren image by Stock and Ginoux [12], depicting shock waves and expansion waves due to a cross-hatched pattern formed from the ablation of a wax cone at Mach 5.3. The effect of these alternating shock and expansion waves on the structure of a turbulent boundary layer was investigated by Ekoto et al. [13], and the left panel is a surface plot of the alternating amplification and attenuation of Reynolds stresses. To isolate the shock-turbulence interaction from these complicating factors, a simpler configuration is desired. The interaction of turbulence with a normal shock wave is one such configuration; that configuration was chosen for the current study, and a schlieren image from this study is shown in the right panel of Figure 2. Research in shock-turbulence interaction, particularly homogeneous turbulence interaction with a normal shock wave, has been previously reviewed by Andreopoulos, Agui, and Briassulis [7] and partly by Lele [6].

The current study aims to provide foundational knowledge of shock-turbulence interaction in a hypersonic flow (M ≈ 6) through experimental characterization of this flow type with Pitot pressure probe measurements. Most previous computational and experimental studies have been at low supersonic Mach numbers, and this was the first known experimental study at a hypersonic Mach number.

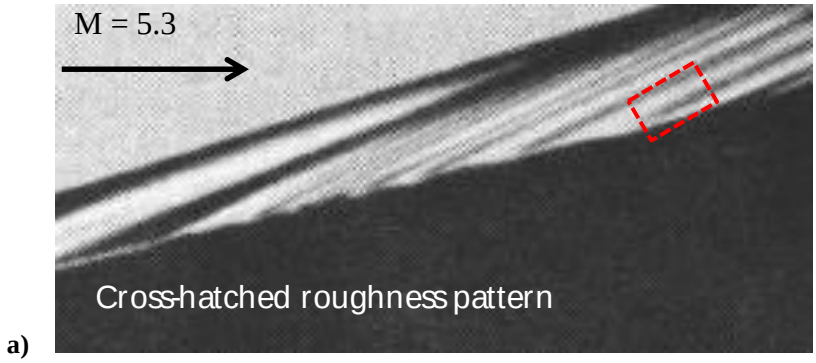

a)

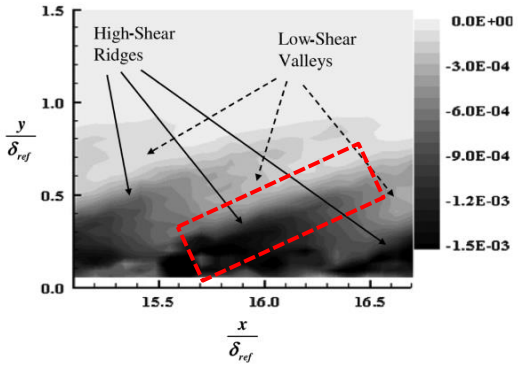

b)

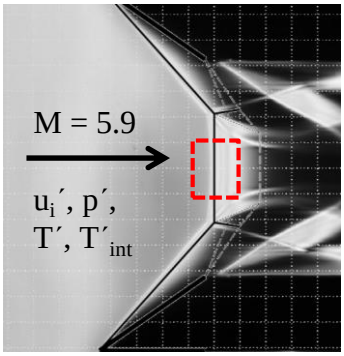

c)

Figure 2. Progression from real-world to canonical shock-turbulence interaction studies.

a) Schlieren image by Stock and Ginoux [12] of shock and expansion waves emanating from cross-hatched ablation patterns on a 28° wax cone at M = 5.3, T_t = 412 K, p_t = 2.9 MPa. Red box indicates phenomena studied in image in panel b).

b) Reynolds stress surface plot by Ekoto et al. [13] indicating effect of shock and expansion waves emanating from distributed surface roughness elements at M = 3, T_t = 315 K, p_t = 690 kPa. Red box indicates phenomena studied in image in panel c).

c) Schlieren image of current study of shock-turbulence interaction at M = 5.9, T_t = 425 K, p_t = 200 kPa.

Role of Current Study in AFOSR BRI Project

The current study was part of a multi-faceted effort funded through an AFOSR BRI grant to understand the effects of thermal nonequilibrium and mechanical nonequilibrium (e.g. a shock wave) on turbulence. Previous experiments from published work (Fuller et al. [14] and Fuller [15]) and unpublished work have suggested strong interactions between thermal nonequilibrium and turbulence. Mechanical nonequilibrium flow phenomena has been shown to redistribute energy in turbulence modes and will perhaps affect internal and external energy distributions in thermal nonequilibrium flows. The overall expected scientific objective of the project is to utilize fundamental understanding of the energy transfer between turbulence modes and different molecular internal modes to predict and control the behavior of turbulence over varying degrees of thermal and mechanical nonequilibrium.

Computational and experimental work are planned to explore and gain understanding of the physics. Planned computational studies will DNS on tens or hundreds of thousands of processors, whereas planned experimental studies will utilize a variety of wind tunnel facilities.

The current work provides a thermal equilibrium baseline, for comparison to thermal equilibrium and nonequilibrium experiments in a pulsed facility and to DNS computations, of the role of a normal shock wave on modifying total pressure fluctuations in a continuous wind tunnel facility.

The planned use of a pulsed facility to conduct these experiments stems from the use of pulsed laser diagnostic techniques to determine the velocity and internal state (and

therefore temperature) of seeded molecules in the flow [16]. Such techniques include MTV, PLIF, and their combination in VENOM ([17]-[23]). The NO and NO_2 molecules seeded into the flow for each of these techniques are relatively expensive and hazardous. Thus, pulsed facilities are desirable because they reduce the usage of the seed molecules, leading to cost reductions and improved operational safety. When the flow is synchronized with the lasers and cameras, the string of images obtained essentially see continuous flow from a pulsed facility. Given a proper supply of air or nitrogen, a pulsed facility can run almost indefinitely.

TAMU NAL

The experiments in the current study were performed at the TAMU NAL. The TAMU NAL was founded in 2004 by R .D. W. Bowersox (TAMU), S. W. North (TAMU), and J. D. Schmisseur (AFOSR). The TAMU NAL is an interdisciplinary laboratory committed to the development and utilization of state-of-the-art research facilities and instrumentation to perform fundamental and applied studies in nonequilibrium fluid and gas dynamics with applications in aerodynamics and aerospace propulsion. Its stated mission is to "provide a venue for faculty, students, research associates, and visiting scientists to improve our knowledge and control of nonequilibrium gaseous flows and their surface interactions."[1] The research thrusts are directed along three topic areas: 1) high-speed flow physics, 2) flow control, and 3) facility and instrumentation development. Several wind tunnel facilities have been established (as part of the third topic

[1] http://nal.tamu.edu/

area) at the TAMU NAL to perform research activities supporting the first and second topic areas.

The current study utilized one of the TAMU NAL wind tunnel facilities (ACE tunnel) and traditional measurement techniques supported at the TAMU NAL (Pitot pressure probe with a foray into hot-wire anemometry). Planned extensions of the current study will, as mentioned before, utilize pulsed facilities and laser diagnostic techniques developed in-house.

Organization of Manuscript

The next section provides a background to shock waves and turbulence. A literature review of previous theoretical, numerical/computational, and experimental studies is also provided.

This is followed by sections describing the experimental setup (wind tunnel facility and model) and then a section describing the measurement techniques utilized in this study. Flow visualization results are then presented. Pitot pressure probe data reduction, results, and analyses are discussed in the sections after that. The last section summarizes the dissertation, includes a set of recommendations to improve the current study, and proposes future directions for this research area.

BACKGROUND

This subsection provides a brief physical and mathematical introduction to the flow phenomena of shock waves and turbulence, individually.

Shock Waves

In response to some disturbance or perturbation, molecules collide with each other and propagate information about this disturbance as a weak pressure wave, which we perceive as a sound wave. This weak pressure wave propagates at the speed of sound.

Consider Figure 3 below (taken from Anderson [24]); in each graphic, an object is traveling from point A to point B. At timed intervals long the way, the object emits a pulse that is manifest as a sound wave propagating away at the speed of sound from the pulse's point of origin.

In the subsonic case, the object is traveling at a speed less than the speed of sound. The molecules are able to propagate information (via sound waves) faster than the velocity of the body's motion. Thus, the fluid ahead of the object is "aware" of the object's incoming presence.

In the supersonic case, the object is traveling at a speed greater than the speed of sound. The molecules are not able to propagate information (via sound waves) faster than the velocity of the body's motion. Thus, the fluid ahead of the object is *not* "aware" of the object's incoming presence. The sound waves that are emanated from the object start coalescing at the edges, and this coalescence is manifest as a shock wave whose thickness is only a few mean free paths and is at an angle μ.to the object's direction of motion.

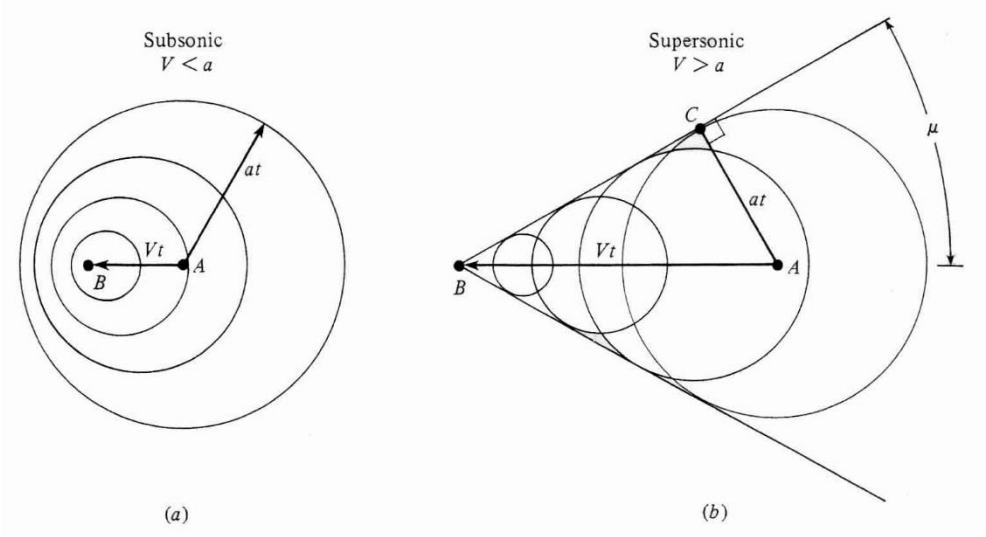

Figure 3. Propagation of disturbances of an object in subsonic and supersonic flow. a) Subsonic flow. b) Supersonic flow. (taken from Anderson [24])

Thus, shock waves are a compressible flow phenomenon present when a body travels near or faster than the speed of sound. Conversely, they are present when fluid travels around a body faster than the speed of sound.

Consider now the simplistic case of a normal shock wave, such as that seen in Figure 4. The shock wave is in a plane perpendicular (normal) to the main flow direction, and the flow is adiabatic since energy is neither added nor removed from the flow. Also, even though the shock thickness is finite, the thickness is much smaller than any other length scale in the flow, so the shock wave is treated as a discontinuity in overall consideration. The equations describing the fluid properties on either side of the shock wave are given by the one-dimensional equations of conservation of mass, momentum,

and energy. The reduced form of these equations are known as the Rankine-Hugoniot equations [25].

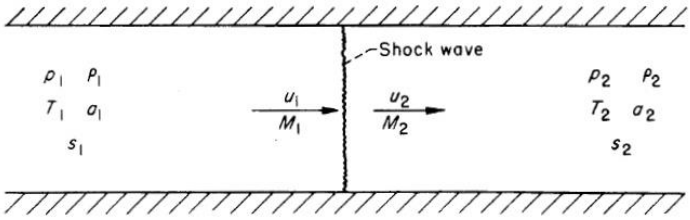

Figure 4. Notation for a normal shock wave.
(taken from NACA Report 1135 [25])

Continuity:

$$\rho_1 u_1 = \rho_2 u_2 \tag{1}$$

Momentum:

$$p_1 + \rho_1 u_1^2 = p_2 + \rho_2 u_2^2 \tag{2}$$

Energy:

$$h_1 + \frac{1}{2}u_1^2 = h_2 + \frac{1}{2}u_2^2 \tag{3}$$

These equations, cast it another form, are known as the Rankine-Hugoniot jump conditions.

$$\left[\!\left[\begin{array}{c} \rho u \\ p + \rho u^2 \\ h + \frac{1}{2}u^2 \end{array} \right]\!\right] = 0 \tag{4}$$

In general, given the upstream conditions, the Rankine-Hugoniot equations must be solved numerically for the properties behind the shock wave. If the fluid is a calorically perfect gas, however, then algebraic equations can be derived to obtain the downstream properties as functions of the upstream properties. These equations can be found in NACA Report 1135 [25]. The relevant equations are given below.

$$M_2^2 = \frac{1 + \frac{(\gamma - 1)}{2} M_1^2}{\gamma M_1^2 - \frac{(\gamma - 1)}{2}} \tag{5}$$

$$\frac{p_{t2}}{p_{t1}} = \left[\frac{(\gamma + 1) M_1^2}{(\gamma - 1) M_1^2 + 2} \right]^{\left(\frac{\gamma}{\gamma - 1}\right)} \left[\frac{\gamma + 1}{2\gamma M_1^2 - (\gamma - 1)} \right]^{\left(\frac{1}{\gamma - 1}\right)} \tag{6}$$

$$\frac{p_2}{p_1} = \frac{2\gamma M_1^2 - (\gamma - 1)}{\gamma + 1} \tag{7}$$

$$\frac{\rho_2}{\rho_1} = \frac{u_1}{u_2} = \frac{(\gamma + 1) M_1^2}{(\gamma - 1) M_1^2 + 2} \tag{8}$$

$$\frac{T_2}{T_1} = \frac{p_2}{p_1} \left(\frac{\rho_2}{\rho_1} \right)^{-1} = \frac{\left[2\gamma M_1^2 - (\gamma - 1) \right] \left[(\gamma - 1) M_1^2 + 2 \right]}{(\gamma + 1)^2 M_1^2} \tag{9}$$

By invoking the second law of thermodynamics, the Mach number downstream of a normal shock, M_2, must be less than the Mach number upstream of the normal shock, M_1. In fact, for a normal shock, M_1 is always supersonic (> 1) and M_2 is always subsonic (< 1). As a result, the downstream static pressure, density, and temperature are all greater than their upstream values. Therefore, it is shown that kinetic properties (such as velocity and Mach number) decrease from upstream of a shock wave to downstream whereas static

properties (such as pressure and temperature) increase across a shock wave. In addition, by Eq. (6), the total pressure decreases across a normal shock.

Turbulence

Hinze [26] described turbulent fluid motion as "an irregular condition of flow in which the various quantities show a random variation with time and space coordinates, so that statistically distinct average values can be discerned." That is to say, at any given point in space and/or time, a particular flow condition is random and not likely to be known exactly, but its statistical properties enable a probabilistic estimate to be made. This view is also expressed by Pope [27]. Pope also expressed that "an important characteristic of turbulence is its ability to transport and mix fluid much more effectively than a comparable laminar flow."

Turbulence is a flow state characterized by fluctuations and *appears* to be irregular and chaotic. Turbulence is also characterized as diffusive and as having multiple length scales, which is observed in a plume of smoke or a fast stream of water from a faucet. Turbulent flows are still governed by the Navier-Stokes equations and are therefore deterministic; DNS, which solves the Navier-Stokes equations directly with no modeling, have been performed for low-Reynolds number flows. For realistic flows, however, solving the equations over the requisite time and length scales makes the problem intractable, so turbulent flows are necessarily treated stochastically.

Decomposition and Closure

The typical process of the stochastic treatment is to decompose variables into a mean value and a fluctuating value. The first decomposition method is Reynolds (time-based) decomposition:

$$u = \bar{u} + u' \tag{10}$$

where

$$\bar{u} = \frac{1}{T}\int_0^T u(t)\,dt \tag{11}$$

The second decomposition method is the Favre (mass-average-based) decomposition [28]:

$$u = \tilde{u} + u'' \tag{12}$$

where

$$\tilde{u} = \frac{\overline{\rho u}}{\bar{\rho}} = \frac{\int_0^T \rho(t)u(t)\,dt}{\int_0^T \rho(t)\,dt} \tag{13}$$

For compressible flows, the Favre decomposition is preferred since the form of the averaged equation using that decomposition is more similar in form to the original equation than the averaged equation obtained with Reynolds decomposition.

The decompositions are substituted for the variables in the governing Navier-Stokes equations, and the equations are averaged. The resulting equations have additional terms, such as the so-called Reynolds stress and the turbulent heat flux, that are created as a result of the averaging process. This results in a closure problem since there

are now more terms than there are equations, and the field of turbulence modeling is devoted to finding suitable models for such terms.

One method to close the turbulence problem is RDT [27]. The underlying assumption is that the time scale of a distortion to the mean flow is much smaller than the time scale of a turbulent structure. Therefore, the resulting flow is dominated by the response to the rapid distortion of the mean flow. In the equations governing the velocity fluctuations, the terms with only fluctuations are negligible compared to the terms with mean velocity gradients. Solutions, including expressions for the changes to the Reynolds stress, have been derived for several types of distortions [27].

Length Scales and Energy Cascade

As mentioned previously, turbulence is characterized as having multiple characteristic length scales. These scales are associated with the energy cascade that is seen in isotropic turbulent flows. The three important length scale types are the integral length scale, the Taylor microscale, and the Kolmogorov length scale; Pope describes these mathematically [27]. The integral length scale is indicative of the larger turbulent structures in the flow (and contain most of the turbulent energy), and the Kolmogorov scale is indicative of the smallest turbulent structures where viscous effects dominate and dissipate the turbulent energy. The Taylor microscale does not have a clear interpretation, but it is a well-defined quantity often used to calculate the Taylor-microscale Reynolds number in DNS studies.

Figure 5 is a notional image of the relative ranges used to describe turbulence scales. At the left (small wavenumbers, large length scales such as the integral length

scale) is the energy-containing range. The energy cascade is the process of energy passing from the energy-containing range through the inertial subrange (where inertial effects are dominant) to the dissipation range (where viscous effects are dominant). The dissipation range is characterized by large wavenumbers (small length scales such as the Kolmogorov length scale).

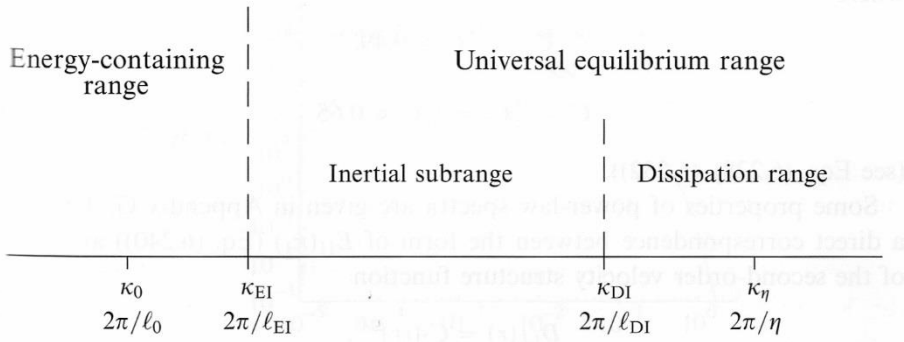

Figure 5. Turbulent ranges in wavenumber space.
(taken from Pope [27])

Figure 6 is a notional depiction of the energy cascade process and relates the process to the various length scales. Energy from the main flow is injected into the turbulent energy cascade through the large-scale (integral), energy-containing structures, which have low wavenumber/frequency. The inertial range is where energy from the large structures passes to the small structures. The energy is then dissipated in the small-scale (Kolmogorov) structures.

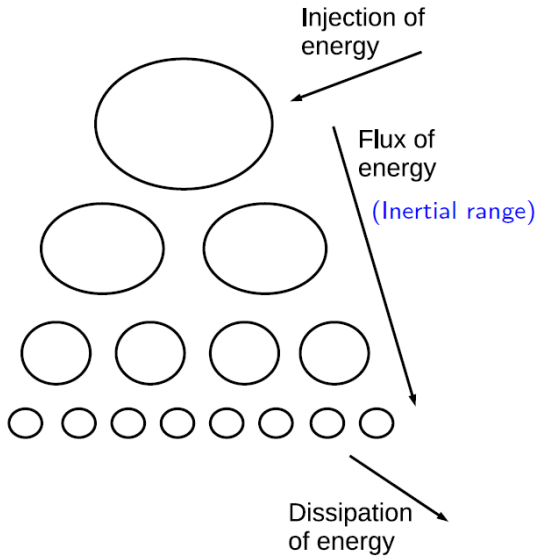

Figure 6. Turbulent energy cascade.
(credit: D. A Donzis)

One of the defining features of a PSD of turbulence is the decay of the PSD in the inertial subrange, which follows Kolmogorov's -5/3 power law, as seen in Figure 7 [27].

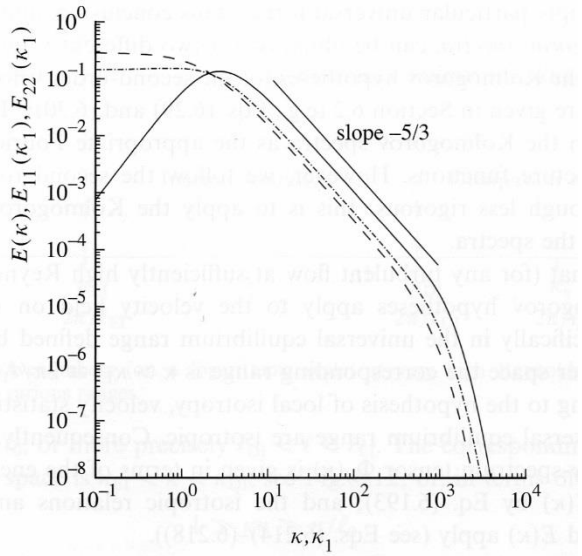

Figure 7. Power spectra in isotropic turbulence.
Dashed lines are unidirectional spectra with aliasing at lower wavenumbers. Solid line is nondimensional spectra.
(taken from Pope [27])

In shock-turbulence interaction studies, the turbulence is commonly decomposed into modes and studied within that context. Kovásznay [29] applied first-order perturbation theory to the Navier-Stokes equations and decomposed supersonic turbulence into three separate modes: acoustic (pressure and irrotational velocity), entropy (temperature), and vorticity (rotational velocity). Assuming that all state variable disturbances are small compared to the mean properties and that the velocity perturbations are small compared to the speed of sound, these three modes were non-interacting and each described by a linear differential equation. This work was expanded by Chu and Kovásznay [30]. If the noninteracting modes pass through a region of steep gradients, i.e., a shock wave, mode interaction could occur.

LITERATURE REVIEW

This section provides a survey of the major efforts in shock-turbulence interaction and is categorized into theoretical studies, computational/numerical studies, and experimental studies. A dedicated review is provided by Andreopoulos, Agui, and Briassulis [7]. Thorough literature reviews are available in Jamme et al. [31], Wouchuk, Huete Ruiz de Lira, and Velikovich [32], and Larsson, Bermejo-Moreno, and Lele [11].

Theoretical Studies

Ribner performed the first theoretical treatments of shock-turbulence interaction, which are formally valid in the limit of high Reynolds numbers and low turbulent Mach numbers. His first analysis assumed the upstream turbulence consisted of only the weak vortical turbulence mode in the form of a single plane, sinusoidal shear wave and that the entire upstream flow field could be described by the superposition of waves of different orientations and wavelengths [33]. Ribner's analytical method, later dubbed as linear interaction analysis (LIA), predicted that a shear wave's passage through a shock wave would modify its inclination and amplitude and would activate the acoustic mode in the form of a pressure wave. Thus, the shock wave altered one turbulent mode and generated fluctuations in another mode. Ribner, for initially isotropic and axisymmetric turbulence behaviors, would later generalize the upstream turbulent (vortical) field to a spectrum of sinusoidal shear waves [34]. LIA remains as a standard in shock-turbulence interaction research due to its ease in obtaining results for quantities of interest, and DNS results are often compared to LIA predictions. Upstream conditions have been shown to be important

to shock-turbulence interaction, but LIA, however, does not account for the effect of all upstream conditions, particularly length scales [7].

Moore [35] used a similar approach as Ribner by considering upstream fluctuations as a linear combination of plane waves of varying strengths and orientations. The interaction was found for each constituent wave, and the downstream results were superposed. The upstream conditions considered included: 1) a convected plane vorticity wave, 2) a propagating plane sound wave approaching the shock wave from upstream, and 3) a propagating sound wave catching up to the shock wave from the downstream side (sound waves propagate at the speed of sound *relative* to the bulk flow rather than *at* the speed of the bulk flow). The results described the characteristic of the isentropic pressure wave and steady vorticity wave behind the shock.

Kerrebrock [36] considered all three modes in the upstream flow and considered their modifications through a normal shock wave and through a flame front. A set of analytical transfer functions were obtained to statistically describe the downstream perturbations. All three modes were found to be generated in comparable strength in the downstream flow if any of the three modes were present in the upstream flow.

Anyiwo and Bushnell [4] applied the linear theory to shock/boundary-layer interaction as a first-guess estimate of the turbulence amplification factor. Their analyses describes three major turbulence amplifier-generation mechanisms. The mechanisms are: 1) direct amplification of incident turbulence across a shocked region, 2) generation of turbulence from incident acoustic and entropy fluctuation modes, and 3) “pumping” of turbulence from the mean flow by “externally driven” shock oscillation.

Lele [37] averaged the conservation equations with the Rankine-Hugoniot jump conditions to calculate changes in turbulent flow conditions across a shock wave and compared those changes to classical theory. The conservation equations were Favre-averaged, and upstream turbulence was assumed to be axisymmetric. Closure was obtained by appealing to homogeneous RDT. RDT is a more restrictive method than LIA; it does not incorporate the Rankine-Hugoniot jump conditions and does not predict the generation of the acoustic or entropy mode from the interaction of the vortical mode with the shock wave [11]. In addition, RDT neglects the mutual effect of turbulence on shock wave structure and the post-shock evolution of the turbulence. To account for the mutual interaction of the turbulence and the shock wave, Zank et al. [38], based on an inviscid form of Burgers's equation (a form of governing equation in which the dynamic/"ram" pressure term dominates), developed a set of self-consistent equations with jump conditions.

Wouchuk, Huete Ruiz de Lira, and Velikovich [32] developed an exact, analytical model for the interaction between a shock wave and a turbulent vorticity field. The vorticity field was decomposed into Fourier modes, and expressions for quantities such as shock pressure perturbations and rotational velocity components were reduced to closed-form, exact, analytical expressions and presented explicitly as functions of γ and M_s. It was found that the TKE, contrary to most cases, was attenuated after the interaction in cases where γ goes to one and the Mach number goes to infinity. The closed-form expressions lent themselves to the possibility of obtaining exact, analytical scaling laws.

Donzis [39] performed scaling analysis and showed that the shock wave thickness in both laminar flow and turbulent flow had incomplete similarity.

Numerical/Computational Studies

Much of the numerical work done in shock-turbulence interaction has been done with DNS in which the conservation equations are solved directly without resorting to a turbulence model. With rapid advances in computational capabilities, DNS are beginning to solve flow problems at more realistic Reynolds numbers while still resolving the fine turbulent scales.

DNS involving shock waves are typically categorized by how the shock waves are treated. The three methods used in the literature reviewed here are: 1) shock resolving, 2) shock capturing, and 3) shock fitting. Shock-resolving methods explicitly introduce the shock waves into the solution and resolve the shock wave region with finer grid spacing. Shock capturing methods do not make any advance considerations for the presence of shock waves; the shock waves are computed ("captured") as part of the solution. The drawbacks of shock-capturing methods are that the shock waves are not sharp but exist over several grid points as a smeared but relatively steep gradient. In addition, spurious oscillations may enter the solution near the shock wave and lead to numerical instability if not properly treated. In shock-fitting methods, the location of the shock wave is solved for by other computational means, and DNS is performed on a grid between the shock wave and a body.

Lee, Lele, and Moin [40] performed one of the first major numerical works for isotropic turbulence interactions with normal shock waves. Weakly compressible, isotropic turbulence (M_t = 0.057 to 0.110) at low turbulent Reynolds numbers interacting with weak shocks (M = 1.05 to 1.20) was studied. Results predicted the amplification of turbulence, TKE, and transverse vorticity components. Furthermore, at these low Mach and turbulent Mach numbers, the results compared favorably with LIA predictions.

Lee, Lele, and Moin [41] extended their analysis to stronger shocks using an essentially non-oscillatory scheme. The Mach numbers in this study were 1.5, 2.0, and 3.0, and M_t for each case was 0.090, 0.108, and 0.110, respectively. The results indicated that the amplification of TKE saturated above Mach 3.0. Again, the DNS results with available counterpart LIA predictions compared favorably. Fluctuations in thermodynamic variables after the interaction were found to be anisotropic due to the generation of the entropic turbulence mode.

Mahesh, Lele, and Moin [42] expanded upon the role of entropy fluctuations by performing DNS of an isotropic turbulent field of vorticity and entropy fluctuations interacting with a normal shock wave. The Mach numbers in this study were 1.29 and 1.80 with LIA predictions ranging from M = 1 to 3. LIA and DNS both showed no amplification of the TKE if the upstream correlation between velocity (vorticity) and temperature (entropy) fluctuations is positive. A negative correlation between velocity and temperature fluctuations, however, was observed to enhance the amplification of the TKE, vorticity, and thermodynamic fluctuations. Thus, the upstream correlation of velocity and temperature fluctuations directly influenced turbulent heat flux values downstream of the

interaction. Bulk compression and baroclinic torques were found to be the two important contributions to the evolution of fluctuating vorticity across a shock wave, and the velocity-temperature fluctuation correlation determined if the two processes enhanced or opposed each other.

Jamme et al. [31] performed DNS of isotropic turbulence interacting with a shock wave for M = 1.2 and 1.5. Three mode combinations for upstream, isotropic turbulence were considered: 1) vorticity only, 2) vorticity and entropy, and 3) vorticity and pressure. The objective of this study was to use the same numerical tool and inflow conditions for the three upstream turbulence types so that any differences in the results would be attributed certainly to the upstream flow differences. Results agreed well with LIA and confirmed earlier findings by different researchers with different codes and different flow conditions.

Larsson and Lele [43] pushed the Mach and turbulent Mach number ranges further than the work of Lee, Lele, and Moin. In this study, M ranged from 1.3 to 6.0, and M_t ranged from 0.16 to 0.38. The Kolmogorov length scales decreased during the shock interaction, implying that the grid resolution needed to properly resolve viscous dissipation is likely finer than grids used in previous studies. Computational grids coarser than the required resolution result in rapid increases in downstream streamwise vorticity variance and large anisotropy of the post-shock Reynolds stresses. The terms “wrinkled” and “broken” were introduced and used to describe the structure of the shock wave in response to the incoming turbulence. A “wrinkled” shock wave structure locally maintains a distinct shock front whereas a “broken” shock wave structure is where the local flow

compresses smoothly. Larsson, Bermejo-Moreno, and Lele [11] expanded the work to include Reynolds- and Mach-number effects with Re_λ = 40 and 72. Those results, like their previous results, indicated that TKE amplification was described well with linearized dynamics but that the post-shock Reynolds stress anisotropy was qualitatively different than LIA predictions.

Wang and Zhong [44] expanded DNS to Mach 30 simulations and showed new trends in turbulent statistics at higher Mach numbers. Main conclusions from this work were that the upward amplification trend for streamwise vorticity fluctuations through a shock wave reaches a maximum at M = 2.8 and then decreases as shock strength is increased. On the other hand, the amplification of the streamwise Reynolds stress decreases as M is increased to Mach 8.8 with a reversal as shock strength is further increased. Their DNS work incorporated a new high-order shock fitting solver for nonequilibrium flow simulations based on 5-species air chemistry with results forthcoming.

Donzis [45] was able to collapse to first-order the streamwise velocity amplification factor curves for canonical shock-turbulence interactions from various DNS by using a parameter that normalized shock wave thickness by the Kolmogorov length scale:

$$K \equiv \frac{M_t}{\left(R_\lambda^{1/2}\Delta M\right)} = \frac{M_t}{R_\lambda^{1/2}\left(M-1\right)} \approx \frac{\delta_l}{\eta} \tag{14}$$

This parameter was also shown to assist in discerning the “wrinkled” and “broken” interaction regimes.

Table 1 lists the reviewed DNS with their M and M_t. The upstream turbulence modes considered in each study are also listed.

Table 1. Numerical/computational DNS shock-turbulence interaction studies and parameters. (adapted and updated from Jamme et al. [31] and Donzis [45])

Author/Year	Ref. No.	Method	M_1	M_t	Upstream Turbulence
Lee 1993	[40]	SR	1.05 – 1.20	0.06 – 0.11	sol
Lee 1997	[41]	SC	1.5 2.0 3.0	0.09 0.11 0.11	sol
Mahesh 1997	[42]	SC	1.29 1.80	0.14	sol/ent
Jamme 2002	[31]	SR	1.20 1.50	0.17	sol/ent/ac
Larsson 2009	[43]	SC	1.3 – 6.0	0.16 – 0.38	sol
Wang 2012	[44]	SF	2.0 – 30.0	0.08 – 0.14	sol
Larsson 2013	[11]	SC	1.05 – 6.00	0.05 – 0.38	sol

Method: SC – shock capturing; SF – shock fitting; SR – shock resolving.

Upstream turbulence mode: sol – solenoid; ac – acoustic; en – entropy.

Experimental Studies

Experiments in normal shock-turbulence have been carried out in shock tubes and supersonic blowdown wind tunnels.

Experiments in shock tubes generally have a mesh grid or other turbulence generator in the driven tube. The shock wave passes through the generator and reflects off of the end wall. The reflected shock wave interacts with the incident shock wave's induced flow that has passed through the turbulence generator. This process is shown in Figure 8. Measurement techniques generally utilize hot-wires and wall-mounted fast-response pressure transducers. A porous end wall is utilized by the Andreopoulos group to control the strength of the reflected shock wave.

For blowdown wind tunnels, a variety of options to generate turbulence have been explored. A mesh grid can be installed in the settling chamber, but the resulting turbulence is anisotropic due to the turbulent eddies stretching at the throat and during the subsequent expansion. A grid acting as a sonic throat has been utilized by Jacquin, Blin, and Geffroy [47] as well as a multinozzle concept by Barre, Alem, and Bonnet [48].

Hesselink and Sturtevant [49] studied the propagation of weak shock waves through a statistically uniform random medium in a shock tube with schlieren and shadowgraph methods. M_s in this study were 1.01, 1.03, and 1.10. Images obtained show distorted shock fronts and pressure changes; the phenomena are interpreted to represent a multiplicity of scattered wave fronts instead of a single highly wrinkled front. The pressure histories of the distorted shock waves reflecting from a normal end wall were seen to be both peaked and rounded, and these are now associated with the "wrinkled" and "broken" shock interaction regimes.

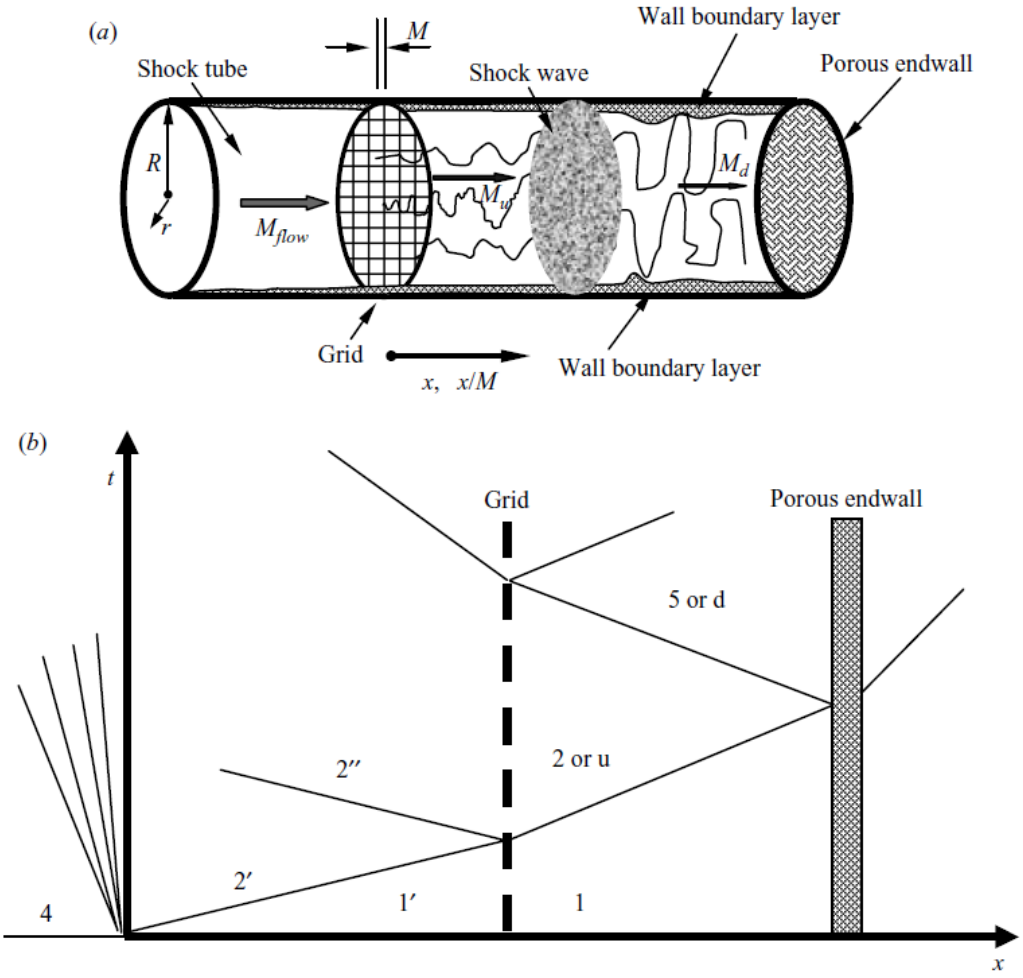

Figure 8. Shock-turbulence interaction studies in shock tubes.
a) Experimental setup. b) Wave diagram.
(taken from Agui et al [46])

Keller and Merzkirch [50] performed shock tube experiments and installed a grid to generate turbulence from the induced flow behind the initial shock wave. Their results, obtained using a quantitative optical method based on speckle photography, showed that density fluctuation amplifications were restricted to lower wavenumbers in the power spectrum.

Jacquin, Blin, and Geffroy [47] used a grid that acted as a sonic throat and obtained Mach 1.4 flow. The normal shock position was controlled by a second throat downstream. Measurements were obtained using LDV with an unusual observation: the lack of turbulence amplification. Andreopoulos, Agui, and Briassulis [7] cast doubt on the results for the following reasons: 1) review of the data showed that the flow upstream of the interaction was decelerating with the likely cause attributed to Mach waves emanating from the grid and flow deceleration has been shown to augment turbulence, 2) the probe volume was too large to accurately resolve the turbulence, and 3) it has also been shown that LDV in compressible flows tends to overestimate turbulence intensities.

Honkan and Andreopoulos [51] studied the interaction of decaying grid-generated turbulence interacting with a shock wave in a shock tube. They found that amplification of the turbulence after the interaction to depend on the length scale of the incoming flow with larger eddies amplified more than smaller eddies.

Barre, Alem, and Bonnet [48] generated an isotropic turbulent flowfield by using a multinozzle generator and formed a normal shock wave through the intersection of two oblique shock waves of opposite directions. A block with multiple $M = 3$ nozzles was placed in a supersonic blowdown wind tunnel, and the shear layers and slip lines between each nozzle decayed into isotropic turbulence a finite distance downstream of the nozzle exits. The turbulence amplification agreed well with LIA, and higher wavenumber content was observed to amplify more than lower wavenumber content. Diagnostics included hot-wire anemometry and LDV. Andreopoulos, Agui, and Briassulis [7] presented concerns with this study: 1) the shear layers from the shock generators accelerated the

flow downstream of the shock wave and were expected to reduce downstream turbulence levels, and 2) the turbulence intensity at the shock wave was extremely low leading to low signal-to-noise ratios.

Xanthos, Briassulis, and Andreopoulos [52] studied the interaction of decaying freestream turbulence with a moving shock wave in a shock tube and quantified the pressure field. The induced flow, whose M ranged from 0.32 to 0.62, interacted with reflected shock waves of varying strengths. Hot-wires, wall-mounted pressure transducers, and Rayleigh scattering were used to make measurements and perform flow visualizations. The mutual interaction between the freestream turbulence and the shock wave resulted in 1) shock wave attenuation due to strong viscous effects and 2) substantial changes in turbulence intensity. Finer grids produced turbulence that attenuated the shock wave more than turbulence produced from coarser grids. The grid spacing also strongly influenced the amplification of pressure fluctuations.

Agui, Briassulis, and Andreopoulos [46] extended the work of Xanthos, Briassulis, and Andreopoulos by quantifying the velocity and vorticity fields. The induced flow was similar to the previous study (M = 0.3 to 0.6), and reflected shock waves varied from M_s = 1.04 to 1.39. 3-wire and 12-wire probes were placed at various axial locations along the shock tube to determine the temporal and spatial evolution of turbulent fluctuations and structures. Measured quantities included longitudinal and lateral length scales, longitudinal and lateral velocity gradient fluctuations, and longitudinal and lateral vorticity fluctuations. Among many other findings, the integral length scale and Taylor's microscale decreased after shock-turbulence interaction.

Table 2 lists shock tube experiments that have been performed to study shock-turbulence interactions. Since the induced flow behind the initial shock wave is used as the freestream, the Mach numbers are subsonic or slightly supersonic. Table 3 lists shock-turbulence interaction experiments that have been performed in continuous-operation wind tunnels. The current study was the first known shock-turbulence interaction study in hypersonic flow.

Table 2. Experimental shock-turbulence interaction studies (shock tube). (adapted and updated from Jamme et al. [31])

Author/Year	Ref. No.	M_1
Hesselink 1988	[49]	1.007 1.03 1.1
Keller 1990	[50]	1.115 1.18 1.22
Honkan 1992	[51]	1.62
Xanthos 2002	[52]	0.321 – 0.623
Agui 2005	[46]	0.321 – 0.623

Table 3. Experimental shock-turbulence interaction studies (blowdown tunnel).
(adapted and updated from Jamme et al [31])

Author/Year	Ref. No.	M_1	M_t	Upstream Turbulence
Jacquin 1991	[47]	1.4	≈ 0.050	sol/ac
Barre 1996	[48]	3	≈ 0.011	sol/ac
Present Study 2014		5.8 – 5.9	TBD	TBD

Upstream turbulence mode: sol – solenoid; ac – acoustic; en – entropy.

Current Study's Applicability

Various aspects of the literature review applied to the current study are discussed here. The wind tunnel used in this study was characterized to have relatively low total pressure fluctuations (from Pitot pressure probe measurements) and mass flux fluctuations (from high-overheat hot-wire anemometry measurements). Regarding velocity and mass flux, the mean values are high since the flow is hypersonic. Therefore, the relative magnitudes of the fluctuations are small, and linearized theories should be fully applicable for this study. Previous studies have shown, however, that for higher Mach numbers, the turbulence amplification diverges from Ribner's linear interaction analysis; this is shown in a compilation by Donzis [45] (Figure 9). Thus, another expected benefit of this test condition is to provide a clear, experimental agreement to DNS or LIA at a hypersonic Mach number.

Another benefit of experimentally studying shock-turbulence interaction in hypersonic flow was that the Mach number behind the normal shock was moderately

subsonic (instead of transonic for a supersonic freestream). For hot-wire anemometry in transonic flow, the thermal response depends on the Mach number; thus, for the planned extended study using hot-wire probes, this hypersonic study will avoid the additional transonic complications behind the normal shock wave.

The relatively low densities of the test flow means that the relatively low-Reynolds number results in this study (experimentally obtained PSD estimates show that the total pressure fluctuations in this study exhibited characteristics of low-Reynolds number turbulence) can be appropriately compared with DNS anchored with the experimental inflow conditions.

Experimentally, this study extends the state of knowledge of pressure fluctuations, which was studied extensively in a shock tube at low Mach numbers by Xanthos, Briassulis and Andreopoulos [52], to hypersonic Mach numbers.

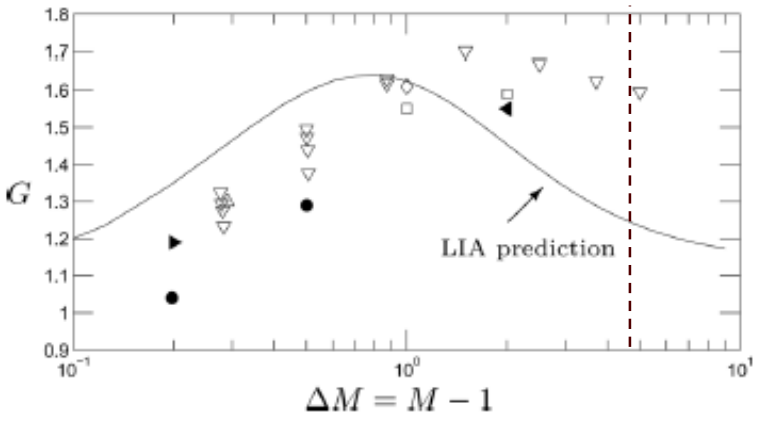

Figure 9. Streamwise velocity amplification factors of various DNS and an experimental study versus the predictions of LIA theory.

Dashed line indicates the Mach number parameter of the current study.

(adapted from Donzis [45])

ACE HYPERSONIC WIND TUNNEL FACILITY

The facility used to conduct these experiments at the TAMU NAL is the Adjustable Contoured Expansion ("ACE") Hypersonic Wind Tunnel. The major parts of the facility and its supporting infrastructure are described in this subsection.

Overview

The ACE hypersonic wind tunnel facility is a M = 5 to 7+ wind tunnel operated in continuous blowdown-vacuum mode for a maximum of 40 seconds once every 2.5-3.0 hours; the flow Re/m ranges from 0.3 to 7.0×10^6/m and is changed by adjusting the settling chamber pressure. The ACE tunnel is one of two, the other being the M6QT, continuous-operation hypersonic wind tunnels at the TAMU NAL complex. First runs of the ACE tunnel and M6QT were performed in 2008. Initially, only one tunnel could be installed at any given time, requiring the time-costly assembly and disassembly of tunnel hardware and instrumentation when switching tunnels. To eliminate that burden, J. W. Hofferth led an effort in late 2009 to modify the infrastructure and install both tunnels in a parallel configuration, allowing for the effortless switching of operation between the two tunnels in any given day.

The description of the design, installation, and preliminary calibration of the ACE tunnel can be found in Semper et al. [53] and Tichenor et al. [54]. A current schematic of the ACE tunnel is shown below in Figure 10.

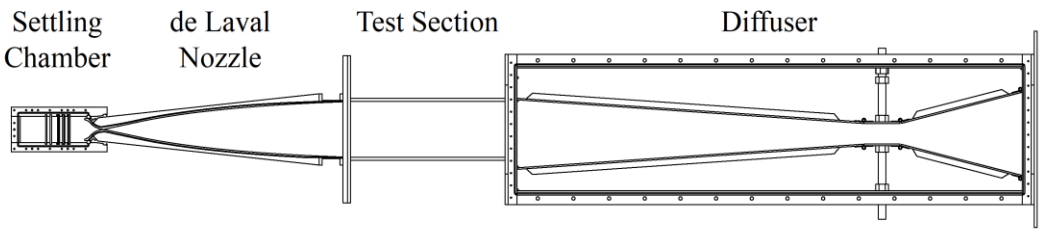

Figure 10. ACE hypersonic wind tunnel schematic.

The ACE tunnel is set up as a typical blowdown-vacuum facility. Air was supplied to the settling chamber from the tunnel infrastructure and expanded through a de Laval nozzle to the test section. A diffuser slows downed the flow in a somewhat controlled manner before it was exhausted to the vacuum created by the ejectors.

One of the defining capabilities of the ACE tunnel is its continuously variable Mach number. The Mach number, *M*, was varied by changing the ratio of the nozzle exit area to the nozzle throat area, which is described inviscidly by the Mach number-area relationship [24]:

$$\left(\frac{A}{A_t}\right)^2 = \frac{1}{M^2}\left[\frac{2}{\gamma+1}\left(1+\frac{\gamma-1}{2}M^2\right)\right]^{\frac{(\gamma+1)}{(\gamma-1)}} \tag{15}$$

or equivalently:

$$\frac{A}{A_t} = \left(\frac{\gamma+1}{2}\right)^{-\frac{\gamma+1}{2(\gamma-1)}} \frac{\left(1+\frac{\gamma-1}{2}M^2\right)^{\frac{\gamma+1}{2(\gamma-1)}}}{M} \tag{16}$$

The ACE tunnel has a rectangular test section with constant width throughout the nozzle and test section. Thus, the Mach number-area relationship can be cast as a Mach number-height relationship:

$$\left(\frac{h}{h_t}\right)^2 = \frac{1}{M^2}\left[\frac{2}{\gamma+1}\left(1+\frac{\gamma-1}{2}M^2\right)\right]^{\frac{(\gamma+1)}{(\gamma-1)}} \tag{17}$$

The ACE tunnel has a constant exit area (and thus constant exit height); therefore, the Mach number was varied by adjusting the nozzle throat height, h_t. With current capabilities, the Mach number was only changed between tunnel runs, and that procedure was done manually. With the eventual installation of actuators, the nozzle throat height adjustment will be performed mechanically between runs, reducing the time needed to change Mach numbers. Then, after the installation of additional appropriate infrastructure to properly change tunnel conditions, the Adjustable Contoured Expansion tunnel will become the Actively Controlled Expansion tunnel with the ability to actuate the nozzle contours and vary the Mach number within a tunnel run. This capability will allow Mach-number-profile experiments to be performed, which include the study of flow hysteresis effects and the study of a hypersonic body's changing flight conditions on boundary layer properties.

To obtain nominal Mach 6 flow, based on previous tunnel calibrations, the throat height was set to 4.37 mm (0.172 in.) at ambient temperature. For inviscid flow, this height yielded a Mach number of 5.87. Typical test parameters are shown below in Table 4. The parameters were chosen based on characterized freestream noise levels, which for a given

Mach number, had two distinct ranges dependent on Re/m. The freestream characterization results are discussed in a later section.

Table 4. Nominal ACE tunnel flow parameters.

Parameter		Low Re/m	High Re/m
M	Mach Number	5.9	5.8
p_t	Settling Chamber Pressure	200 kPa (29 psia)	365 kPa (53 psia)
T_t	Settling Chamber Temperature	425 K (305 °F)	425 K (305 °F)
p_1	Test Section Pressure	140 Pa (1.05 Torr)	285 Pa (2.14 Torr)
T_1	Test Section Temperature	53.4 K (-364 °F)	55.0 K (-361 °F)
Re/m	Test Section Unit Reynolds Number	2.07×10^6/m	3.95×10^6/m

Settling Chamber

This subsection describes the hardware and instrumentation of the ACE tunnel settling chamber.

Hardware

Air was supplied to the settling chamber from the tunnel infrastructure (described later). The purpose of the settling chamber was to condition the flow for expansion to hypersonic Mach numbers. The settling chamber accepted air from the tunnel infrastructure through four inlets (two on top, two on bottom) to promote the uniform distribution of the air in the first section of the settling chamber. Figure 11 shows the settling chamber with its flow conditioning parts.

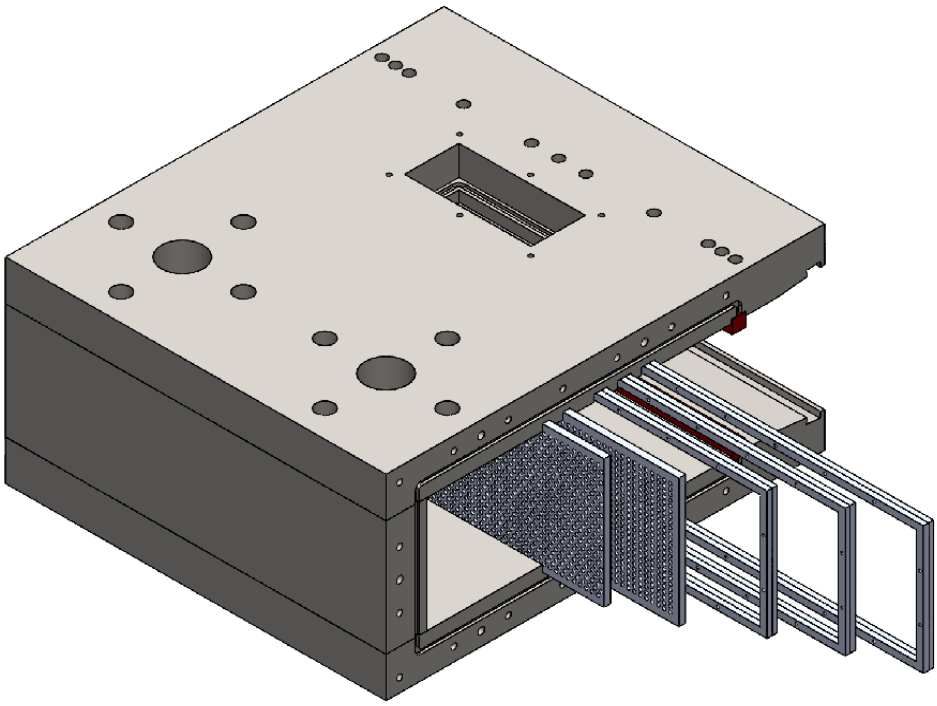

Figure 11. ACE tunnel settling chamber with aerogrids and mesh screen frames.

The air then proceeded through two "aerogrids." Each "aerogrid" was a plate machined with a large number of uniformly distributed holes. Each hole acted similarly to an injector. The backpressure created by the "aerogrid" and the uniform distribution of the holes further served to promote the uniformity of the air supplied to the nozzle. The holes in the second "aerogrid" were offset from the holes of the first "aerogrid" with the purpose again to distribute the flow.

Following the two "aerogrids" were a series of three frames holding wire cloth mesh screens. The mesh screens were of increasing grid density and served to break up any remaining large-scale turbulent structures into smaller turbulent structures, which

were more easily dissipated. The grid densities, from upstream to downstream are listed in Table 5.

Table 5. ACE tunnel settling chamber wire cloth mesh properties.

Location	Grid Density		Wire Diameter		Open Area
	grids/cm	grids/in.	μm	in.	
1st	7.9	20	406.4	0.0160	46%
2nd	23.6	60	190.5	0.0075	31%
3rd	59.1	150	66.0	0.0026	38%

To enable the adjustment of the nozzle throat height for Mach number adjustment, a square strip of silicone rubber bar was used as a flexible seal at the interface of the settling chamber to the nozzle planes (Figure 12).

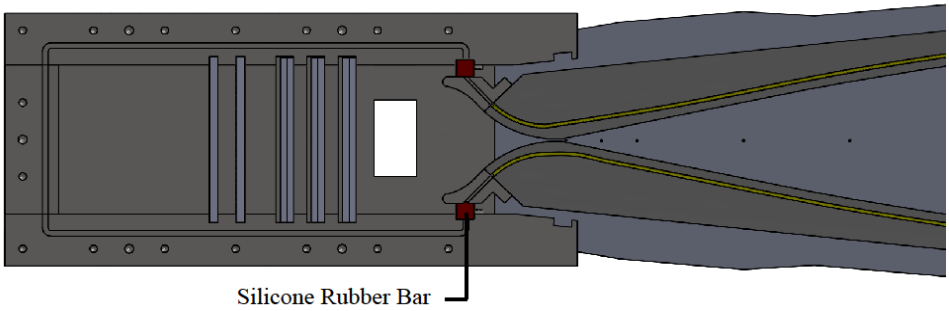

Figure 12. ACE tunnel settling chamber interface with nozzle contour.

Access and instrumentation ports available on the top, bottom, and sides of the settling chamber allowed access to the volume between the last mesh screen and nozzle contraction (Figure 13). The top port was used for instrumentation whereas the other three ports were plugs that could be taken out for access to the settling chamber interior without

having to remove the settling chamber from the tunnel and disassembling a sidewall (a time- and labor-intensive process). A typical reason to access the settling chamber interior was to measure the nozzle throat height after an adjustment and/or after heating the tunnel.

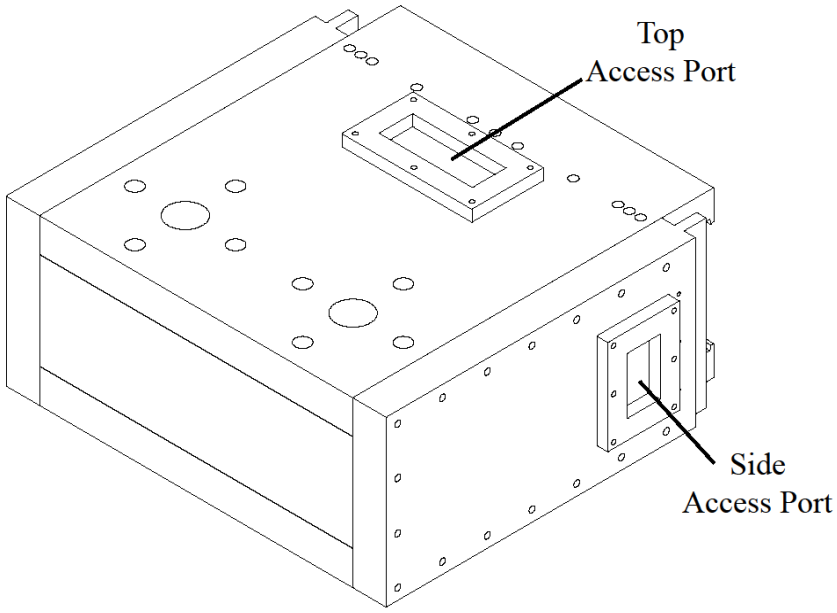

Figure 13. ACE tunnel settling chamber access ports.

Due to the large static temperature decrease typical of hypersonic wind tunnels, the fluid in the settling chamber was heated to a high temperature to avoid liquefaction (condensation) of molecular oxygen in the test environment. Air from the tunnel infrastructure was heated, and to minimize the heat loss from the main heater to the tunnel, ceramic-insulated strip heaters were mounted to the outside walls of the settling chamber. An Omegalux HCS-080-240V (250 W) heater was mounted on each side wall of the settling chamber whereas an Omegalux HCS-120-240V (500 W) heater was mounted on

the top wall (Figure 14); the total heater power is 1000 W. Within an hour of turning the heaters on, the exterior setting chamber wall reached a temperature of about 340 K (150 °F); by the end of the working day, the exterior temperature was about 360 K (200 °F).

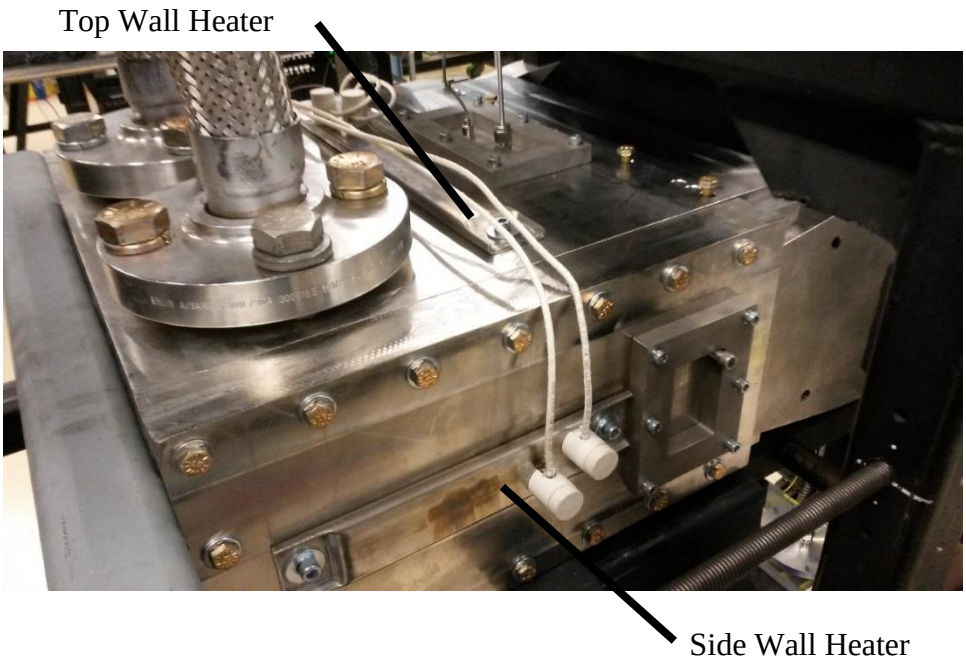

Figure 14. ACE tunnel settling chamber with ceramic heaters installed.

Instrumentation

The settling chamber pressure and temperature were recorded as part of the DAQ process for each tunnel run. They, in addition to other measurements described later, were used to calculate the majority of the test section flow properties. Both measurements were made downstream of the final mesh screen and prior to the contraction section of the nozzle; thus, these measurements were the proper values for the total pressure and

temperature in the isentropic flow equations used to calculate the test section flow parameters.

A Pitot pressure tube was welded to the top access port of the settling chamber. The tube was 3.2 mm (0.125 in.) in diameter with a wall thickness of 0.71 mm (0.028 in.), resulting in an inner diameter of 1.75 mm (0.069 in.). The estimated tube volume was 206.8 mm^3 (0.0126 $in.^3$). The pressure lag due to the tubing was calculated to be negligible; calculations were made according to an equation published by Bauer [55] and referred to in a compilation by Volluz [56]. An Endevco 8540-200 piezoresistive pressure transducer was installed into the top access port into the Pitot pressure probe and measured the settling chamber pressure. It is well-known that piezoresistive sensor parameters are temperature-sensitive ([57]-[59]); therefore, the settling chamber pressure was temperature-corrected in post-processing using Endevco-supplied temperature calibration curves, the sensor voltage (obtained by backing it out of the pressure calculated with the ambient-temperature calibration), and the measured settling chamber temperature.

The settling chamber temperature was measured with an Omega type K thermocouple. The thermocouple consisted of two 0.5 mm (0.020 in.) wires (one wire is chromium-nickel alloy and the other is aluminum-nickel alloy) junctioned into a bead. The bead was exposed to the flow to minimize response time. Based on the response time curves provided by Omega and making rough adaptations to match the flow conditions in this study, the estimated response time of the thermocouple in the ACE tunnel is about 1.0 s. Because of its relatively slow response time, the settling chamber temperature was recorded as an average of the sampling points for each sampling record (250 ms).

ACE Nozzle

This subsection briefly describes the design and instrumentation of the ACE tunnel adjustable nozzle.

Design

The ACE tunnel nozzle was a planar (two-dimensional) nozzle whose contour was calculated using a method-of-characteristics code written by R. D. W. Bowersox, which includes viscous corrections. The nozzle design was verified with CFD using various turbulence models by R. Srinivasan. The nozzle was designed around the Mach 7 flow condition, but it was determined that the rotation of the nozzle planes about the nozzle exit resulted in small discrepancies in the initial wall angle for Mach numbers as low as 5. For more information regarding the nozzle design, see various works by Semper and Tichenor ([53]-[54], [60]-[62]). The throat height was set by a shimming system that sets the distance between a supporting brace attached to the nozzle contour and the nozzle supporting frame.

Instrumentation

The nozzle side wall was outfitted with pressure taps along the sidewall centerline in the expansion region near the throat for diagnostics, which were not needed in these studies. An MKS Baratron 631C-10 capacitance manometer[2] was installed at a pressure tap 11.4 cm (4.5 in.) upstream of the nozzle exit plane, which was well beyond the last

[2] http://www.mksinst.com/docs/R/631C-MAN.pdf

characteristic, to measure the nozzle static pressure. The Baratron transducer was accurate to 0.5% of the reading and was actively heated to 423 K (150 °C, 300 °F) to minimize error due to temperature effects. The nozzle exit Mach number was calculated using an isentropic flow equation with the settling chamber pressure and nozzle static pressure:

$$\frac{p_t}{p} = \left(1 + \frac{\gamma - 1}{2} M^2\right)^{\frac{\gamma}{\gamma - 1}} \tag{18}$$

which is rearranged to:

$$M = \left(\frac{2}{\gamma - 1}\left[\left(\frac{p_t}{p}\right)^{\frac{\gamma - 1}{\gamma}} - 1\right]\right)^{1/2} \tag{19}$$

Test Section

The ACE tunnel test section had a constant area cross-section with dimensions 0.232 m x 0.359 m (9.13 in. x 14.13 in.). The test section was rectangular and is 0.686 m (27.0 in.) long. On each side of the test section were three 127 mm-diameter (5.0 in.) access/instrumentation ports that could accept 152 mm-diameter (6.0 in.) discs/windows. The ports were centered 15.2 cm (6.0 in.), 34.2 cm (13.5 in.), and 53.3 cm (21.0 in.) downstream from the nozzle exit. Figure 15 shows a schematic of the ACE tunnel test section.

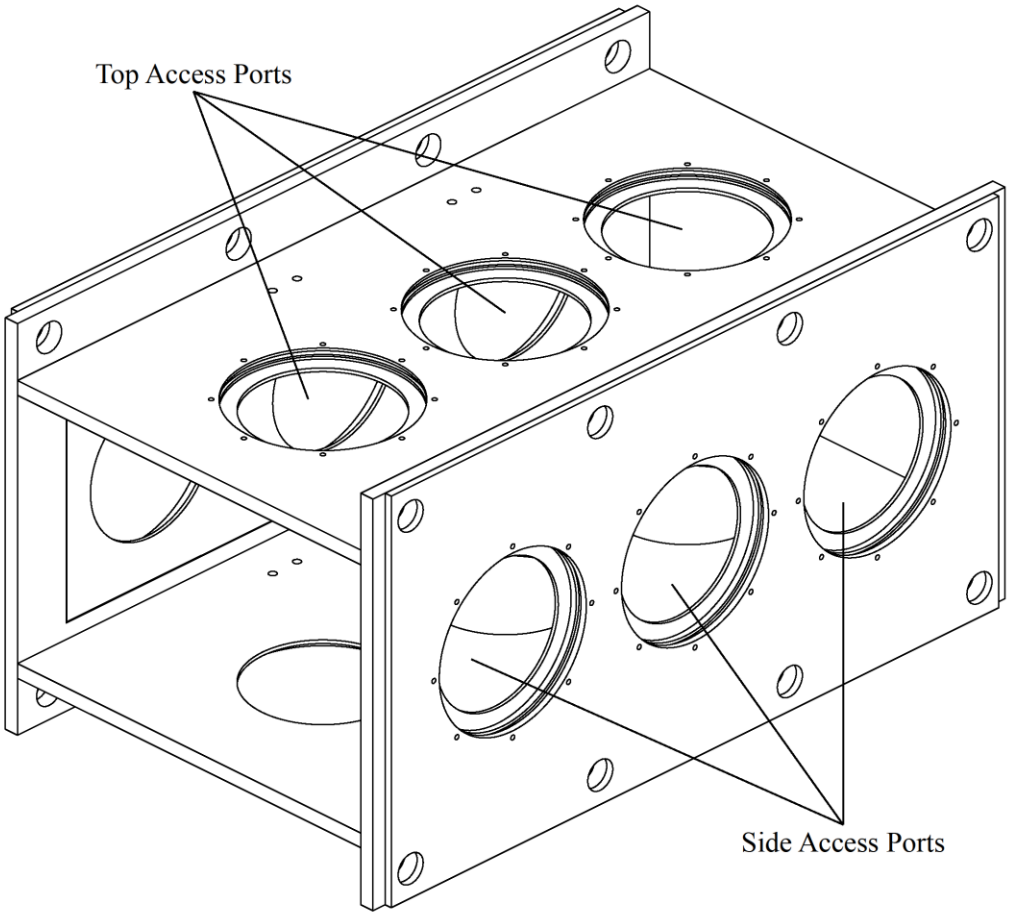

Figure 15. ACE tunnel test section.

Diffuser

Diffusers are mechanisms that slow the test flow and recompress the fluid before it is exhausted through an ejector or to a vacuum tank. Diffusers reduce the driving pressure needed to achieve supersonic or hypersonic flow, and Anderson [24] stated that "diffuser design is more of an art than a science." The ACE tunnel diffuser design, shown below in Figure 16, was based on work by Wegener and Lobb [63] and Bertram [64], and

the geometry was chosen to match Bertram ([53]-[54], [60]-[62]). The diffuser efficiency (defined as the diffuser pressure at the throat divided by the theoretical pressure behind a normal shock at the operational Mach number) was experimentally determined by Semper [62] to be approximately 0.7 – 0.8. In the current study, with the relatively large blockage area presented by the models, the diffuser throat was set at a relatively large height of 21.3 cm (8.375 in.).

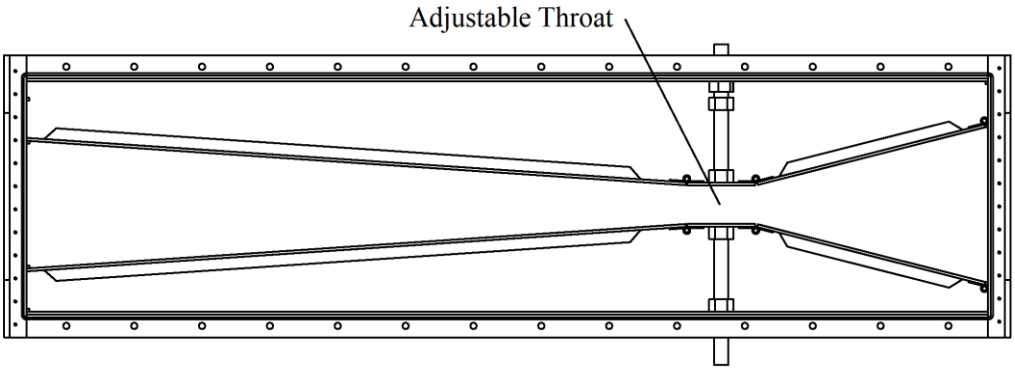

Figure 16. ACE tunnel diffuser.
(chosen throat height not depicted in this figure)

Supporting Infrastructure

The ACE tunnel and M6QT were supported in their operations by extensive infrastructure. This section describes the major components of that infrastructure, which were the compressors, the heater, and the ejectors.

Compressed Air

Compressed air was required to drive the ejectors (described later) and the tunnels. The air was kept in a 23.2 m^3 (820 $ft.^3$) storage tank at a maximum pressure of 17.3 MPa (2500 psig). The storage capacity and the mass flow requirements of the tunnel (about 1 kg/s) and the ejectors (about 21 kg/s) *limited the run time of the ACE tunnel or M6QT to about 40 s*. The storage tank was recharged by two, recently installed CompAir Reavell 5442 compressors, each with a pumping capacity of 3.7 standard m^3 per minute (130 standard $ft.^3$ per minute). Given the pumping rate and the typical pressure remaining in the storage tank after a typical tunnel run, *the duty cycle of the ACE tunnel and M6QT was about 2.5-3.0 hours*.

Compressed air from the compressors was post-processed through a cyclone separator to remove large particles, two filters to remove oil droplets and smaller particles, and a dryer to reduce the dew point to 233 K (-40 °C, -40 °F) before being stored in the tank. Two pipelines from the storage tank routed the compressed air to the ejectors (4 in. steel pipe) and to the tunnel supply infrastructure (2 in. stainless steel pipe).

Heater

Air directed through the tunnel supply infrastructure enters a 500 kW heater with a maximum output temperature of 533 K (260 °C, 500 °F). The air was heated to avoid liquefaction (condensation) of oxygen when the air was expanded in the nozzle. The infrastructure from the heater to the tunnel was equipped with heaters and fiberglass insulation to minimize thermal losses. Maximum and nominal temperatures are listed in Table 6.

Table 6. Maximum and nominal temperatures for heater and ACE tunnel settling chamber.

	Heater			Settling Chamber		
	K	°C	°F	K	°C	°F
Maximum Temp	533	260	500	480	205	405
Nominal Temp	500	225	440	425	150	305

Tunnel Supply

The heated air proceeded into the laboratory and flowed through a 1-μm filter obtained as part of the M6QT infrastructure. Afterwards, the air was directed towards either the ACE tunnel or M6QT with a set of manually-operated ball valves. When operating the ACE tunnel, this supply line was directed into the four inlets of the settling chamber.

Ejectors

The vacuum portion of the blowdown-vacuum method of operation was provided by a two-stage ejector. The ejector operates on the principle of the Venturi effect in which fluid pressure is reduced when its velocity increases.

Each stage of the ejector was a nozzle that expanded its supplied air across an orifice of a pressure vessel. For the first stage, the pressure vessel were the wind tunnels. For the second stage, the pressure "vessel" was the exhaust of the first stage. Each ejector stage was supplied by air regulated to desired pressures by two regulators. Further information about the ejector system, including performance characteristics, are found in an appendix of Tichenor's dissertation [61].

The ejectors typically established a vacuum of about 1300 Pa (10 Torr). This created an increase in the pressure ratio (defined as ratio of settling chamber pressure to diffuser pressure) necessary to "start" the tunnel (i.e., the flow goes supersonic/hypersonic). The ejectors maintained the vacuum during the run, which provided a high enough pressure ratio during the run to maintain hypersonic flow. Estimated pressure ratios for starting and maintaining hypersonic flow can be found in Pope and Goin [65].

Typical Tunnel Operational Procedure

This subsection provides a general list of steps involved in a typical tunnel run of the ACE tunnel and M6QT.

- Preheat (heat air to desired operating temperature)
    - Open knife gate valve for appropriate tunnel.
    - Open tunnel supply valve for appropriate tunnel.
    - Open actuated 2 in. stainless steel pipeline valve.
    - Increase heater set point.
    - Open actuated tunnel supply valve.
    - Allow air from heater to increase to operating temperature while letting outgoing air convectively heat the tunnel.
    - Decrease heater set point at appropriate time to stabilize temperature of ceramic elements and air supply for the impending, actual tunnel operation.
    - Close actuated tunnel supply valve.
    - Sound warning horn and observe external cameras for bystanders.
- Operation
    - Open actuated 4 in. steel pipeline valve.
    - Load ejector supply regulators to start regulators.
    - Ejector stages establish a vacuum in the tunnel.
    - Open actuated tunnel supply valve to provide settling chamber pressure.

- Tunnel “starts” when proper pressure ratio is achieved.
- Adjust tunnel operating parameters, as necessary.
- Collect/record data for up to 40 s.
- Unload the ejector supply regulators.
- Close actuated 4 in. steel pipeline valve.
- Close actuated 2 in. stainless steel pipeline valve.
- Allow remaining air in 2 in. stainless steel pipeline to vent via tunnel to ejectors.
- Close actuated tunnel supply valve.
- Close tunnel supply valve.
- Close tunnel knife gate valve.

MACH STEM GENERATOR MODEL DESIGN

This section describes the design and implementation of the Mach stem generators used in this study. Dimensional drawings are provided in Appendix C.

Generating a Normal Shock or Mach Stem

Creating a normal shock to perform fundamental shock-turbulence interaction studies can generally be done in one of two ways:

- Generating a traveling normal shock from the sudden exposure of a high-pressure region to a low-pressure region (e.g. a shock tube). Most shock-turbulence interaction studies performed with a shock tube have been by the Andreopoulos research group ([7], [46], [51]-[52]).
- The prescribed intersection of two oblique shock waves generating a Mach stem in a continuous-operation wind tunnel, such as that in the work by Barre, Alem, and Bonnet [48].

This shock-turbulence study used a generated Mach stem as the normal shock wave. The Mach stem originated from the intersection of symmetric, oblique shock waves emanating from wedge models placed in the test section.

The desired leading wedge angle was calculated using compressible flow and shock wave theory. The required leading edge angle must be:

- large enough to require a Mach reflection and that a Mach stem (normal shock) is generated to maintain flow symmetry and

- not so large that the oblique shock wave is no longer attached to the wedge leading edge.

Typically, when an oblique shock wave impinges on a solid surface or an axis/plane of symmetry, a reflected shock is emanated to turn the flow behind the initial oblique shock wave to become parallel to the surface or axis/plane and satisfy geometric constraints [24]. Figure 17 depicts this situation.

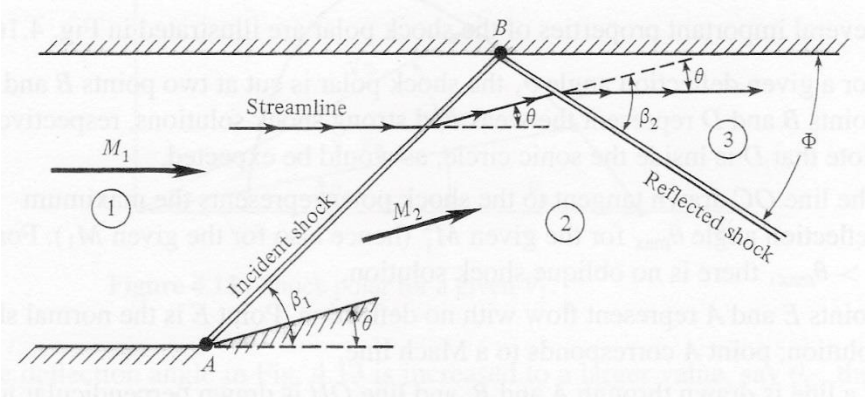

Figure 17. Regular, oblique shock wave reflection.
(taken from Anderson [24])

Sometimes, though, the flow's Mach number is low enough that a regular reflection will not be enough to properly turn the flow. A Mach reflection then occurs and a Mach stem (normal shock) emanates from the wall or axis/plane of symmetry to maintain flow tangency to the wall or axis/plane of symmetry. This situation is shown in Figure 18 and briefly introduced in Anderson [24].

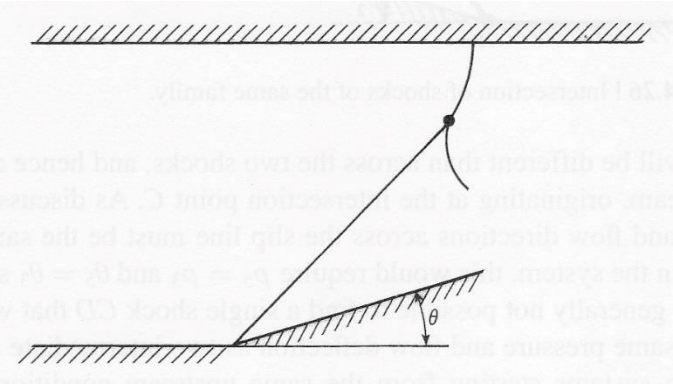

Figure 18. Irregular, Mach stem reflection.
(taken from Anderson [24])

The procedure to estimate the desired leading wedge angle, coded in MATLAB [66], is described:

- For a given Mach number, M_1:
    - The smallest shock wave angle is that of a Mach wave and corresponds to a deflection angle of $\delta = 0°$.

$$\theta_{1,\min} = \sin^{-1}\left(\frac{1}{M_1}\right) \tag{20}$$

    - The largest shock wave angle there could possibly be is that of a normal shock wave.

$$\theta_{1,\max} = 90° \tag{21}$$

- For the range of θ_1 from $\theta_{1,\min}$ to $\theta_{1,\max}$, there is a corresponding range of deflection angles δ_1 supported at this Mach number (Eq. 139a from NACA Report 1135 [25]).

$$\delta_1 = \tan^{-1}\left(2\cot\theta_1 \frac{M_1^2 \sin^2\theta_1 - 1}{2 + M_1^2\left(\gamma + 1 - 2\sin^2\theta_1\right)}\right) \tag{22}$$

- The maximum deflection angle δ_1 corresponding to the range from $\theta_{1,\min}$ to $\theta_{1,\max}$ for a particular M_1 is the *incident shock critical deflection angle*, i.e., the leading wedge angle must be less than this deflection angle to keep the oblique shock attached to the wedge.
- M_2 can now be calculated for each combination of (M_1, θ_1, δ_1) (Eq. 131 from NACA Report 1135 [25]):

$$M_2 = \frac{1}{\sin\left(\theta_1 - \delta_1\right)} \sqrt{\frac{\left(\gamma - 1\right) M_1^2 \sin^2\theta_1 + 2}{2\gamma M_1^2 \sin^2\theta_1 - \left(\gamma - 1\right)}} \tag{23}$$

- For a Mach number of M_2 behind the oblique shock wave, a similar process as that for M_1 is carried out to find the supported range of deflection angle δ_2.

$$\theta_{2,\min} = \sin^{-1}\left(\frac{1}{M_2}\right) \tag{24}$$

$$\theta_{2,\max} = 90° \tag{25}$$

$$\delta_2 = \tan^{-1}\left(2\cot\theta_2 \frac{M_2^2 \sin^2\theta_2 - 1}{2 + M_2^2\left(\gamma + 1 - 2\sin^2\theta_2\right)}\right) \tag{26}$$

- For each combination of (M_1, θ_1, δ_1), starting with the combination of (M_1, $\theta_{1,\min}$, $\delta_{1,\min}$), calculate the corresponding M_2 and its range of θ_2 and δ_2.
    - If the maximum δ_2 for the particular combination of (M_1, θ_1, δ_1) is greater than that particular δ_1, then the flow behind the oblique

shock wave *can* still turn back the deflection angle δ_1 with a regular reflection (another oblique shock wave). Repeat the process now using a slightly larger θ_1.

- If the maximum δ_2 for the particular combination of (M_1, θ_1, δ_1) is less than that particular δ_1, then the flow behind the oblique shock wave *cannot* turn back the deflection angle δ_1 with a regular reflection. Therefore, a Mach reflection will occur, and a Mach stem will be generated. This δ_1 is the *reflected shock critical deflection angle* for this particular value of M_1, i.e., the leading wedge angle must be greater than this δ_1 to obtain a Mach stem.

- For a particular M_1, both critical deflection angles are now known. Figure 19 shows the incident and reflected shock critical deflection angles for each Mach number. The red line shows the chosen leading wedge angle for the ACE tunnel Mach number parameter space.

Since the ACE tunnel's operational Mach number is between 5 and 7, *a leading wedge angle of 35°* was chosen since it is between the two curves (greater than the reflected shock critical angle and less than the incident shock critical angle) in that Mach number range.

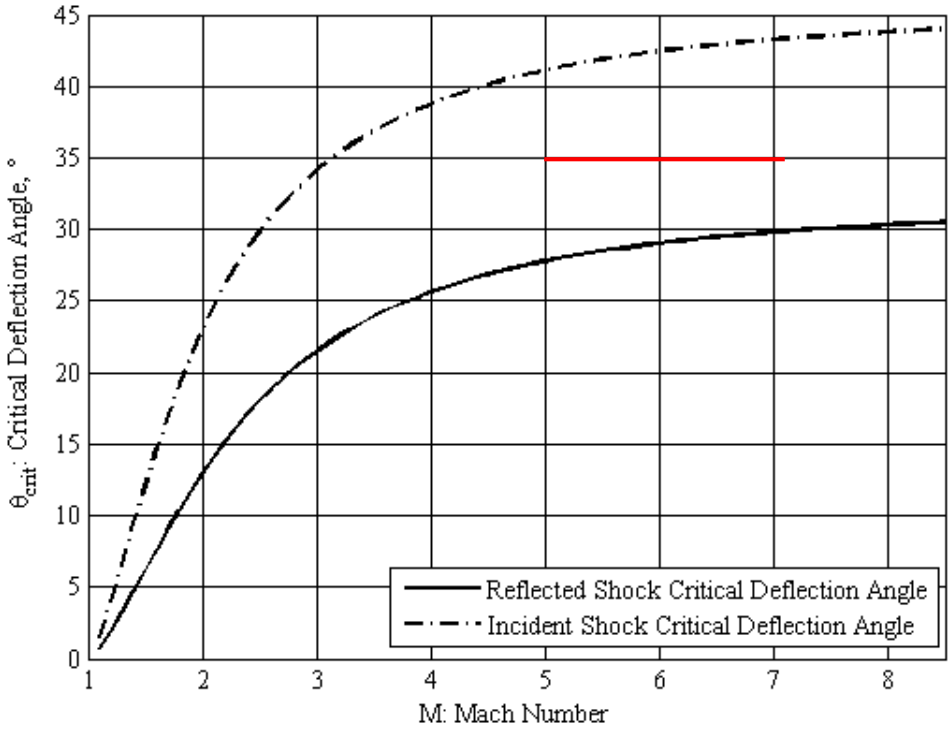

Figure 19. Oblique shock wave critical deflection angles versus Mach number.
The red line denotes the wedge leading angle chosen for the ACE tunnel's Mach number parameter space.

Struts and Supports

To mount the Mach stem generator wedges to the tunnel test section, a set of struts and supports were designed. The struts, like the wedges, had a sharp leading edge to keep the shock waves attached and had shallow-angle trailing surfaces to keep the flow attached to the struts.

Anderson [24] stated that since the region behind a Mach stem is subsonic, prediction and analyses of the resulting flow field must be performed with sophisticated

numerical techniques. Thus, it is not easily known what the height of the Mach stem will be and how the distance between the Mach stem generator wedge models affected the overall wave structure. It was, therefore, initially desirable to design the supports with the capability to adjust the spacing between the wedges (by adjusting the height of the wedges relative to the tunnel test section floor and ceiling) so that the optimal spacing could be determined experimentally.

The Mach stem generator wedges were fastened to an inner strut (Figure 20), which is shaped similarly to a supersonic airfoil in that it has a sharp leading edge angling out to a flat section, followed by shallow-angled surfaces ending in a sharp trailing edge. The inner strut has two 6.4 mm (0.25 in.) thru holes spaced 9.5 mm (0.375 in.) apart to secure it to the outer strut.

The outer strut was assembled from two parts and forms a "pocket" that the inner strut sat in. The external profile of the outer strut assembly resembled the profile of the inner strut. The outer strut had four 6.4 mm (0.25 in.) thru holes spaced 9.5 mm (0.375 in.) apart, matching the size and spacing for the inner strut's thru holes. To secure the inner strut to the outer strut, 6.4 mm (0.25 in) dowel pins were inserted through the thru holes of the outer and inner struts. The thru hole spacing allows the adjustment of each Mach stem generator wedge's height by 9.5 mm (0.375 in.). Figure 21 shows the exploded assembly.

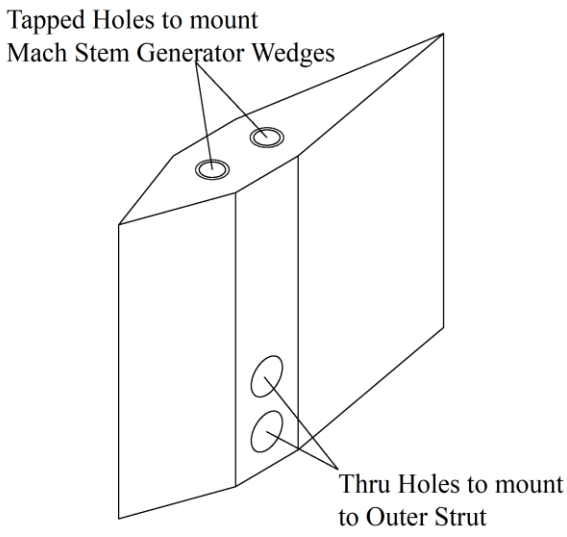

Figure 20. Mach stem generator wedge model inner strut schematic.

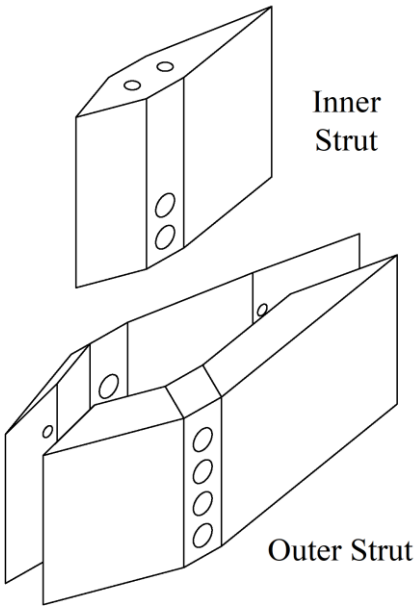

Figure 21. Mach stem generator wedge model inner and outer struts (exploded assembly).

An additional mechanism for the height adjustment of each wedge was a spacer between the outer strut assembly and the test section floor or ceiling. The spacers had the same external profile as the outer strut assembly and added 19.1 mm (0.75 in.) to the height of the overall assembly.

The wedge, strut, and spacer assembly was mounted to the test section via a plug that fit into one of the test section's access/instrumentation ports. The full support assembly is shown in Figure 22.

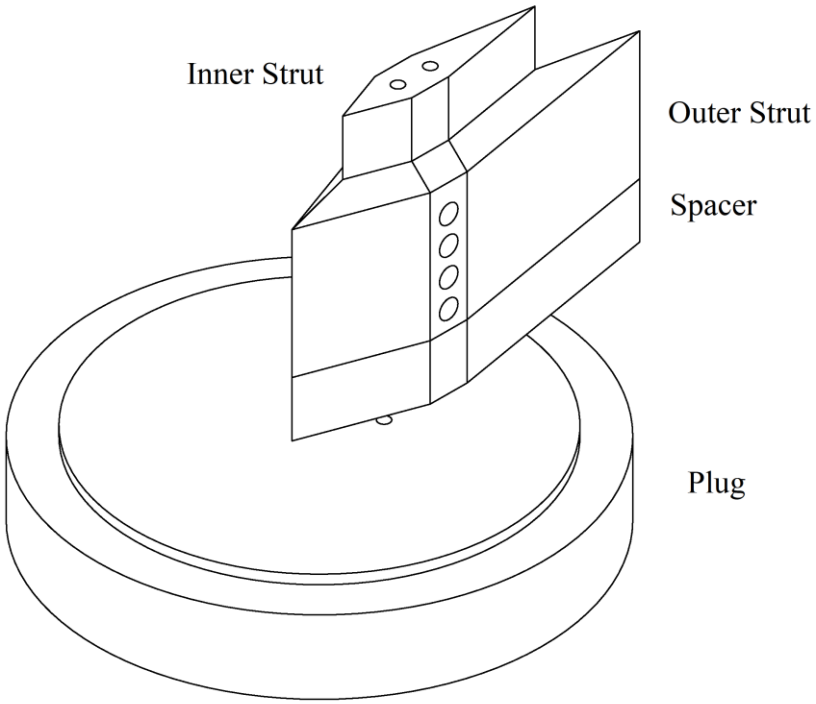

Figure 22. Mach stem generator wedge model struts, spacer, and plug assembly.

Mouton and Hornung

A predictive, theoretical tool was developed by Mouton and Hornung [67] to determine the height of the Mach stem in steady flow given a non-dimensional wedge geometry. Based on the generalized geometric solution, an in-house MATLAB program was written to compute and plot the initial flow structures given a wedge geometry [66]; details of the calculations are provided in Appendix B. The structure properties computed and plotted were:

- wedge surface,
- oblique shock wave,
- triple point intersection,
- reflected shock wave,
- Mach stem,
- leading and trailing expansion wave from wedge expansion corner,
- initial slip line/shear layer, and
- sonic throat.

Figure 23 is an example of a plot generated from the MATLAB code compared with a schlieren image obtained experimentally. The parameters used to generate the plot are listed in Table 7.

Table 7. Parameters used for Figure 23.

Parameter		Value
M	Mach Number	5.85
γ	Specific Heat Ratio/Adiabatic Index	1.4
θ_1	Initial Wedge Angle	35°
g^+	Non-Dimensional Wedge Spacing (= g/w)	0.85

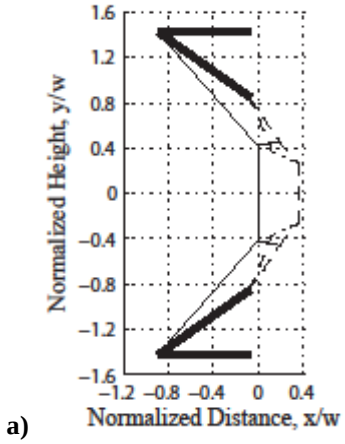

a)

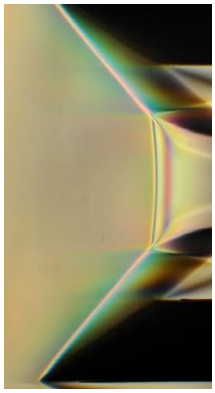

b)

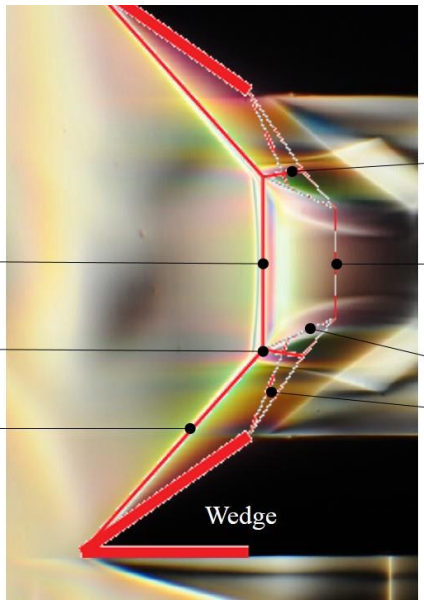

c)

Figure 23. Mach stem flow structure comparison (wide wedges) between theory and experiment.

a) Generalized solution method from Mouton and Hornung [67].

b) Schlieren image of initial flow structure between Mach stem generator wedges.

c) Overlay of Mouton and Hornung solution onto experimental schlieren image.

Wedge Sizing

With the Mach stem generator wedge angle determined, the tunnel blockage was considered. Models placed in the tunnel test section restrict the available cross-sectional area to pass the necessary mass flow. Too much blockage prevents the tunnel from passing the initial requisite mass flow and starting shock wave and does not allow the tunnel to "start." Previous blockage studies showed that the largest blockage permissible was from a 7.6 cm (3.0 in.) diameter capsule (blunt body). Therefore, the first set of Mach stem generator wedge models were designed so that the frontal area of the Mach stem generator wedges and the supporting struts did not exceed 45.6 cm^2 (7.0 $in.^2$). Given the minimum reasonable size of struts and supports needed, the first set of Mach stem generator wedges were 12.7 mm (0.5 in.) thick and 76.2 mm (3.0 in.) wide.

To stabilize the wave structure, the wedges were designed with a long, flat portion after the initial leading angle. This was later determined to not be necessary since Ben-Dor et al [68] determined theoretically, and Chpoun and Leclerc [69] determined experimentally, that the wedge expansion angle did not affect the Mach stem height. To keep the flow attached and reduce blockage, the wedges had a gradual angle opening back to the original area. Figure 24 shows the designed and actual model of the initial set of Mach stem generator wedges. Figure 25 is a SolidWorks assembly of the initial Mach stem generator wedge assembly installed in the ACE tunnel test section.

a) 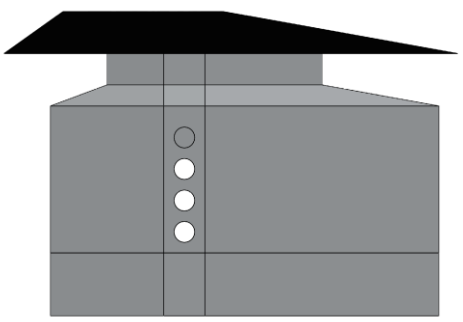 b) 

Figure 24. Mach stem generator wedge (initial set) model assembly (side view).
a) SolidWorks model. b) Physical model.

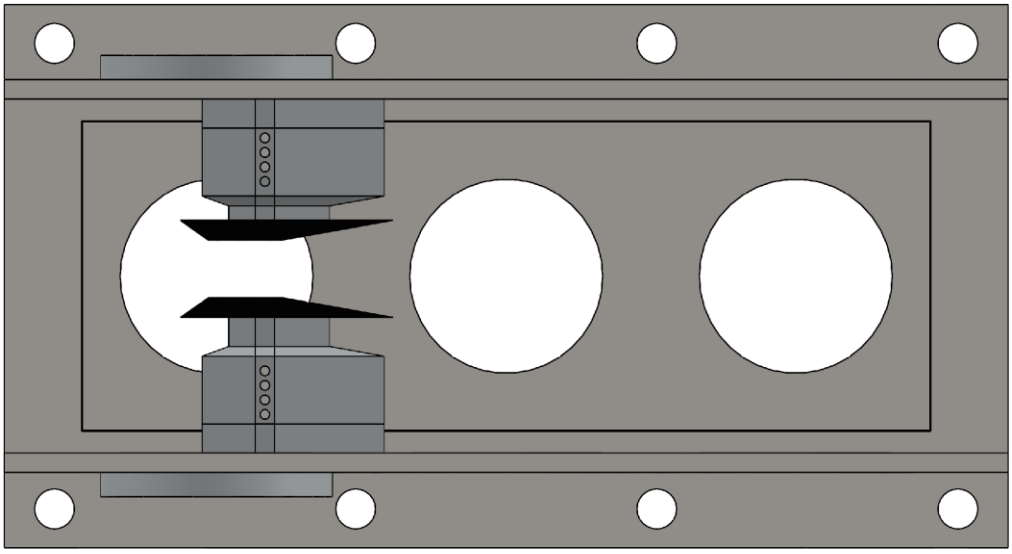

Figure 25. Mach stem generator wedge (initial set) model assembly in ACE tunnel test section (side view).

A few wedge separation distances were tested with this initial set. The schlieren images of the three distances tested are shown in Figure 26.

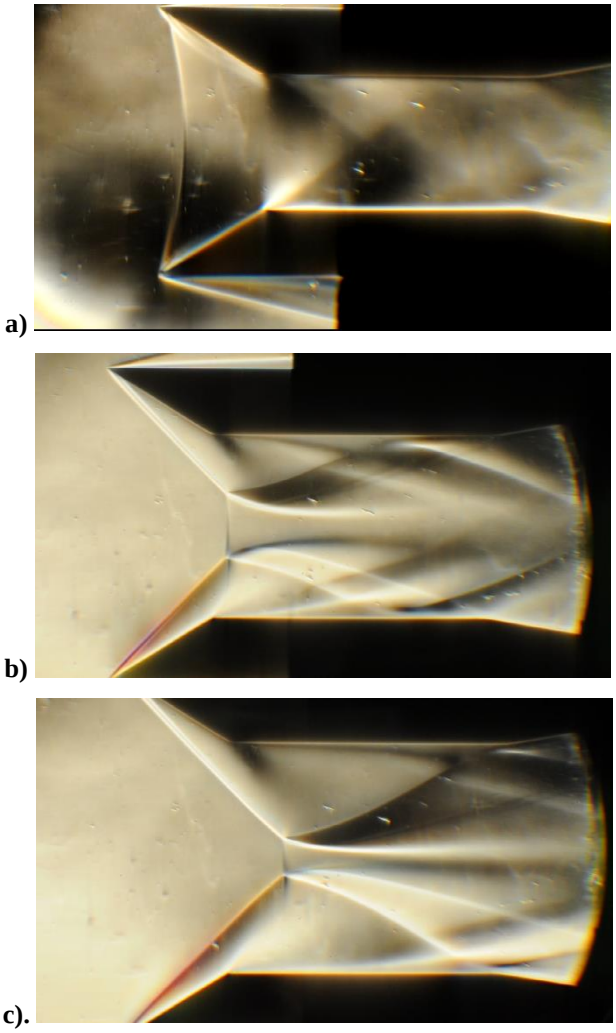

Figure 26. Mach stem generator wedge model separation distance comparison.
Distances are between the inner flat portions of the wedge models.
a) 27 mm (1.07 in.). (Run 1806)
b) 37 mm (1.44 in.). (Run 1807)
c) 46 mm (1.82 in.). (Run 1808)

The first panel shows a separation distance of about 27 mm (1.07 in.) between the inner flat portions. The shock structure is not formed, and it was believed the separation between the wedges was too small to properly pass the starting shock and establish the

shock structure. The second panel shows a separation distance of about 37 mm (1.44 in.) between the inner flat portions, and the expected pattern of oblique shock waves intersecting irregularly and generating a Mach stem was observed. In the third panel, the separation distance was further increased to 46 mm (1.82 in.). The Mach stem was established, but was much smaller than in the previous panel. From the schlieren images of these shakedown tests, a separation distance of 37 mm (1.44 in.) was used for the next sets of tests.

A set of preliminary data with this initial set of Mach stem generator wedges showed unexpected results upstream of the Mach stem; hot-wire mean and fluctuation data were increasing well in front of the Mach stem (starting 6 mm in front) when both mean and fluctuation values should have been almost constant. It was believed that this phenomenon was due to pronounced probe-shock interaction. Since the aspect ratio (width-to-height ratio of the spacing in between the wedges) was relatively small, the three-dimensional relieving effects at the side edges of the model possibly had a relatively strong influence on the test area, which may have exacerbated the probe-shock interaction's effect on the results.

To mitigate the possible effect of the three-dimensional pressure relieving at the sides of the model on the test area in the center of the model, a wider set of Mach stem generator wedges were designed and machined. The "wide" wedges were 203 cm (8.0 in.) in width, more than double of the initial set of wedges. A width that spanned nearly all of the test section (35.9 cm, 14.13 in.) was not desirable since the model might cause the sidewall boundary layer to separate and increase blockage. The thickness remained the

same as the previous set at 12.7 mm (0.5 in.). Increasing the width meant increasing the blockage area. Since the 7.6 cm (3.0 in.) diameter model limit was based on a blunt body (which established a bow shock "presenting" a relatively large blockage area), it was reasoned that the tunnel would likely "start" with a wider wedge model, since the shock waves would be attached ("presenting" a relatively smaller blockage area than a blunt body). The tunnel, in fact, did start successfully with the wider Mach stem generator wedges.

Figure 27 shows two schlieren images comparing the flow structures present between the initial set of wedges and the wide set of wedges. It is obvious that the Mach stem was larger between the wide set of wedges and existed in a position more upstream than the Mach stem between the initial set of wedges. Thus, it can be concluded that the three-dimensionality of the geometry had a relatively strong influence on the flow in the narrower (initial) set of wedge models.

a)

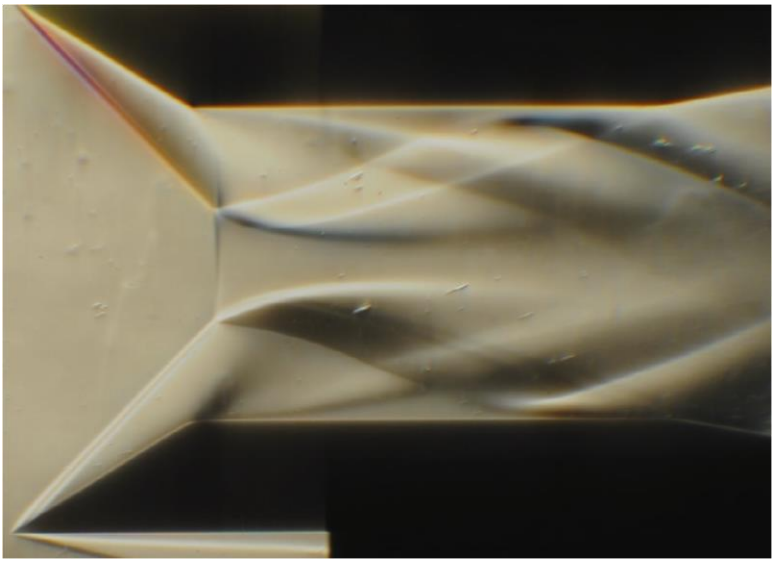

b)

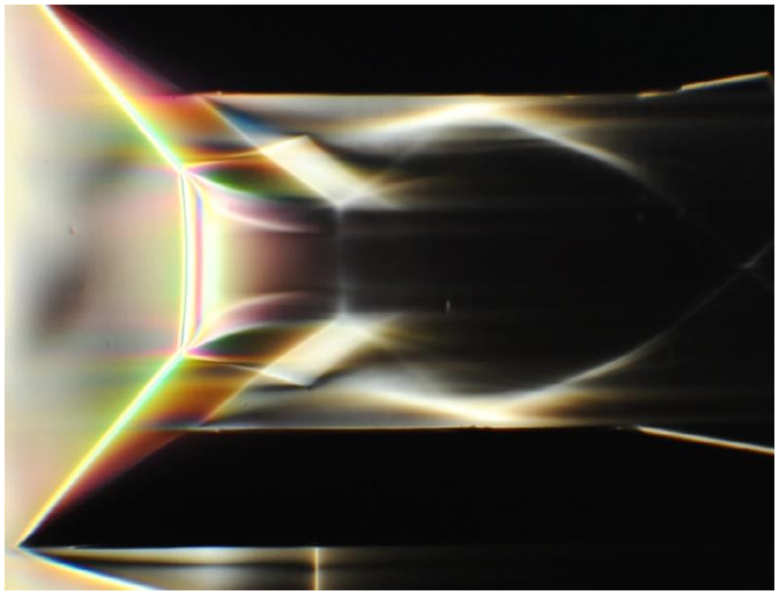

Figure 27. Mach stem generator wedge model width comparison with schlieren imaging.

Images are of comparable scale.

a) 76.2 mm (3.0 in.)-wide model with horizontally-oriented schlieren imaging knife-edge. (Run 1807)

b) 203 mm (8.0 in.)-wide model with vertically-oriented schlieren imaging knife-edge. (Run 2058)

Schlieren imaging movies were recorded during the tunnel runs. It was observed that the Mach stem position moved slightly downstream by about 1 mm (0.039 in.) with increased freestream pressure (Re); Figure 28 shows a comparison. The Mach stem was also observed to move slightly, depending on an instrument probe tip's location relative to the Mach stem with the effect more pronounced when the probe tip was upstream of the Mach stem. With these variations, it was desirable to reduce the relative effect of the probe on the position of the Mach stem. Based on intuition and [66], it was rationalized that scaling up the wedge geometry (wedge thickness and separation distance) would scale up the Mach stem height and make it larger relative to the size of the instrument probes. To make the Mach stem height about ten times greater than the typical instrument probe diameter (3.2 mm, 0.125 in.), the geometry was scaled up by 75% to give a Mach stem height of about 30.5 mm (1.2 in.). Scaling the geometry required some compromises given the space constraints of the test section. The major changes were 1) the flat portion had to be shortened to maintain the same leading and trailing angles (recall that this does not change the Mach stem height), and 2) the model had to be moved further upstream in the test section for proper clearance of the traverse strut that supported the instrument probes.

a)

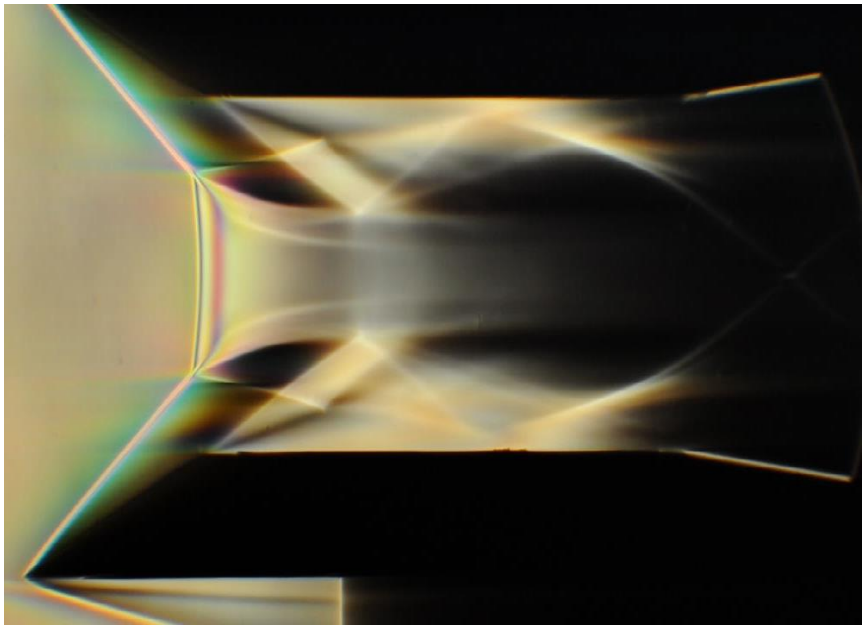

b)

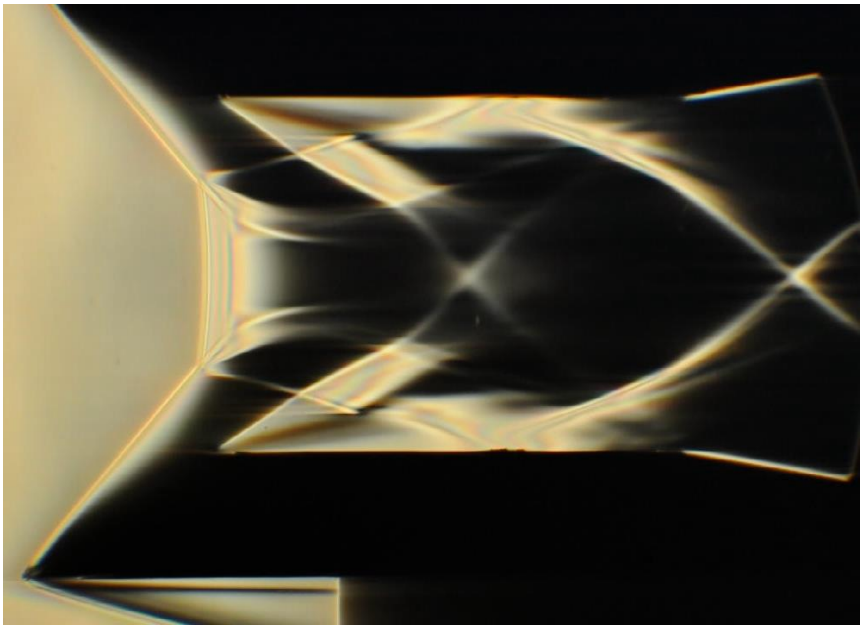

Figure 28. Flow structure variation observed with schlieren imaging. (Run 2059) Images are of same scale. Mach stem position variation of about 0.9 mm (0.035 in.). a) p_{t1} = 1.38×10^5 Pa (20 psia). b) p_{t1} = 5.17×10^5 Pa (75 psia).

Figure 29 shows the thick wedge SolidWorks and physical models. Figure 30 is a SolidWorks assembly of the thick wedge model assembly in the ACE tunnel test section. Figure 31 compares the theoretical flow structure to a schlieren image taken during a tunnel run. As expected, the flow structures scaled up with the wedge geometry. The new wedge separation distance is 67 mm (2.625 in.). Scaling the geometry did not affect how the Mach stem moves with pressure (Reynolds number); however, now when an instrument probe is downstream of the Mach stem, the Mach stem position no longer changes. *The thick wedge model set was used for the remainder of this study.*

Table 8 summarizes the parameters of the various Mach stem generator wedges. A comparison of data obtained with the wide wedges and data obtained with the thick wedges are presented in Appendix G.

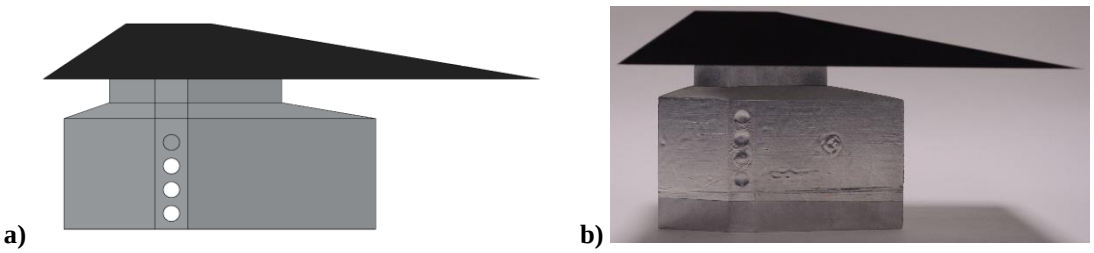

a) **b)**

Figure 29. Mach stem generator wedge (thick set) model assembly side view.
a) SolidWorks model. b) Physical model.

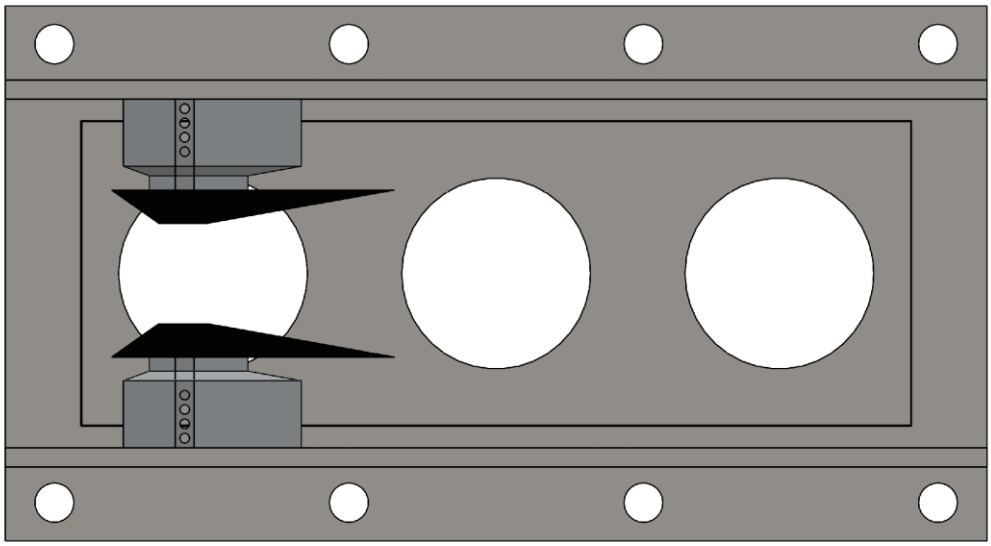

Figure 30. Mach stem generator wedge (thick set) model in ACE tunnel test section.

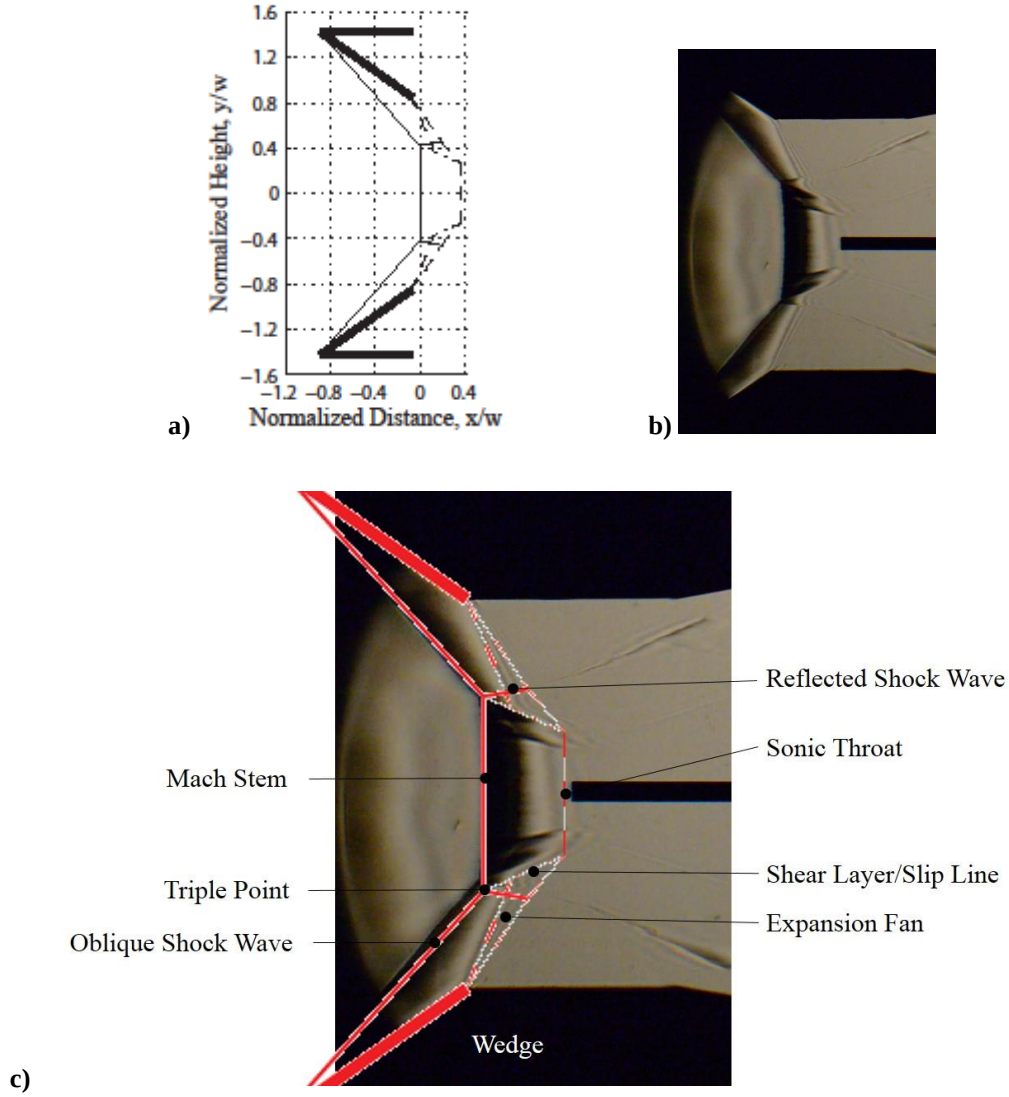

Figure 31. Flow structure comparison (thick wedges) between theory and experiment.

a) Generalized solution method from Mouton and Hornung [67].

b) Schlieren image of initial flow structure between Mach stem generator wedges.

c) Overlay of Mouton and Hornung solution onto experimental schlieren image.

Table 8. Mach stem generator wedge parameters.

	Initial	Wide	Thick
Design-Against Parameter	Blockage	3-D Effects	Probe Effects
Leading Wedge Angle	35°	35°	35°
Width	76.2 mm (3.0 in.)	**203.2 mm (8.0 in.)**	203.2 mm (8.0 in.)
Thickness	12.7 mm (0.500 in.)	12.7 mm (0.500 in.)	**22.2 mm (0.875 in.)**
Flat Length	49.5 mm (1.95 in.)	49.5 mm (1.95 in.)	**32.8 mm (1.29 in.)**
Trailing Edge Angle	10°	10°	10°
Overall Length	139.7 mm (5.5 in.)	139.7 mm (5.5 in.)	**190.5 mm (7.5 in.)**
Separation Distance	37 mm (1.44 in.)	37 mm (1.44 in.)	**67 mm (2.63 in.)**

Wedge Alignment

The alignment of the Mach stem generator wedge models in the ACE tunnel test section was accomplished in conjunction with the alignment of the main schlieren imaging optical beam. The schlieren optical beam path was aligned in the left-to-right direction (upstream-to-downstream in tunnel reference frame), and the wedges were aligned in the "yaw" angle according to this beam. The wedge "yaw" alignment was verified by making measurements of the wedge leading edge relative to the tunnel nozzle exit plane.

The wedge "roll" and "pitch" angles were aligned independently to within 0.15° with a digital inclinometer (the resolution of the inclinometer was 0.10°), and better alignment was difficult to achieve. The "pitch" alignment was verified by measuring the

distances between the leading edges of the wedges and the distances between the trailing edges of the wedges. The schlieren optical beam was then aligned up-to-down (wall normal in the tunnel reference frame) to the “roll”-aligned wedges.

FLOW VISUALIZATION AND MEASUREMENT TECHNIQUES

This subsection describes the various techniques used to visualize the flow and obtain measurements.

Schlieren Imaging

In making shock-turbulence interaction measurements, it is imperative to know where the Mach stem resides and the location of an instrument probe relative to the Mach stem. Shock waves, while transparent, create strong density gradients and are relatively easy to observe with methods that rely on density gradients (or the second spatial derivative of density) such as schlieren imaging. A Z-type schlieren system was set up and used for most of the tunnel runs to visualize the flow and the location of the Pitot pressure probe. The schlieren imaging system was also very useful, given the limited tunnel run time (40 s) and long duty cycle (2.5 hr), to determine in real time if the proper flow structures were seen at tunnel startup; if not, the tunnel could be shut down immediately, which would decreasing the waiting time for the air storage tank to recharge for the next tunnel run. A description of the principle of schlieren imaging and the Z-type schlieren setup can be found in Settles [70].

As mentioned in the wedge alignment subsection, the alignment of the main optical path was done in conjunction with the alignment of the Mach stem generator wedge models. First, the optical beam was aligned left-to-right (upstream-to-downstream in the test section reference frame). Parallel bars were placed in the ACE tunnel test section and

aligned with the side wall. The first field mirror was adjusted side-to-side until the halos disappeared from the shadow of the parallel bars.

The up-to-down mirror alignment was not performed with the parallel bars since there was a 0.5° difference across the span of the test section. Instead, the Mach stem generator wedge models were aligned in the "yaw" angle with the side-to-side-aligned (upstream-to-downstream in test section reference frame) optical beam path. The "yaw" alignment was checked with measurements from the wedge leading edge to the ACE nozzle exit plane.

The Mach stem generator wedge models were then aligned in the "roll" and pitch" angles with a digital inclinometer. The first field mirror was then adjusted up-to-down (wall-normal in test section reference frame) to minimize halos from the top and bottom of the wedge shadows.

The typical components used in the schlieren imaging setup for this study are listed in Table 9. With the below setup, the resolution was about 10.2 px/mm (260 px/in.), and the field of view (determined by the camera) was about 125 mm (4.9 in.) by 70 mm (2.8 in.).

Table 9. Z-type schlieren imaging components.

Component	Company	Notes
Light Source	John Unertl Optical Company	Incandescent light source. DC transformer with adjustable power. Rotatable slit; adjustable slit height.
Field Mirrors	Edmund Optics	Parabolic mirrors. 6 in. diameter; 36 in. focal length; f/# = 6.
Optical Glass	Russell Optics	BK7 optical flats. 6 in. diameter; double surface, λ/4.
Knife Edge	--	Single-edge razor blade painted flat black. Oriented horizontally or vertically. Mounted on linear & angular optomechanics.
Focusing Lens	Thorlabs	Plano-convex lens. 75 mm dia.; 200 mm focal length, f/# = 2.67.
Image Plane	Nikon	D5000 DSLR camera. 1280 px × 720 px, 24 fps movie recording; no manual exposure settings for movie recordings.

There were some variations in the schlieren imaging components to achieve different purposes. The first variation was the choice of cutoff. Typically, a knife-edge is used with the blade orientation perpendicular to the sensitivity direction desired (e.g. the knife-edge blade is oriented vertically if horizontal sensitivity is desired), and the extended light source slit is oriented the same direction as the knife-edge. Another "cutoff" that can be used is a color mask for color schlieren imaging. Color masks typically have color variations in a preferred direction that allows one to choose the direction of sensitivity. Figure 32 is a compilation of schlieren images obtained with different cutoffs methods.

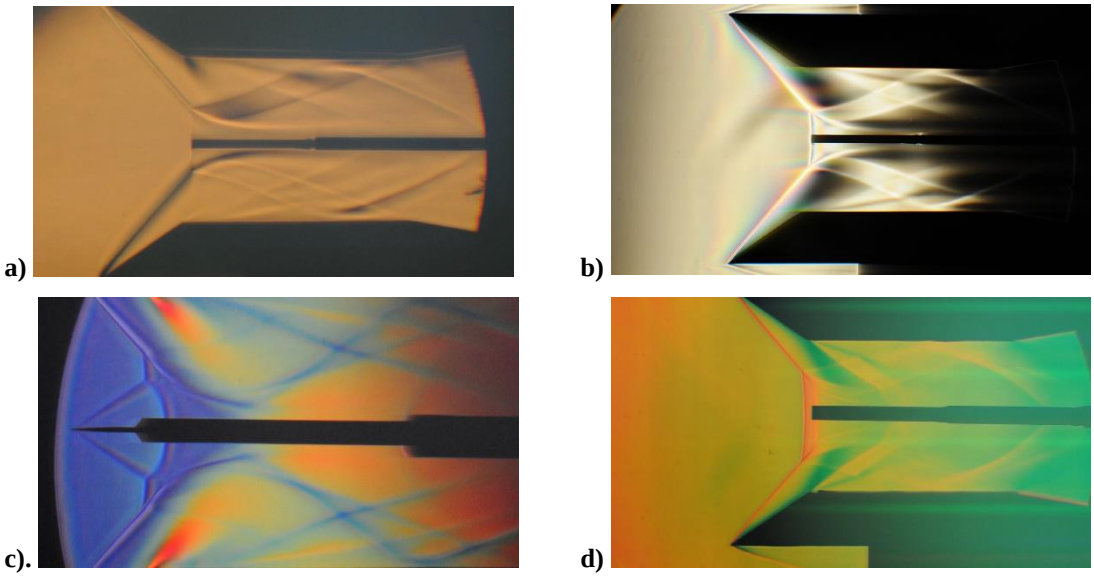

Figure 32. Schlieren imaging cutoff comparisons.
a) Horizontally-oriented knife-edge (Run 2020). b) Vertically-oriented knife-edge (Run 2026).
c) Vertically-oriented color mask (Run 2036). d) Vertically-oriented color mask (Run 2077).

Another variation was changing the focusing lens to zoom (reduce the field of view) into the Mach stem region to obtain more accurate estimates of Mach stem positions and location of probe tips relative to the Mach stem. Following the equations in section 3.1 of Settles [70], the typical focusing lens was replaced with a plano-convex lens with a focal length of 500 mm and a diameter of 50 mm. The resolution increased to 22 px/mm (560 px/in.), and the field of view decreased to 58 mm (2.3 in.) by 33 mm (1.3 in.). A comparison of the fields of view is shown in Figure 33.

a) 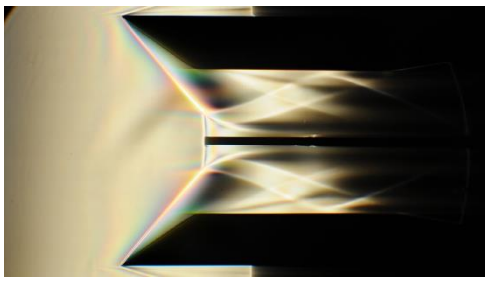 b) 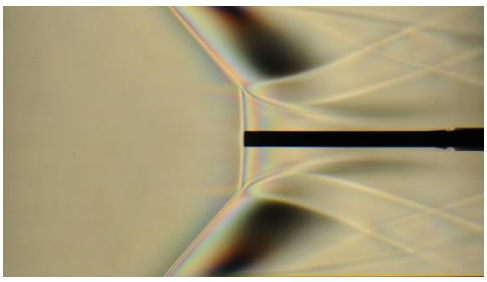

Figure 33. Schlieren imaging field of view comparison.
a) 200 mm focal length lens (Run 2026). b) 500 mm focal length lens (Run 2028).

Another variation was the temporary upgrade of the imaging camera to a Nikon D800 DSLR camera. Improved qualities over the Nikon D5000 DSLR camera include:

- movies recorded at 1920 px × 1080 px at 30 fps,
- manual movie exposure settings (shutter speed, ISO/"film speed", exposure compensation), and
- remote control of movie recording start and stop from a computer.

The Nikon D800 camera was used with the typical focusing lens that provided a large field of view. The resolution was about 11 px/mm (280 px/in.), and the field of view was 175 mm (6.9 in.) by 98 mm (3.9 in.). Figure 34 shows two images, at different settling chamber pressures, taken with the Nikon D800. The shutter speed was set to its fastest value of 1/8000 s, which allowed the visualization of the more subtle fluctuations. This was evident at higher settling chamber pressures (corresponding to higher Re/m) where the Mach stem structure showed more waviness than at the lower settling chamber pressure (lower Re/m). This corresponded to increased noise as the nozzle boundary layer state changed around Re/m = 2.5–3.0 × 10^6/m.

a) 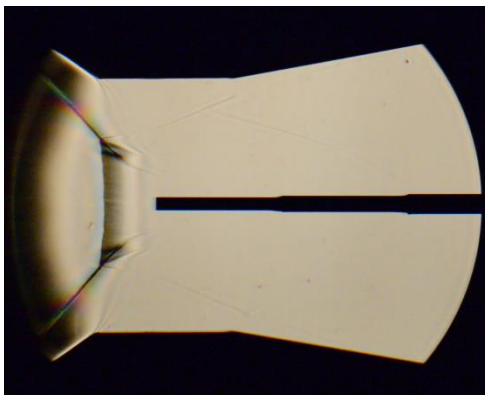 b) 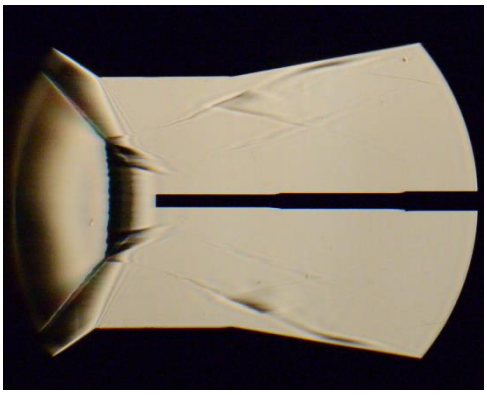

Figure 34. Schlieren imaging with Nikon D800 DSLR camera. (Run 2135)

a) 1/8000 s shutter speed, ISO 6400, p_{t1} = 25 psia.

b) 1/8000 s shutter speed, ISO 6400, p_{t1} = 65 psia.

A summary of the typical resolutions and fields of view is given below in Table 10.

Table 10. Schlieren imaging resolutions and fields of view.

Camera	Focusing Lens Focal Length	Resolution	Field of View
Nikon D5000	200 mm	10.2 px/mm (260 px/in.)	120 mm × 75 mm (4.9 in. × 2.8 in.)
	500 mm	22.0 px/mm (560 px/in.)	58 mm × 33 mm (2.3 in. × 1.3 in.)
Nikon D800	200 mm	11.0 px/mm (280 px/in.)	175 mm × 98 mm (6.9 in. × 3.9 in.)

Motion Control and Data Acquisition

Traverse motion control and data acquisition were accomplished by LabVIEW VIs [71]. Data acquisition tasks were separated into two major categories.

Tunnel and infrastructure parameter data were acquired by the "NAL-DAQ" LabVIEW VI for each tunnel run. The program was conceived by R. Flach in Virtual Basic, rewritten in LabVIEW by J. W. Hofferth, and then extensively rewritten again in 2013 by J. W. Hofferth. Data were acquired at 100 S/s on an NI USB-6255 M-Series DAQ system,[3] and acquisition was triggered by the motive pressure in the output line of the second-stage ejector. Data acquired include:

- air storage tank pressure,
- ejector motive pressures,
- tunnel supply line pressures,
- tunnel settling chamber pressure and temperature,
- nozzle static pressure,
- any slow-response data channels, as needed, and
- diffuser pressures.

Raw data were output in a spreadsheet and reduced data (averaged from the raw data at 10 S/s) were output in another spreadsheet with charts. The collection and visualization of the data enabled near-effortless verification of on-condition performance for the ACE tunnel and M6QT as well as the supporting infrastructure. For off-condition performance of the tunnels or the infrastructure, the data provided useful, initial diagnostics for troubleshooting.

Experimental data were acquired by "ACE-DAQ," which was a separate LabVIEW VI [71] and resided on a different PC than the "NAL-DAQ." The "ACE-DAQ" VI was conceived by J. W. Hofferth, modified by M. T. Semper, and further modified for this study. The "ACE-DAQ" VI was started manually by a second tunnel operator when

[3] http://sine.ni.com/ds/app/doc/p/id/ds-20/lang/en

tunnel conditions were appropriate. Data were acquired by an NI USB-6366 X-Series DAQ system with a sampling rate of 2 MS/s per channel.[4] The following channels were recorded:

- settling chamber pressure (time-series),
- settling chamber temperature (averaged),
- nozzle static pressure (averaged),
- instrument raw (DC-coupled) voltage(s) (time-series), and
- instrument AC-coupled voltage(s) (time-series).

The primary instrument used in this study were Pitot pressure probes; some preliminary hot-wire data were also acquired. Data were recorded into a binary file (which is the smallest file size without requiring a specialized file format, such as NI TDMS). Data were also recorded into a summary spreadsheet file, which provided a useful "first-look" check to verify proper data collection and determine which data points were valid (some data points were missed due to mistiming of starting the DAQ process or due to tunnel off-condition performance).

The "ACE-DAQ" VI also controlled the motion of a single-stage traverse. The VI synchronized the motion of the traverse with the DAQ process and is illustrated in Figure 35. Typically, a location CSV file was uploaded to the VI, which specified the position of the traverse for each sampling record. After the traverse moves to the specified position and its actual position was verified, the VI waited a specified settling time of 250 ms before collecting 250 ms of data. At a sampling rate of 2 MS/s per channel, 500,000 sampling points were collected per channel at each traverse location. The VI then moved

[4] http://sine.ni.com/ds/app/doc/p/id/ds-164/lang/en

the traverse to the next position where the process was repeated for all of the points specified in the location CSV file.

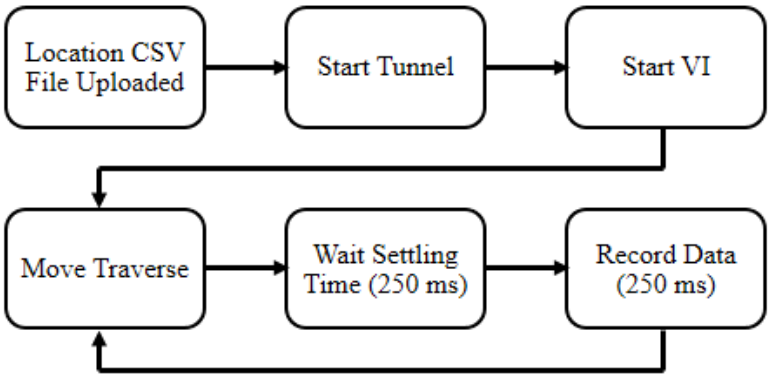

Figure 35. "ACE-DAQ" motion control and DAQ process.

For each tunnel run that experimental data were collected, the instrument signal (either Pitot pressure probe voltage or hot-wire anemometer voltage) was filtered and recorded according to Figure 36.

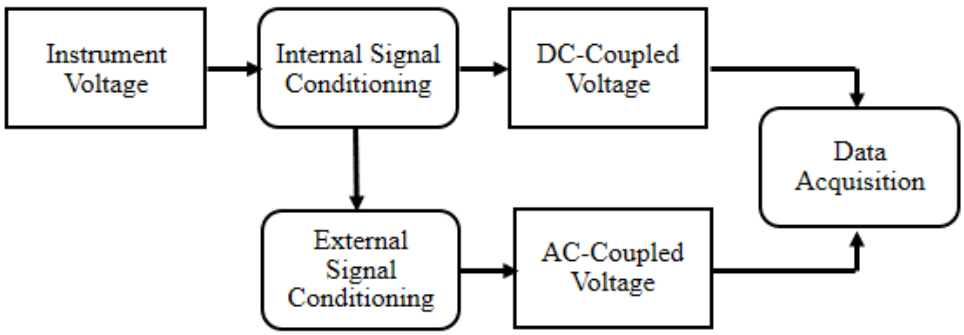

Figure 36. Instrument signal conditioning and acquisition process.

At a sampling rate of 2 MS/s, the maximum frequency of possible interest (the so-called Nyquist frequency) is 1 MHz with any frequency content above that aliasing into lower frequencies. Spectral analyses of the raw signals have shown that content higher than about 60 kHz have negligible energy, and no anti-aliasing filter was applied to the DC-coupled signal. The signal conditioning applied to the AC-coupled signal is detailed later.

Pitot Pressure Probe

Total pressure fluctuation measurements were made by flush-mounting a fast-response pressure transducer to a tube/probe exposed to the flow. Fast-response transducers, when flush-mounted, are able to resolve content in the frequency of tens or hundreds of kHz.

The transducer used in this study was a Kulite XCEL-100-5A piezoresistive pressure transducer.[5] A summary of its properties is listed in Table 11.

As mentioned before, a piezoresistive sensor is relatively sensitive to temperature ([57]-[59]). This Kulite transducer was equipped with a thermal compensation module external to the sensor housing, which provided compensation within the stated compensated temperature range and minimized the thermal shift of the sensitivity and zero to within the stated specifications. The flow total temperature of 425 K (152 °C, 305 °F) was within the compensated range.

[5] http://www.kulite.com/docs/products/XCEL-100.pdf

Table 11. Kulite XCEL-100-5A pressure transducer properties.

Property	Value	
Measuring Range	0-34.5 kPa	0-5 psia
Full-Scale Output	100 mV (nom.)	100 mV (nom.)
Diameter	2.57 mm	0.101 in.
Resonant Frequency	150 kHz (nom.)	150 kHz (nom.)
Combined Error (non-linearity, hysteresis, and repeatability)	0.1% FSO BFSL (typ.)	0.1% FSO BFSL (typ.)
Compensated Temperature Range	298-508 K	25-235 °C 80-450 °F
Temperature Sensitivity Shift	± 1.8%/100 K	± 1.8%/100 °C ± 1%/100 °F
Temperature Zero Shift	± 1.8% FS/100 K	± 1.8% FS/100 °C ± 1% FS/100 °F

The Pitot pressure probe was constructed by placing the pressure transducer into precision stainless steel tubing of progressively increasing diameters (Figure 37). The several pieces of stainless steel tubing were bonded to each other using J-B WELD, a two-part, high-temperature epoxy adhesive. Table 12 is a listing of the constituent pieces of tubing used to construct the probe. The transducer is mounted into the tubing using an RTV rubber compound that was designed for high-temperature applications. The flexibility of the RTV compound minimized the stress transferred to the transducer housing. The RTV compound was also applied at the tubing exit to minimize stress and strain on the fragile transducer wires.

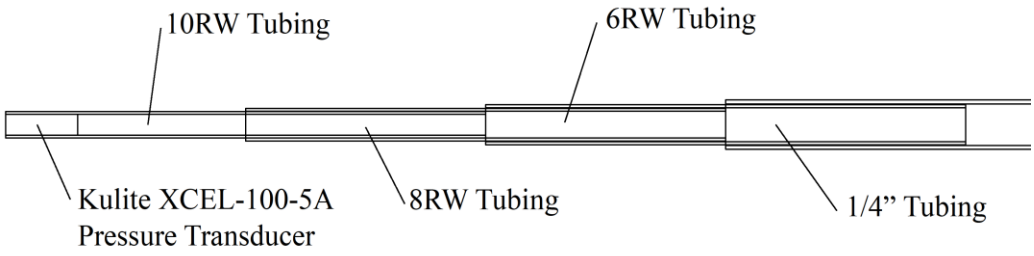

Figure 37. Pitot pressure probe cutaway schematic.

Table 12. Pitot pressure probe constituent tubing properties.

Gauge and Wall Size	Inner Diameter		Outer Diameter	
Kulite XCEL-100-5A	--	--	2.57 mm	0.101 in.
10RW	2.69 mm	0.106 in.	3.40 mm	0.134 in.
8RW	3.43 mm	0.135 in.	4.19 mm	0.165 in.
6RW	4.39 mm	0.173 in.	5.16 mm	0.203 in.
¼” × 0.020”	5.33 mm	0.210 in.	6.35 mm	0.250 in.

An estimate of the shock standoff distance was calculated using the Ambrosio and Wortman correlations [72]. Given the axisymmetric shape of the probe, the sphere correlation was used (as opposed to the cylinder correlation). However, the correlation was not directly applicable since the probe was flat-faced instead of spherical. In addition, the probe, instead of being a sphere, had essentially infinite depth in the freestream direction. Thus, the calculation would only be an order-of-magnitude estimate. For the given size of the probe at the tip and $M_1 = 5.85$, the standoff distance was calculated to be about 0.27 mm (0.011 in.).

The transducer was connected to a custom-built power supply and signal-conditioning circuit built by J. W. Hofferth. The circuit design originated from S.

P. Schneider's research group at Purdue University [73]. The design was modified by J. W. Hofferth to incorporate a TI REF102 integrated circuit that provides a clean and stable 10.0 V excitation source. Other modifications from the original design resulted in the configuration described next.

The signal conditioning of the transducer output voltage is illustrated in Figure 38. The output voltage from the Kulite transducer was gained by 100 and high-pass filtered with a first-order RC circuit at 482.5 kHz. This conditioned signal was the raw (DC-coupled) voltage output of the signal conditioner, and its full scale output is nominally 10 V (100 mV × 100), which spanned the nominal, positive voltage range for typical DAQ hardware, such as the NI USB-6366 DAQ system used in this study.

The AC-coupled signal was obtained by branching off of the DC-coupled output, low-pass filtering with a first-order RC circuit at 842 Hz (corresponding to ~ 1 ms response time), gaining by 28.9 (for a total gain of 2890 from the transducer voltage fluctuation), and then high-pass filtering again with a first-order RC circuit at 482.5 kHz. After the signal conditioner, the AC-coupled signal was further conditioned by passing it through an 8-pole Butterworth filter with unity gain. A Butterworth filter is desired since phase response is not of concern in this study, and the filter's frequency response nominally has no ripples. The filter was a module in a Krohn-Hite FMB3002 chassis,[6] and modules with cutoff frequencies of 50 kHz and 100 kHz were available and utilized. Since most of the energy content, excluding effects of the sensor's natural resonant frequency, were at

[6] http://www.krohn-hite.com/htm/filters/PDF/FMB3002Data.pdf

frequencies less than 50 kHz (Figure 39), *all AC-coupled results presented have been filtered with the 50-kHz Butterworth filter* (100-kHz low-pass filtered data were also recorded); the filter's frequency response is presented in Appendix E. Both the DC-coupled and the AC-coupled voltage outputs were acquired by the "ACE-DAQ" system.

Because the Kulite XCEL-100-5A transducer did not come with temperature calibration curves, an *in situ* calibration was performed. The Pitot pressure probe transducer was mounted inside the tunnel test section to a traverse situated along the tunnel centerline. A second Pitot pressure probe was inserted into the tunnel with its aperture (5.1 cm) 2.0 in. away from the tunnel centerline in the spanwise direction. Figure 40 shows a schlieren image of the two Pitot pressure probes during a calibration run.

This second Pitot pressure probe served as the calibration pressure reference for the Kulite Pitot pressure probe. Previous (and soon-to-be published) freestream uniformity characterizations have shown that the tunnel has a uniform test core (Mach number deviation from centerline < 5%) at least 12.7 mm (5.0 in.) away from the centerline. Mounted to the second Pitot pressure probe, external of the tunnel test section, was an MKS Baratron 631C-100 high-temperature capacitance manometer, which had a full-scale output of 13.3 kPa (100 Torr) and an accuracy of 0.5% of the reading (as opposed to a percentage of the FSO). The transducer sensor was heated and temperature-controlled to 423 K (150 °C, 302 °F), minimizing the effect of the tunnel operating temperature on the pressure reading. Because of its accuracy in percentage of

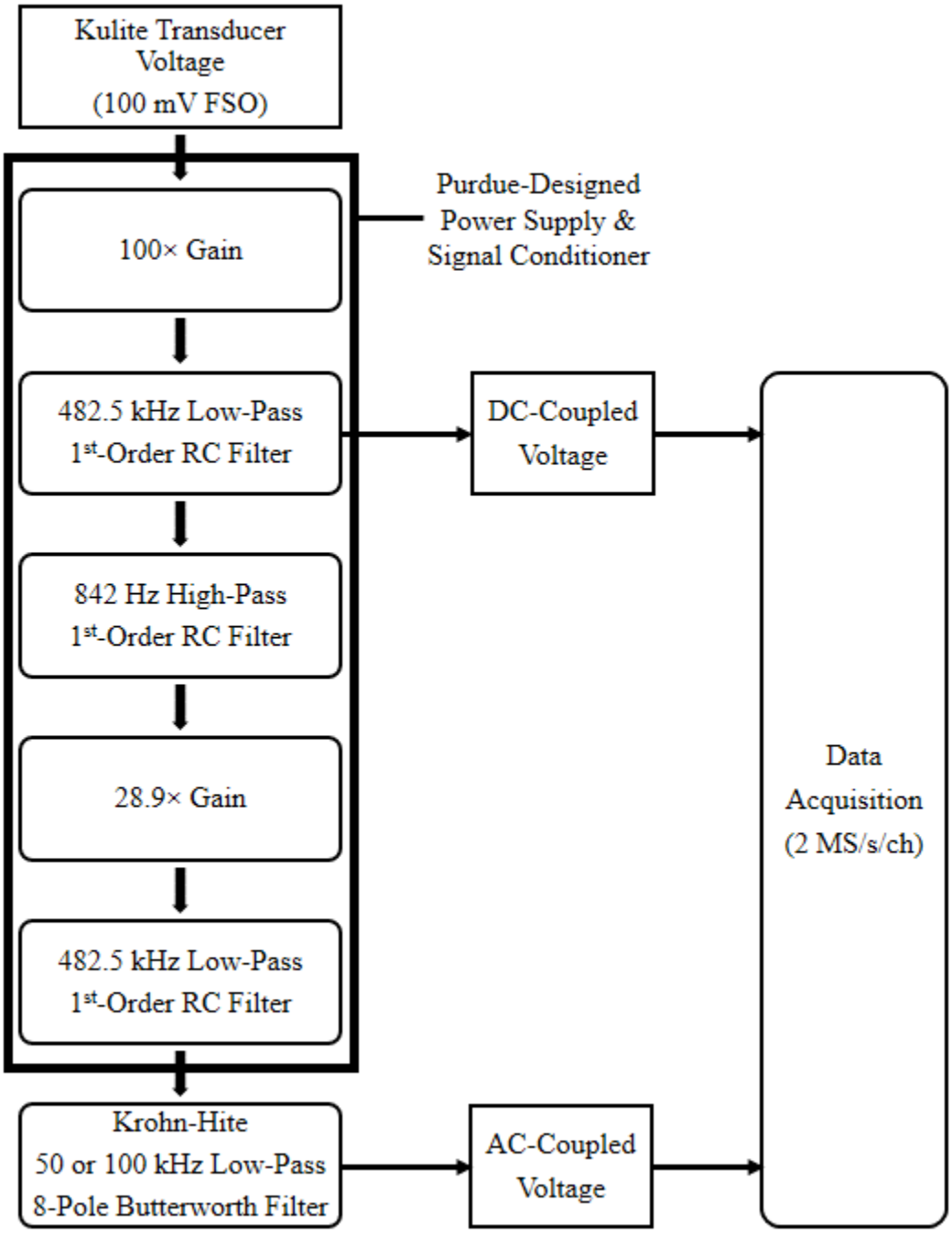

Figure 38. Kulite pressure transducer signal conditioning process.

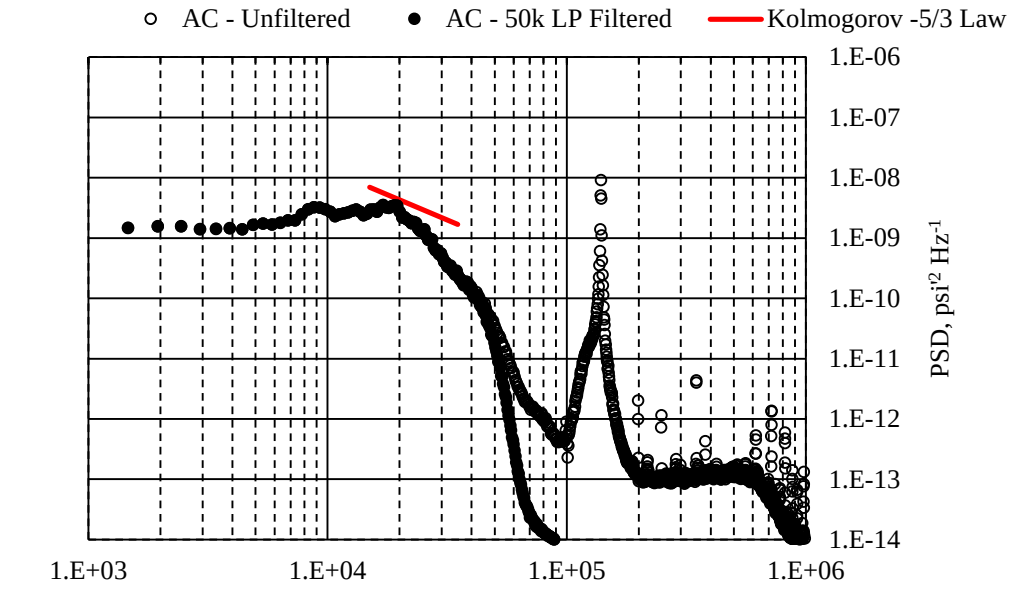

a)

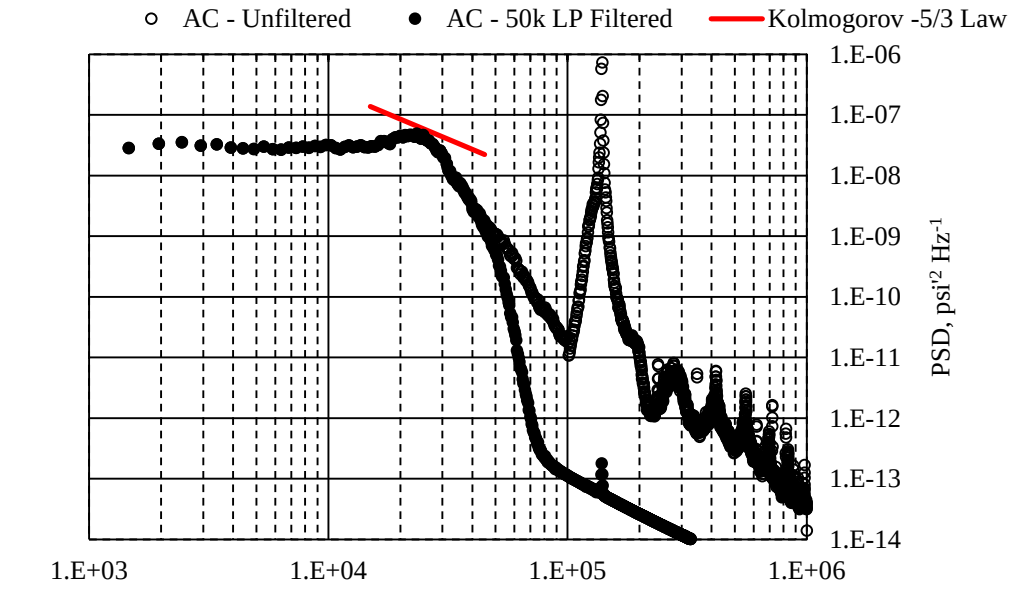

b)

Figure 39. Effect of 50-kHz low-pass filtering.

a) Low Re/m condition. b) High Re/m condition.

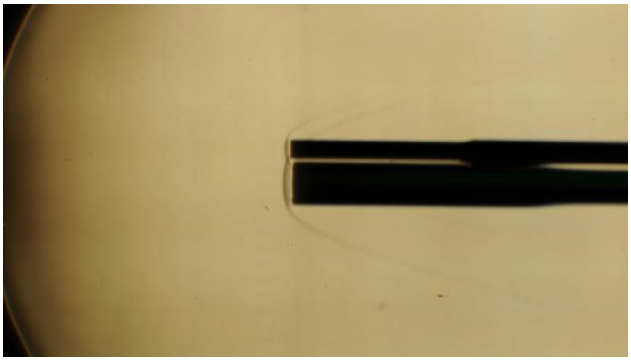

Figure 40. Pitot pressure probe calibration schlieren image. (Run 2095)
Top probe: flush-mounted fast-response Kulite Pitot pressure probe.
Bottom probe: reference Pitot pressure probe read by an MKS Baratron capacitance manometer.
Probes are offset by 50.8 mm (2.0 in.) in direction normal to the page.

reading and its active temperature control, the MKS Baratron transducer was very well-suited as a basis for calibrating transducers. The transducer had a response time of 50 ms and because it was situated outside of the tunnel test section, the transducer itself was not suitable for fluctuation measurements. The pressure lag time constant, according to Bauer [55] and Volluz [56], was 5.6 ms at the low-pressure operating condition and 3.1 ms at the high-pressure operating condition. These calculations were made by assuming that the pressure change (calibration was performed with a continuously increasing pressure sweep) across the 250 ms recording time (per sampling record) was applied instantaneously at the beginning of the recording time. Thus, the time constants, when compared to the sample recording time, introduced minimal error to the pressure reading. The calculations are provided in Appendix D. The transducer was connected to

an MKS PR4000B power supply/readout.[7] This readout supplied a custom-scale analog output that was read by the "ACE-DAQ" system.

Whereas the MKS Baratron transducer was minimally affected by small changes in the tunnel operating temperature, it was unknown how repeatable the Kulite thermal shifts were. Six calibration tunnel runs were performed with Pitot pressure spanning from 5.33 kPa (40 Torr, 0.77 psia) to 13.3 kPa (100 Torr, 1.93 psia) and temperature spanning from 413 K (140 °C, 284 °F) to 431 K (158 °C, 316 °F), and the coefficient of determination (R^2) of the best-fit straight line through these five runs was 0.9996. The percentage difference between the calibration line and the data points was 0.46% RMS. Since the calibration temperature range of the six runs covered the typical tunnel operation range with a high R^2 value and low percentage difference, any shift in the transducer parameters due to temperature variations during a run were deemed negligible. Figure 41 shows the data points from the calibration runs.

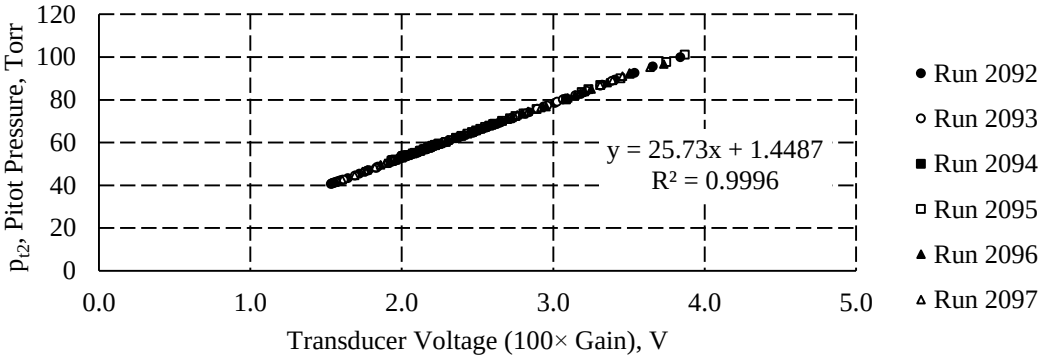

Figure 41. Pitot pressure probe calibration chart.

[7] http://www.mksinst.com/docs/UR/PR4000B-RoHSds.pdf

Traverse

To easily make measurements upstream and downstream of the Mach stem, a traverse system was designed to move the Pitot pressure probe in the freestream direction of the tunnel.

The traversing platform was an Aerotech, Inc. ATS100-200 mechanical bearing, ball-screw stage.[8] The traverse had a total travel of 200 mm (7.87 in.), although only 25.4 mm (1.0 in.) was used in the final design; the traverse had an accuracy of ±6.0 μm (2.4×10^{-4} in.). The traverse stage was mounted to an extruded aluminum frame assembled around the test section. A vertical traverse strut was attached to the stage with optical posts and right-angle post clamps (Figure 42). This design allowed some flexibility in finely setting the vertical position of the strut. The traverse stage and strut could be coarsely adjusted vertically by adjusting parts of the extruded aluminum frame.

The traverse strut was designed with a sharp leading edge and a 20° half-angle leading wedge to keep a shock wave attached. The leading wedge angle is followed by a flat portion and then by a 12.5° half-angle trailing wedge to a sharp trailing edge; the strut was 19.1 mm (0.75 in.) wide at it widest (at the flat portion). At the bottom of the traverse strut, which was inside the tunnel test section, a 12.7 mm-diameter (0.50 in.) thru hole aligned in the axial direction allowed a probe or probe adapter to be inserted for axial measurements. Figure 43 is a schematic of the traverse vertical strut.

[8] http://www.aerotech.com/media/440567/ats100.pdf

Figure 42. Traverse and mounted strut.

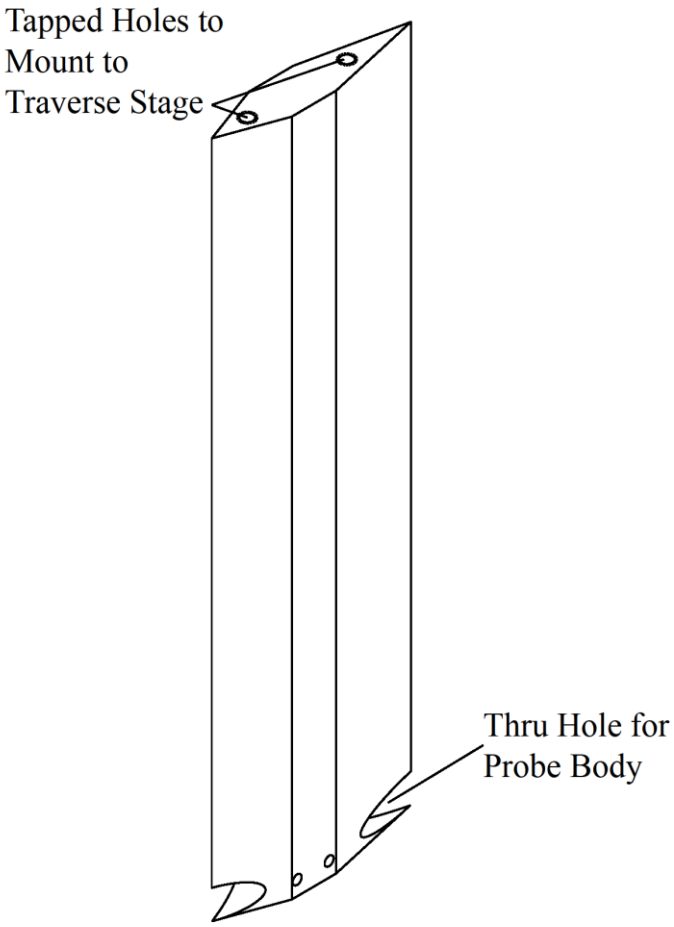

Figure 43. Traverse vertical strut schematic.

The traverse strut entered the test section through a designed plug at the top center port. The slot in the plug was designed with clearance to allow free motion of the strut. A sliding seal minimized air leakage into the test section. The sliding seal mechanism consisted of a 3.2 mm-thick (0.125 in.) silicone rubber sheet in between two 6.4 mm-thick (0.25 in.) aluminum plates with cutouts that matched the profile of the traverse strut. The cutouts were made in the aluminum plates by wire EDM and in the silicone rubber by a laser cutter. The silicone sheet seals around the strut while the aluminum plates provided

structure to the seal. The bottom aluminum plate slid on a silicone O-ring on the plug. To enhance the seal and reduce the friction on sliding surfaces, vacuum grease was applied on the strut where the silicone rubber sheet sealed around it and on the O-ring on the window plug where contact was made with the sliding aluminum plate. Figure 44 is an exploded view of the traverse assembly.

As mentioned before, the traverse strut had a 12.7 mm-diameter (0.50 in.) thru hole aligned in the axial direction. A 12.7 mm-diameter (0.50 in.) pipe machined into a sleeve adapter was fastened in this thru hole. The pipe had an inner diameter of 6.5 mm (0.255 in.) and provided structural support for a 6.4 mm-diameter (0.25 in.) Pitot pressure probe body or hot-wire probe shield fastened to the sleeve adapter. The design allowed a large range of adjustment in the axial direction between 1) the traverse strut and the sleeve adapter and 2) the sleeve adapter and the instrument body. Figure 45 is a schematic of an instrument body in the sleeve adapter mounted in the vertical traverse strut. Figure 46 is a schematic of the traverse assembly and the Mach stem generator wedge model in the ACE tunnel test section.

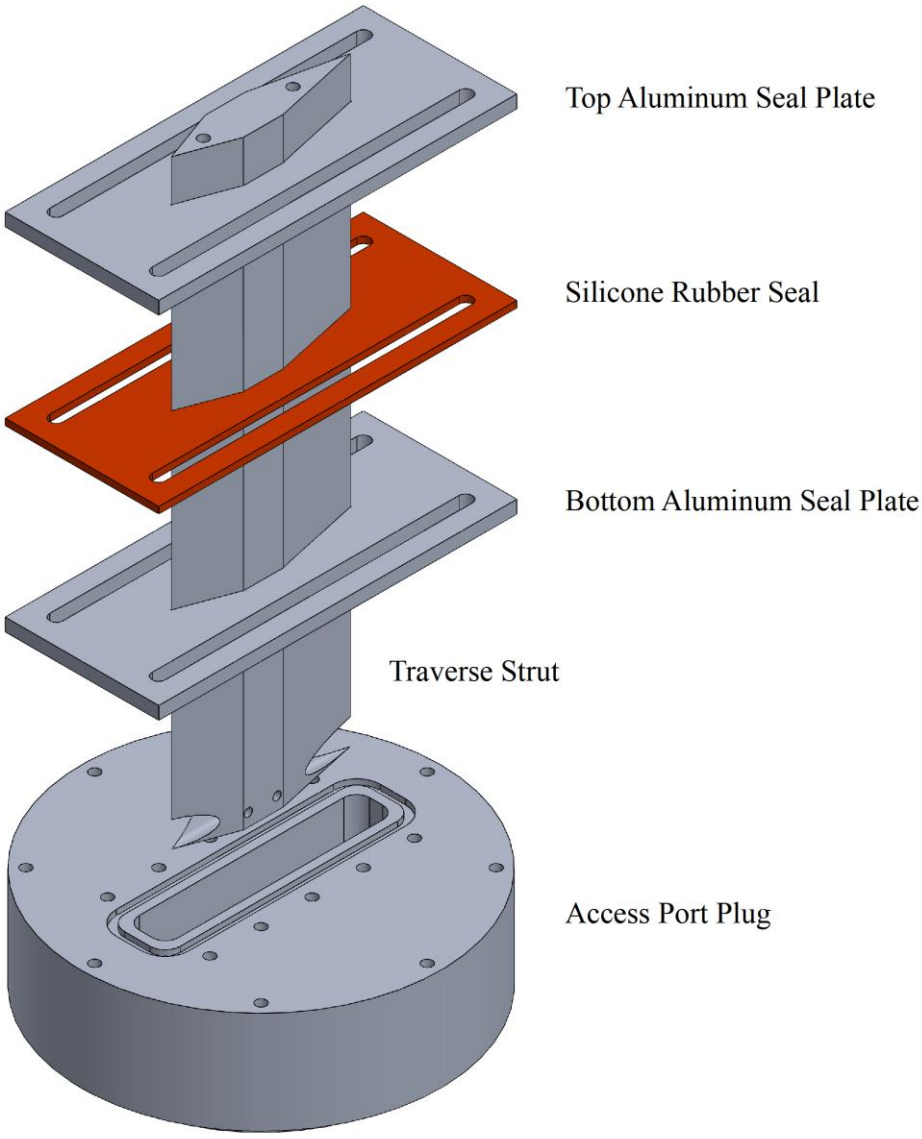

Figure 44. Traverse assembly (exploded view).

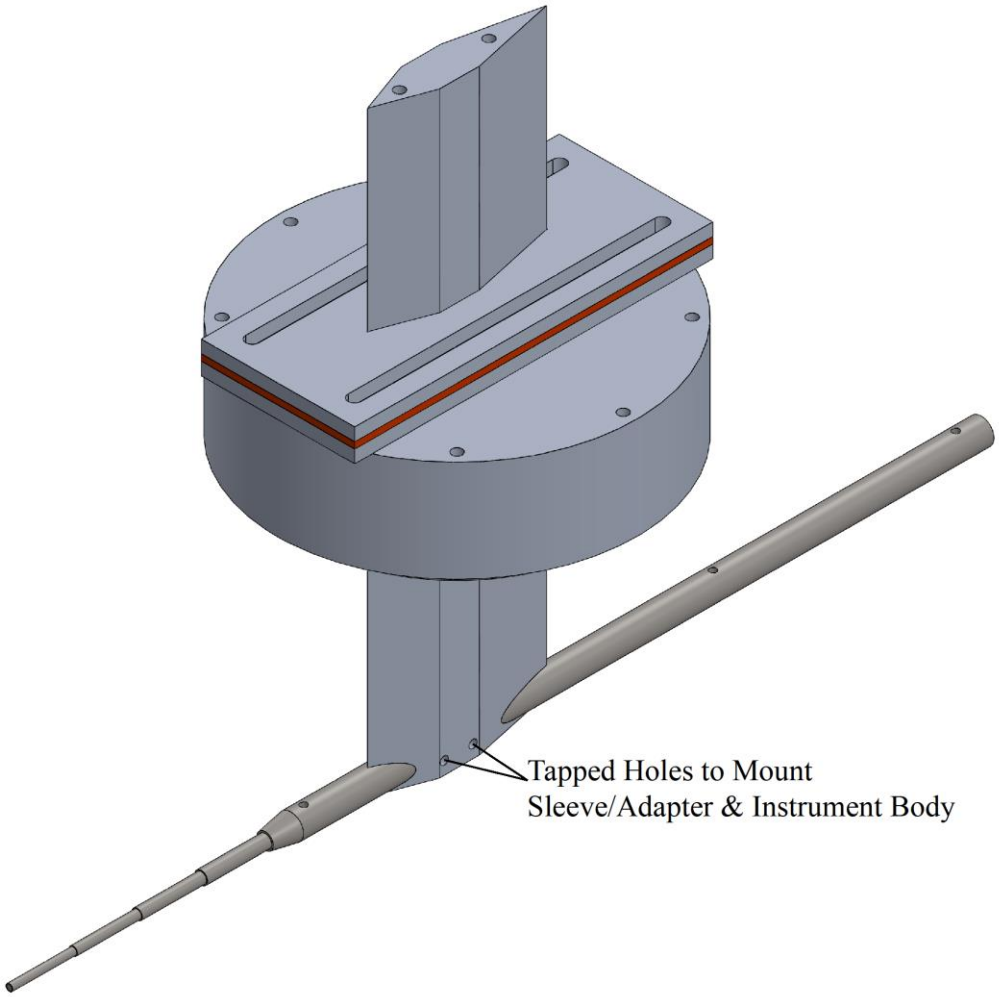

Figure 45. Traverse assembly with instrument body.

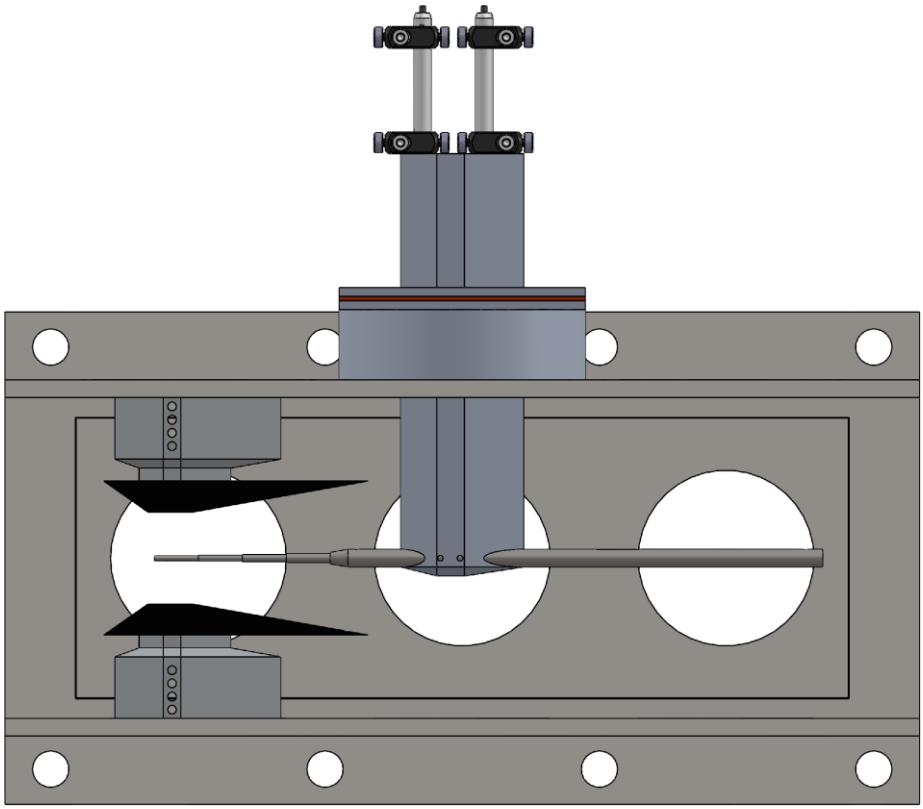

Figure 46. Traverse assembly and Mach stem generator wedge model (thick set) in ACE tunnel test section.

FLOW VISUALIZATION RESULTS AND DISCUSSION

The flow structures and relative position of the instrument probe to the Mach stem were determined by schlieren imaging. The DSLR cameras had video recording capabilities, and this operational mode was opted over single-shot images. The movies were recorded in AVI (Nikon D5000) or MOV (Nikon D800) file formats. PNG images were extracted with VLC Media Player for Windows [74]; see Figure 47 for an example. Using the extracted PNG images, the pixel locations of features of interest (e.g. Mach stem and probe location) were chosen manually and measured by ImageJ image processing software (developed by an NIH employee and maintained in his retirement) [75]. Calibration of the image pixel resolution was provided by objects in the images (e.g. Pitot pressure probe diameter, Mach stem generator wedge model separation distance, or Mach stem generator wedge model thickness).

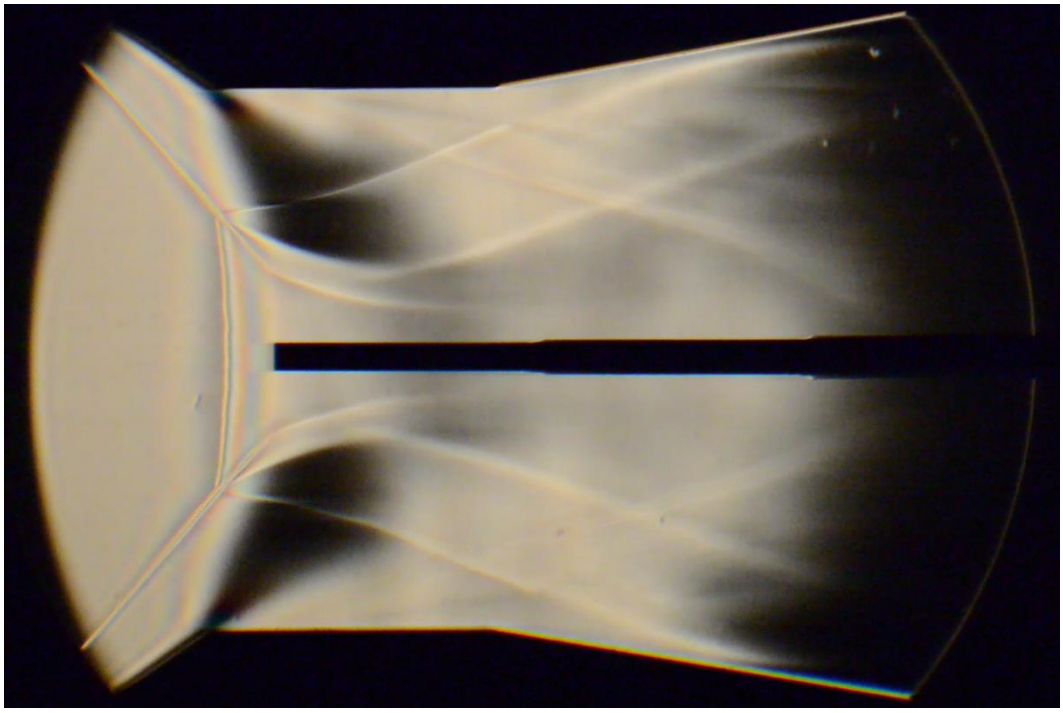

Figure 47. Typical schlieren image of flow structure between thick wedges. (Run 2141)

If tunnel conditions were constant and an instrument probe was not traversing, then the position of the Mach stem was visibly fixed. As mentioned in the wedge design subsection, however, the Mach stem moved slightly downstream with increased pressure (about 1 mm); Figure 48 illustrates this. One possible reason for this movement was backpressure effects between the wedges. Another possible reason was that due to the small angle between the wedge surface and the oblique shock wave (~ 13° by inviscid theory), the boundary layer on the wedge was likely exerting influence on the oblique shock near the wedge leading edge and vice-versa in a phenomena termed viscous interaction [76]. As the pressure increased, the Reynolds number increased, the boundary

layer thickness decreased, which, in turn allowed the oblique shock wave to be at a shallower angle slightly changing the location of the Mach stem.

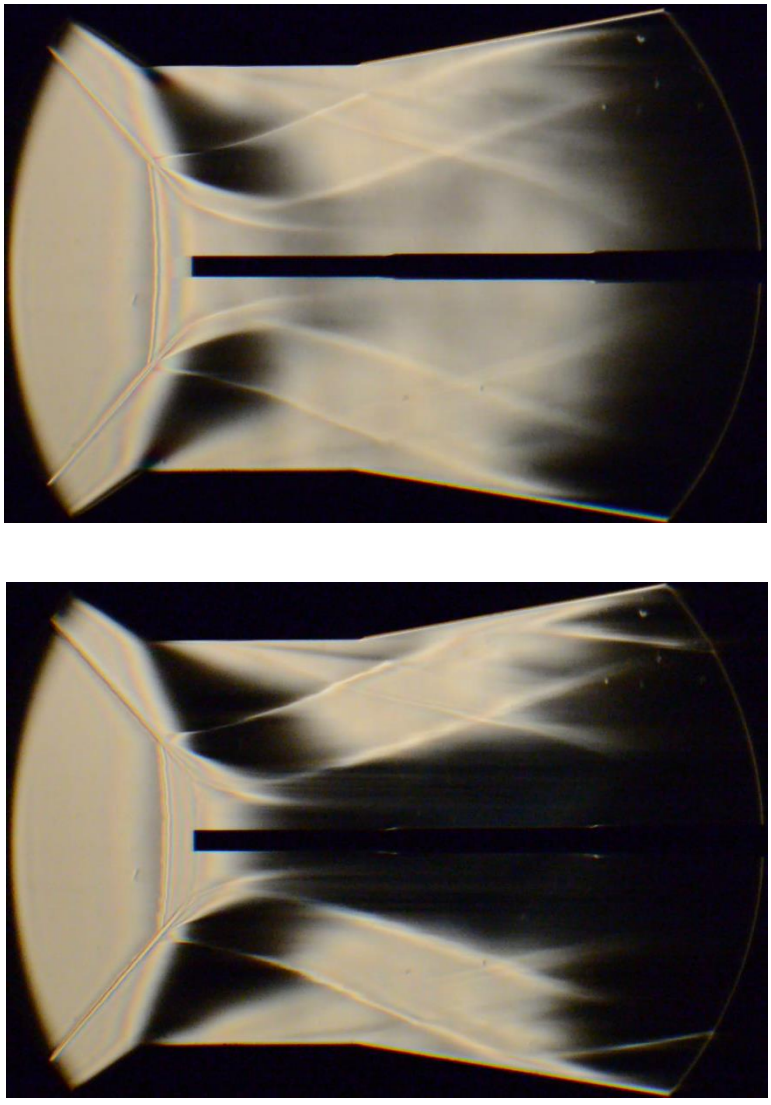

Figure 48. Schlieren image comparison at different pressures. (Run 2141)
Images are of same scale. Mach stem position variation of about 1.0 mm (0.039 in.).
a) p_{t1} = 1.72×10^5 Pa (25 psia). b) p_{t1} = 4.48×10^5 Pa (65 psia).

The Mach stem also moved slightly with an instrument probe's relative location. The effect occurred when the probe tip was upstream of the Mach stem. As the probe went further upstream, so did the Mach stem (Figure 49). It was believed that the movement of the Mach stem was due to probe-shock interaction. When upstream of the Mach stem, a separate bow shock upstream of the Mach stem was emitted from the instrument probe tip. The impingement of the bow shock onto the Mach stem may have influenced the Mach stem's position. In addition, the bow shock from the instrument probe tip appeared more intense with the wedge models installed than the bow shock without the wedge models installed, lending credibility to the probe-shock interaction explanation.

There was no observable movement of the Mach stem with the thick wedge models when the probe tip was downstream (Figure 50). With the Mach stem generator wedge models installed, the only measurements of interest were those downstream of the Mach stem, so the Mach stem does not move appreciably and *no major consideration of the position variation was necessary*.

a)

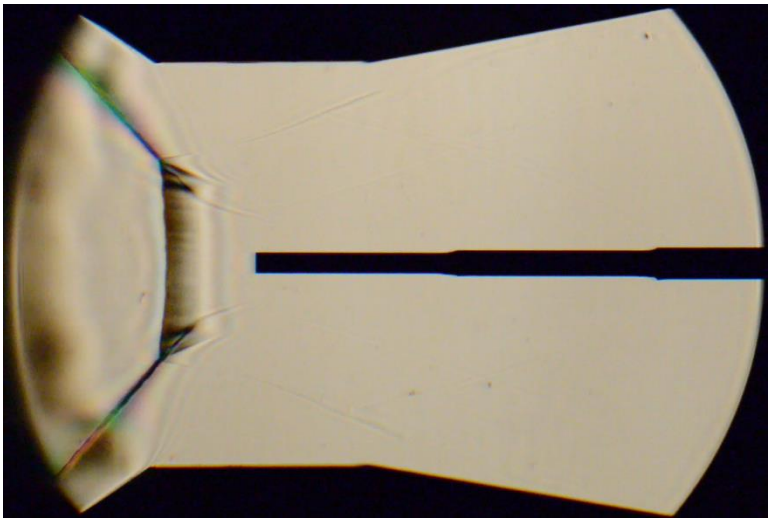

b)

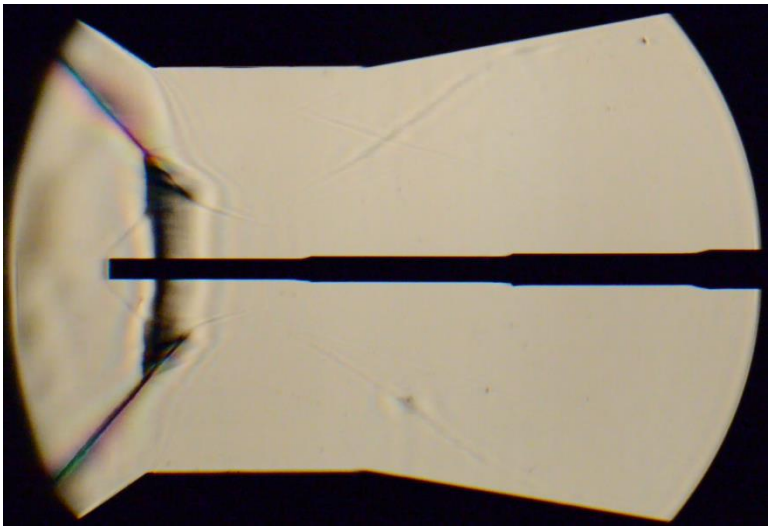

Figure 49. Schlieren image comparison at downstream and upstream probe positions. (Run 2132) Images are of same scale.

a) Probe behind Mach stem. b) Probe in front of Mach stem.

a)

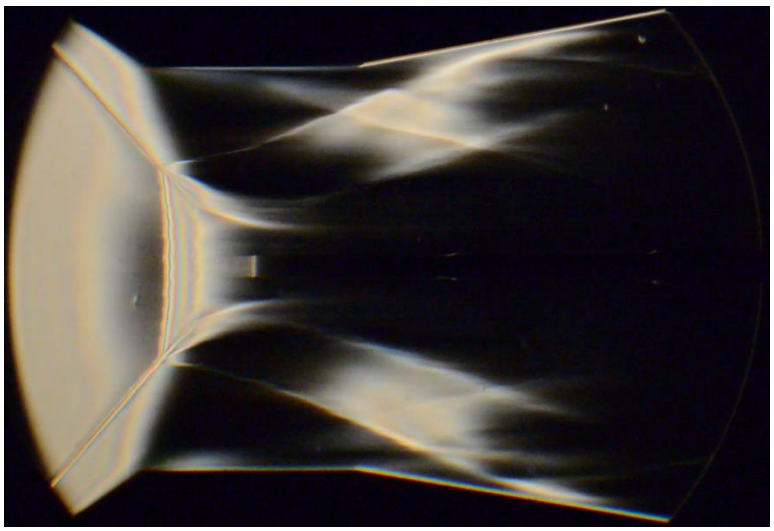

b)

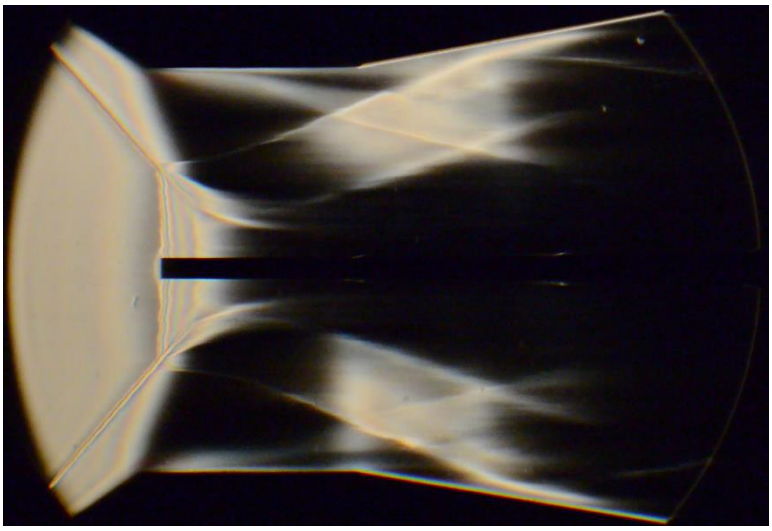

Figure 50. Schlieren image comparison at different downstream probe positions.(Run 2137) Images are of same scale.

a) Probe behind Mach stem. b) Probe at Mach stem.

While the Mach stem was the primary flow feature of interest since it served as the normal shock wave in this study of shock-turbulence interaction, the flow just downstream of the Mach stem needed to be understood so that downstream measurements could be properly interpreted. It is known that a shear layer/slip line emanates from the triple point intersection of the oblique shock wave, the Mach stem, and the reflected shock wave. Discontinuous properties can exist across the shear layer except for the flow angle and the pressure. Because density can be different across the shear layer, it is visible in schlieren imaging. The shear layers on each side of the Mach stem converge towards the centerline. Since the flow behind the Mach stem, which is a normal shock wave, is certainly subsonic, the converging shear layers indicate a duct of decreasing area; therefore, the flow behind the Mach stem is accelerating. This is accounted for in Mouton and Hornung [67]. Andreopoulos, Agui, and Briassulis [7] noted this fact about the work by Barre, Alem, and Bonnet [48] and believed that their results were biased.

Utilizing the schlieren imaging and equations of fluid dynamics, the flow properties behind the Mach stem were estimated. Using one of the schlieren imaging movies of a traverse-type run, an average frame was obtained from all frames of the movie in which there was an established flow structure (Figure 51). In the averaged frame, the Pitot pressure probe appears smeared since it was traversed during the run. An averaged frame is much cleaner than any single movie frame, since the image sensor noise and any bulk effects (e.g. currents in the ambient air or thermal plumes emanating from the heated tunnel) are averaged.

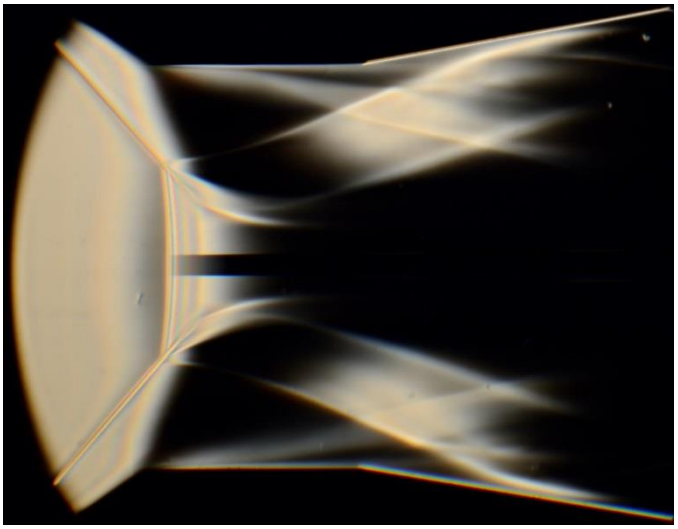

Figure 51. Average frame from schlieren imaging movie. (Run 2137)

Using ImageJ [75], pixels along the shear layer were measured. The pixels were adjusted relative to the Mach stem and a calibration applied to convert to physical units. This determined the changing area of the duct downstream of the Mach stem. Knowing the properties immediately behind the Mach stem due to normal shock relations (Eqs. (5)-(9)) and assuming isentropic, quasi-1-D flow, the post-Mach stem properties were calculated. Knowing the initial height of the Mach stem and the varying height of the "duct" behind the Mach stem, a Mach number at each position was calculated with an adaptation of Eq. (17):

$$\left(\frac{h}{h_{MS}}\right)^2 = \frac{M_{MS}^2}{M^2}\left[\frac{2}{\gamma+1}\left(1+\frac{\gamma-1}{2}M_{MS}^2\right)\right]^{-\frac{(\gamma+1)}{(\gamma-1)}}\left[\frac{2}{\gamma+1}\left(1+\frac{\gamma-1}{2}M^2\right)\right]^{\frac{(\gamma+1)}{(\gamma-1)}} \qquad (27)$$

The throat height (critical height) was constant through the near-post-Mach stem region, since an isentropic flow field existed. Eq. (27) is simply a ratio of Eq. (17) for the duct

height to the Mach stem height. The subscript MS denotes conditions just after the Mach stem. This equation must be solved numerically since there is no analytical expression for the Mach number as a function of the height ratio.

Now knowing the Mach number at various points behind the Mach stem, isentropic flow relations were used to obtain the static pressure and temperature:

$$\frac{T_{t,MS}}{T} = 1 + \frac{\gamma - 1}{2} M^2 \tag{28}$$

$$\frac{p_{t,MS}}{p} = \left(\frac{T_{t,MS}}{T} \right)^{\frac{\gamma}{\gamma - 1}} = \left(1 + \frac{\gamma - 1}{2} M^2 \right)^{\frac{\gamma}{\gamma - 1}} \tag{29}$$

The speed of sound, assuming a calorically perfect gas, and velocity were then calculated.

$$a = \sqrt{\gamma RT} \tag{30}$$

$$u = Ma \tag{31}$$

The static pressure and velocity were normalized by their respective values at the Mach stem. The area ratio, Mach number, and the normalized pressure and velocity are shown in Figure 52. At about 3.0 mm behind the Mach stem, the deviation from the Mach stem value is only about 0.5% for the static pressure and about 1.5% for the velocity. At about 4.6 mm behind the Mach stem, the deviation is about 1.5% for the static pressure and about 7% for the velocity. *When looking at the near-Mach stem properties, the shear layer is not expected to significantly bias the results.*

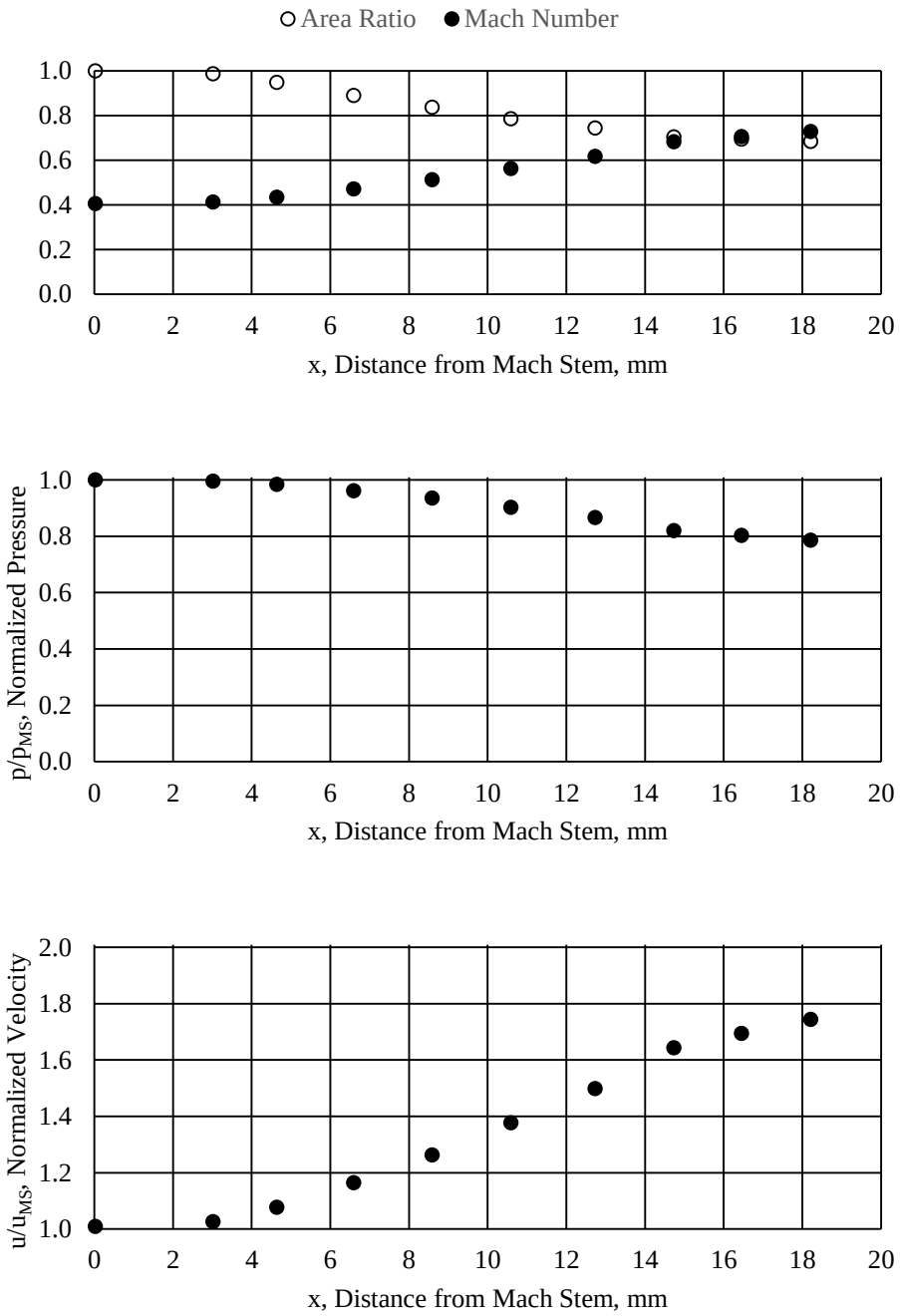

Figure 52. Sample post-Mach stem property variations. (Run 2137)

PITOT PRESSURE DATA REDUCTION

This section describes how the data from Pitot pressure measurements were reduced and analyzed. The summary spreadsheet and binary files containing acquired data during tunnel runs were read and processed by a MATLAB [66] data reduction and analysis m-script. The summary spreadsheet provided a quick way to determine if there were any off-condition sampling records. The MATLAB code had the capability to choose a starting sampling record and ending sampling record, so that unacceptable sampling records (which may occur for any number of reasons in experimental work) were not processed and analyzed unnecessarily. Processed data were compiled into a structure variable and output to a Microsoft Excel [77] spreadsheet for further processing and data visualization using a MATLAB script that invoked the function "xlswrite1."[9] Figures created were output using the function "export_fig."[10]

The terminology used regarding data acquisition is as follows. For each tunnel run, there are 20 to 50 sampling records, one for each pressure/Reynolds number (for a pressure sweep-type run) or one for each traverse location (for a traverse-type run). Within each sampling record were numerous sampling points (500,000 sampling points for a 250 ms data acquisition sampling record at a sampling rate of 2 MS/s).

---

[9] Swartz, M., "xlswrite1," MATLAB Central File Exchange, retrieved 23 Jan 2014 (http://www.mathworks.com/matlabcentral/fileexchange/10465-xlswrite1).

[10] Woodford, O., "export_fig," MATLAB Central File Exchange, retrieved 9 Dec 2013 (http://www.mathworks.com/matlabcentral/fileexchange/23629-export-fig).

This subsection will first describe the calculation of the freestream flow parameters, followed by the calibration and preparation of the data for fluctuation analyses, and then the process of calculating the fluctuation-derived quantities.

Freestream Flow Parameters

This subsection describes the procedures and lists the equations used to determine the tunnel freestream flow parameters. As part of the data acquisition, the settling chamber pressure (p_{t1}), settling chamber temperature (T_{t1}) and nozzle static pressure (p_1) were recorded. From these three variables, the remaining freestream flow parameters were calculated.

The settling chamber pressure was time-resolved (2 MS/s for 250 ms) to be able to determine if there were any abnormal pressure variations during a tunnel run. The response time of this measurement was limited by the Pitot tubing, and the typical flow noise was between the electrical noise floor of 0.4% and 0.7%. The settling chamber temperature and nozzle static pressure were sampled at the same fast sampling rate, but because of their relatively slow response time, their values were averaged over the 250 ms sampling record, and one value for each parameter was recorded for each sampling record. The settling chamber pressure data were averaged for each sampling record as part of the data reduction. The calculated freestream flow parameters, therefore, were averaged values at each sampling point.

As mentioned in the Pitot pressure probe subsection, the Pitot pressure probe transducer is temperature-sensitive ([57]-[59]). As part of the data processing, the settling

chamber was corrected with the temperature calibration curves provided by Endevco. The static pressure transducer (MKS Baratron) was actively heated, so it did not need a temperature calibration.

The nozzle/test section Mach number was calculated from the isentropic pressure relationship:

$$\frac{p_{t1}}{p_1} = \left(1 + \frac{\gamma - 1}{2} M_1^2\right)^{\frac{\gamma}{\gamma - 1}} \tag{32}$$

This is rearranged to:

$$\bar{M}_1 = \left(\frac{2}{\gamma - 1} \left[\left(\frac{\bar{p}_{t1}}{\bar{p}_1} \right)^{\frac{\gamma - 1}{\gamma}} - 1 \right] \right)^{1/2} \tag{33}$$

The nozzle/test section static temperature was then calculated from its isentropic relationship:

$$\bar{T}_1 = \bar{T}_{t1} \left(1 + \frac{\gamma - 1}{2} \bar{M}_1^2\right)^{-1} \tag{34}$$

The nozzle/test section static density was calculated from the ideal gas law:

$$\bar{\rho}_1 = \frac{\bar{p}_1}{R\bar{T}_1} \tag{35}$$

The nozzle/test section speed of sound is then computed, assuming a calorically perfect gas. The velocity was then determined.

$$\bar{a}_1 = \left(\gamma R \bar{T}_1\right)^{1/2} \tag{36}$$

$$\bar{u}_1 = \bar{M}_1 \bar{a}_1 \tag{37}$$

The dynamic viscosity was determined from the static temperature using Keyes viscosity model for air [78]:

$$\bar{\mu}_1 = \frac{1.488\times10^{-6}\left(\bar{T}_1\right)^{1/2}}{1+\left(\frac{122.1}{\bar{T}_1}\right)\times10^{-5/\bar{T}_1}} \tag{38}$$

The linearized average mass flux and Re/m were then computed:

$$\overline{\left(\rho u\right)_1} = \bar{\rho}_1 \bar{u}_1 \tag{39}$$

$$\mathrm{Re/m}_1 = \frac{\bar{\rho}_1 \bar{u}_1}{\bar{\mu}_1} \tag{40}$$

The Pitot pressure was also calculated for comparison to the experimental, mean pressure data from the Pitot pressure probe transducer:

$$\bar{p}_{t2} = \bar{p}_{t1}\left[\frac{\left(\gamma+1\right)\bar{M}_1^2}{\left(\gamma-1\right)\bar{M}_1^2+2}\right]^{\frac{\gamma}{\gamma-1}}\left[\frac{\gamma+1}{2\gamma\bar{M}_1^2-\left(\gamma-1\right)}\right]^{\frac{1}{\gamma-1}} \tag{41}$$

Calibration and Preparation

The Pitot pressure was not recorded directly. Instead, the amplified and filtered voltages were recorded into the binary data file, and a calibration was applied in the data processing code.

In preparation for further data processing based on the fluctuations, a detrending procedure (MATLAB's "detrend" function) was applied to remove a linear fit from the time-series record for each sampling record. Both the DC-coupled and AC-coupled data

were processed similarly. Any additional gain applied only to the AC-coupled channel was divided out in the data reduction so that a direct quantitative comparison could be made between the DC-coupled and AC-coupled channels.

Fluctuation-Derived Quantities

The following fluctuation-derived quantities were computed and plotted: noise (acoustic/total pressure fluctuations), autocorrelation coefficient functions, integral time scales, and PSD estimates (line plots and spectrograms). The fluctuation signals were assumed to be stationary; that is, the average properties of the fluctuations were assumed to be constant within a sampling record no matter which subset of data from the sampling record was used.

Fluctuations/Noise

The pressure fluctuations obtained with the Pitot pressure probe, being acoustic in nature, are also called noise. The noise was simply calculated for each sampling record as:

$$\%\ \text{noise RMS} = \frac{\left(\overline{\left(p'_{t2}\right)^2}\right)^{1/2}}{\overline{p}_{t2}} \times 100 \tag{42}$$

Autocorrelation Coefficient Functions and Time Scales

Autocorrelations were performed by first dividing the 250 ms sampling record (500,000 sampling points) into segments. Each window was 1,024 points (about 500 μs of data at 2 MS/s; the transit time through the test section length was about 760 μs) and a

50% overlap was used, leading to 974 segments. No windowing profile was applied for the autocorrelation calculations.

The autocorrelations were calculated using MATLAB's "xcorr" cross-correlation function with the "unbiased" estimate option enabled. MATLAB performs the autocorrelation using the FFT method instead of the more time-consuming direct method. The direct method was coded in a separate script with no noticeable differences in the results from those of the built-in MATLAB function; the MATLAB function was used because of its robustness and speediness. The autocorrelation function of each segment was normalized by the variance of the segment. The normalized autocorrelation coefficient functions of all the segments for each sampling record were then averaged to obtain the autocorrelation coefficient function for that sampling record.

The integral time scale of a sampling record is calculated from the averaged autocorrelation function of that sampling record. Typically, the integral time scale is defined as:

$$t_{11} = \int_0^\infty f(\tau)\, d\tau \tag{43}$$

where f is the averaged, normalized autocorrelation function for a sampling record. However, an alternate definition using the FWHM of the two-sided autocorrelation function, shown in Figure 53, was employed to define the integral time scale [79]. A

MATLAB function named "crossing"[11] was used to calculate the time scale from the discrete points of the autocorrelation functions.

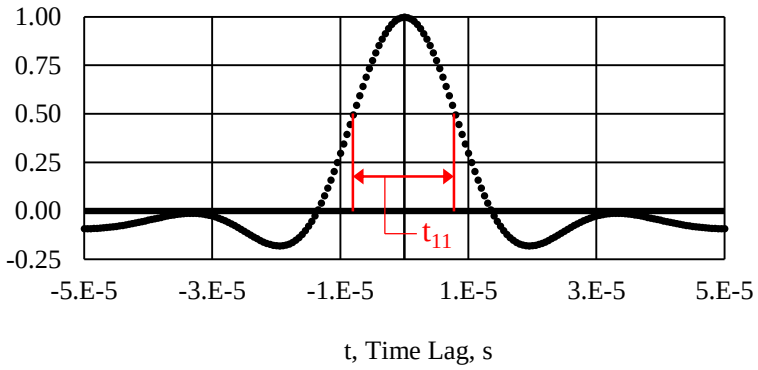

Figure 53. Illustration of definition of integral time scale based on FWHM of autocorrelation function.

Typically, to obtain the integral length scale, Taylor's hypothesis is invoked [27]. Taylor's hypothesis assumes that the turbulent structures are "frozen" into the flow and convected along at the flow's bulk velocity. The hypothesis is appropriately applied when $u' \ll \bar{u}$.

$$L_{11} = \bar{u}_1 t_{11} \tag{44}$$

The mean velocity used in Taylor's hypothesis is the *local* mean velocity. Since the mean velocity differential between the freestream value and the post-Mach stem value is large, it would be difficult to compare the freestream length scales and the post-Mach stem

[11] Brueckner, S., "crossing," MATLAB Central File Exchange, retrieved 2 Mar 2014 (http://www.mathworks.com/matlabcentral/fileexchange/2432-crossing).

length scales and determine the effect due to shock-turbulence interaction versus the effect simply due to a shock wave in a flow with no disturbances or fluctuations. Thus, *the following analyses considered the modifications to only the integral time scales*, since the measurements made were time-series records.

Power Spectral Density Estimates

Welch's method (MATLAB function "pwelch") was used for PSD estimation. Each 500,000-point sampling record was divided into 50% overlapping segments of 2,048 (2^{11}) points each. The default Hamming window was applied to each of the 487 segments per sampling point. The maximum frequency in the PSD estimate was determined by the sampling rate (for 2 MS/s, the maximum frequency is 1 MHz):

$$f_{\max} = \frac{\text{sampling rate}}{2} \tag{45}$$

The number of frequencies considered is based on the segment length (for 2,048 points at 2 MS/s, each frequency division is about 976 Hz):

$$\Delta f = \frac{\text{sampling rate}}{N} \tag{46}$$

While the spectra were estimated in terms of frequency, they are often most presented in the literature in terms of the wavenumber κ:

$$\kappa = \frac{2\pi f}{\bar{u}} \tag{47}$$

with the appropriate *local* mean velocity in the denominator. Based on similar arguments as to why the integral time scales were considered in this analyses instead of the integral

length scales, *power spectral density estimates were considered in frequency space instead of wavenumber space*.

The spectra could also be expressed versus a nondimensionalized distance. Larsson, Bermejo-Moreno, and Lele [11] brought up the question of an appropriate length scale for nondimensionalization and implied that different length scales should be used for larger scales versus smaller scales, but no suggestion is offered for either scale. For DNS studies and experimental studies like this one where there is not a grid that generates turbulence, it is difficult to define a length scale for what is essentially free fluid interaction.

When the abscissa of a spectra plot is plotted logarithmically, it is suggested that the spectra be "preamplified" or "compensated" (i.e., the spectra amplitude at each wavenumber is multiplied by the wavenumber) so that equal areas under the curve correspond to equal amounts of energy [80]. This aids in interpreting energy shifts in the wavenumber space.

Another method of presenting spectrum data is to normalize the spectrum, which depicts the frequency components of physical fluctuations, by the mean of the square of the fluctuations represented by that spectrum; this removes the physical units from the spectrum data.

$$\mathrm{PSD}_{\mathrm{norm}} = \frac{\mathrm{PSD}}{\overline{\left(p'_{t2}\right)^2}} \tag{48}$$

Presenting normalized spectra shows relative redistributions in frequency content of the fluctuations. *This normalization was employed here to calculate amplification factors*.

This follows the suggestion by Ribner [81] in his reply to the work by Barre, Alem and Bonnet [48], who provided a response [82].

FREESTREAM PITOT PRESSURE RESULTS AND DISCUSSION

This section describes the results and provides a discussion of the characterization of the freestream Pitot pressure fluctuations, which served as the inflow condition to this study of shock-turbulence interaction. The results presented in this section used the "thick wedge" model set. The AC-coupled data were filtered with the 50-kHz low-pass, 8-pole Butterworth filter option (in addition to all of the conditioning and filtering shown in Figure 38). In freestream wavenumbers, this corresponds to a cutoff of about κ = 360 rad/m. *The low-pass filter cutoff is denoted by a red line in all of the PSD estimates.*

Two types of tunnel operating modes were used: 1) a traverse of the probe at constant tunnel conditions and 2) a pressure (Re) sweep at constant probe location. For the traverse runs, two nominal Re/m conditions were obtained: the low Re/m condition corresponded to a nominal Re/m of 2.0×10^6/m and the high Re/m condition corresponded to a nominal Re/m of 4.0×10^6/m.

Freestream disturbances in a supersonic/hypersonic wind tunnel come from various sources. The incoming air supply has gone through heaters, filters, pipe bends, corrugated hoses and many other things before it expands through the nozzle. Each of these components affect the turbulence, considered in Kovásznay's three modes [29], prior to and after the expansion. A notional drawing of freestream disturbances and their origins, from Schneider [83], is shown in Figure 54.

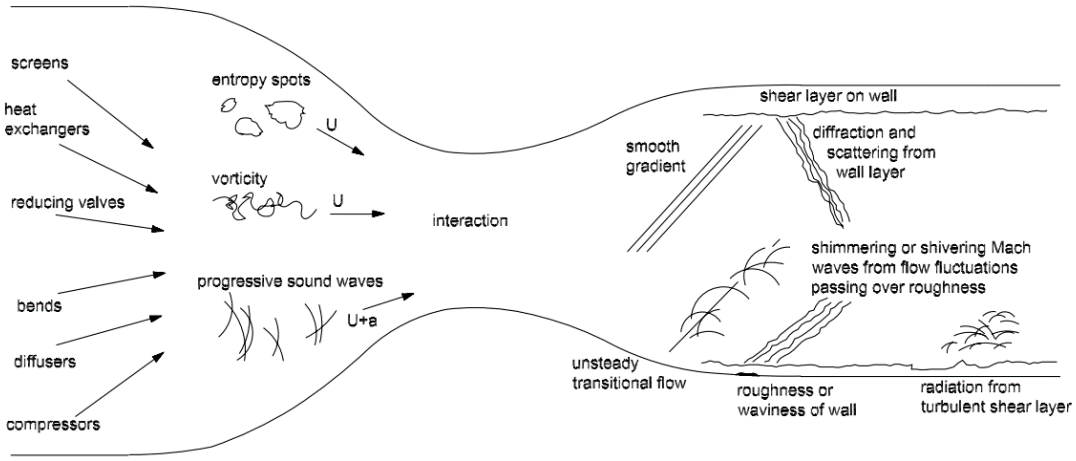

Figure 54. Freestream disturbances in a supersonic/hypersonic wind tunnel. (taken from Schneider [83])

The inflow/upstream turbulence used in this study of shock wave-turbulence interactions was the innate, freestream noise of the ACE nozzle. No other turbulence-generating mechanisms (e.g. a metal mesh/grid) were considered in this study, and a careful characterization of the freestream flow was necessary to accurately determine the effects of the shock-turbulence interaction. The variations in fluctuation intensities with Re/m supported studies of the influence of upstream conditions on amplification factors. The following results served as the inflow/upstream conditions of the shock-turbulence interaction.

Pressure (Reynolds Number) Sweep: Freestream

This subsection presents the noise, autocorrelation coefficient functions, integral time scales, and the PSD estimates from a freestream pressure sweep. The pressure sweep was accomplished by changing the pressure supplied to the settling chamber, which in turn, affected the test section static pressure, density, and Re/m. The Pitot pressure probe

was in a fixed position throughout the sweep. Table 13 shows the average run parameters for the data presented in this subsection.

Table 13. Tunnel parameters for freestream flow pressure sweep run.

Run No.	Run Type	M_{avg}
2126	FS – Re/m Sweep	5.87

Fluctuations/Noise: Freestream Sweep

Previously presented (Tichenor et al. [54] and Semper, Pruski, and Bowersox [60]) and soon-to-be-published results detail the freestream characteristics of the ACE tunnel nozzle across multiple *M* and Re/m. The most recent, prior to this study, Pitot pressure fluctuations were characterized using a fast-response Pitot pressure probe mounted with a Kulite XCEL-062-100A transducer.

Freestream noise characterization has shown that for the entire Mach number range, the noise was about 0.5% RMS for Re/m below 2.5×10^6/m. In the Re/m range of $2.5\text{-}3.5\times10^6$/m, the noise gradually increased to almost 2.0%. The high-Reynolds number stabilizing effect was seen as the noise gradually decreased for Re/m above 3.5×10^6/m. It is believed that this is indicative of the nozzle boundary layer being in a laminar state at the lower Re/m, in a transition state for the mid-Re/m range, and in a turbulent state at the higher Re/m.

Another freestream, Pitot pressure fluctuation characterization was performed in this with the Kulite XCEL-100-5A (see Pitot Pressure probe subsection) in the vicinity of where the Mach stem would be when the Mach stem generator wedge models were

installed. The exit plane results and the current characterization are shown in Figure 55. In the low Re/m regime, the noise was higher than at the nozzle exit plane. The rise to high noise also occurred at a smaller Re/m. In the high Re/m regime, the noise was comparable to what they were at the nozzle exit plane. It was concluded that the noise in the low Re/m range was sensitive to distance along the test section whereas the noise in the high Re/m range was insensitive. This agrees with previous findings and points to the boundary layer state being the cause of the differences in fluctuations over a range of Re/m at a particular location. For a particular low Re/m, a further downstream location corresponds to a higher Reynolds number and likely explains the higher noise and the noise increase at a lower Re/m. Once the boundary layer is turbulent, however, the noise level becomes insensitive to the Reynolds number.

Figure 56 shows notional images of the influence of the nozzle boundary layer state on the freestream disturbance level. The left panel is at a low Re/m condition in which the boundary layer is laminar and minimally affects the freestream disturbance level. In contrast, the right panel is at a high Re/m condition in which the boundary layer is turbulent and radiates noise into the freestream and increases the disturbance level.

The implication of these results was that this study of shock-turbulence interaction could utilize two different freestream/incoming noise levels: a low noise level associated with a lower Re/m and a high noise level associated with a higher Re/m.

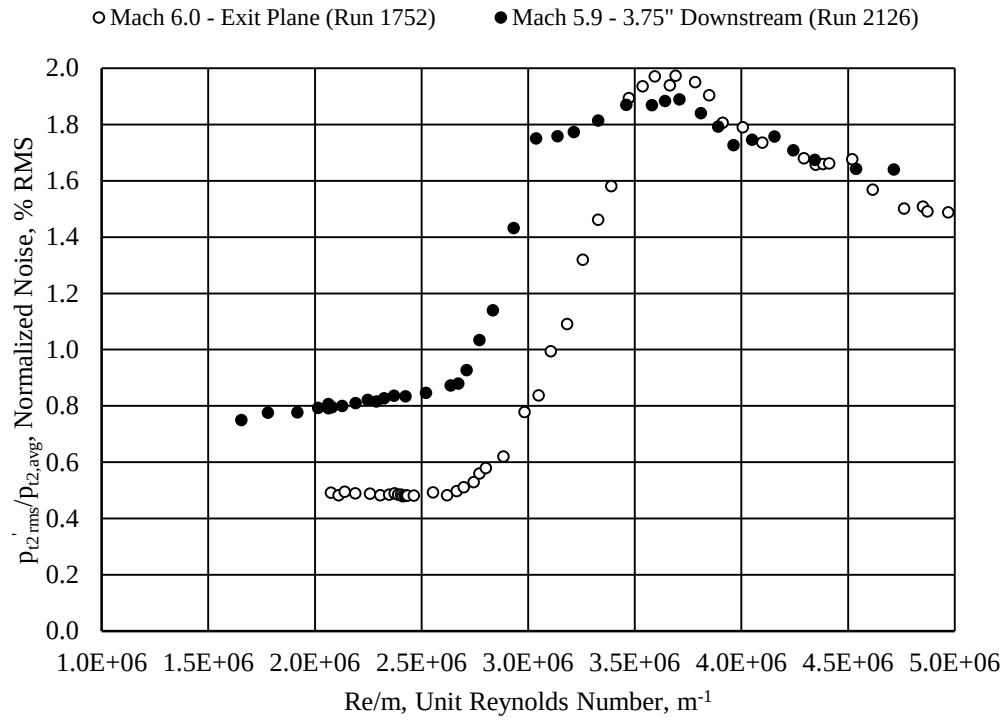

Figure 55. ACE tunnel freestream flow noise at nozzle exit plane and 95 mm (3.75 in.) downstream.

Figure 56. Notional drawings showing influence of nozzle boundary layer state on freestream disturbance levels.

a) Laminar boundary layer at low Re/m. **b) Turbulent boundary layer at high Re/m.**

(credit: R. D. W. Bowersox)

Autocorrelation Coefficient Functions and Time Scales: Freestream Sweep

The autocorrelation coefficient functions at three different Re/m conditions are shown in Figure 57. The top panel is at the low Re/m condition. The middle panel is at an Re/m condition in which the noise level was about halfway between the low and high noise levels. The bottom panel is at the high Re/m condition. The profiles are qualitatively similar leading to the expectation that the integral time scale does not change drastically for various Re/m.

The integral time scales are plotted in Figure 58, and indeed, there was only a modest change throughout the range of Re/m. At the low Re/m condition, the integral time scale decreased with increasing Re/m. In the transitional Re/m range, the integral time scale increased by about 20% before continuing its shortening trend with increasing Re/m.

This variation in the integral time scale may be explained with the state of the nozzle and test section boundary layers. At the transitioning Reynolds numbers, the boundary layer had just gone turbulent and emanated large structures that interacted with the ellipsoidal turbulent vortices in the freestream that emanated from the settling chamber. As the Reynolds number increased, the turbulent energy cascade established and the stabilizing effect reduced the size of the structures emanated from the boundary layer and reduced the resulting integral time scale of the freestream fluctuations.

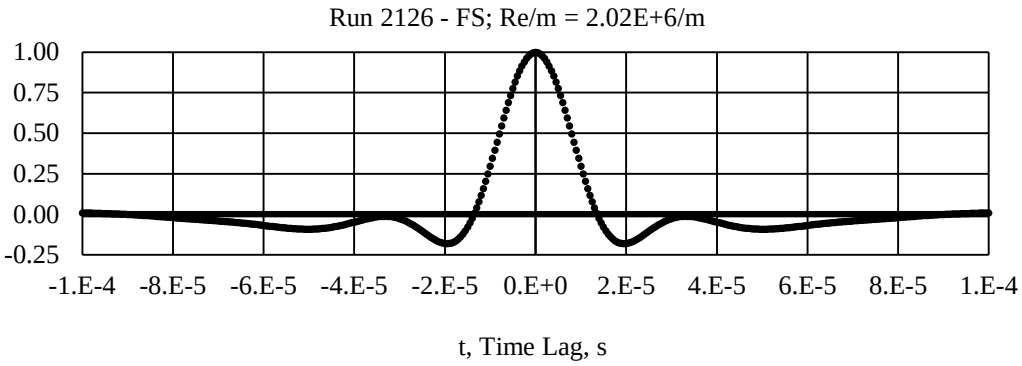

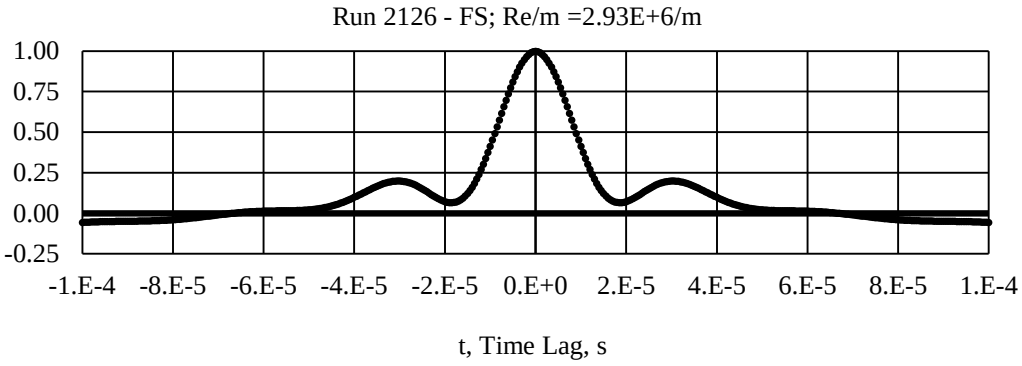

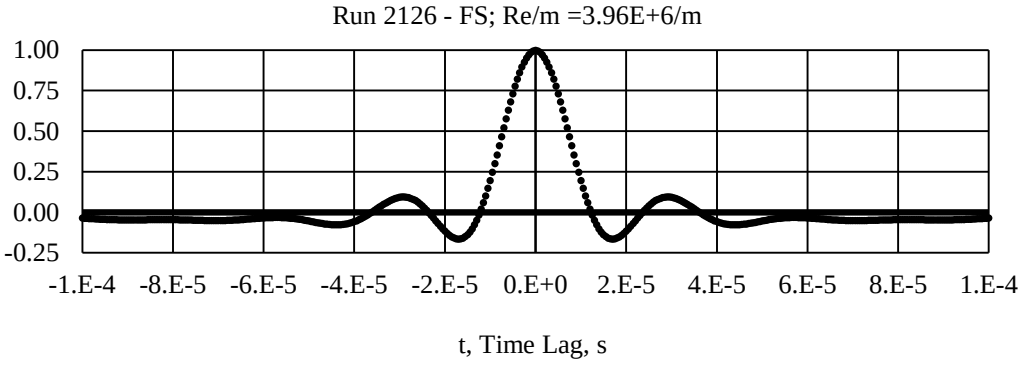

Figure 57. Autocorrelation functions of freestream flow noise for different Re/m conditions.

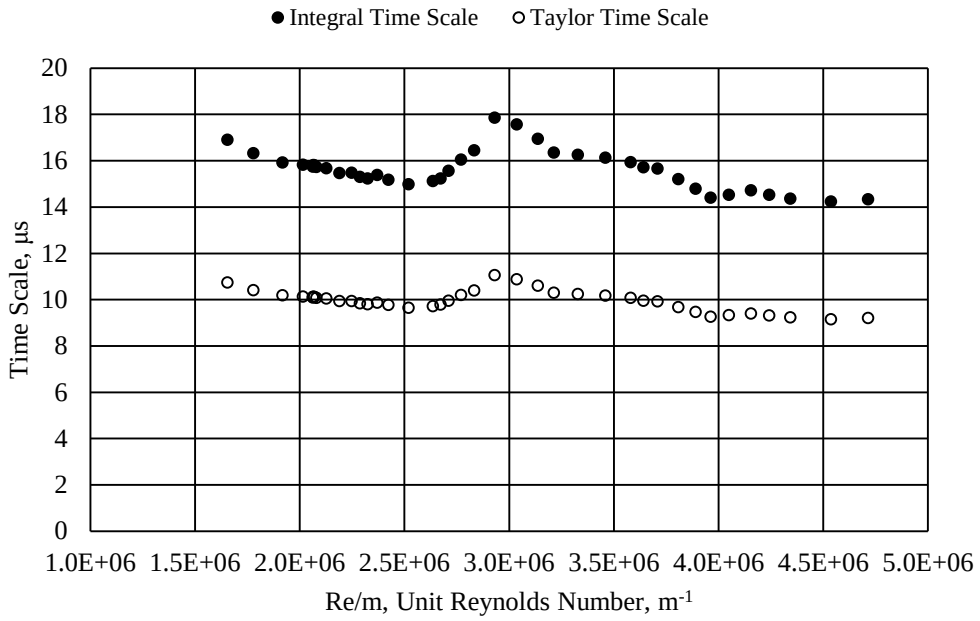

Figure 58. Time scales of freestream flow noise for different Re/m conditions.(Run 2126)

The Taylor time scale is also plotted in Figure 58. The time scale was obtained by the definition of the Taylor time scale. An osculating parabola was fitted to the zero time lag point and two additional time lag points on one side of the autocorrelation coefficient functions. The time-intercept of the parabola is the value of the Taylor time scale. The Taylor time scale was observed to trend along and be of the same order as the integral time scale, indicating that the tunnel freestream turbulence was low-Reynolds-number turbulence (where low is used in the sense of the broad range of fluid flow Reynolds numbers). An advantage of the low-Reynolds-number turbulence was that the flow is more accessible to DNS for comparisons and further analyses. A disadvantage, however, was that classical scaling, which is typically for high-Reynolds number turbulence, does not apply as well.

Power Spectral Density Estimates: Freestream Sweep

The freestream noise spectra at the same Re/m conditions as the autocorrelation coefficient functions are shown in the top panel of Figure 59. With increasing Re/m, the overall contribution to the increase in fluctuation levels was spread across the full range of wavenumbers. At a transitional Re/m condition, the spectrum showed that the low frequency content increased first, which is in agreement with the corresponding increase in the integral time scale and the large structures emanated by a transitional boundary layer. The overall broadband increase, indicative of radiated acoustic fluctuations, lent further credence to the theory that the increase in noise levels was due to the boundary layer going to a turbulent state. In addition, the PSD estimates lacked a clear inertial subrange following Kolmogorov's -5/3 power law, thus strengthening the notion that the tunnel freestream noise exhibited characteristics of low Reynolds-number turbulence.

The bottom panel of Figure 59 show the PSD normalized by the mean of the square of the total pressure fluctuations. The normalized spectra provide a better interpretation of shifting frequency content. The normalized PSD of each Re/m are similar except for the transitional Re/m PSD at low frequencies, which further shows that large structures are being emanated by the transitional boundary layer.

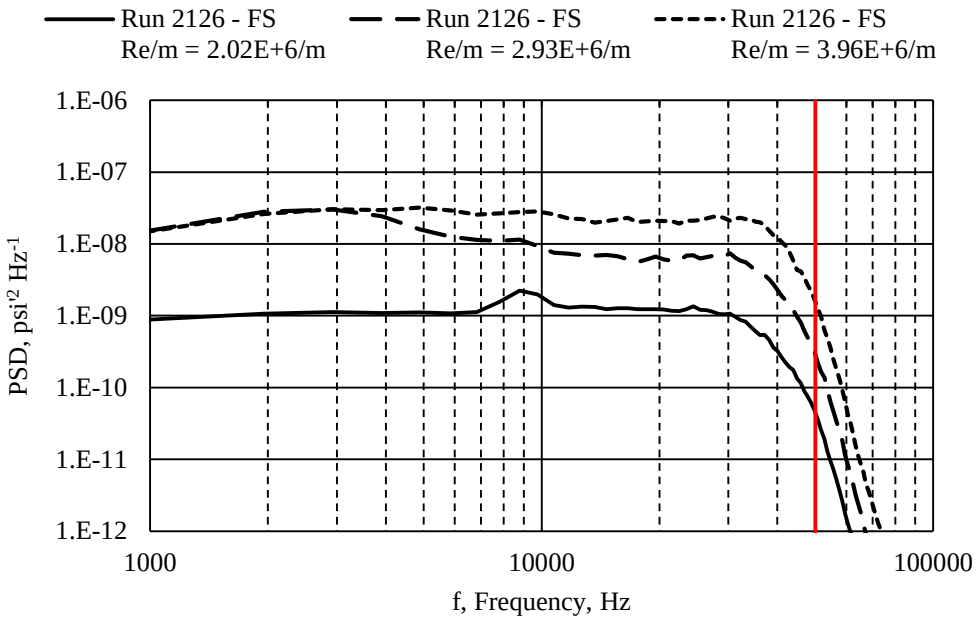

a)

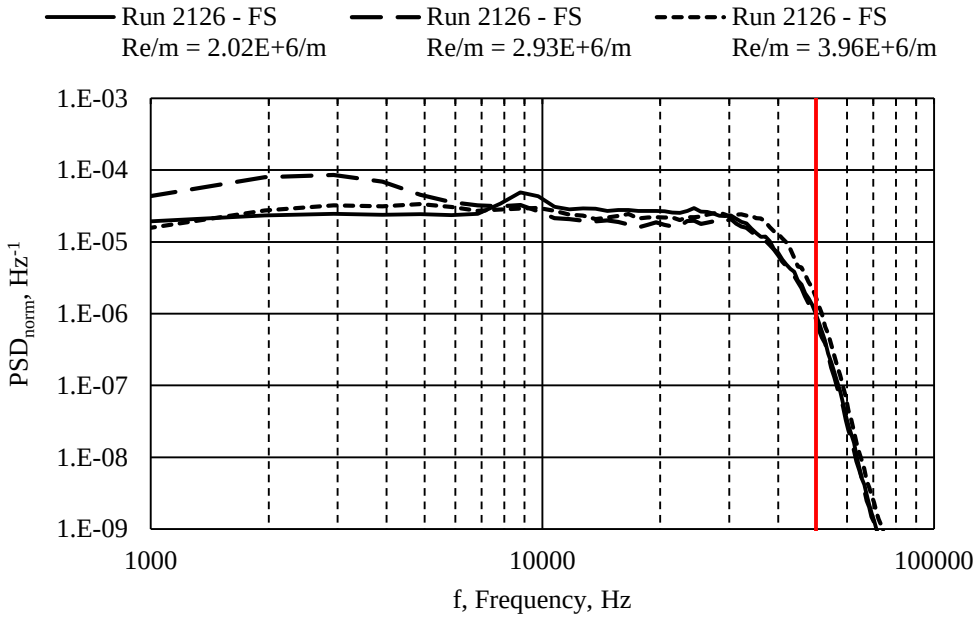

b)

Figure 59. PSD estimate line plots of freestream flow noise for different Re/m conditions.

a) Power spectral density estimates.

b) Normalized power spectral density estimates.

Figure 60 is a spectrogram of the noise mapped against frequency and Re/m (instead of time). An obvious broadband increase in the noise level in the transitional Re/m range was seen with the low frequency content increasing first.

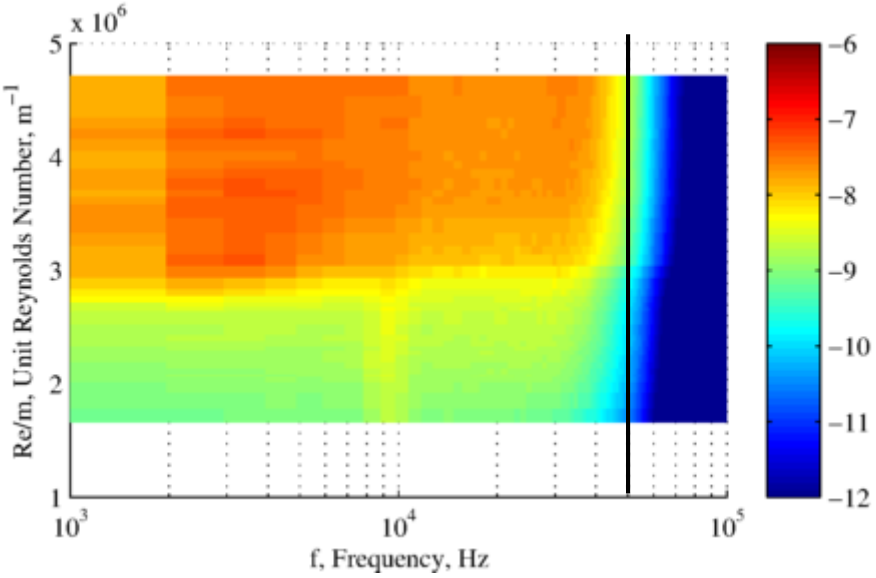

Figure 60. Spectrogram of freestream flow noise for different Re/m. (Run 2126)
The color scale is the log of the PSD.

Spatial Evolution (Traverse): Freestream

The second type of tunnel run to characterize the freestream noise were runs in which the probe was traversed in the freestream direction and tunnel conditions were kept as "constant" as possible (given the limitations of the tunnel hardware and infrastructure). The following results will show near-constant noise properties in the region where the Mach stem would be generated. So while the pressure (Reynolds number) sweep results presented previously show variations in noise with downstream location, this variation

was deemed negligible in the small spatial region of measurements around the Mach stem. Table 14 shows the average run parameters for the data presented in this subsection.

Table 14. Tunnel parameters for freestream flow traverse runs and comparison run.

Run No.	Run Type	M_{avg}	Re/m_{avg}
2126	FS – Re/m Sweep	5.87	--
2129	FS – Traverse – Low Re/m	5.99	1.95×10^6/m
2127	FS – Traverse – High Re/m	5.82	3.95×10^6/m

Fluctuations/Noise: Freestream Traverse

Figure 61 shows the freestream noise at various locations along the freestream direction. Two runs were performed: one run at the nominal low Re/m condition and one run at the nominal high Re/m condition. The freestream noise values from the freestream pressure sweep are interpolated to each traverse run's average Re/m, and they are included for comparison.

For the low Re/m condition traverse data, the freestream noise level showed an increasing trend, and this was expected from the conclusions drawn in the previous subsection for the freestream noise level sensitivity to distance from the nozzle exit plane. A trend was not clearly obvious for the freestream noise level for the high Re/m condition traverse data, and this was also expected from the conclusions drawn from the freestream pressure sweep comparisons at different distances from the nozzle exit plane.

The noise values from the Re/m-interpolated freestream pressure sweep matched well and are were within the scatter of variations in operating conditions across tunnel runs. The generated Mach stem was expected to be about 104 mm downstream of the

nozzle exit plane, whereas the freestream pressure sweep (described in the last subsection) was made 95 mm downstream of the nozzle exit plane. Figure 61 shows that while there is a finite difference (about 5% for the low Re/m case), the inherent variation in tunnel performance repeatability casted a similar uncertainty.

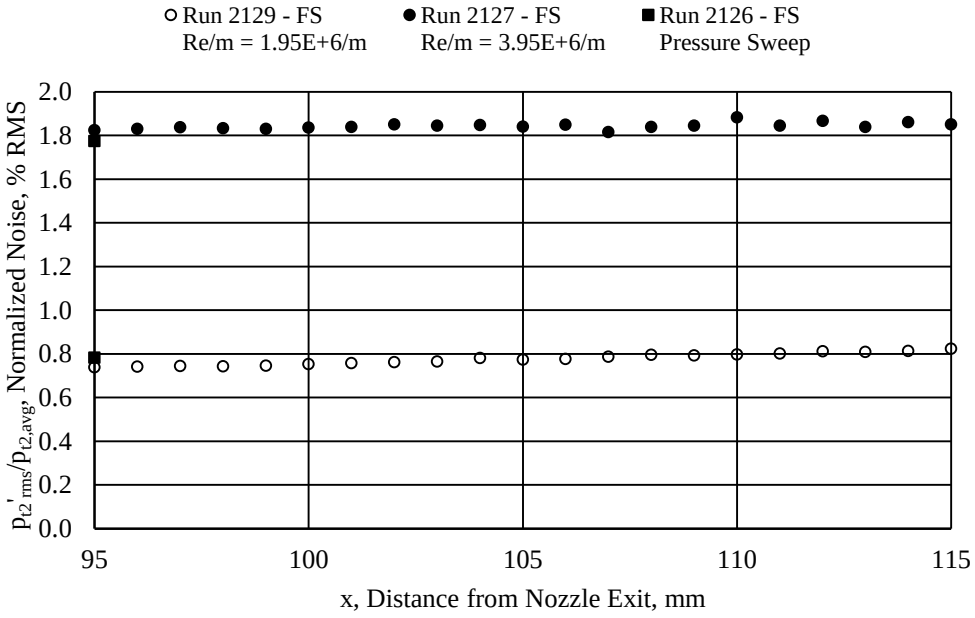

Figure 61. ACE tunnel freestream flow noise spatial evolution.

Autocorrelation Coefficient Functions and Time Scales: Freestream Traverse

Autocorrelation coefficient functions are shown at various locations downstream from the nozzle exit plane for both low Re/m (Figure 62) and high Re/m (Figure 63) conditions. Similar to the near- invariance of the freestream noise with distance from the nozzle exit plane, the autocorrelation profiles at each location for a particular Re/m condition were qualitatively (and near-quantitatively) identical to each other.

The integral time scales, as a result of the near-invariance of the autocorrelation coefficient functions, also exhibited near-invariance with downstream distance as seen in Figure 64. A comparison between the Re/m conditions show that the integral time scale was shorter for higher Re/m conditions. The integral time scale from the freestream pressure sweep were interpolated for the Re/m of each traverse run and shown for comparison. The traverse values matched the interpolated freestream pressure sweep values to within the scatter of tunnel repeatability.

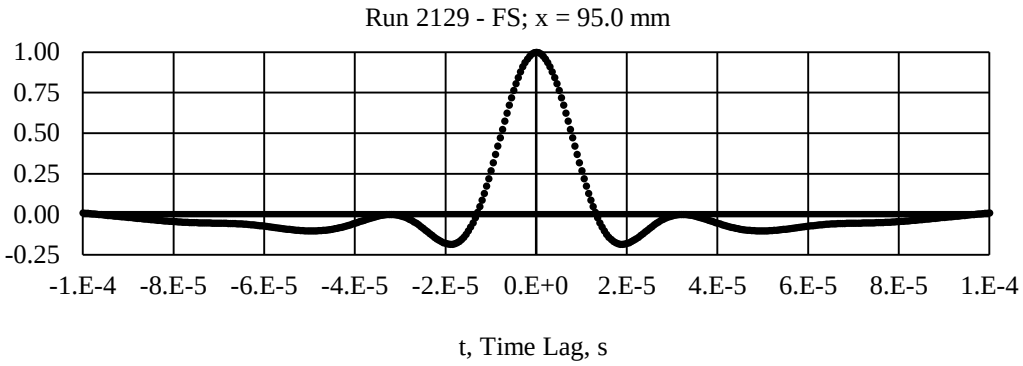

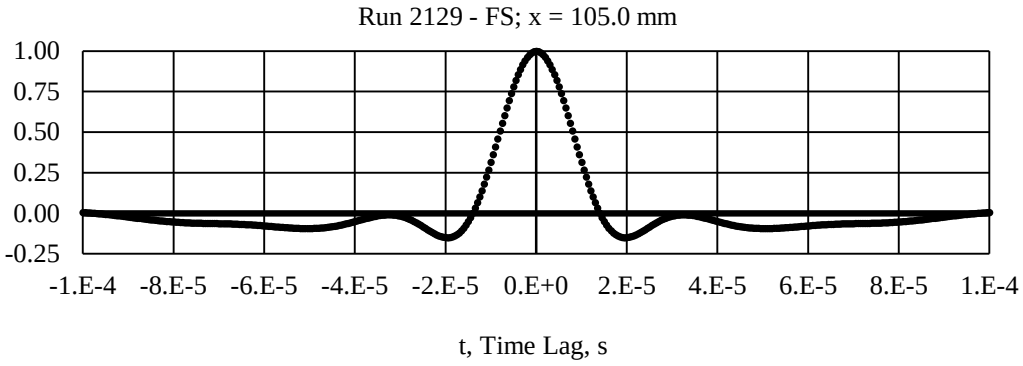

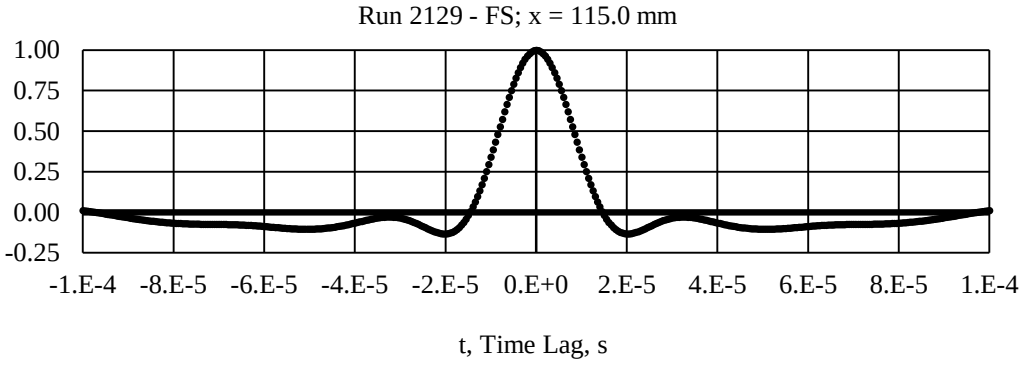

Figure 62. Autocorrelation coefficient functions of freestream flow noise at different positions for low Re/m condition. (Run 2129)

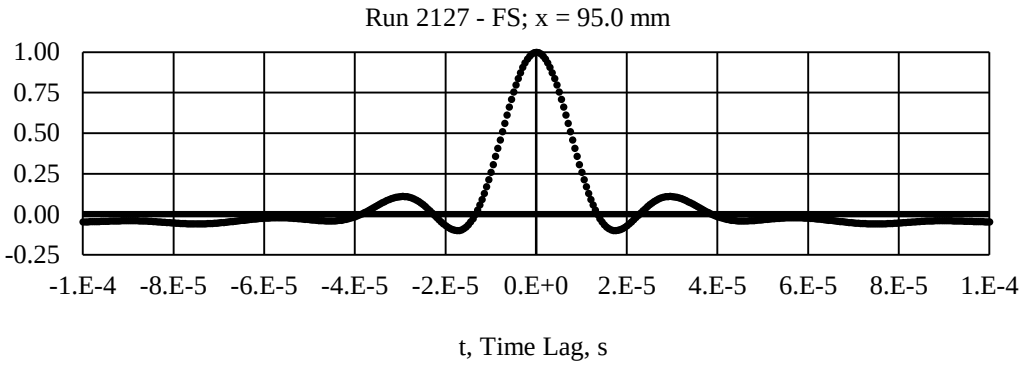

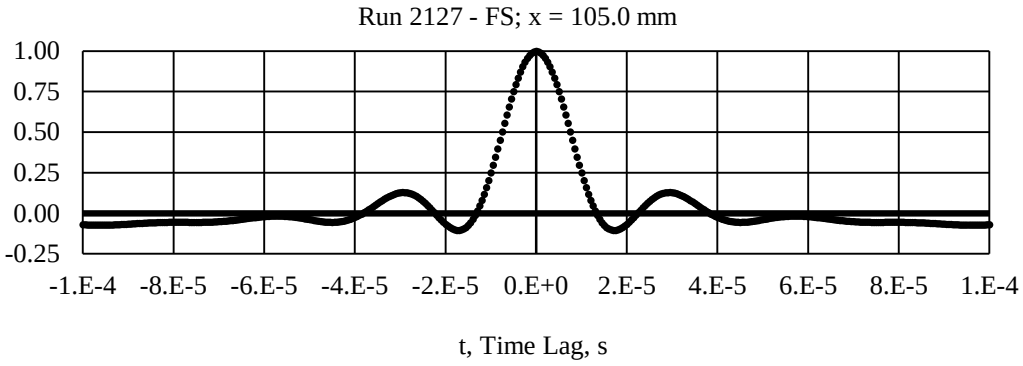

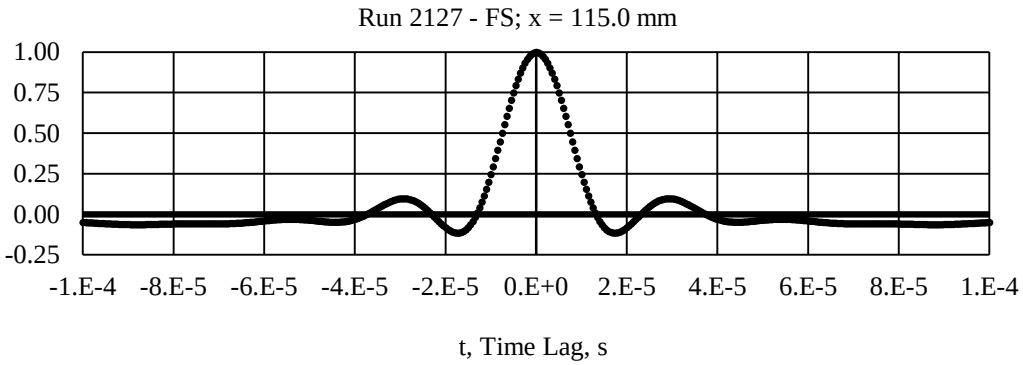

Figure 63. Autocorrelation coefficient functions of freestream flow noise at different positions for high Re/m condition. (Run 2127).

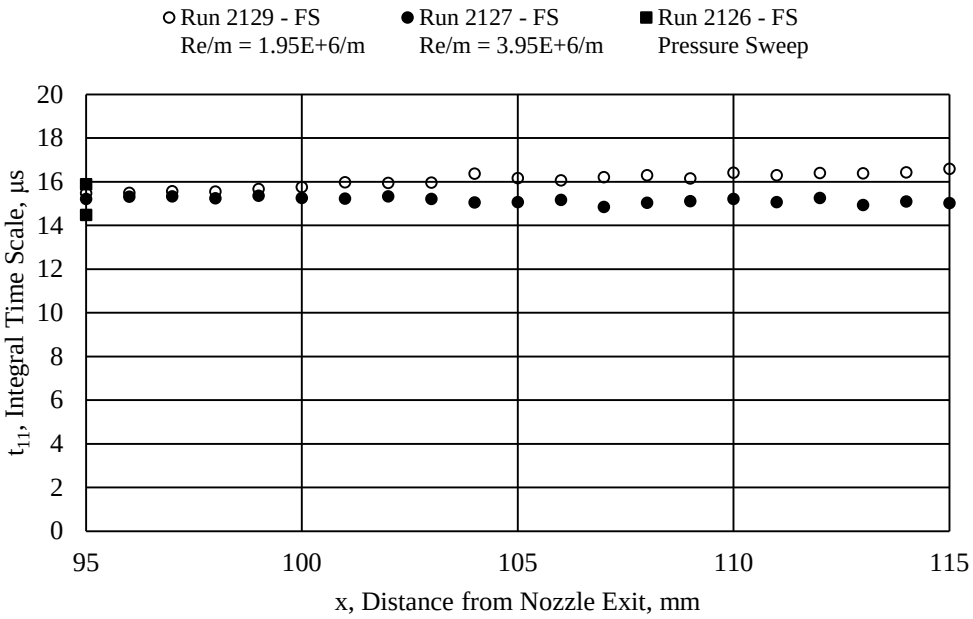

Figure 64. Integral time scale of freestream flow noise at different positions.

Power Spectral Density Estimates: Freestream Traverse

PSD estimates are calculated and presented to further validate the near-invariance of flow properties in the freestream direction. Figure 65 shows PSD estimate line plots at three different positions downstream from the nozzle exit plane, which are similar to each other. This provides validation of the near-invariance of the noise properties in the region around where the Mach stem will be. Figure 66 shows the normalized PSD estimate line plots.

Lastly, spectrograms showing PSD on a position/frequency map are presented in Figure 67 for both Re/m conditions. The lack of color shift among frequencies through all of the positions show again that there is invariance with position. The streak that persisted through all positions in the top panel of Figure 67 (low Re/m condition) at a frequency of

about f = 9,000 Hz may be acoustic resonance between the bow shock (which stood off away from the body) and the Pitot pressure probe sensor. Another explanation is mechanical vibration of the traverse assembly.

Summary: Freestream Characterization

As with previous ACE tunnel characterizations, two distinct total pressure fluctuation regimes existed as a function of Re/m. At Re/m less than 2.5×10^6/m, the normalized noise was about 0.8% rms. At Re/m higher than 3.0×10^6/m, the normalized noise was about 1.8% rms. The PSD estimates of these two ranges showed a broadband increase from low to high Re/m, supporting the notion that the noise variation was due to the transitioning state of the nozzle boundary layer.

The integral time scales decreased with increasing Re/m with the exception of the transitional Re/m range where there was a noticeable increase. This further supports the notion of a transitioning nozzle boundary layer. In addition, the Taylor time scales are on the same order of the integral time scales, indicating that the tunnel freestream noise was low-Reynolds-number turbulence in character. The lack of a clear inertial subrange and the Kolmogorov -5/3 power law in the power spectral density estimates were further indicators of low-Reynolds-number turbulence. An advantage of this behavior was that the low-Reynolds-number environment should be tractable for DNS, allowing more direct comparisons between computations and experiments. The disadvantage was that classical turbulence scaling does not apply.

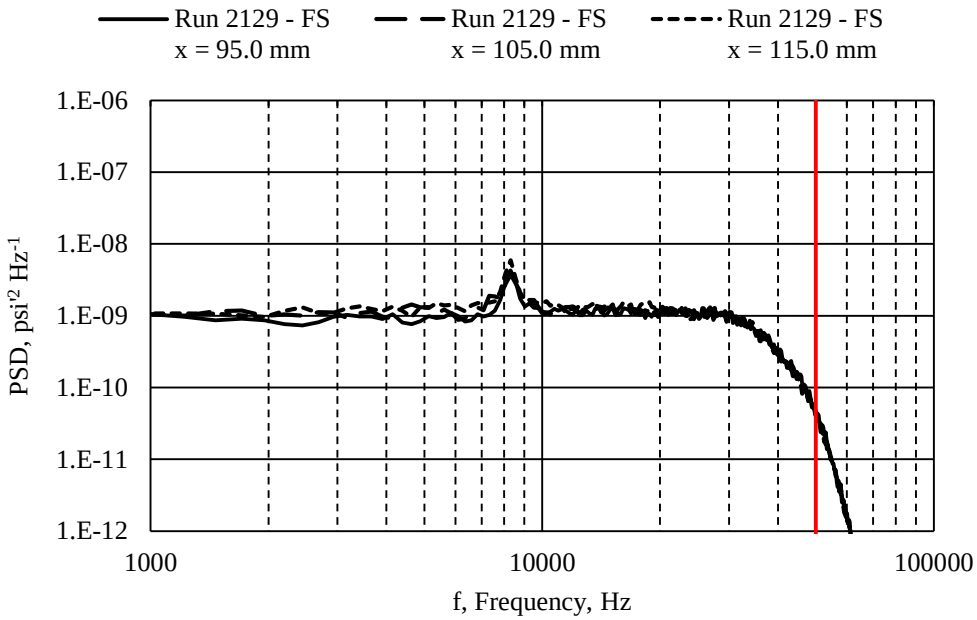

a)

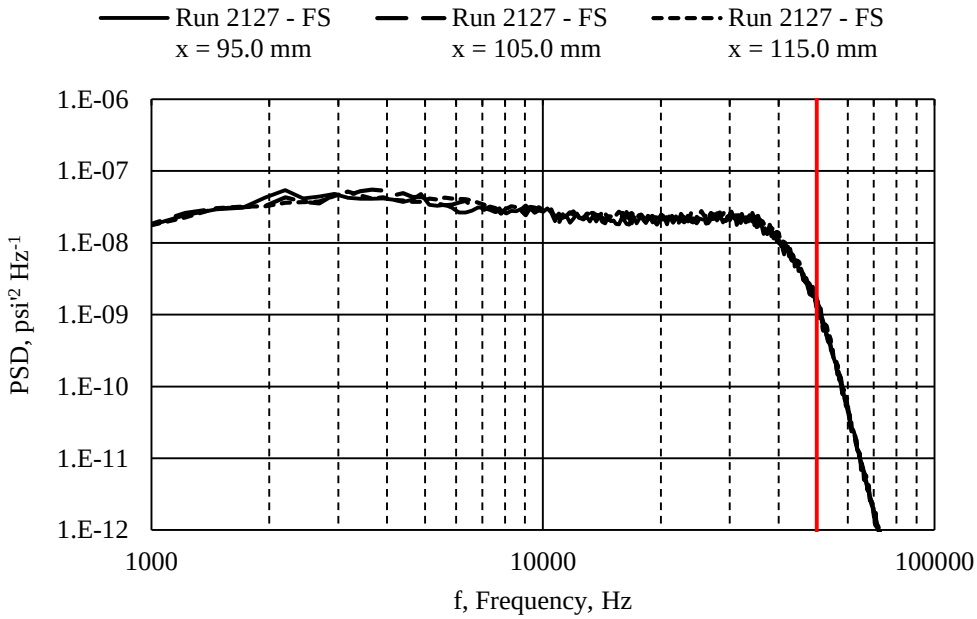

b)

Figure 65. PSD estimates line plots of freestream flow noise at different positions.

a) Low Re/m condition. (Run 2129)

b) High Re/m condition. (Run 2127)

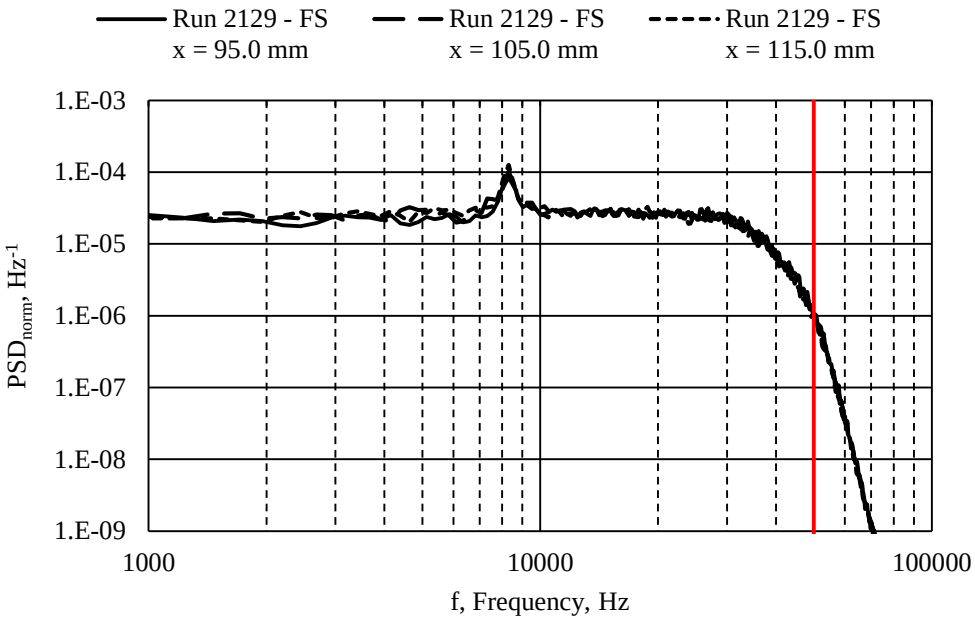

a)

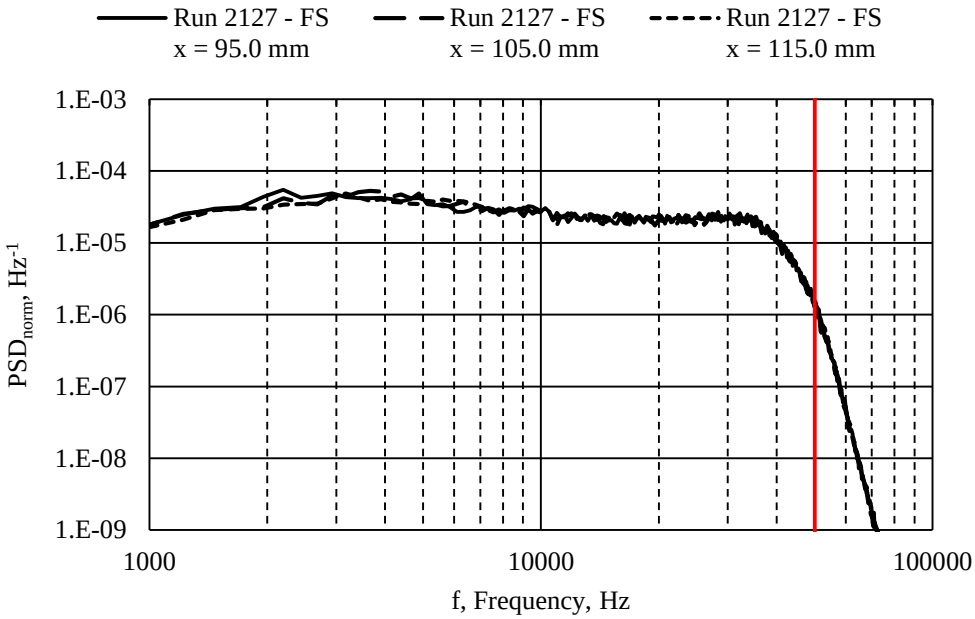

b)

Figure 66. Normalized PSD estimates line plots of freestream flow noise at different positions.

a) Low Re/m condition. (Run 2129)

b) High Re/m condition. (Run 2127)

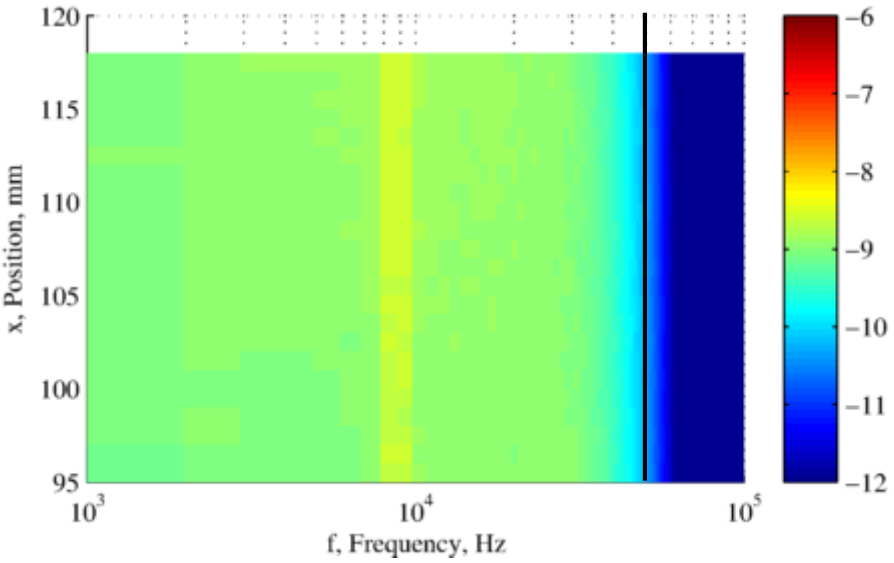

a)

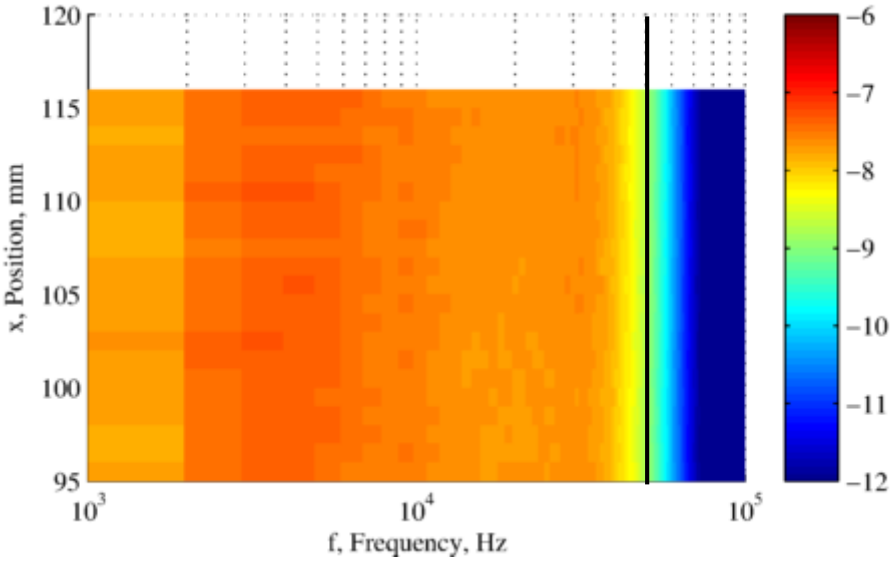

b)

Figure 67. Spectrogram of freestream flow noise at different positions.

Color scales are log of PSD.

a) Low Re/m condition. (Run 2129)

b) High Re/m condition. (Run 2127)

POST-MACH STEM PITOT PRESSURE RESULTS AND DISCUSSION

This subsection presents Pitot pressure measurements made with the Mach stem generator wedge models installed. Appropriate comparisons are made with the upstream/inflow conditions measured during the freestream characterization.

Spatial Evolution (Traverse): Post-Mach Stem

The spatial evolution (traverse) results are presented first, since those results influenced where pressure (Reynolds number) sweeps were obtained. These results established the nonuniformity behind the Mach stem. Two traverse runs were performed at the low Re/m condition, and two traverse runs were performed at the high Re/m condition. For each Re/m condition, one run was a coarse spacing of sampling locations separated by 1.00 mm (0.039 in.), and the other run was a fine spacing of sampling locations separated by 0.25 mm (0.010 in). Table 15 shows the average run parameters for the data presented in this subsection.

Table 15. Tunnel parameters for Mach stem flow traverse runs and comparison runs.

Run No.	Run Type	M_{avg}	Re/m_{avg}
2129	FS – Traverse – Low Re/m	5.99	1.95×10^6/m
2132	MS – Traverse – Low Re/m – 1 mm Spacing	5.88	2.03×10^6/m
2138	MS – Traverse – Low Re/m – 0.25 mm Spacing	5.87	2.03×10^6/m
2127	FS – Traverse – High Re/m	5.82	3.95×10^6/m
2131	MS – Traverse – High Re/m – 1 mm Spacing	5.81	4.00×10^6/m
2137	MS – Traverse – High Re/m – 0.25 mm Spacing	5.79	3.88×10^6/m

Fluctuations/Noise: Post-Mach Stem Traverse

Figure 68 depicts the spatial evolution of the Pitot pressure fluctuations relative to the Mach stem. Both profiles at both Re/m conditions showed a slight decrease in the noise levels at the location of the Mach stem. This was likely an artifact of the probe tip being in the vicinity of the interaction of its bow shock with the generated Mach stem. This artifact likely extended to about 1-2 mm behind the Mach stem where the noise levels reached a local maximum. For the low Re/m condition between 2 and 4 mm behind the Mach stem, the noise levels decreased whereas they were almost constant for the high Re/m condition in that spatial range.

More than 4 mm behind the Mach stem, the noise level increased linearly for both Re/m conditions. There is no explanation for this phenomenon yet, but the results that far downstream were likely biased due to the flow acceleration inferred from the "duct" geometry formed by the shear layers emanating from the triple point of the shock intersection. Andreopoulos, Agui, and Briassulis [7] reasoned that such an acceleration would result in lower turbulence being measured. However, the noise level increased without any discernible asymptotic state, and so it is believed that the shear layers may be turbulent and emitting additional noise into the "duct."

For both Re/m conditions, the finely spaced noise results compared very well to the corresponding coarsely spaced noise results, indicating that the phenomena exhibited by the noise profiles were repeatable.

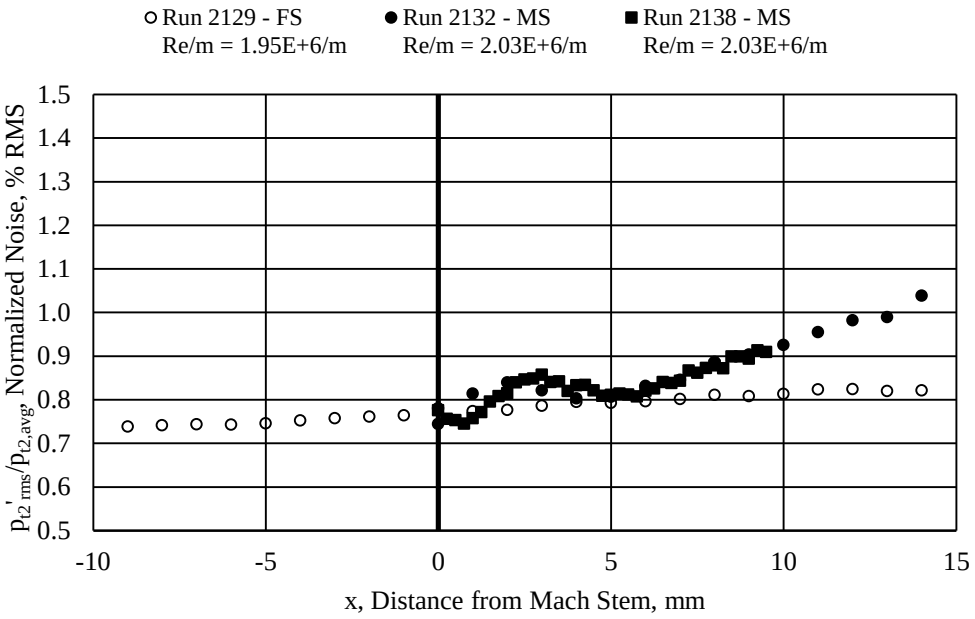

a)

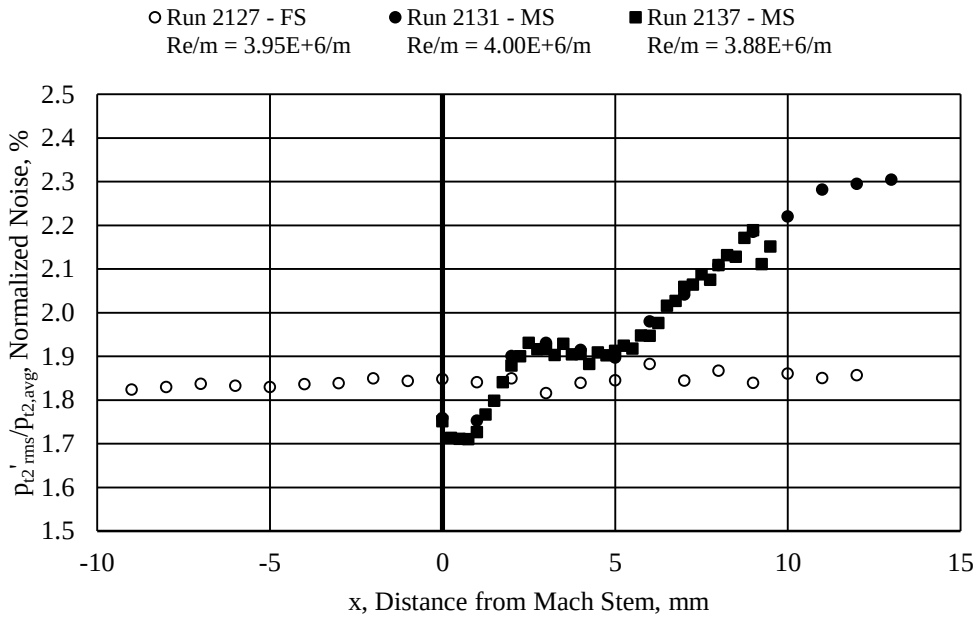

b)

Figure 68. Noise spatial evolution comparisons between freestream and Mach stem flows.

a) Low Re/m condition.

b) High Re/m condition.

All further comparisons in this subsection between freestream characterization and Mach stem characterization will compare the freestream 0 mm position to the Mach stem +2.0 mm position (the first local maximum behind the Mach stem) and the Mach stem +4.0 mm position.

Noise amplification factors were estimated at the +2.0 mm and +4.0 mm positions by comparing to the freestream flow noise level at the position where the Mach stem would be. These estimates are in Table 16. Noise values are given in percent normalized RMS in the freestream and at the two specified locations downstream of the Mach stem. The freestream variation was the range of the freestream flow noise values in a region ± 2 mm of the Mach stem. The amplifications were modest compared to the pressure fluctuation amplification of 1.25-2.80 found in Xanthos, Briassulis, and Andreopoulos [52] in shock tube studies with grid-generated turbulence.

Table 16. Noise amplification estimates in Mach stem flow for low and high Re/m conditions.

	Low Re/m (Run 2138)		High Re/m (Run 2137)	
	RMS %	Amplification	RMS %	Amplification
Freestream	0.78%	--	1.85%	--
2 mm Downstream	0.82%	1.04	1.88%	1.03
4 mm Downstream	0.83%	1.07	1.91%	1.02
Freestream Variation	0.020%	--	0.009%	--

Amplification factors at downstream locations are shown in Figure 69. Again, it was believed that the results within 1-2 mm of the Mach stem, where the amplification factors were less than 1, are biased due to interference between the Pitot pressure probe and the Mach stem. Beyond 5 mm downstream from the Mach stem, the amplification

factors were comparable between the low and high Re/m conditions. Again, results that far downstream may be showing effects of the "duct" geometry behind the Mach stem rather than the evolution of the turbulence due to the normal shock wave. In the region of interest, between 2 and 4 mm, the amplification factor peaked at 1.10 for the low Re/m condition and at about 1.05 for the high Re/m condition.

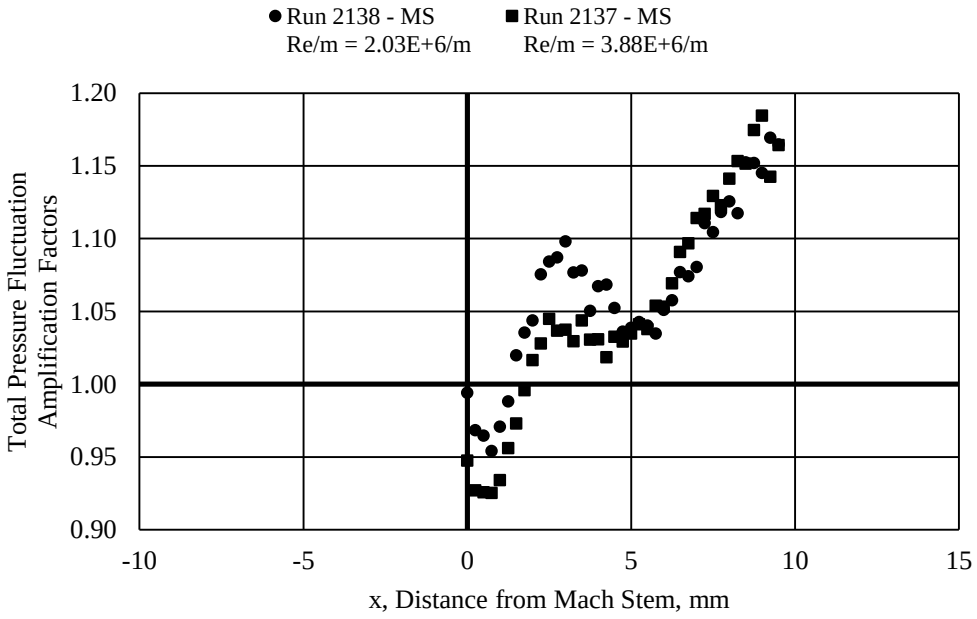

Figure 69. Total pressure fluctuation amplification factors for Mach stem traverse.

Autocorrelation Coefficient Functions and Time Scales: Post-Mach Stem Traverse

Autocorrelation coefficient functions at different locations are presented in Figure 70 (low Re/m condition) and Figure 71 (high Re/m condition). The autocorrelation coefficient functions between the freestream characterization and the Mach stem

characterization are qualitatively similar, and it can be inferred that the integral time scale did not change discontinuously in the near region behind the Mach stem.

Figure 72 shows the integral time scales and the time scale amplification factors. The top panel shows a comparison of integral time scales between freestream and Mach stem flows for both low and high and Re/m conditions. The behavior of the time scales behind the Mach stem were qualitatively similar. Both showed a decrease immediately behind the Mach stem in the region believed to be affected by probe-Mach stem interference. After that, the integral time scale increased and peaked at 5 mm behind the Mach stem before a slight decreasing trend occurred. When the time scales were normalized by the freestream integral time scale at the Mach stem for their respective Re/m conditions, the amplification factors for both Re/m conditions were almost identical. Based on these two Re/m conditions, it appeared that the amplification factor is insensitive to the freestream noise levels.

Jamme et al. [31] noted that, aside from the work by Barre, Alem, and Bonnet [48], experimental data have shown an overall increase in microscales, which has long contradicted the results of theory and simulation. Lele [6] also discussed this discrepancy. Estimates of the Taylor microscale in this work showed that it and the integral times scales trend together, as can be intuitively expected. Barre, Alem, and Bonnet found an overall decrease in the length scales when invoking Taylor's hypothesis. The decrease in length scale was more than what could be accounted for by the difference in the local mean velocity on each side of the shock wave; thus, they had observed a substantial decrease in the integral time scale.

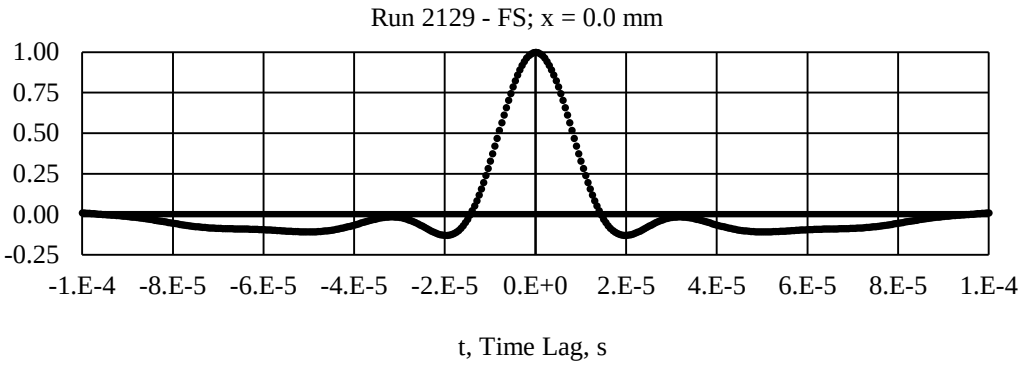

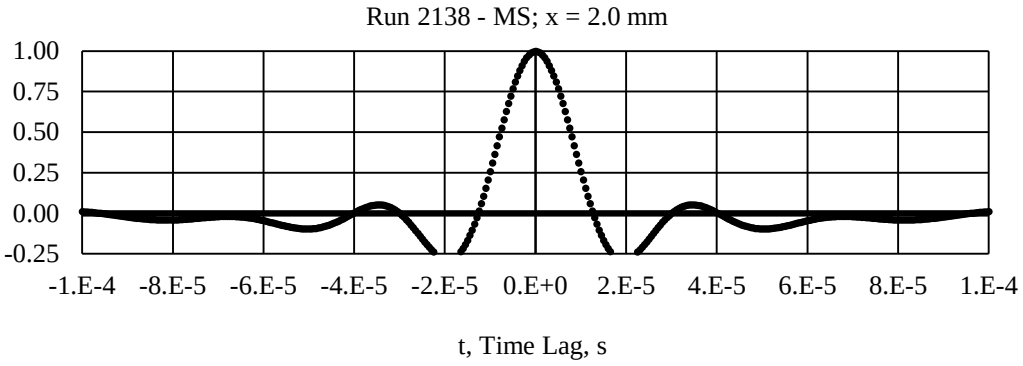

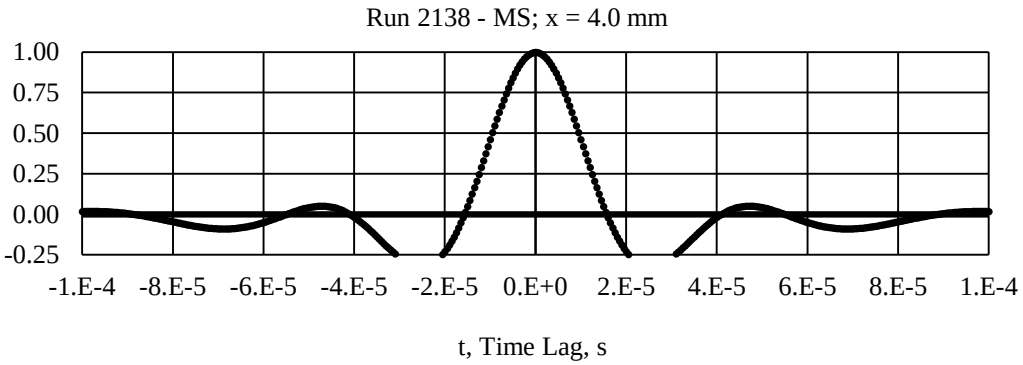

Figure 70. Autocorrelation coefficient function comparisons between freestream and Mach stem flow noise for low Re/m condition.

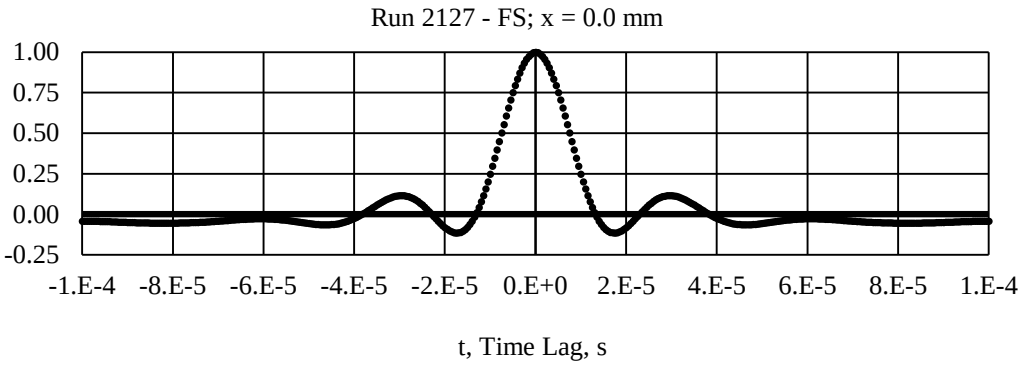

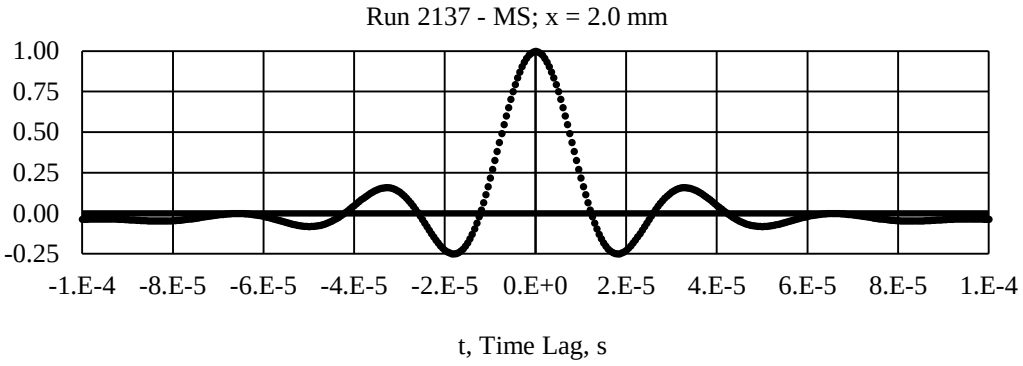

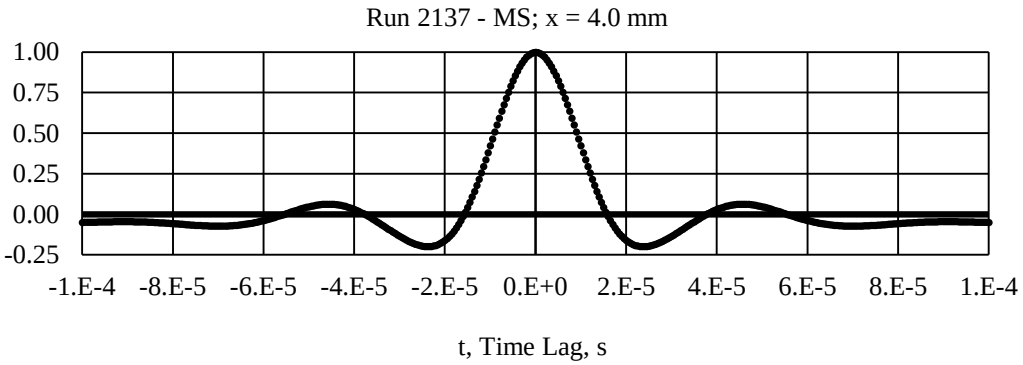

Figure 71. Autocorrelation coefficient function comparisons between freestream and Mach stem flow noise for high Re/m condition.

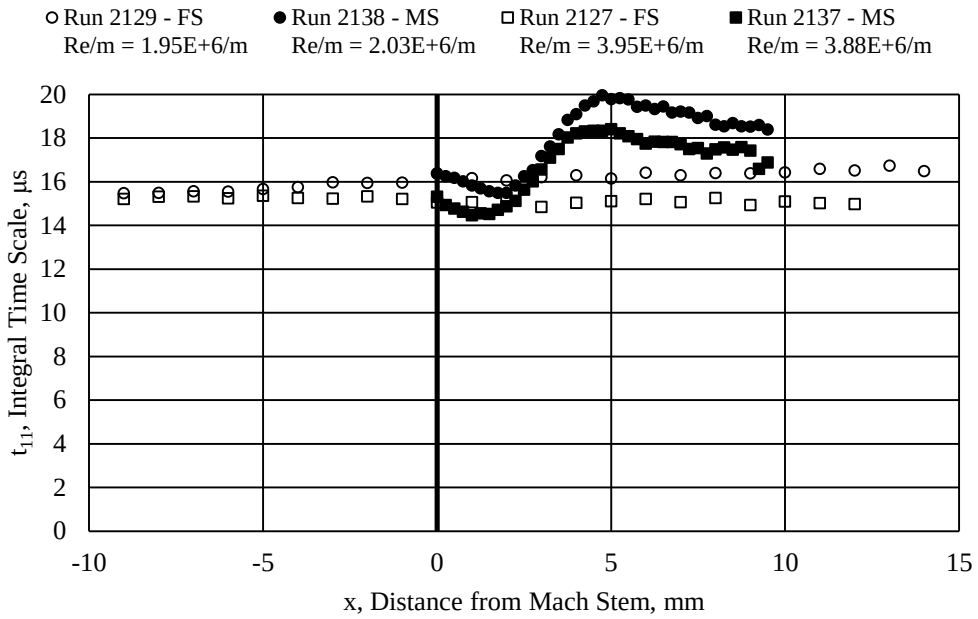

a)

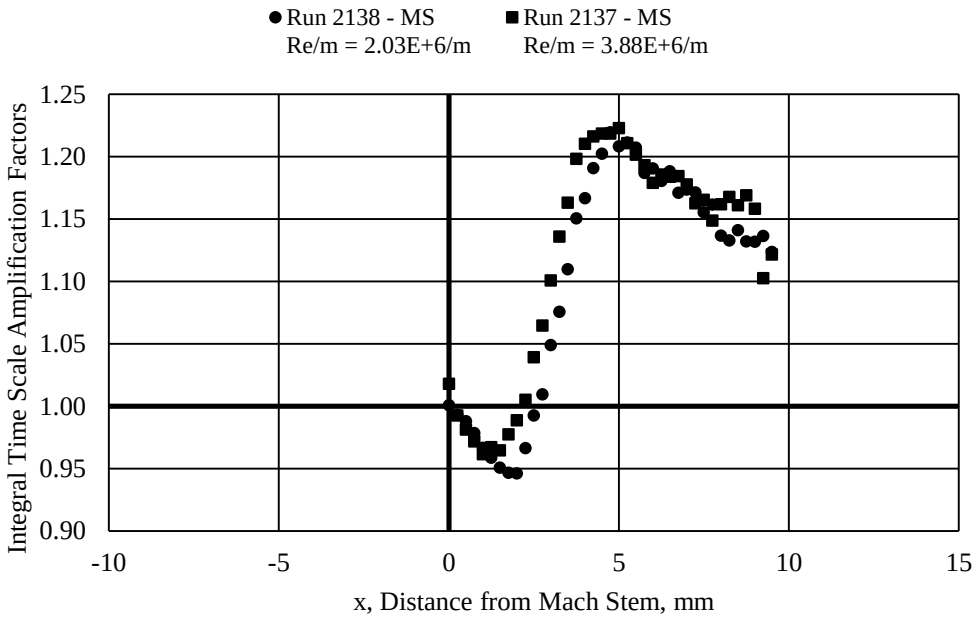

b)

Figure 72. Integral time scale comparisons between freestream and Mach stem flow noise.

a) Integral time scales.

b) Amplification factors.

A possible explanation for the discrepancy among theories, simulations, and experiments is that the current study observed total pressure fluctuations whereas Barre, Alem, and Bonnet observed mass flux (and velocity through assumptions associated with the strong Reynolds analogy) fluctuations. Another possible explanation of the discrepancy is that the inflow conditions to shock-turbulence interaction are not matched among theories, computations, and experiments. As mentioned in the literature review, Mahesh, Lele, and Moin [42] found contradicting effects on several turbulent quantities stemming from the upstream correlation of the vortical and entropy fluctuations.

Power Spectral Density Estimates: Post-Mach Stem Traverse

Normalized power spectral density estimates line plots are shown in Figure 73, and amplification factor line plots are shown in Figure 74. Figure 73 shows that the normalized spectra agreed with each other for low-frequency content. Relatively substantial attenuation and amplification occurred at frequencies greater than f = 10 kHz. Amplification factor plots show that behind the Mach stem, the higher-frequency content has the most substantial amplification. Going from 2.0 mm behind the Mach stem to 4.0 mm behind the Mach stem, the frequency of peak amplification decreased. While doing so, the peak amplification amplitude increased. This suggests that short turbulent structures emanated from the Mach stem stretched as they progressed downstream.

The amplification factors were on the order of the turbulent velocity amplification factors seen in the reply by Barre, Alem, and Bonnet [82] to Ribner [81] regarding their initial publication. In addition, the peak amplification factor for Pitot pressure fluctuations at a particular location is higher for lower, incoming freestream noise.

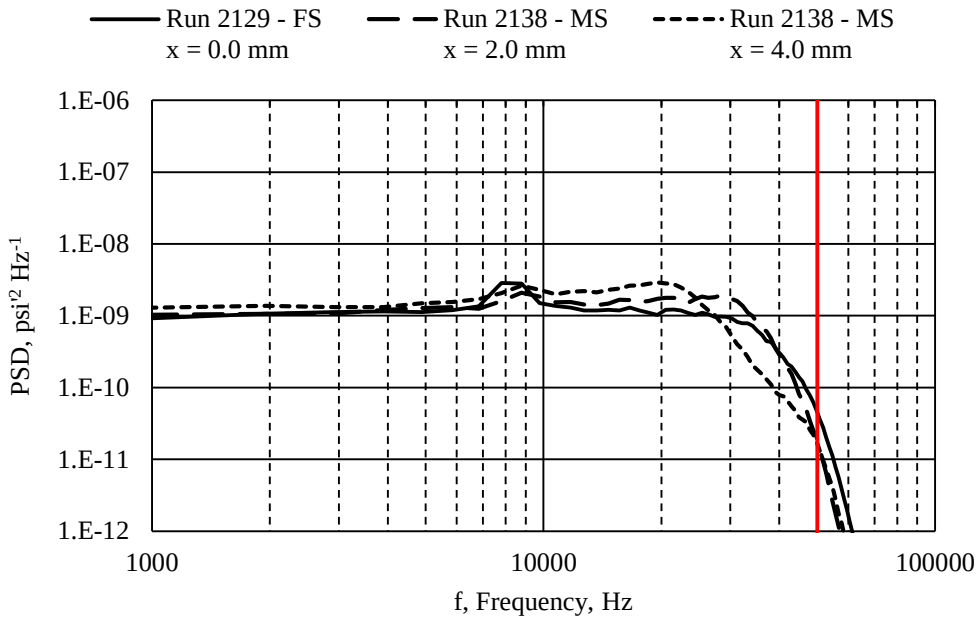

a)

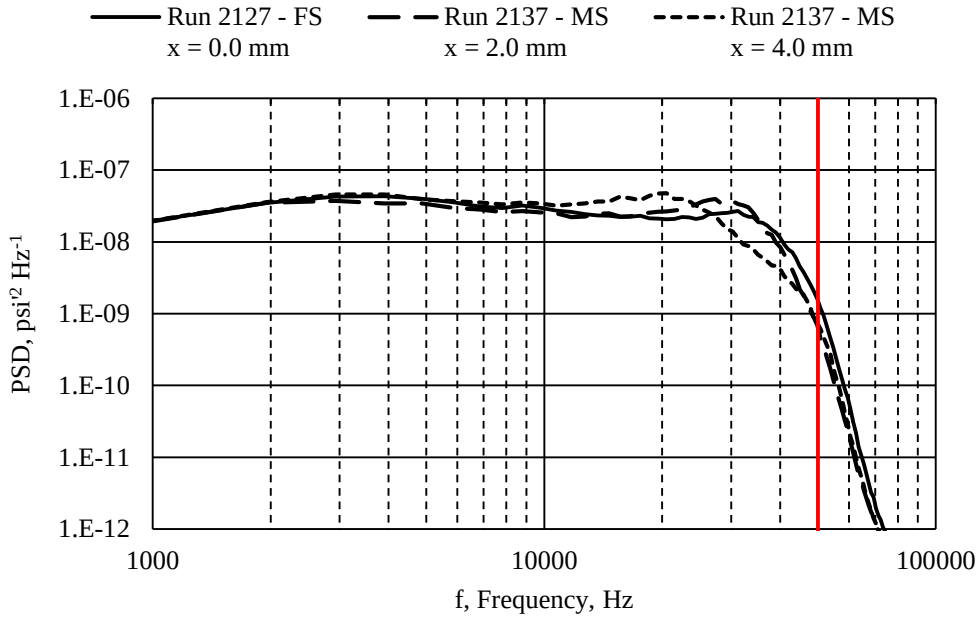

b)

Figure 73. PSD estimate line plot comparisons of freestream and Mach stem flow noise.

a) Low Re/m condition.

b) High Re/m condition.

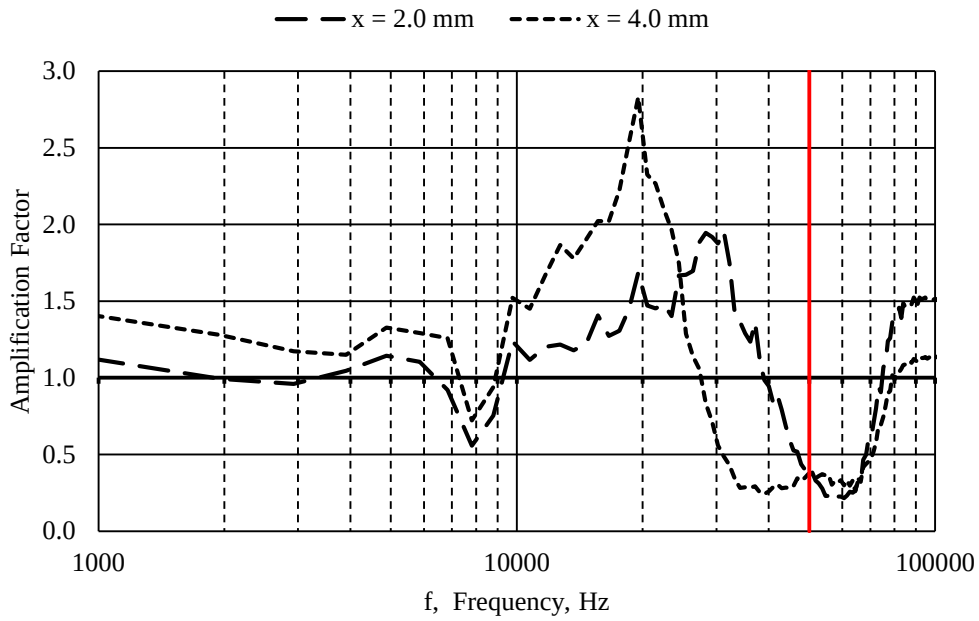

a)

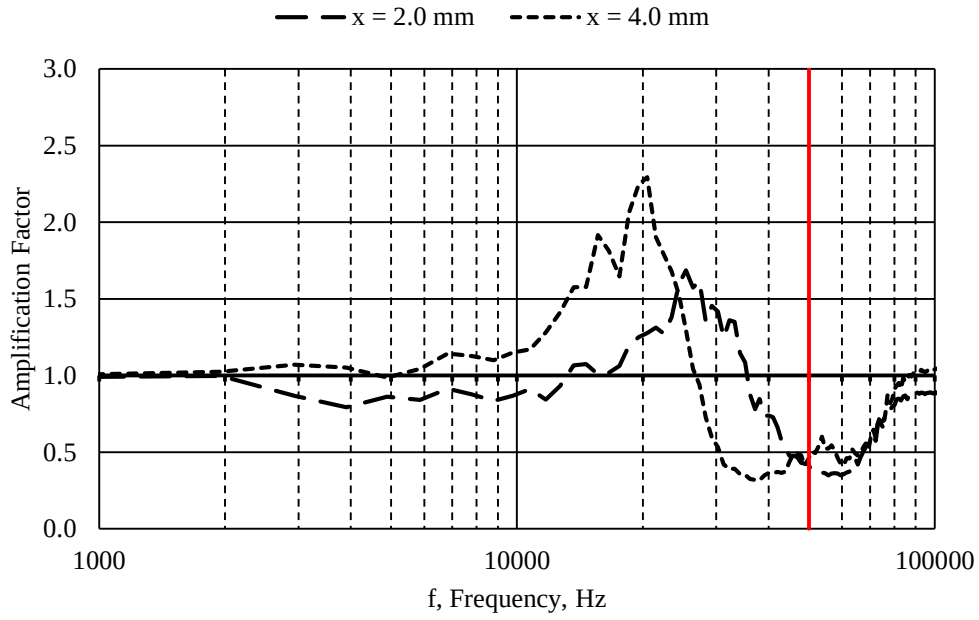

b)

Figure 74. PSD estimate amplification factor line plots.

a) Low Re/m condition. (Run 2138)

b) High Re/m condition. (Run 2137)

Figure 77 shows PSD estimate line plots from the current study and from Barre, Alem, and Bonnet's reply to Ribner. While this study was using a Pitot pressure probe in a hypersonic wind tunnel, and the Barre, Alem, and Bonnet study was using a hot-wire probe in a supersonic tunnel, the spectra are very comparable. The pre-shock and post-shock PSD cross each other and the larger wavenumbers are amplified across the shock wave.

Figure 76 shows the ratio of downstream PSD estimates to upstream PSD estimates for the current study and the later work of Barre, Alem, and Bonnet. Qualitatively, these ratios (or PSD amplification line plots) compare well with each other.

The favorable comparison of the PSD estimates and the amplification factors lends confidence to the use of a Pitot pressure probe in capturing the effects of shock-turbulence interaction.

Some experimental work have found amplification of the lower frequency/wavenumber components, contradicting the results of theory and computational studies. Keller and Merzkirch as well as Honkan and Andreopoulos observed strong amplifications of the lower wavenumber components ([50]-[51]). Barre, Alem, and Bonnet [48], as seen above, contradicted those findings and observed amplification of the larger wavenumber content. None of these studies gave physical reasons for this occurrence, but Keller and Merzkirch suggested a notion that the less relative effect of viscosity on larger scales is more inclined to accept energy from the shock wave interaction better that the more viscosity-dominated smaller scales.

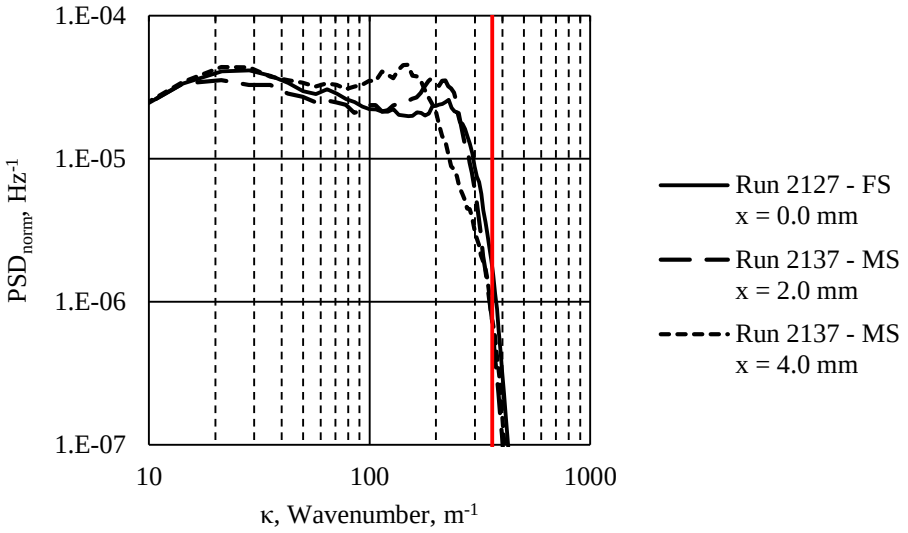

a)

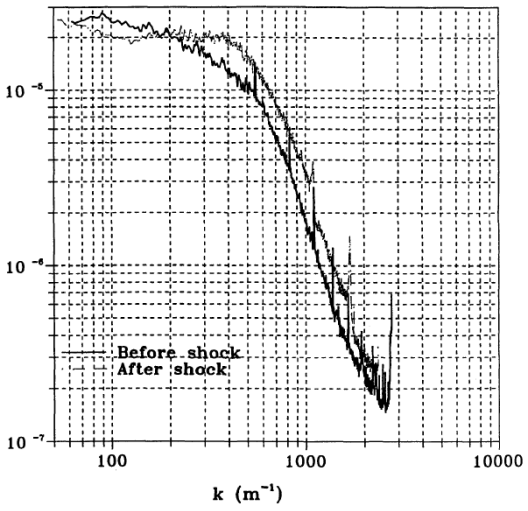

b)

Figure 75. PSD estimate line plot comparisons of current study and previous study.

a) PSD line plot of current study (high Re/m condition traverse).

b) PSD line plot from Barre, Alem, and Bonnet [82].

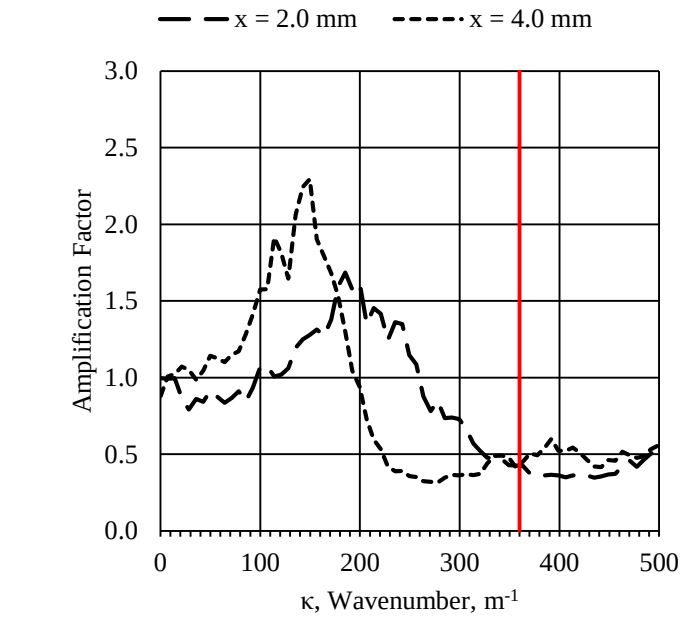

a)

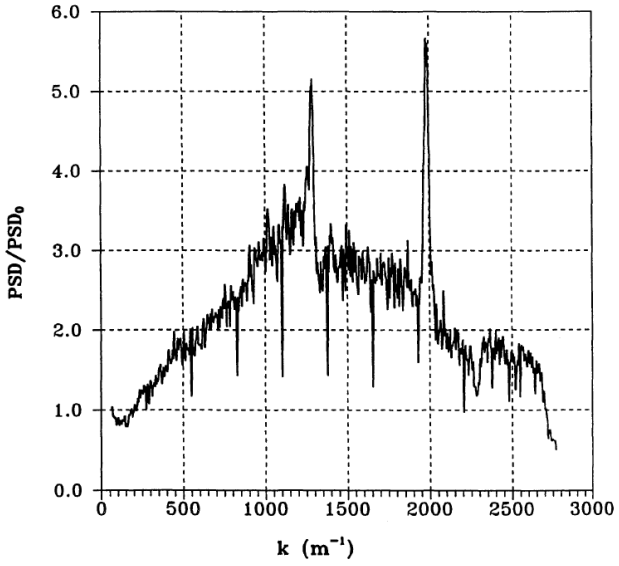

b)

Figure 76. Amplification factor line plot comparisons of current study and previous study.

a) Amplification factor of current study (high Re/m condition traverse).

b) Amplification factor from Barre, Alem, and Bonnet [82].

Pressure (Reynolds-Number) Sweep: Post-Mach Stem

This section presents results from pressure sweeps performed at a couple of locations behind the Mach stem and compares them to the freestream pressure sweep results. Table 17 shows the average run parameters for the data presented in this subsection.

Table 17. Tunnel parameters for Mach stem flow pressure sweep runs and comparison run.

Run No.	Run Type	M_{avg}
2126	FS – Re/m Sweep	5.87
2144	MS – Re/m Sweep – 2.4 mm Downstream	5.84
2145	MS – Re/m Sweep – 4.4 mm Downstream	5.83

Fluctuations/Noise: Post-Mach Stem Sweep

Figure 77 compares noise results of the freestream flow pressure sweep with those of the Mach stem flow pressure sweeps at 2.4 mm and 4.4 mm behind the Mach stem. Qualitatively, the Mach stem flow noise results followed the typical noise profile of a pressure sweep-type run. A slight amplification in the noise behind the Mach stem was inferred by the slight separation of the Mach stem flow results from the freestream flow results.

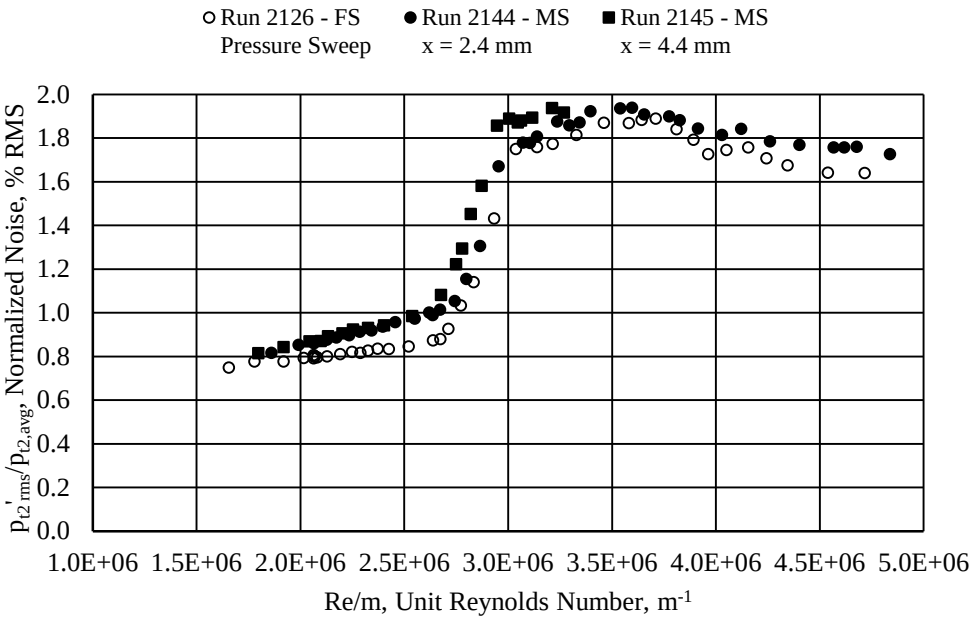

Figure 77. Comparisons of freestream and Mach stem flow noise at various positions.

Amplification factors between the Mach stem flow results and the freestream flow results throughout the range of Re/m were estimated. A direct calculation of the amplification factors was not performed, since data points among runs were not "unit Reynolds number-locked" and are not directly comparable. To circumvent this, the results of each tunnel run were binned by Re/m and averaged within each bin. Each Re/m bin spanned 0.25×10^6/m and contained one to five original data points. Amplification factors were calculated per Re/m bin. Binned noise results and amplification factors are shown in Figure 78. Amplification factors in the transitional Re/m range are not filled, since the noise values were very sensitive in that transient and skewed the amplification factor calculations.

A few generalizations can be made. Amplification factors in the low Re/m range were higher than those in the high Re/m range; this implied the dependence of amplification factors on Re and/or the intensity of the inflow/upstream acoustic disturbances. In the high Re/m range, amplification factors were typically slightly higher for locations further downstream from the Mach stem, which was expected from the traverse results shown in Figure 68; while only two locations are shown here, pressure sweep data at other locations verified this trend. For the two locations under study, the amplification factors were all less than 1.15 with most below 1.10. Again, these were modest amplification factors compared to previous studies capturing pressure fluctuations.

Autocorrelation Coefficient Functions and Time Scales: Post-Mach Stem Sweep

Figure 79 and Figure 80 show that the autocorrelation coefficient functions behaved consistently throughout the Re/m range at the two post-Mach stem locations under observation.

Figure 81 shows the integral time scales versus Re/m for both post-Mach stem locations. Their profiles were similar to the integral time scales profile of the freestream pressure sweep shown in Figure 58 and reproduced here for comparison.

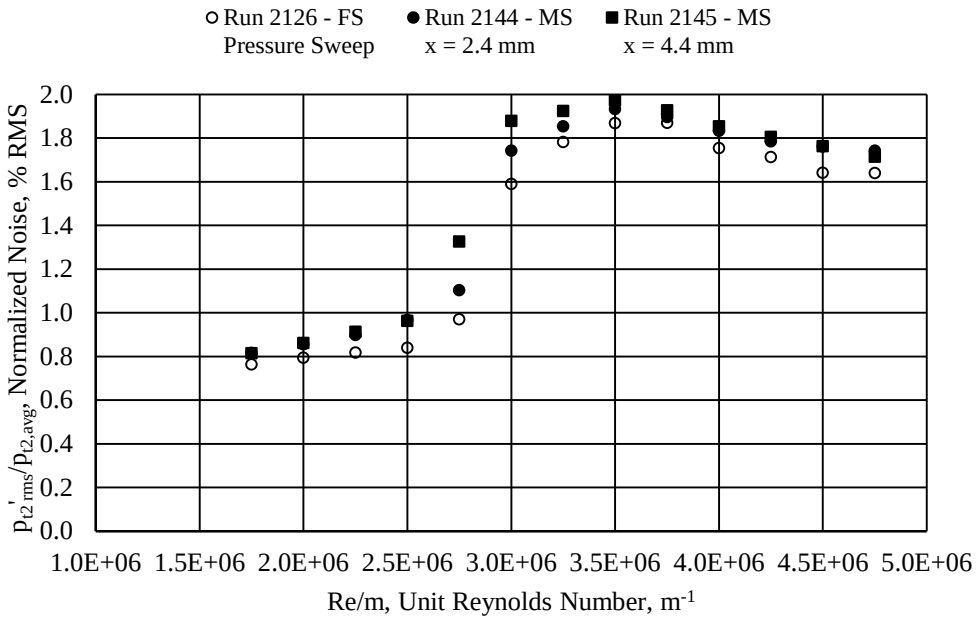

a)

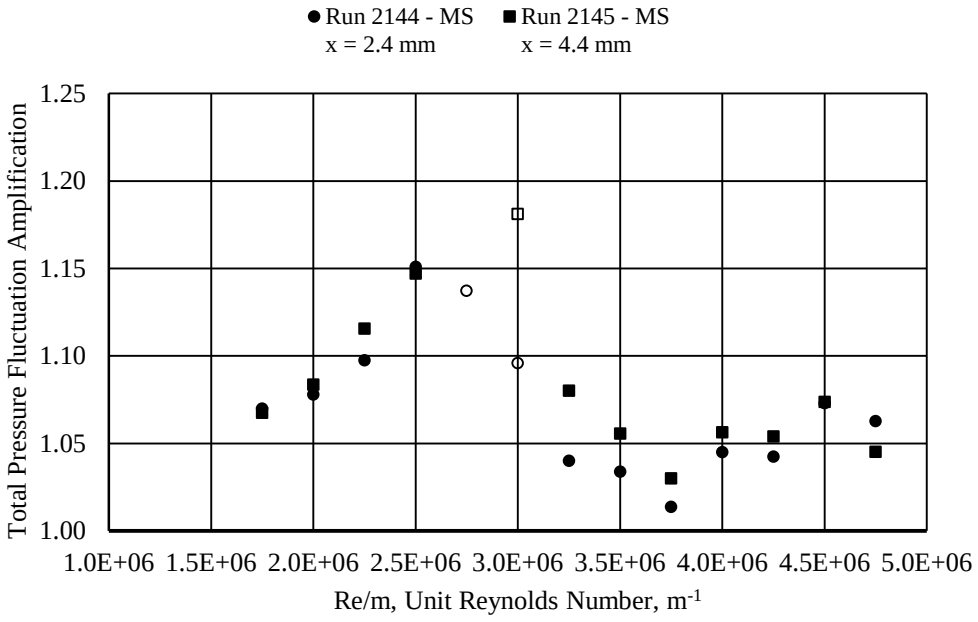

b)

Figure 78. Comparisons of freestream and Mach stem flow noise at binned Re/m.

a) Noise percentages.

b) Amplification factors.

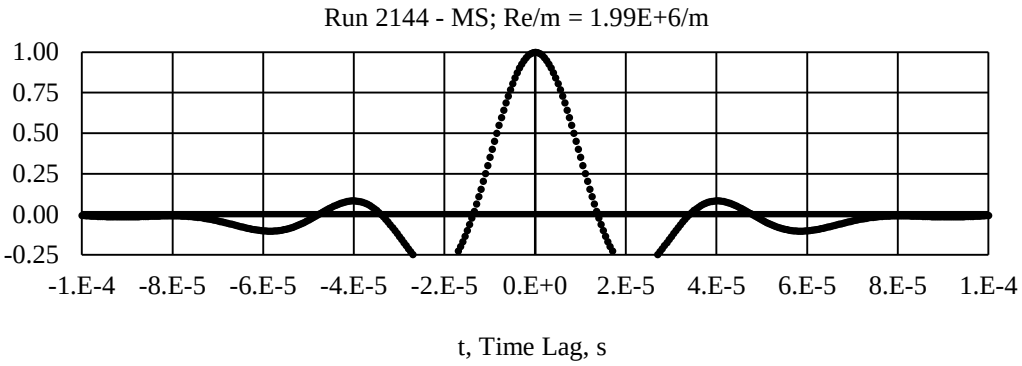

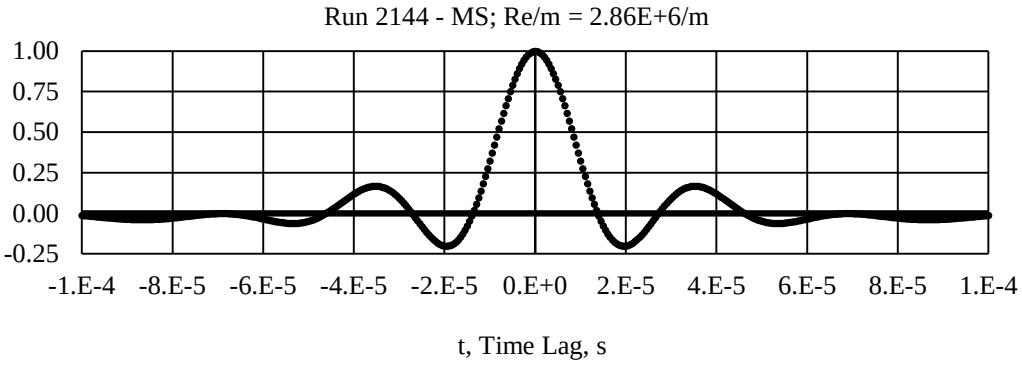

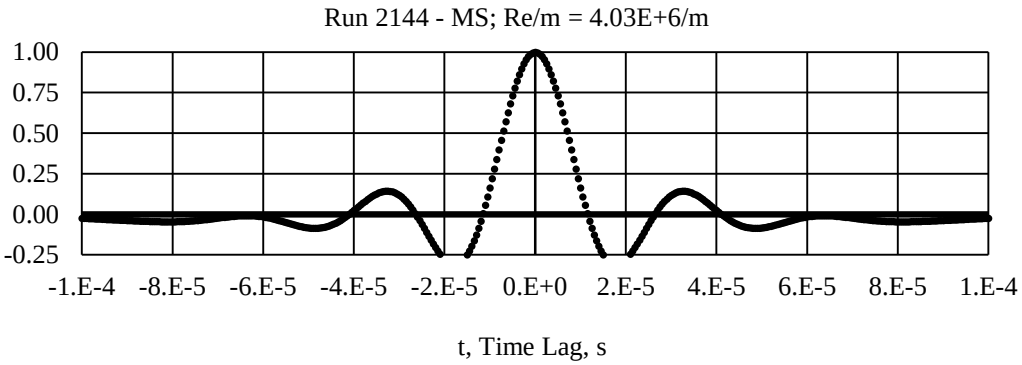

Figure 79. Autocorrelation coefficient functions of Mach stem flow noise (2.4 mm).

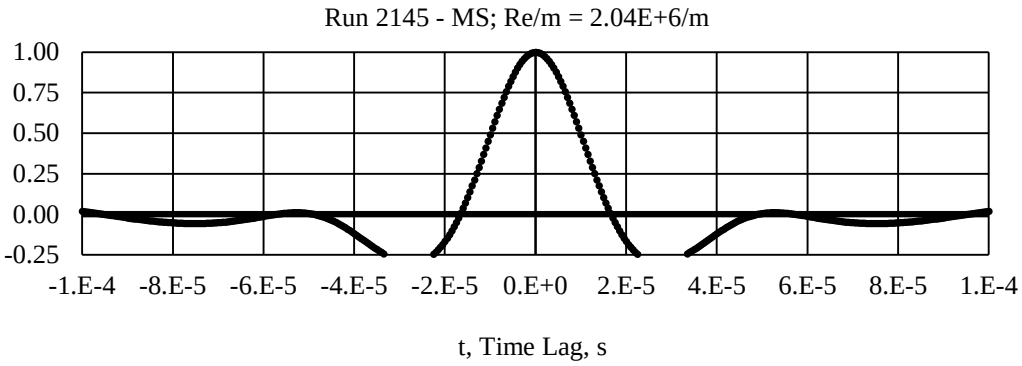

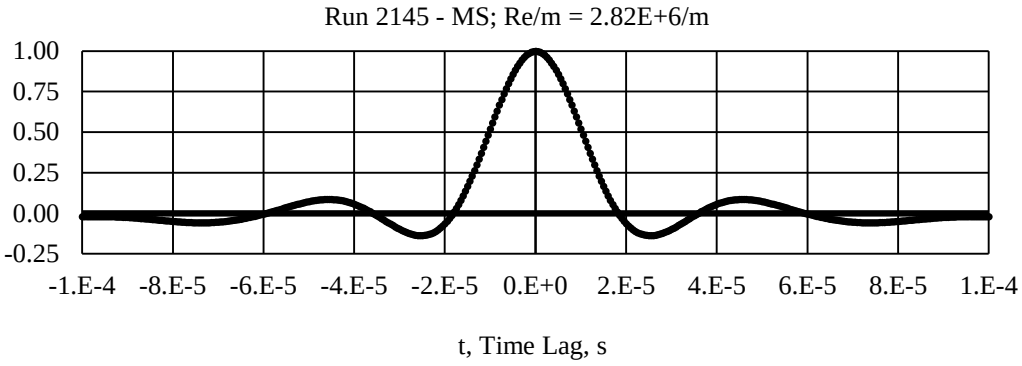

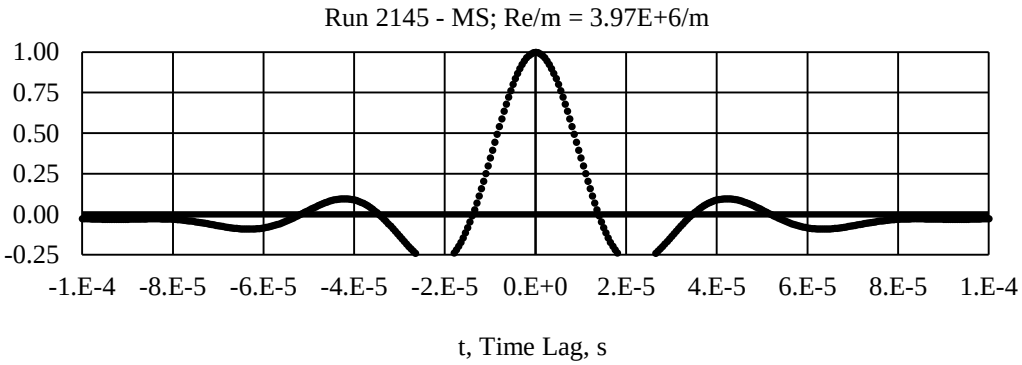

Figure 80. Autocorrelation coefficient functions of Mach stem flow noise (4.4 mm).

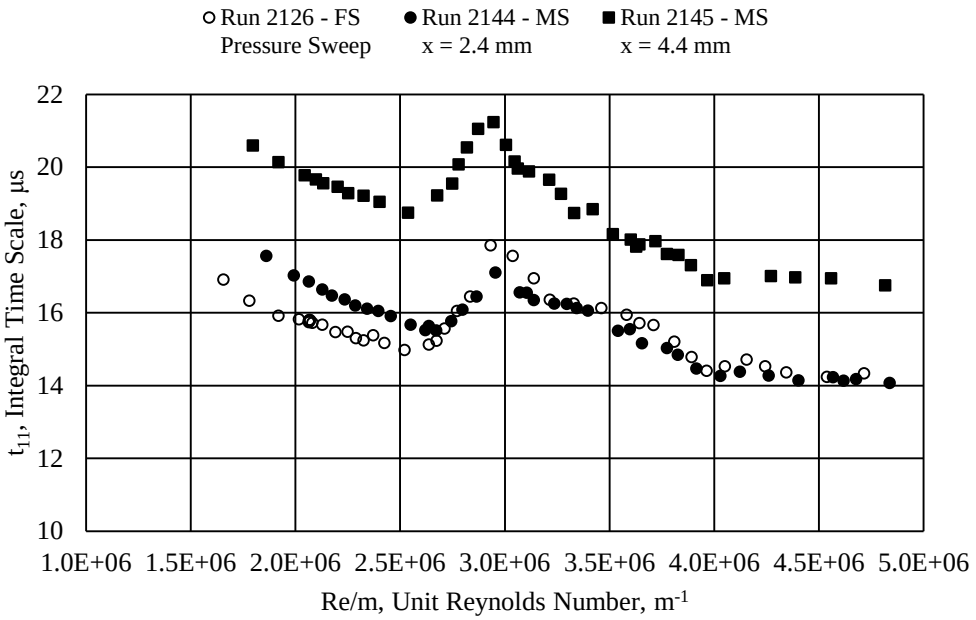

Figure 81. Comparisons of integral time scale of Mach stem flow noise at different positions and Re/m conditions.

Like the noise data, the integral time scale data were binned according to Re/m, and amplification factors were calculated. Figure 82 shows the binned data and amplification factors. The amplification factor chart shows that the integral time scale at 2.4 mm behind the Mach stem were comparable to the freestream integral time scale whereas the amplification factors at 4.4 mm behind the Mach stem were generally in between 1.15 and 1.25. This indicates that perhaps the turbulent structures were stretching in the freestream direction and still evolving in the region near the Mach stem. Again, amplification factors were higher for the lower freestream noise condition than for the higher freestream noise condition.

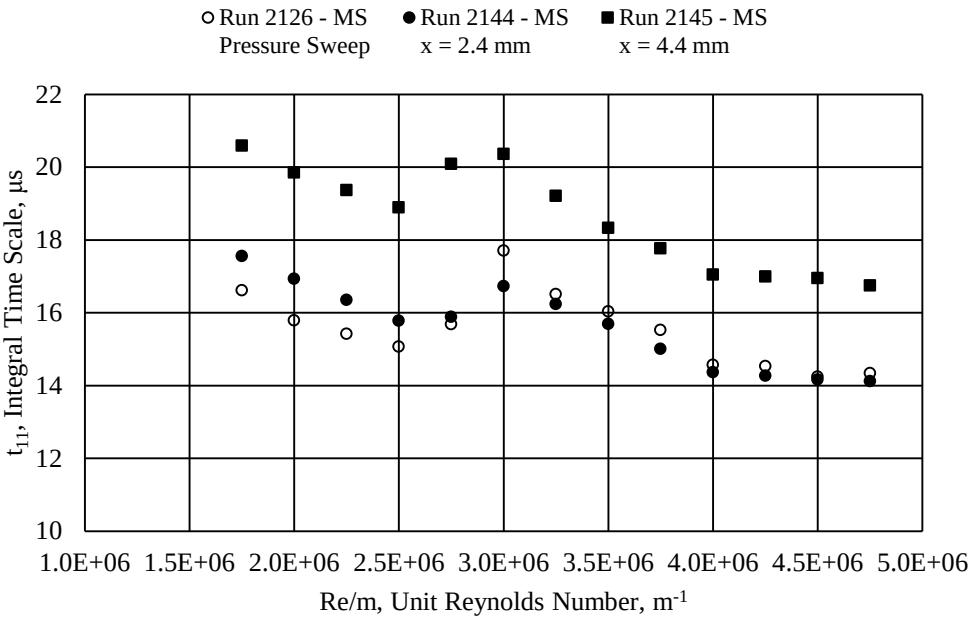

a)

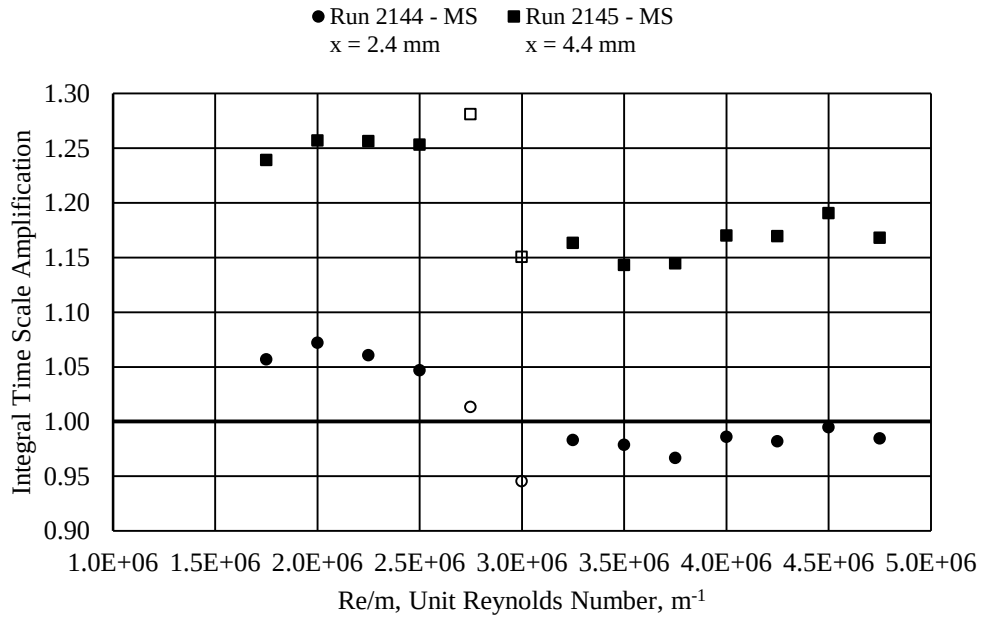

b)

Figure 82. Comparisons of freestream and Mach stem flow integral time scales at binned Re/m.

a) Noise percentages.

b) Amplification factors.

Power Spectral Density Estimates: Post-Mach Stem Sweep

Line plots of PSD estimates and normalized PSD estimates are shown in Figure 83 (2.4 mm behind the Mach stem) and in Figure 84 (4.4 mm behind the Mach stem). Compared to the freestream flow pressure sweep spectra line plots in Figure 59, these results were qualitatively similar. Increases in spectra amplitude at the higher wavenumbers were observed relative to the freestream flow results, which followed the conclusions drawn from the Mach stem traverse data.

Summary: Post-Mach Stem

Based on flow visualization and the traverse data, it was determined that data collected within 2 mm behind the Mach stem would be contaminated by the probe-Mach stem interference. Furthermore, data collected beyond 5 mm was likely biased due to the "duct" geometry formed by the slip line emanating from the triple point intersection of the Mach stem structure. Thus, only data between 2 mm and 5 mm were considered to be accurate.

Overall, amplification factors for noise, integral time scales, and power spectral density estimates were higher for lower freestream noise levels (i.e., low Re/m condition). In addition to being higher for lower freestream noise interactions, the amplification factor was also more sensitive at the low noise levels. The maximum amplification observed was 1.15 with typical amplifications less than 1.10.

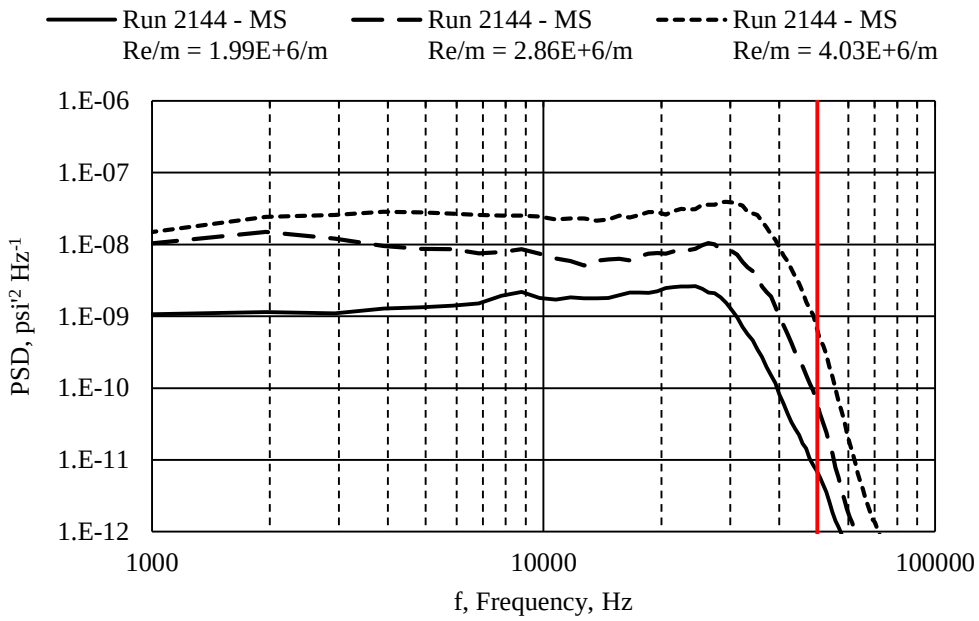

a)

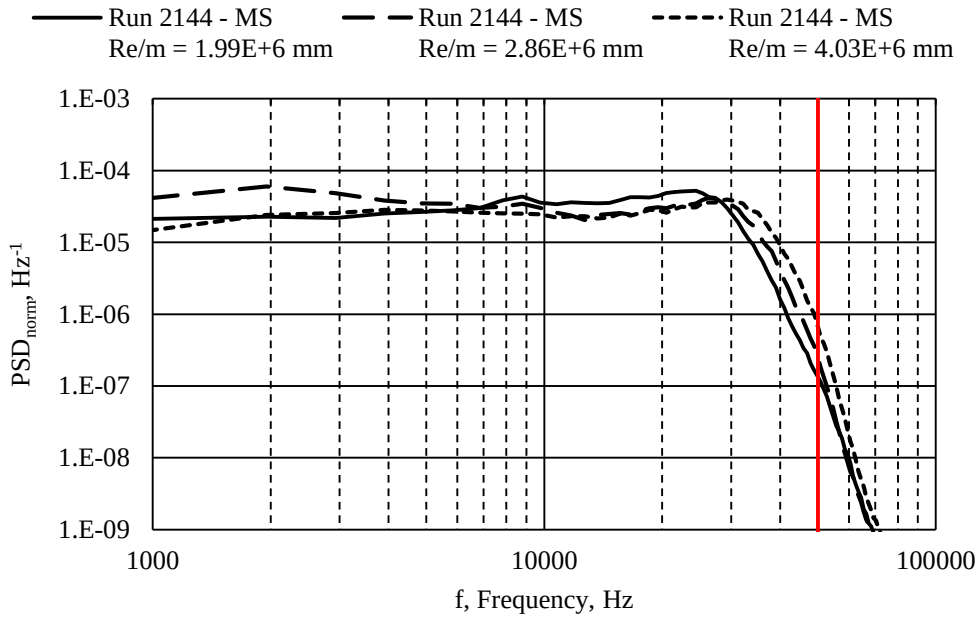

b)

Figure 83. PSD estimate line plots of Mach stem flow noise (2.4 mm).

a) Typical line plot.

b) Normalized line plot.

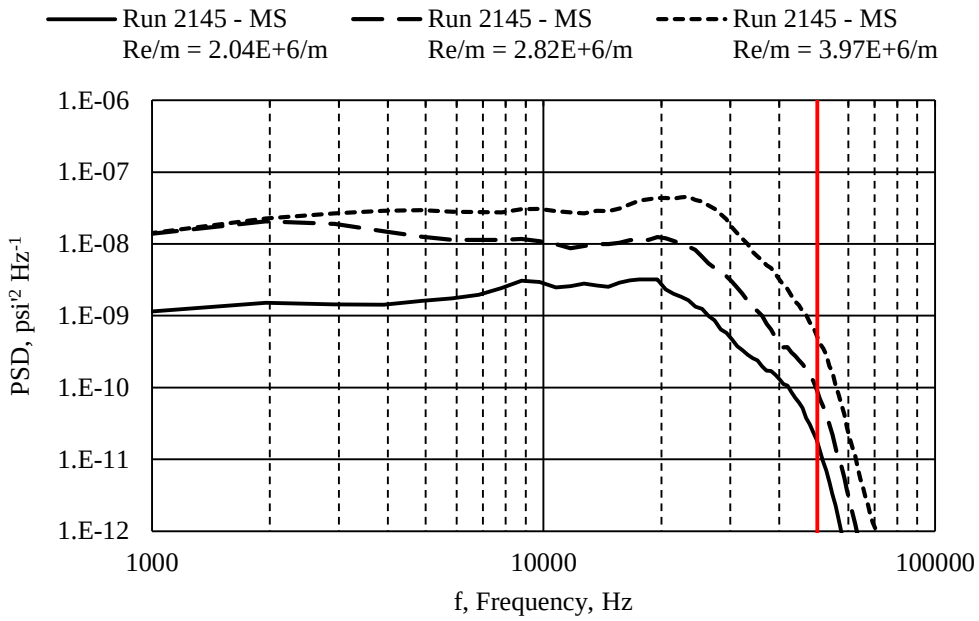

a)

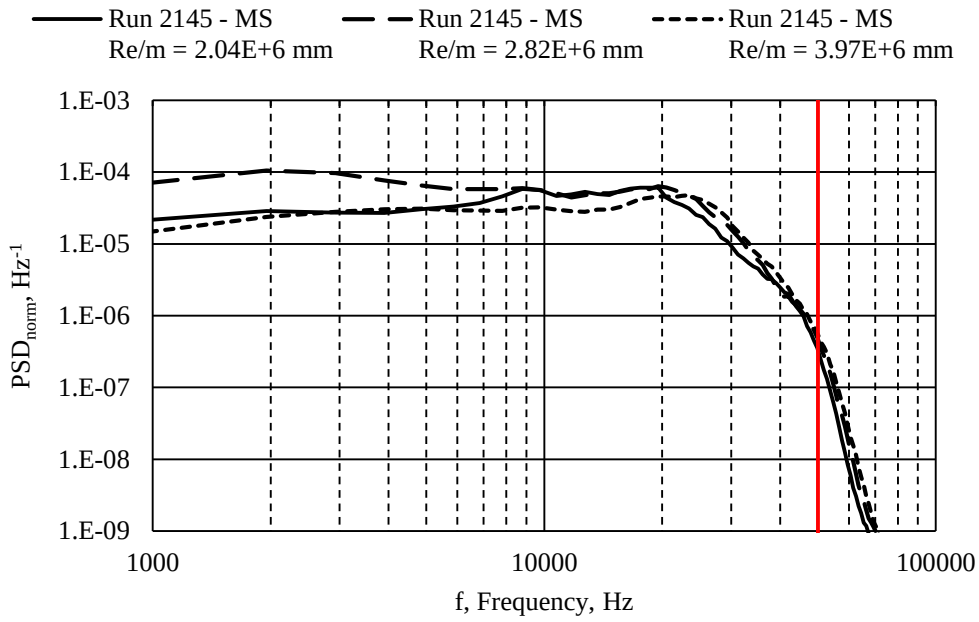

b)

Figure 84. PSD estimate line plots of Mach stem flow noise (4.4 mm).

a) Typical line plot.

b) Normalized line plot.

Within the region of interest, the integral time scale increased with distance from the Mach stem with a maximum amplification of 1.25. The increase implied that the turbulent structures were being stretched and had not yet fully evolved after the interaction with the Mach stem.

PSD estimates showed an increase in higher frequency content behind the Mach stem. The frequency of peak amplification decreased with increasing distance from the Mach stem. The current PSD estimates were qualitatively similar with hot-wire PSD estimates from a previous supersonic shock-turbulence interaction study. Ratios of downstream PSD estimates to upstream PSD estimates were also qualitatively similar. The favorable comparisons seems to validate the Pitot pressure probe as a useful instrument for shock-turbulence interactions.

SUMMARY AND RECOMMENDATIONS

This sections provides a summary of the current study and addresses the three experimental phases and the associated research questions about turbulent noise modifications due to a normal shock wave. Afterwards, recommendations for near-term improvements and long-term extensions to the current study are provided.

Summary

Shock-turbulence interactions occur in several engineering applications. In regards to hypersonic vehicles, surface roughness creates alternating shock-expansion regions that influence the behavior of a turbulent boundary layer and the resulting skin friction and heat transfer. Shocks at the front of an engine inlet will modify the incoming turbulence and affect combustion efficiency. These examples, however, have complicating effects that make it difficult to determine the effect of only the shock wave in modifying turbulent structures. Thus, it is desirable to perform fundamental studies by examining modifications to freestream turbulence due to a normal shock wave.

The overarching research objective of this study was to provide thermal equilibrium data of shock-turbulence interaction to serve as a baseline in a greater research effort to extend knowledge of turbulence interaction with normal shock waves to hypersonic flows and to thermal nonequilibrium flows.

The current study is believed to be the first hypersonic shock-turbulence interaction experiments conducted of any kind. The effect of a normal shock wave in the near-region on the total pressure fluctuations in a low-density hypersonic wind tunnel were

characterized. Total pressure fluctuations were measured with a flush-mounted fast-response Pitot pressure probe mounted to a single-stage traverse in the test section.

A Pitot pressure probe study was performed because of the robustness of the instrument. Hot-wire anemometry measurements are planned and will provide data on the vortical and entropic turbulence modes to complement the Pitot pressure data presented in this dissertation.

In the exploratory stage of this study, it was believed that the upstream/inflow condition could be measured with the Mach stem generator wedge models in place and with the Pitot pressure probe tip (or hot-wire) upstream of the Mach stem. A bow shock would form in front of the probe, but it was expected that the flow behind the bow shock, for the most part, would be supersonic and that there would be minimal influence from the flow downstream of the probe tip. However, due to unforeseen and (currently) unexplainable probe-bow shock interaction with the Mach stem, the data obtained upstream of the Mach stem did not compare well with data taken at the same position without the wedge models installed (i.e., freestream data). As a result of this finding, it was necessary to measure the upstream (freestream) data in separate tunnel runs from the downstream data.

Freestream Noise Characterization

In lieu of an external turbulence-generation mechanism, the innate freestream disturbances in a low-density hypersonic wind tunnel served as the inflow condition to shock-turbulence interaction. Thus, one major effort of the current study was to characterize the freestream disturbances. This and previous characterization efforts

showed two distinct ranges of noise levels based on Re/m. A relatively low noise regime (~0.80% normalized rms) existed at Re/m below 2.5×10^6/m, and a relatively high nose regime (~1.80% normalized rms) existed at Re/m above 3.5×10^6/m. A transitional regime exists between these two ranges. PSD estimates of the noise showed a broadband increase with increasing Re/m and implied that the increase in noise is due to the nozzle boundary layer transitioning to a turbulent state that radiates noise into the freestream. For this study of shock-turbulence interaction, the two different regimes enabled the study of upstream/inflow conditions on amplification factors. Data taken by a Pitot pressure probe traversing along the centerline established the sensitivity to the axial direction; noise levels, time scales, and PSD estimates show acceptable uniformity to establish upstream conditions.

Mach Stem Characterization

The normal shock in this shock-turbulence interaction was a Mach stem generated by the irregular (Mach) reflection of two oblique shocks. The oblique shocks were generated from wedge models symmetrically installed in the tunnel test section. The wedge model angles were chosen based on compressible flow theory and a Mach stem theory. The Mach stem and other flow structures were characterized with flow visualization techniques. The Mach stem position was observed to vary slightly with the pressure (or Re/m) and was believed to be due to viscous interaction between the wedge boundary layer and the oblique shock emanating from the wedge. The Mach stem also moved when the Pitot pressure probe tip was upstream or near-downstream of it. The wedge model design was reiterated to minimize the movement of the Mach stem and to

minimize the 3-D effects, since the wedge models did not span the entire test section for blockage reasons. The Mach stem visualized with conventional schlieren imaging compared well with the prediction from the theory of Mouton and Hornung. The slip line emanating from the triple point (intersection of oblique shock wave, Mach stem, and reflected shock) created a region of accelerating flow behind the Mach stem. The properties behind the Mach stem were estimated, and the region within 5 mm of the Mach stem was determined to be acceptably invariant, and analyses were performed on data collected in that region.

Post-Mach Stem Noise Characterization

A set of data taken along the centerline in the axial direction established regions downstream of the flow not believed to be biased due to probe-shock interactions or due to flow phenomena altering the region downstream of the Mach stem. Measurements in the near-region (2-5 mm) downstream of the Mach stem were made, and the noise, time scales, and PSD estimates were compared with the freestream data.

Overall, it was observed that amplification factors for the noise, time scales, and power spectral density estimates content were higher for the lower Re/m condition (i.e., lower freestream noise) than for the higher Re/m condition (i.e., higher freestream noise). In addition, the amplification factors across the range of Re/m were higher at 4.4 mm downstream from the Mach stem than for 2.4 mm downstream, indicating that the turbulent structures perhaps took time to grow after crossing the shock wave.

In the downstream range of interest, the noise amplification was less than 1.10 for the low Re/m (lower noise) condition (Re/m $\approx 2.0\times10^6$/m) and less than 1.05 for the high

Re/m (higher noise) condition (Re/m ≈ 4.0×10^6/m). These amplifications were very modest in comparison to previous experimental results. The maximum amplification factors observed in traverse runs were also observed in pressure (Re/m) sweep runs. In comparing pressure sweep results at two different locations downstream of the Mach stem, both positions had amplification factors less than 1.10 for a range of lower Re/m and about 1.05 (typically 1.02 to 1.08) for a range of higher Re/m.

The integral time scale amplification factor through the Mach stem in the downstream region of interest increased with downstream distance and was at most about 1.25. The PSD estimates obtained in this study indicated an increase in content at the higher frequency range behind the Mach stem. The frequency of peak amplification decreased with increasing distance from the Mach stem. In comparing this study's total pressure fluctuation results to the velocity fluctuations results from a previous supersonic shock-turbulence interaction study, the PSD estimates were qualitatively similar. The amplification factors calculated from the PSD estimates were also similar for both studies, suggesting that fast-response Pitot pressure probe are able to provide meaningful results in shock-turbulence interaction studies.

Improvements to Current Study

This subsection provides recommendations that can be implemented relatively quickly to continue or improve the study discussed in this dissertation.

Spanwise Independence Tests

All of the measurements presented in this dissertation were obtained along the centerline of the tunnel test section and Mach stem generator wedge models. Since the current wedge models (203 mm/8.0 in. wide) did not span the entire width of the test section (359 mm/14.1 in. wide) for blockage reasons, there were some three-dimensional effects at the side of the wedge models that may have altered the measurement region at the centerline. The two-dimensional Mouton and Hornung [67] theoretical estimate compared well to the centerline shock structure observed with conventional schlieren images and preliminary focusing schlieren images (Appendix F), so it was postulated that the three-dimensional effects were minimal.

To complement the flow visualization, spanwise independence tests should be performed. A traversing apparatus has been designed and manufactured to obtain measurements 15.9 mm (0.625 in.), which is more than four probe diameters, away from the centerline.

To have the spanwise independence results be meaningful, the ACE tunnel flow uniformity must be established. Mach number uniformity has been previously characterized utilizing a Pitot pressure probe and an MKS Baratron 631C-100 capacitance manometer (accuracy of 0.5% of the reading). Using this setup, the Mach number rms variation across the nozzle exit plane for $M = 6$ was less than 0.5% of the mean exit Mach number [60].

Additional Flow Measurements

From the available literature, it is important that the inflow/upstream conditions be well-known for better prediction and understanding of shock-turbulence interaction. The current Pitot pressure probe measurements can be used to quantify the pressure fluctuations. In conjunction with multiple-overheat hot-wire anemometry and asymptotic limits of M, it will be possible to obtain velocity and temperature fluctuations so that the upstream conditions can be quantified in terms of the three turbulence modes and the predicted interaction can be verified downstream of the Mach stem.

Ribner showed that the anisotropy of the inflow/upstream conditions affected the results of shock-turbulence interaction [34]. Thus, transverse fluctuations need to be characterized using cross-wire anemometry. In preparation for these tests, two cross-wire probes and the associated hardware have been procured. A parallel hot-wire probe is also available; the wires can be set to different overheat ratios and a time-resolved decomposition of the mass flux and total temperature can be obtained.

Lastly, the hardware developed for the spanwise independence tests was designed to allow two off-axis probes to be used. Assuming there is no spanwise variance in the turbulence statistics, the dual-probe setup would improve the reliability and correlation of data between different instruments, since the data would be simultaneously recorded at the same flow conditions and not in different tunnel runs.

Flow Visualization

Conventional schlieren images show strong diffraction effects behind the Mach stem. In addition, for a given setup, there is a tradeoff in the amount of knife-edge cutoff

between the sensitivity and the range of density gradients observed. Since the experiments were conducted in a low-density wind tunnel, a relatively high sensitivity was required to clearly observe the shock waves (even though density gradients across a shock wave are strong). The high sensitivity required reduced the observable range of density gradients; this resulted in relatively large regions of the flow saturating the schlieren imaging range, and the regions appeared as very bright regions or very dark regions with no observable details. While these technically did not pose a large problem in measuring distances using the schlieren images, cleaner images could be obtained of the entire flow region.

The diffraction and saturation effects can be minimized or eliminated by replacing the opaque knife-edge with a color filter mask. A few images obtained using a color filter mask were shown in the flow visualization results section. Diffraction is expected to be reduced since there is no sharp, physical knife-edge where most diffraction effects occur. The measuring range (and therefore saturation), assuming a given setup, depends on the type of color mask (e.g. two solid colors or continuous color variation) used. A set of color filter masks have been obtained, and a more concentrated effort to obtain quality schlieren images is underway. Custom color filter masks could also be made in-house.

Mach Stem Generator Wedge Models

The Mach stem theory of Mouton and Hornung [67] indicated that the Mach stem height, for a given wedge geometry, is very sensitive to the separation distance between the wedges and that the current adjustability of the Mach stem generator wedge models in 9.5 mm (0.375 in.) increments) was too coarse. This was also observed in the schlieren images of the initial set of wedges (Figure 26). To optimize the Mach stem height for a

given wedge model geometry, it is recommended to design new struts with finer height increments.

Future Studies

This subsection describes recommendations for long-term future studies to build upon the scientific contributions of the work described in this dissertation.

Turbulence Generation

Previous experimental shock-turbulence interaction studies typically used a mechanism to generate velocity perturbations that were allowed to decay into isotropic turbulence before it interacted with a shock wave ([7], [46]-[48], [50]-[52]). Since the ACE tunnel has been characterized to have low-level disturbances, artificially increasing the turbulence may show a greater discrepancy between freestream and post-Mach stem flow disturbances and decrease the relative uncertainty in amplification factors. This could easily be done with the installation of an appropriate grid.

An extension to the typical grid is the design and installation of a heated grid so that both vortical and entropy turbulence modes are present upstream of the shock-turbulence interaction. To induce additional acoustic perturbations, speakers can be mounted to the test section and programmed to emit sound waves of a particular frequencies and amplitudes. Kuester and White [84] applied active noise control concepts to the KSWT for noise cancellation; similar concepts could perhaps be used to amplify or simulate noise instead of attenuating it.

Since one of the overarching objectives of the AFOSR BRI project that funded the work detailed in this dissertation was to extend the knowledge of shock-turbulence interactions to include thermal nonequilibrium energy exchange mechanisms, a novel turbulence-generating method was proposed. The concept, named LINE turbulence, plans to utilize a laser to dissociate seeded molecules. The molecular or atomic remnants would have a nonequilibrium external and internal energy distribution, and the particular distribution depends on which molecules were seeded for laser photolysis (e.g. the photolysis of C_6F_6, hexafluorobenzene, with a 266 nm laser is expected to create a nonequilibrium state dominated by the vibrational energy mode, [85]-[86]). Turbulence is expected to be generated by the strong perturbations induced by the high velocity of the photolysis fragments; Figure 85 shows a DNS data set of turbulence being generated from the photolysis of seeded molecules. A shock wave (a form of mechanical nonequilibrium), which generates turbulence modes downstream when at least one mode is present upstream, is believed to act as a mechanism to exchange energy among the internal and external energy modes. A notional schematic of experiments characterizing the interaction of thermal nonequilibrium and mechanical nonequilibrium is shown in Figure 86.

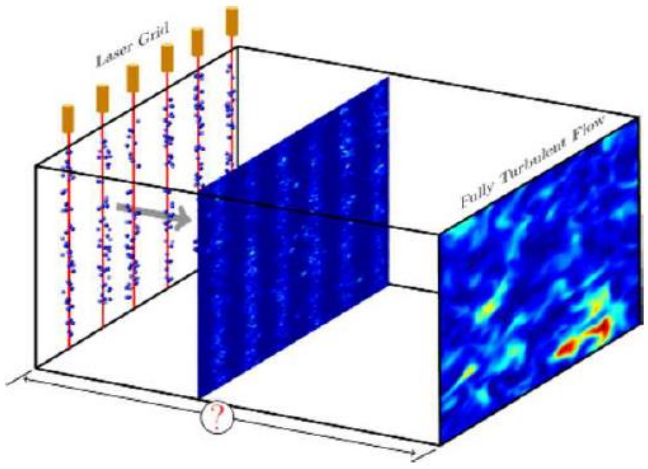

Figure 85. DNS of laser photolysis generating LINE turbulent flow.
(credit: D. A. Donzis)

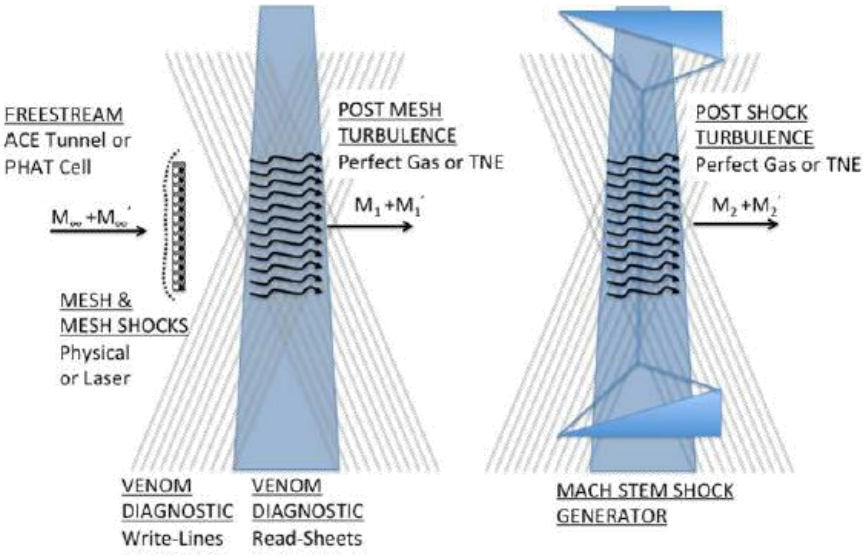

Figure 86. Notional schematic of generated thermal nonequilibrium turbulence interacting with a mechanical nonequilibrium phenomenon (normal shock wave).
(taken from proposal submitted for AFOSR BRI grant)

Extended Noise Ranges in M6QT

The ACE tunnel is one of two continuous-operation hypersonic wind tunnels at the TAMU NAL. The other tunnel, the M6QT, is an one-of-a-kind, continuous-operation tunnel specifically designed to study hypersonic boundary-layer transition ([87]-[88]). The tunnel incorporates features to maintain a laminar boundary layer in the nozzle and provide "quiet" flow (i.e., flow with very low pressure/acoustic disturbances to replicate what is seen in flight) to properly study the influences of various mechanisms in the transition process.

Figure 87 shows the freestream total (Pitot) pressure characterization of the M6QT (obtained from [89]). The M6QT Pitot pressure fluctuations are less than 0.05% up to a Re/m of about 11×10^6/m. An exact determination of the fluctuation levels was currently unattainable because the fluctuations were below the noise floor of available instrumentation. At Re/m above 11×10^6/m, the boundary layer will become turbulent regardless of the designed flow conditioning features. Therefore, the M6QT can counterintuitively provide a natural extension of this study to hypersonic, noisy flow environments.

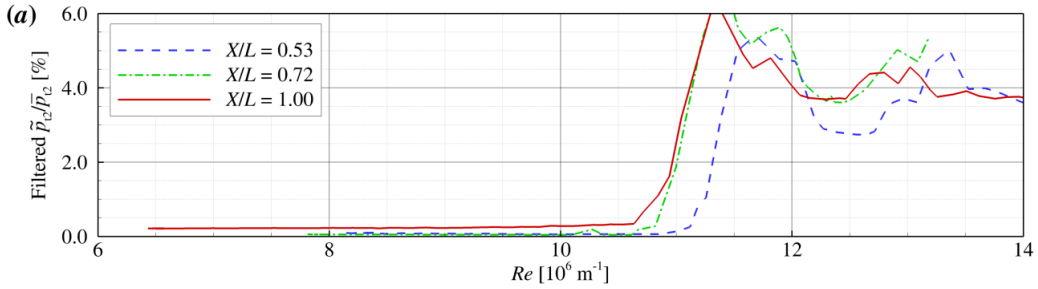

Figure 87. M6QT freestream total pressure fluctuations.
(taken from Hofferth [89])

Avoiding Shock-Shock Interference

One of the major findings in the current study was the inability to use intrusive measurements (e.g. Pitot pressure probes and hot-wire probes) upstream of the Mach stem as the incoming conditions to the shock-turbulence interaction because of unforeseen interaction between the probe bow shock and the Mach stem. The interaction affected both the mean data and the fluctuation data, and this was especially noticeable in preliminary hot-wire results. Thus, upstream/incoming fluctuations had to be measured in different tunnel runs than the downstream/outgoing fluctuations, and tunnel conditions were not exactly duplicated among runs. In addition, it was not possible to obtain reliable measurements immediately downstream of the Mach stem because of the same probe/Mach stem interference effect.

To obtain measurements before and after the Mach stem in the same run and also to obtain measurements close to the Mach stem, nonintrusive measurement methods that

are optically-based or laser-based are advocated. One possible method is background-oriented schlieren, a quantitative schlieren-based technique [70]. Laser-based methods, which are currently available at the TAMU NAL, include MTV and VENOM. MTV is a fluorescence-based technique to obtain velocity measurements ([90]-[91]). VENOM is combined MTV and PLIF to obtain *simultaneous* velocity and temperature measurements ([17]-[23]). Figure 88 is a schematic of the VENOM setup ([21], [23]).

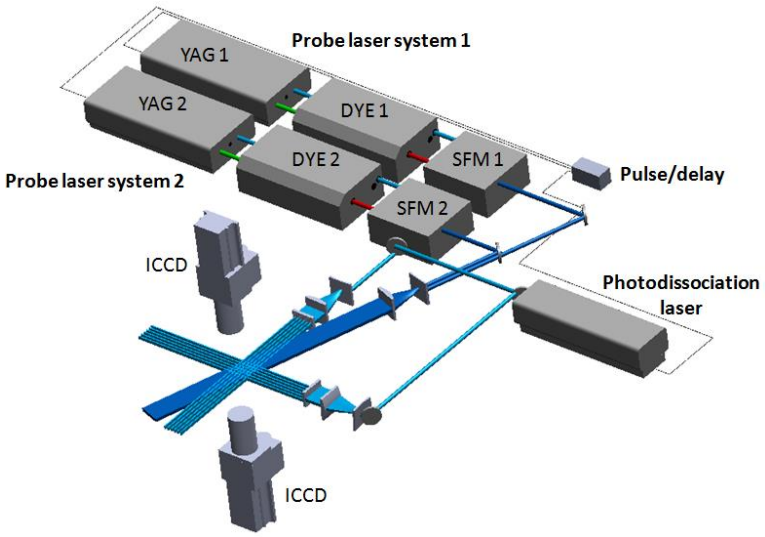

Figure 88. Vibrationally-Enhanced Nitric Oxide Monitoring setup.
(taken from Sánchez-González [23])

Pulsed Wind Tunnel Facilities

In conjunction with the pulsed operation of laser-based diagnostics, a pulsed wind tunnel facility operated in synchronization is recommended. The laser-based diagnostics require seeded molecules, which are expensive and toxic. Pulsed facilities would reduce

the amount of gas used versus what would be required for a continuous facility like the ACE tunnel. Furthermore, the infrastructure required for a pulsed wind tunnel are much less burdensome than for a continuous facility. Pulsed operation would also enable more efficient troubleshooting and on-the-fly variations of experiments.

A pulsed wind tunnel facility has been under development and is planned to perform the bulk of the experiments for the AFOSR BRI project on understanding the effect of thermal and mechanical nonequilibrium on turbulent behavior. The facility's design was largely based on the ACE wind tunnel mainly because of its low-noise characteristics at low Re/m at $M = 7$.

Figure 89 is a SolidWorks assembly of the facility, the Pulsed Hypersonic Adjustable Contoured Expansion Nozzle for Aerothermochemical Test Environments. The settling chamber has similar flow conditioning "aerogrids" and wire mesh screens, and the converging nozzle section has a similar profile. The nozzle contours are based on the ACE tunnel nozzle contours, including its designed capability for variable Mach numbers by adjusting the throat height. An initial characterization campaign is planned to commence soon.

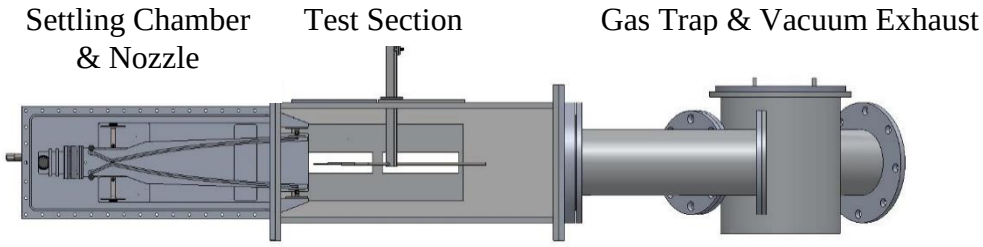

Figure 89. Pulsed Hypersonic Adjustable Contoured Expansion Nozzle for Aerothermochemical Test Environments (PHACENATE).
(credit: E. K. Marcotte and B. T. McManamen)

ACE Tunnel Test Section

The current study was designed around currently existing infrastructure and hardware. In particular, the fixed access/instrumentation ports in the top and bottom of the test section limited the placement of the Mach stem generator wedge models and the capabilities of the traverse (i.e., there was only 25.4 mm (1.0 in.) of traverse range in the design whereas the traverse had a full travel range of 200 mm (7.87 in.). The first recommendation is the design and manufacturing of a new test section based largely on the design of the M6QT test section by J. W. Hofferth. The main body would be an aluminum shell with wide open holes on the top, bottom, and sides. Removable and customizable panels with insets would fill in these holes and provide the majority of the test section walls. The panels would be fastened to the test section with clamps (instead of the current stud-nut method), which would facilitate test section access between tunnel runs. Customized panels would be designed and machined to fit the requirements of the experiment (e.g. optical access, traverse range, model and grid mounting).

Data Acquisition Format

Lastly, the implementation of the NI TDMS format in the DAQ process should be investigated so that recorded data can be better documented and managed, and the need is reduced for external bookkeeping to properly read and interpret the data at a future time by the original researcher or a new student.

REFERENCES

[1] Mayle, R. E., "The Role of Laminar-Turbulent Transition in Gas Turbine Engines," *Journal of Turbomachinery*, Vol. 113, No. 4, 1991, pp. 509-536. doi: 10.1115/1.2929110

[2] Bertin, J. J., and Cummings, R. M., "Fifty years of hypersonics: where we've been, where we're going," *Progress in Aerospace Sciences*, Vol. 39, No. 6-7, 2003, pp. 511-536. doi: 10.1016/S0376-0421(03)00079-4

[3] Adamson, T. C., Jr., and Messiter, A. F., "Analysis of Two-Dimensional Interactions Between Shock Waves and Boundary Layers," *Annual Review of Fluid Mechanics*, Vol. 12, 1980, pp. 103-138. doi: 10.1145/annurev.fl.12.010180.000535

[4] Anyiwo, J. C., and Bushnell, D. M., "Turbulence Amplification in Shock-Wave Boundary-Layer Interaction," *AIAA Journal*, Vol. 20, No. 7, 1982, pp. 893-899.doi: 10.2514/3.7954

[5] Délery, J. (ed.), *Turbulent Shear-Layer/Shock-Wave Interactions*, IUTAM Symposium, Palaiseau, France, Springer-Verlag, Berlin, Sept. 1985. doi: 10.1007/978-3-642-82770-9

[6] Lele, S. K., "Compressibility Effects on Turbulence," *Annual Review of Fluid Mechanics*, Vol. 26, 1994, pp. 211-254. doi: 10.1146/annurev.fl.26.010194.001235

[7] Andreopoulos, Y., Agui, J. H., and Briassulis, G., "Shock Wave-Turbulence Interactions," *Annual Review of Fluid Mechanics*, Vol. 32, 2000, pp. 309-345. doi: 10.1146/annurev.fluid.32.1.309

[8] Dolling, D. S., "Fifty Years of Shock-Wave/Boundary-Layer Interaction Research: What Next?," *AIAA Journal*, Vol. 39, No. 8, 2001, pp. 1517-1531. doi: 10.2514/2.1476

[9] Babinsky, H., and Harvey, J. K. (eds.), *Shock Wave-Boundary-Layer Interactions*, Cambridge University Press, Cambridge, 2011.

[10] Clemens, N. T., and Narayanaswamy, V., "Low-Frequency Unsteadiness of Shock Wave/Turbulent Boundary Layer Interactions," *Annual Review of Fluid Mechanics*, Vol. 46, 2014, pp. 469-492. doi: 10.1146/annurev-fluid-010313-141346

[11] Larsson, J., Bermejo-Moreno, I., and Lele, S. K., "Reynolds- and Mach-Number effects in canonical shock-turbulence interaction," *Journal of Fluid Mechanics*, Vol. 717, Feb. 2013, pp. 293-321.
doi: 10.1017/jfm.2012.573

[12] Stock, H. W., and Ginoux, J. J., "Experimental Results on Crosshatched Ablation Patterns," *AIAA Journal*, Vol. 9, No. 5, 1971, pp. 971-973.
doi: 10.2514/3.6315

[13] Ekoto, I. W., Bowersox, R. D. W., Beutner, T., and Goss, L., "Response of Supersonic Boundary Layers to Local and Global Mechanical Distortions," *Journal of Fluid Mechanics*, Vol. 630, Jul. 2009, pp. 225-265.
doi: 10.1017/S0022112009006752

[14] Fuller, T. J., Hsu, A., Bowersox, R. D. W., and North, S. W., "The Effect of Vibrational Non-Equilibrium on the Decay of Grid Generated Turbulence," AIAA Paper 2009-593, Jan. 2009.
doi: 10.2514/6.2009-593

[15] Fuller, T. J., "Experimental Analysis of the Effect of Vibrational Non-Equilibrium on the Decay of Grid-Generated Turbulence," Ph.D. Dissertation, Department of Aerospace Engineering, Texas A&M University, College Station, TX, 2009.

[16] Sánchez-González, R., Srinivasan, R., Hofferth, J., Kim, D. Y., Tindall, A. J., Bowersox, R. D. W., and North, S. W., "Repetitively Pulsed Hypersonic Flow Apparatus for Diagnostic Development," *AIAA Journal*, Vol. 50, No. 3, 2012, pp. 691-697.
doi: 10.2514/1.J051327

[17] Hsu, A., Srinivasan, R., Bowersox, R. D. W., and North, S. W., "Application of Molecular Tagging Towards Simultaneous Vibrational Temperature and Velocity Mapping in an Underexpanded Jet Flowfield," AIAA Paper 2009-1447, Jan. 2009.
doi: 10.2514/6.2009-1447

[18] Hsu, A., Srinivasan, R., Bowersox, R. D. W., and North, S. W., "Two-Component Molecular Tagging Velocimetry Utilizing NO Fluorescence Lifetime and NO_2 Photodissociation Techniques in an Underexpanded Jet Flowfield," AIAA Paper 2009-4049, Jun. 2009.
doi: 10.2514/6.2009-4049

[19] Hsu, A. G., "Application of Advanced Laser and Optical Diagnostics Towards Non-Thermochemical Equilibrium Systems," Ph.D. Dissertation, Department of Chemistry, Texas A&M University, College Station, TX, 2009.

[20] Hsu, A. G., Srinivasan, R., Bowersox, R. D. W., and North, S. W., "Molecular Tagging Using Vibrationally Excited Nitric Oxide in an Underexpanded Jet Flowfield," *AIAA Journal*, Vol. 47, No. 11, 2009, pp. 2597-2604. doi: 10.2514/1.39998

[21] Sánchez-González, R., Tindall, A., Hsu, A. G., Bowersox, R. D. W., and North, S. W., "Towards Simultaneous Velocimetry and Thermometry Measurements Using the VENOM Diagnostic Technique," AIAA Paper 2010-4349, Jun.-Jul. 2010. doi: 10.2514/6.2010-4349

[22] Sánchez-González, R., Srinivasan, R., Bowersox, R. D. W., and North, S. W., "Simultaneous Velocity and Temperature Measurements in Gaseous Flow Fields using the VENOM Technique," *Optics Letters*, Vol. 36, No. 2, 2011, pp. 196-198. doi: 10.1364/OL.36.000196

[23] Sánchez-González, R., "Advanced Laser Diagnostics Development for the Characterization of Gaseous High Speed Flows," Ph.D. Dissertation, Department of Chemistry, Texas A&M University, College Station, TX, 2012.

[24] Anderson, J. D., *Modern Compressible Flow with Historical Perspective*, 3rd ed., McGraw-Hill, Boston, 2003, Chaps. 3-4, 6.

[25] "Equations, Tables, and Charts for Compressible Flow," NACA Rept. 1135, 1953.

[26] Hinze, J. O., *Turbulence: An Introduction to Its Mechanism and Theory*, McGraw-Hill, New York, 1959, Chap. 1.

[27] Pope, S. B., *Turbulent Flows*, Cambridge University Press, Cambridge, England, UK, 2000, Chaps. 1, 6, 11. doi: 10.1017/CBO9780511840531

[28] Favre, A. J., "The Equations of Compressible Turbulent Gases," Institut de Mecanique Statistique de la Turbulence, Marseille, France, Jan. 1965.

[29] Kovásznay, L. S. G., "Turbulence in Supersonic Flow," *Journal of the Aeronautical Sciences*, Vol. 20, No. 10, 1953, pp. 657-674, 682. doi: 10.2514/8.2793

[30] Chu, B., and Kovásznay, L. S. G., "Non-linear Interactions in a Viscous Heat-Conducting Compressible Gas," *Journal of Fluid Mechanics*, Vol. 3, No. 5, 1958, pp. 494-514. doi: 10.1017/S0022112058000148

[31] Jamme, S., Cazalbou, J.-B., Torres, F., and Chassaing, P., "Direct Numerical Simulation of the Interaction between a Shock Wave and Various Types of Isotropic Turbulence," *Flow, Turbulence and Combustion,* Vol. 68, No. 3, 2002, pp. 227-268.
doi: 10.1023/A:1021197225166

[32] Wouchuk, J. G., Huete Ruiz de Lira, C., and Velikovich, A. L., "Analytical Linear Theory for the Interaction of a Planar Shock Wave with an Isotropic Turbulent Vorticity Field," *Physical Review E. Statistical, Nonlinear, and Soft Matter Physics,* Vol. 79, No. 6, 2009, 066315.
doi: 10.1103/PhysRevE.79.066315

[33] Ribner, H. S., "Convection of a Pattern of Vorticity Through a Shock Wave," NACA TR 1164, 1954.

[34] Ribner, H. S., "Shock-Turbulence Interaction and the Generation of Noise," NACA TR 1233, 1954.

[35] Moore, F. K., "Unsteady Oblique Interaction of a Shock Wave with a Plane Disturbance," NACA TR 1165, 1954.

[36] Kerrebrock, J. L., "The Interaction of Flow Discontinuities with Small Disturbances in a Compressible Fluid," Ph.D. Dissertation, Department of Mechanical Engineering, California Institute of Technology, Pasadena, CA, 1956.

[37] Lele, S. K., "Shock-Jump Relations in a Turbulent Flow," *Physics of Fluids A,* Vol. 4, No. 12, 1992, pp. 2900-2905.
doi: 10.1063/1.858343

[38] Zank, G. P., Zhou, Y., Matthaeus, W. H., and Rice, W. K. M., "The Interaction of Turbulence with Shock Waves: A Basic Model," *Physics of Fluids,* Vol. 14, No. 11, 2002, pp. 3766-3774.
doi: 10.1063/1.1507772

[39] Donzis, D., "Shock Structure in Shock-Turbulence Interaction," *Physics of Fluids,* Vol. 24, No. 12, 2012, 126101.
doi: 10.1063/1.4772064

[40] Lee, S., Lele, S. K., and Moin, P., "Direct Numerical Simulation of Isotropic Turbulence Interacting with a Weak Shock Wave," *Journal of Fluid Mechanics,* Vol. 251, 1993, pp. 533-562.
doi: 10.1017/S0022112093003519

[41] Lee, S., Lele, S. K., and Moin, P., "Interaction of Isotropic Turbulence with Shock Waves: Effect of Shock Strength," *Journal of Fluid Mechanics*, Vol. 340, Jun. 1997, pp. 225-247.
doi: 10.1017/S0022112097005107

[42] Mahesh, K., Lele, S. K., and Moin, P., "The Influence of Entropy Fluctuations on the Interaction of Turbulence with a Shock Wave," *Journal of Fluid Mechanics*, Vol. 334, Mar. 1997, pp. 353-379.
doi: 10.1017/S0022112097004576

[43] Larsson, J., and Lele, S. K., "Direct Numerical Simulation of Canonical Shock/Turbulence Interaction," *Physics of Fluids*, Vol. 21, No. 12, 2009, 126101.
doi: 10.1063/1.3275856

[44] Wang, X., and Zhong, X., "DNS of Strong Shock and Turbulence Interactions with Thermochemical Non-Equilibrium Effects," AIAA Paper 2012-3162, Jun. 2012.
doi: 10.2514/6.2012-3162

[45] Donzis, D., "Amplification Factors in Shock-Turbulence Interactions: Effect of Shock Thickness," *Physics of Fluids*, Vol. 24, No. 1, 2012, 011705.
doi: 10.1063/1.3676449

[46] Agui, J. H., Briassulis, G., and Andreopoulos, Y., "Studies of Interactions of a Propagating Shock Wave with Decaying Grid Turbulence: Velocity and Vorticity Fields," *Journal of Fluid Mechanics*, Vol. 524, Feb. 2005, pp. 143-195.
doi: 10.1017/S0022112004002514

[47] Jacquin, L., Blin, E., and Geffroy, P., "An Experiment on Free Turbulence/Shock Wave Interaction," *Reynolds Flows 8: Selected Papers from the Eighth International Symposium on Reynolds Flows*, edited by F. Durst, R. Friedrich, B. E. Launder, F. W. Schmidt, U. Schumann, and J. H. Whitelaw, Springer, Munich, Germany, Sep. 1991, pp. 229-247.
doi: 10.1007/978-3-642-77674-8_17

[48] Barre, S., Alem, D., and Bonnet, J. P., "Experimental Study of a Normal Shock/Homogeneous Turbulence Interaction," *AIAA Journal*, Vol. 34, No. 5, 1996, pp. 968-974.
doi: 10.2514/3.13175

[49] Hesselink, L. and Sturtevant, B., "Propagation of Weak Shocks Through a Random Medium," *Journal of Fluid Mechanics*, Vol. 196, Nov. 1988, pp. 513-553.
doi: 10.1017/S0022112088002800

[50] Keller, J., and Merzkirch, W., "Interaction of a Normal Shock Wave with a Compressible Turbulent Flow," *Experiments in Fluids*, Vol. 8, No. 5, 1990, pp. 241-248.
doi: 10.1007/BF00187225

[51] Honkan, A., and Andreopoulos, J., "Rapid Compression of Grid-Generated Turbulence by a Moving Shock Wave," *Physics of Fluids A*, Vol. 4, No. 11, 1992, pp. 2562-2572.
doi: 10.1063/1.858443

[52] Xanthos, S., Briassulis, G., and Andreopoulos, Y., "Interaction of Decaying Freestream Turbulence with a Moving Shock Wave: Pressure Field," *Journal of Propulsion and Power*, Vol. 18, No. 6, Nov.-Dec. 2002, pp. 1289-1298.
doi: 10.2514/2.6066

[53] Semper, M. T., Tichenor, N. R., Bowersox, R. D. W., Srinivasan, R., and North, S. W., "On the Design and Calibration of an Actively Controlled Expansion Hypersonic Wind Tunnel," AIAA Paper 2009-0799, Jan. 2009.
doi: 10.2514/6.2009-799

[54] Tichenor, N. R., Semper, M. T., Bowersox, R. D. W., Srinivasan, R., and North, S. W., "Calibration of an Actively Controlled Expansion Hypersonic Wind Tunnel," AIAA Paper 2010-4793, Jun.-Jul. 2010.
doi: 10.2514/6.2010-4793

[55] Bauer, R. C., "A Method of Calculating the Response Time of Pressure Measuring Systems," Arnold Engineering Development Center, Rept. AEDC TR 56-7, Tullahoma, TN, Nov. 1956.

[56] Volluz, R. J., "Wind Tunnel Instrumentation and Operation," *Handbook of Supersonic Aerodynamics*, edited by I. D. V. Faro, NAVORD Report 1488 (Vol. 6), Johns Hopkins University Applied Physics Laboratory, Silver Spring, MD, Jan. 1961, pp. 43-44.

[57] Kim, S., and Wise, K. D., "Temperature Sensitivity in Silicon Piezoresistive Pressure Transducers," *IEEE Transactions on Electron Devices*, Vol. 30, No. 7, 1983, pp. 802-810.
doi: 10.1109/T-ED.1983.21213

[58] Blazquez, G., Pons, P., and Boukabache, A., "Capabilities and Limits of Silicon Pressure Sensors," *Sensors and Actuators*, Vol. 17, No. 3-4, 1989, pp. 387-403.
doi: 10.1016/0250-6874(89)80026-5

[59] Doll, J. C., and Pruitt, B. L., *Piezoresistor Design and Applications*, Springer, New York, 2013, Chap. 5.
doi: 10.1007/978-1-4614-8517-9

[60] Semper, M. T., Pruski, B. J., and Bowersox, R. D. W., "Freestream Turbulence Measurements in a Continuously Variable Hypersonic Wind Tunnel," AIAA Paper 2012-0732, Jan. 2012.
doi: 10.2514/6.2012-732

[61] Tichenor, N. R., "Characterization of the Influence of a Favorable Pressure Gradient on the Basic Structure of a Mach 5.0 High Reynolds Number Supersonic Turbulent Boundary Layer," Ph.D. Dissertation, Department of Aerospace Engineering, Texas A&M University, College Station, TX, 2010.

[62] Semper, M. T., "Examining a Hypersonic Turbulent Boundary Layer at Low Reynolds Number," Ph.D. Dissertation, Department of Aerospace Engineering, Texas A&M University, College Station, TX, 2013.

[63] Wegener, P. P. and Lobb, R. K., "An Experimental Study of a Hypersonic Wind Tunnel Diffuser," *Journal of the Aeronautical Sciences*, Vol. 2, No. 10, 1953, pp. 105-110.
doi: 10.2514/8.2549

[64] Bertram, M. H., "Investigation of the Pressure-Ratio Requirements of the Langley 11-Inch Hypersonic Tunnel with a Variable-Geometry Diffuser," NACA RM L50I13, Langley Aeronautical Laboratory, Langley Air Force Base, VA, 1952.

[65] Pope, A., and Goin, K. L., *High-Speed Wind Tunnel Testing*, Robert E. Krieger, Malabar, FL, 1965, p. 35.

[66] MATLAB, Matrix Laboratory, Software Package, Ver. 8.1.0.604, The MathWorks, Inc., Natick, MA, 2013.

[67] Mouton, C. A., and Hornung, H. G., "Mach Stem Height and Growth Rate Predictions," *AIAA Journal*, Vol. 34, No. 8, 2007, pp. 1977-1987.
doi: 10.2514/1.27460

[68] Ben-Dor, G., Elperin, T., Li, H., Vasiliev, E., Chpoun, A., and Zeitoun, D., "Dependence of Steady Mach Reflections on the Reflecting-Wedge Trailing-Edge Angle," *AIAA Journal*, Vol. 35, No. 11, 1997, pp. 1780-1782.
doi: 10.2514/2.28

[69] Chpoun, A., and Leclerc, E., "Experimental Investigation of the Influence of Downstream Flow Conditions on Mach Stem Height," *Shock Waves*, Vol. 9, No. 4, 1999, pp. 269-271.
doi: 10.1007/s001930050164

[70] Settles, G. S., *Schlieren and Shadowgraph Techniques*, Springer-Verlag, Berlin, 2001, Chaps. 3-4, 10.
doi: 10.1007/978-3-642-56640-0

[71] LabVIEW, Laboratory Virtual Instrument Engineering Workbench, Software Package, Ver. 12.0.1 (32-bit), National Instruments Corporation, Austin, TX, 2012.

[72] Ambrosio, A., and Wortman, A., "Stagnation Point Shock Detachment Distance for Flow Around Spheres and Cylinders," *ARS Journal*, Vol. 32, No. 2, 1962, p. 281.
doi: 10.2514/8.5988

[73] Schneider, S. P., and Haven, C. E., "Quiet-Flow Ludwieg Tube for High-Speed Transition Research," *AIAA Journal*, Vol. 33, No. 4, 1995, pp. 688-693.
doi: 10.2514/3.12434

[74] VLC Media Player for Windows, Software Package, Ver. 2.1.3, VideoLAN, Paris, France, 2014.

[75] ImageJ, Software Package, Ver. 1.47, National Institutes of Health, Bethesda, MD, 2013.

[76] Anderson, J. D., Jr., *Hypersonic and High-Temperature Gas Dynamics*, 2nd ed., AIAA Education Series, AIAA, Reston, VA, 2006, Ch. 1.

[77] Microsoft Excel, Software Package, Ver. 15.0.4603.1000, Microsoft Corporation, Redmond, WA, 2013.

[78] Keyes, F. G., "A Summary of Viscosity and Heat-Conduction Data for He, A, H_2, O_2, N_2, CO, CO_2, H_2O, and Air," *Transactions of the American Society of Mechanical Engineers*, Vol. 73, No. 7, 1951, pp. 589-596.

[79] Terry, J. L., Zweben, S. J., Hallatschek, K., LaBombard, B., Maqueda, R. J., et al., "Observations of the Turbulence in the Scrape-Off-Layer of Alcator C-Mod and Comparisons with Simulation," *Physics of Plasmas*, Vol. 10, No. 5, 2003, pp. 1739-1747.
doi: 10.1063/1.1564090

[80] Kim, K. C., and Adrian, R. J., "Very Large-Scale Motion in the Outer Layer," *Physics of Fluids*, Vol. 11, No. 2, 1999, pp. 417-422.
doi: 10.1063/1.869889

[81] Ribner, H. S., "Comment on "Experimental Study of a Normal Shock/Homogeneous Turbulence Interaction"," *AIAA Journal*, Vol. 36, No. 3, 1987, p. 494.
doi: 10.2514/2.397

[82] Barre, S., Alem, D., and Bonnet, J. P., "Reply by the Authors to H. S. Ribner," *AIAA Journal*, Vol. 36, No. 3, 1998, p. 495.
doi: 10.2514/2.398

[83] Schneider, S. P., "Development of Hypersonic Quiet Tunnels," *Journal of Spacecraft and Rockets*, Vol. 45, No. 4, 2008, pp. 641-664.
doi: 10.2514/1.34489

[84] Kuester, M. S., and White, E. B., "Acoustic Forcing and Control of Reflected Waves in the Klebanoff-Saric Wind Tunnel," AIAA Paper 2012-2862, Jun. 2012.
doi: 10.2514/6.2012-2862

[85] Michaels, C. A., Lin, Z., Mullin, A. S., Tapalian, H. C., and Flynn, G. W., "Translational and Rotational Excitation of the CO_2 (00^00) Vibrationless State in the Collisional Quenching of Highly Vibrationally Excited Perfluorobenzene: Evidence for Impulsive Collisions Accompanied by Large Energy Transfers," *Journal of Chemical Physics*, Vol. 106, No. 17, 1997, pp. 7055-7071.
doi: 10.1063/1.473675

[86] Mitchell, D. G., Johnson, A. M., Johnson, J. A., Judd, K. A., Kim, K., Mayhew, M., Powell, A. L., and Sevy, E. T., "Collisional Relaxation of the Three Vibrationally Excited Difluorobenzene Isomers by Collisions with CO_2: Effect of Donor Vibrational Mode," *Journal of Physical Chemistry A*, Vol. 112, No. 6, pp. 1157-1167.
doi: 10.1021/jp0771365

[87] Hofferth, J. W., Bowersox, R. D. W., and Saric, W. S., "The Mach 6 Quiet Tunnel at Texas A&M: Quiet Flow Performance," AIAA Paper 2010-4794, Jun.-Jul. 2010.
doi: 10.2514/6.2010-4794

[88] Hofferth, J. W., and Saric, W. S., "Boundary-Layer Transition on a Flared Cone in the Texas A&M Mach 6 Quiet Tunnel," AIAA Paper 2012-0923, Jan. 2012.
doi: 10.2514/6.2012-923

[89] Hofferth, J. W., "Boundary-Layer Stability and Transition on a Flared Cone in a Mach 6 Quiet Wind Tunnel," Ph.D. Dissertation, Department of Aerospace Engineering, Texas A&M University, College Station, TX, 2013.

[90] Koochesfahani, M. M., and Nocera, D. G., "Molecular Tagging Velocimetry," *Handbook of Experiment Fluid Dynamics*, edited by C. Tropea, A. L. Yarin, and J F. Foss, Springer Handbooks, Springer-Verlag, Berlin, 2007, pp. 362-382.

[91] Lempert, W. R., and Koochesfahani, M. M., "Molecular Tagging Velocimetry and Thermometry," *Flow Visualization Technique and Examples*, 2nd ed., edited by A. J. Smits and T. T. Lim, Imperial College Press, London, 2012, pp. 77-106.

[92] Azevedo, D. J., "Analytic Prediction of Shock Patterns in a High-Speed, Wedge-Bounded Duct," Ph.D. Dissertation, State University of New York, Buffalo, NY, 1989.

[93] Azevedo, D. J., and Liu, C. S., "Engineering Approach to the Prediction of Shock Patterns in Bounded High-Speed Flows," *AIAA Journal*, Vol. 31, No. 1, 1993, pp. 83-90.
doi: 10.2514/3.11322

[94] Weinstein, L. M., "Large-Field High-Brightness Focusing Schlieren System," *AIAA Journal*, Vol. 31, No. 7, 1993, pp. 1250-1255.
doi: 10.2514/3.11760

[95] Hofferth, J. W., Humble, R. A., Floryan, D. C., and Saric, W. S., "High-Bandwidth Optical Measurements of the Second-Mode Instability in a Mach 6 Quiet Tunnel," AIAA Paper 2013-0378, Jan. 2013.
doi: 10.2514/6.2013-378

[96] Kovásznay, L. S. G., "The Hot-Wire Anemometer in Supersonic Flow," *Journal of the Aeronautical Sciences*, Vol. 17, No. 9, 1950, pp. 565-572, 584.
doi: 10.2514/8.1725

[97] Smits, A. J., Hayakawa, K., and Muck, K. C., "Constant Temperature Hot-Wire Anemometer Practice in Supersonic Flows, Part 1: The Normal Wire," *Experiments in Fluids*, Vol. 1, No. 2, 1983, pp. 83-92.
doi: 10.1007/BF00266260

[98] Bruun, H. H., *Hot-Wire Anemometry: Principles and Signal Analysis*, Oxford University Press, Oxford, 1995, Chaps. 2-4.

[99] Bowersox, R. D. W., "Compressible Turbulence in a High-Speed High Reynolds Number Mixing Layer," Ph.D. Dissertation, Department of Aerospace and Ocean Engineering, Virginia Polytechnic Institute and State University, Blacksburg, VA, 1992.

[100] Freymuth, P., "Frequency Response and Electronic Testing for Constant-Temperature Hot-Wire Anemometers," *Journal of Physics E: Scientific Instruments*, Vol. 10, No. 7, 1977, pp. 705-710. doi: 10.1088/0022-3735/10/7/012

[101] SignalExpress Full, Software Package, Ver. 2013, National Instruments Corporation, Austin, TX, 2013.

APPENDIX A

DISCLAIMER

The views and conclusions contained herein are those of the author and should not be interpreted as necessarily representing the official policies or endorsements, either expressed or implied, of the Department of Defense or the United States government.

APPENDIX B

MACH STEM STRUCTURE THEORY*

This appendix describes the calculations, based on the generalized geometric solution method of Mouton and Hornung [67], coded into a MATLAB script [66] to predict and plot the flow structure resulting from the irregular (Mach) reflection of an oblique shock onto a solid surface (single-wedge configuration) or symmetry plane (dual-wedge configuration).

Previous Work

The theoretical work of Ben-Dor et al. [68] and experimental work Chpoun and Leclerc [69] (Figure 90) show that the downstream conditions did not affect the Mach stem height; thus Mouton and Hornung did not consider the flow downstream of the expansion wave corresponding to the sonic throat.

Mouton and Hornung built on the Mach stem height prediction work of Azevedo ([92]-[93]). Azevedo stipulated in his work that in the converging flow behind the Mach stem, the sonic throat's position is where the leading characteristic of the expansion fan intersects the slip line. Azevedo's geometry was also inconsistent, namely in that the slip line, the leading expansion wave from the reflected shock to the slip line, and the sonic throat do not intersect at a point. Mouton and Hornung relaxed some of the assumptions

---

made by Azevedo and created a geometric solution in which a system of equations is derived from the fixed geometry of the flow features.

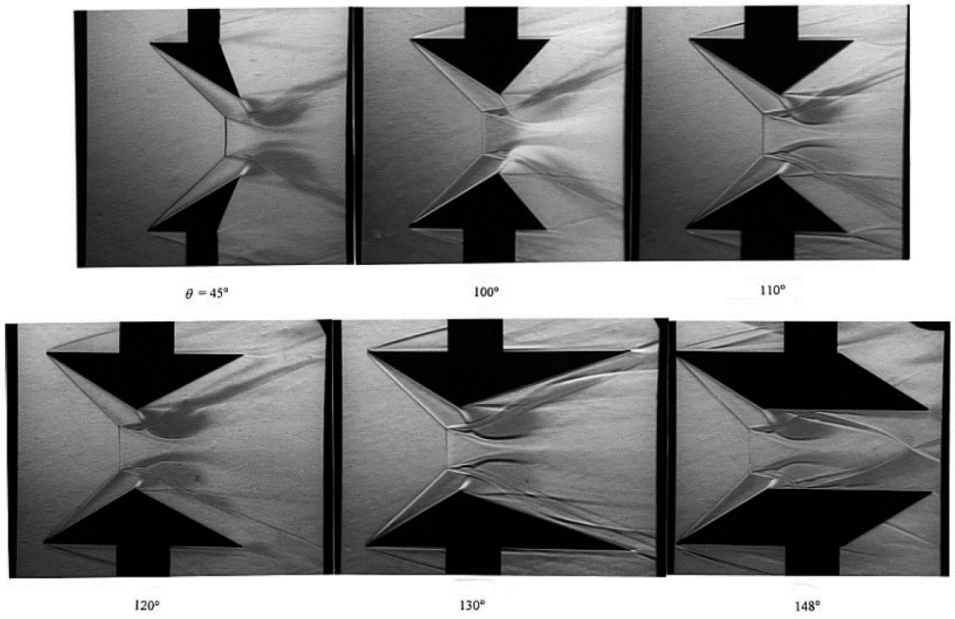

Figure 90. Schlieren photographs of Mach stem height versus downstream angles. Flow is at M = 4.96. Leading wedge angle is 32°. Angle captions denote angle of wedge just downstream of Mach stem. Top row (l-r): 45°, 100°, 110°. Bottom row (l-r): 120°, 130°, 148°. (taken from Chpoun and Leclerc [69])

The Azevedo and geometric solutions, however, assumed that the sonic throat behind the Mach stem occurred at the leading characteristic of the expansion fan. Mouton and Hornung then derived a generalized geometric solution, which allowed the sonic throat to occur further downstream from the Mach stem. A key assumption of the generalized geometric solution was that the flow right above the sonic throat was parallel

to the freestream flow. Figure 91 is an illustration of the flow structure used in the generalized geometric solution method for the Mach stem height prediction.

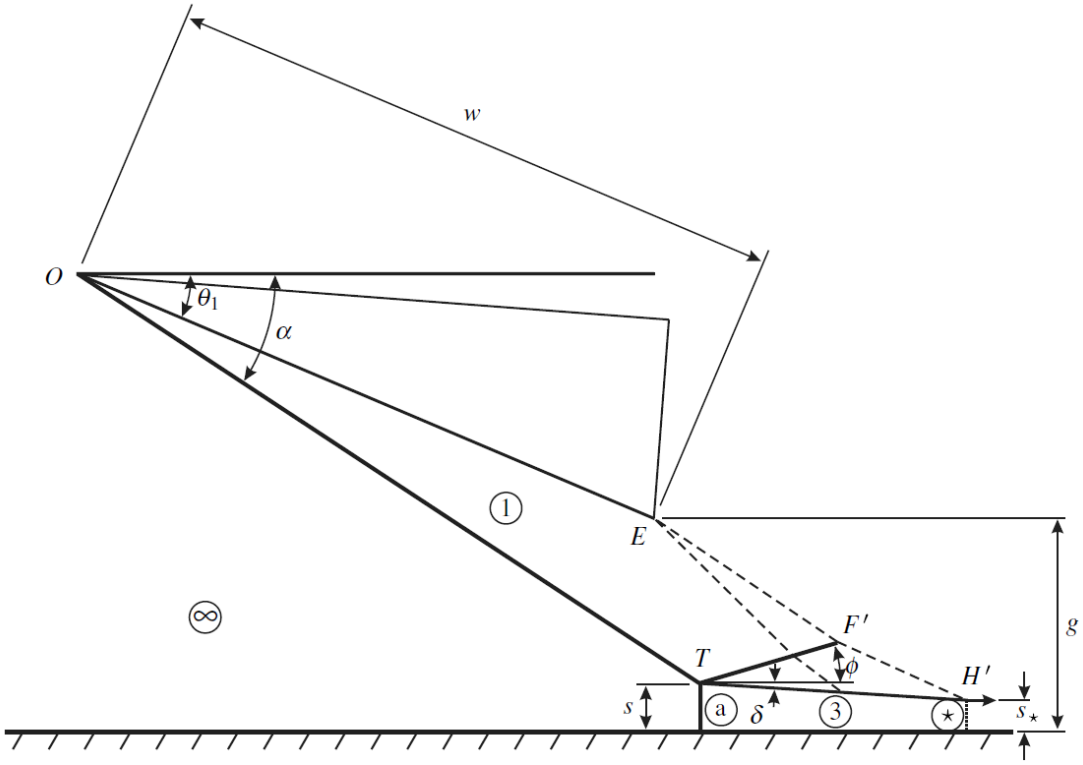

Figure 91. Flow structure schematic of generalized geometric solution of Mach stem height. (taken from Mouton and Hornung [67])

Generalized Geometric Solution

Mouton and Hornung nondimensionalized the geometry by *w*, the wedge length. Nondimensionalized lengths are denoted by a plus sign (+). Pressures are nondimensionalized by γM_{∞}^{2}. Table 18 lists the parameters of the generalized geometric solution found in Figure 91.

Table 18. Generalized geometric solution parameters.

Parameter	Description
θ_1	angle of wedge surface
α	angle of leading oblique shock wave
ϕ	angle of triple-point reflected shock
δ	angle of triple-point slip line
$\mu_{1'}$	angle of Mach wave corresponding to the sonic throat in region 1´
$\mu_{2'}$	angle of Mach wave corresponding to the sonic throat in region 2´
w	length of wedge leading surface
s	half-height of Mach stem (for a symmetric setup)
s_*	half-height of sonic throat (for a symmetric setup)
A_r	ratio of Mach stem height to sonic throat height ($= s / s_*$)
g	half-height of spacing between near-surface of wedge and symmetry plane
$\overline{OE}$	length from wedge leading edge to expansion corner
$\overline{OT}$	length of leading oblique shock wave (wedge leading edge to triple point)
$\overline{EF'}$	length from expansion corner to intersection of reflected shock wave and Mach wave corresponding to the sonic throat
$\overline{F'H'}$	length of Mach wave corresponding to sonic throat from intersection with reflected shock wave to intersection with slip line
$\overline{TF'}$	length of reflected shock wave from triple point to intersection with Mach wave corresponding to the sonic throat

The calculation procedures are now described step-by-step. Given a geometry (θ_1, w, and g), freestream Mach number (M_∞), and fluid specific heat ratio (γ), calculations can be made to determine properties of the leading oblique shock wave, region 1, the post-Mach stem properties, and region "a" using shock wave theory. The leading oblique shock wave angle, α, is determined iteratively from:

$$\cot\theta_1 = \tan\alpha\left(\frac{(\gamma+1)M_\infty^2}{2\left(M_\infty^2\sin^2\alpha-1\right)}-1\right) \tag{49}$$

The nondimensionalized static pressure, P_1^+, and Mach number, M_1, behind the leading oblique shock wave in region 1 are:

$$P_1^+ = \frac{1}{\gamma M_\infty^2}\frac{2\gamma M_\infty^2\sin^2\alpha-(\gamma-1)}{\gamma+1} \tag{50}$$

$$M_1 = \left(\frac{(\gamma-1)M_\infty^2\sin^2\alpha+2}{\sin^2(\alpha-\theta_1)\left(2\gamma M_\infty^2\sin^2\alpha-(\gamma-1)\right)}\right)^{1/2} \tag{51}$$

The nondimensionalized static pressure, P_a^+, and Mach number, M_a, behind the Mach stem (normal shock wave) in region "a" are:

$$P_a^+ = \frac{1}{\gamma M_\infty^2}\frac{2\gamma M_\infty^2-(\gamma-1)}{\gamma+1} \tag{52}$$

$$M_a = \left(\frac{(\gamma-1)M_\infty^2+2}{2\gamma M_\infty^2-(\gamma-1)}\right)^{1/2} \tag{53}$$

The triple point is now considered. While the Mach stem is typically treated as a normal shock wave in the overall picture, a proper triple point calculation requires that the Mach stem be treated as an oblique shock wave. Figure 92 illustrates the triple point.

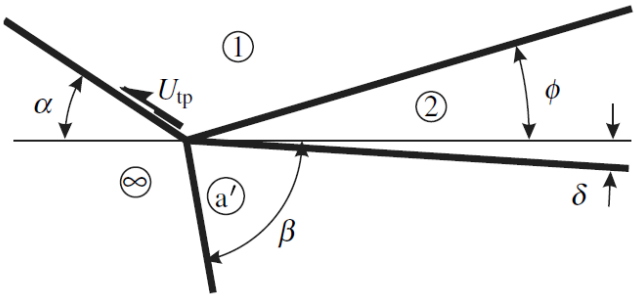

Figure 92. Triple point flow structure schematic.
(taken from Mouton and Hornung [67])

The triple point theory enables the calculation of the angle the reflected shock makes with the freestream direction (φ) as well as the angle between the slip line and initial Mach stem (β). There is no analytical solution, and the two angles must be solved for iteratively. The two conditions that must be satisfied at the slip line (across regions 2 and "a′") are equality of static pressure and identical flow deflection angles:

$$P_2^+ = P_{a'}^+ \tag{54}$$

$$\delta_2 = \delta_{a'} \tag{55}$$

By the triple point theory, those two boundary conditions provide the system of equations for the angle of the reflected shock wave, φ , and the angle of the Mach stem at the triple point, β:

$$P_1^+ \frac{2\gamma M_1^2 \sin^2(\phi+\theta_1)-(\gamma-1)}{\gamma+1} = \frac{1}{\gamma M_\infty^2} \frac{2\gamma M_\infty^2 \sin^2\beta-(\gamma-1)}{\gamma+1} \tag{56}$$

$$\tan(\phi+\theta_1)\left(\frac{(\gamma+1)M_1^2}{M_1^2\sin^2(\phi+\theta_1)-1}-2\right) = \tan\beta\left(\frac{(\gamma+1)M_\infty^2}{M_\infty^2\sin^2\beta-1}-2\right) \tag{57}$$

Knowing φ, the slip line deflection angle, δ, can then be calculated:

$$\cot(\theta_1-\delta) = \tan(\phi+\theta_1)\left(\frac{(\gamma+1)M_1^2}{2\left(M_1^2\sin^2(\phi+\theta_1)-1\right)}-1\right) \tag{58}$$

Now knowing the properties of region 1 and the structure of the triple point, the properties of region 2 can now be calculated with oblique shock theory and isentropic expansion wave theory. The nondimensionalized static pressure, Mach number, and Mach wave angle in region 2 are:

$$P_2^+ = P_1^+ \frac{2\gamma M_1^2 \sin^2(\phi+\theta_1)-(\gamma-1)}{\gamma+1} \tag{59}$$

$$M_2 = \left(\frac{(\gamma-1)M_1^2\sin^2(\phi+\theta_1)+2}{\sin^2(\phi+\delta)\left(2\gamma M_\infty^2\sin^2\alpha-(\gamma-1)\right)}\right)^{1/2} \tag{60}$$

$$\mu_2 = \sin^{-1}\left(\frac{1}{M_2}\right) \tag{61}$$

The area ratio of the Mach stem to the sonic throat, A_r, is calculated by using the conservation of mass and momentum:

$$A_r = \frac{1}{M_a}\left(\frac{2}{\gamma+1}\left(1+\frac{\gamma-1}{2}M_a^2\right)\right)^{\frac{\gamma+1}{2(\gamma-1)}} \tag{62}$$

Recall that the key point of the generalized geometric solution method is that the sonic throat is allowed to sit further downstream than the intersection of the leading Mach wave characteristic with the slip line. The assumption is that the flow above the sonic throat has been deflected to be parallel with the freestream direction; that is, the flow must turn through an angle δ, the angle of the slip line from the triple point:

$$\delta = \nu\left(M_{2'}\right) - \nu\left(M_2\right) \tag{63}$$

Where ν is the Prandtl-Meyer function:

$$\nu\left(M\right) = \sqrt{\frac{\gamma+1}{\gamma-1}}\tan^{-1}\sqrt{\frac{\gamma-1}{\gamma+1}\left(M^2-1\right)} - \tan^{-1}\sqrt{M^2-1} \tag{64}$$

Already knowing δ and M_2, the Prandtl-Meyer function for $M_{2'}$ can be calculated. $M_{2'}$ is then iteratively determined, and the angle of the Mach wave corresponding to the sonic throat in region 2´ can be calculated:

$$\mu_{2'} = \sin^{-1}\left(\frac{1}{M_{2'}}\right) \tag{65}$$

Consider now the flow that passes through the leading oblique shock wave, an expansion fan, and the reflected shock wave. The flow must turn an angle, δ_e, in addition to δ. Oblique shock theory provides another system of equations to solve simultaneously for δ_e and $M_{1'}$:

$$\cot\left(\theta_1 - \delta - \delta_e\right) = \tan\left(\theta_1 - \delta - \delta_e + \phi\right)\left(\frac{\left(\gamma+1\right)M_{1'}^2}{2\left(M_{1'}^2\sin^2\left(\theta_1 - \delta - \delta_e + \phi\right) - 1\right)} - 1\right) \tag{66}$$

$$\delta + \delta_e = \nu\left(M_{1'}\right) - \nu\left(M_1\right) \tag{67}$$

Knowing $M_{1'}$, the angle of the Mach wave corresponding to the sonic throat in region 1´ can be calculated:

$$\mu_{1'} = \sin^{-1}\left(\frac{1}{M_{1'}}\right) \tag{68}$$

Given the geometry, freestream Mach number, and fluid specific heat ratio, the flow properties in the major regions have been determined as well as the angles of the flow structures relative to the freestream direction. The next step is to solve for the geometry of the flow structures given the constraints. A system of equations based on geometrical constraints is derived from the illustration in Figure 91. Each equation of the system is described. In each figure corresponding to the equation, the red arrows denote components of the left-hand side of the equation whereas the blue arrows denote components of the right-hand side of the equation.

The first equation relates the vertical components of the leading oblique shock wave and the Mach stem to the wedge geometry and separation distance. The corresponding figure and equation are shown below in Figure 93 and Eq. (69).

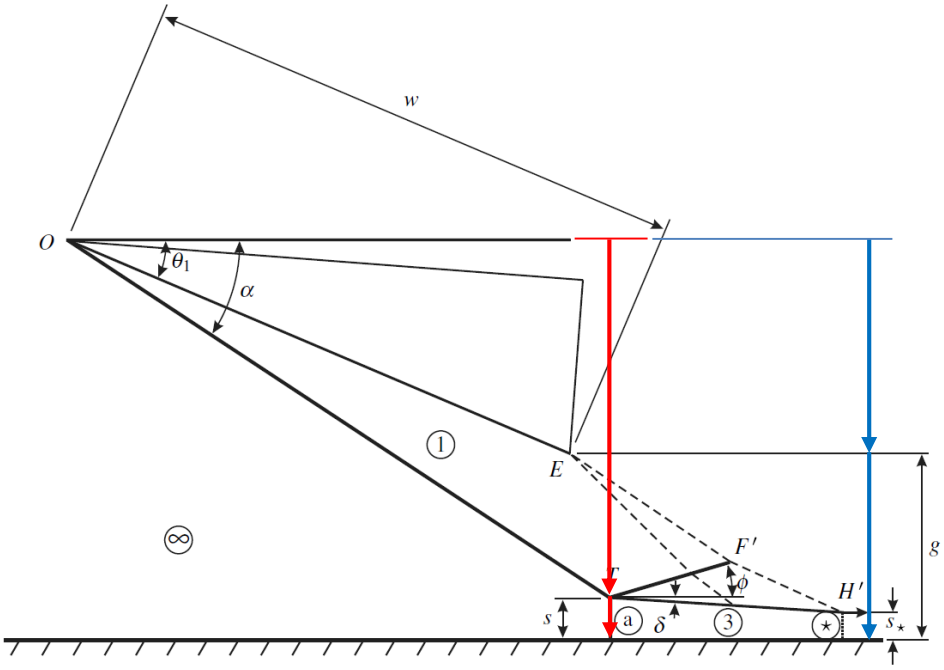

Figure 93. Generalized geometric solution's schematic of first geometric constraint. (adapted from Mouton and Hornung [67])

$$\overline{OT}^{+}\sin\alpha + A_r s_*^{+} = \sin\theta_1 + g^{+} \tag{69}$$

The second equation relates the vertical components of the characteristic wave (corresponding to the sonic throat) and the sonic throat itself to the wedge separation distance. The corresponding figure and equation are shown below in Figure 94 and Eq. (70).

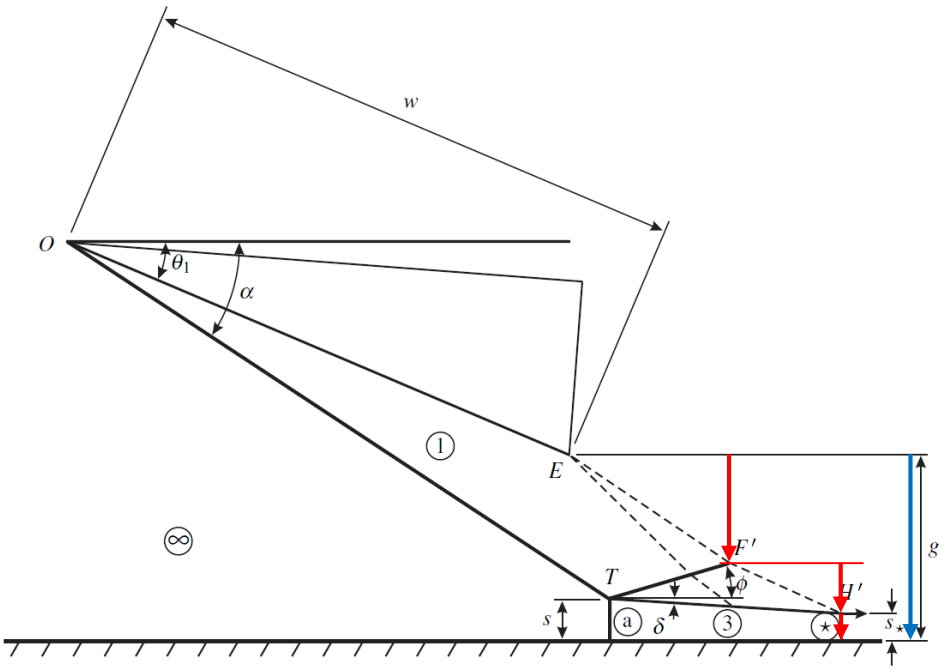

Figure 94. Generalized geometric solution's schematic of second geometric constraint. (adapted from Mouton and Hornung [67])

$$\overline{EF'}^{+}\sin\left(\mu_{1'}+\theta_1\right)+\overline{F'H'}^{+}\sin\left(\delta+\mu_{2'}\right)+s_{*}^{+}=g^{+} \tag{70}$$

The third equation relates the horizontal components of the oblique shock wave, slip line, and characteristic wave (corresponding to the sonic throat) to the wedge geometry. The corresponding figure and equation are shown below in Figure 95 and Eq. (71).

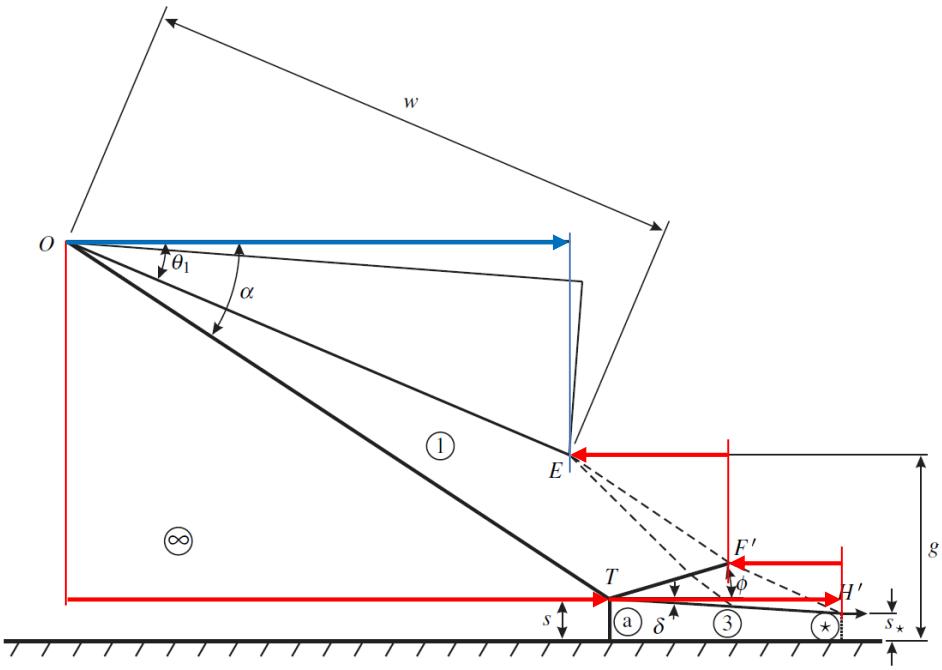

Figure 95. Generalized geometric solution's schematic of third geometric constraint. (adapted from Mouton and Hornung [67])

$$-\overline{OT}^{+}\cos\alpha - s_{*}^{+}\cot\delta\left(A_{r}-1\right)+\overline{F'H'}^{+}\cos\left(\delta+\mu_{2'}\right)+\overline{EF'}^{+}\cos\left(\mu_{1'}+\theta_{1}\right) = -\cos\theta_{1} \tag{71}$$

The fourth equation relates the horizontal components of the oblique shock wave, the reflected shock wave, and characteristic wave (corresponding to the sonic throat) to the wedge geometry. The corresponding figure and equation are shown below in Figure 96 and Eq. (72).

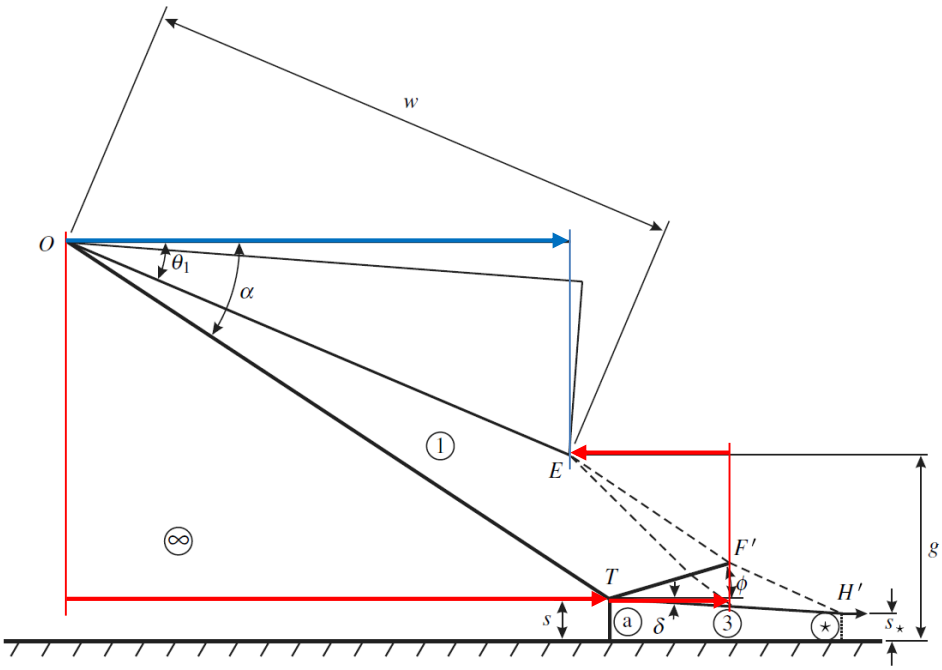

Figure 96. Generalized geometric solution's schematic of fourth geometric constraint. (adapted from Mouton and Hornung [67])

$$-\overline{OT}^{+}\cos\alpha-\overline{TF'}^{+}\cos\phi+\overline{EF'}^{+}\cos\left(\mu_{1'}+\theta_1\right)=-\cos\theta_1 \tag{72}$$

The fifth equation relates the vertical components of the oblique shock wave, the reflected shock wave, and characteristic wave (corresponding to the sonic throat) to the wedge geometry. The corresponding figure and equation are shown below in Figure 97 and Eq. (73).

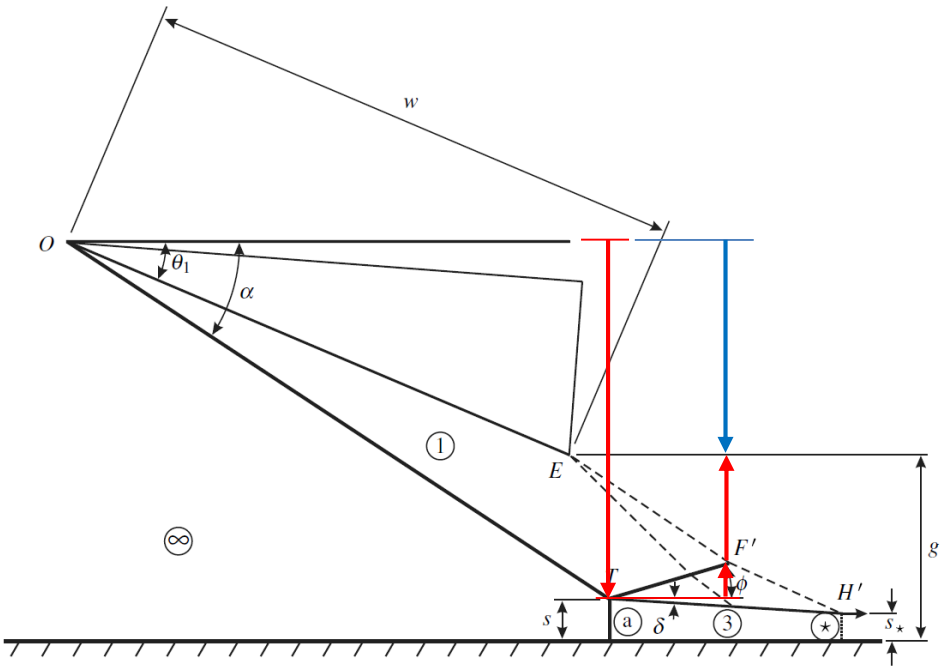

Figure 97. Generalized geometric solution's schematic of fifth geometric constraint. (adapted from Mouton and Hornung [67])

$$-\overline{OT}^{+}\sin\alpha+\overline{TF'}^{+}\sin\phi+\overline{EF'}^{+}\sin\left(\mu_{1'}+\theta_1\right)=-\sin\theta_1 \tag{73}$$

The five geometric constraints constituting the system of equations are cast into matrix form in Eq. (74).

$$\begin{pmatrix} \sin\alpha & A_r & 0 & 0 & 0 \\ 0 & 1 & \sin(\delta+\mu_{2'}) & \sin(\mu_{1'}+\theta_1) & 0 \\ -\cos\alpha & \cot\delta(1-A_r) & \cos(\delta+\mu_{2'}) & \cos(\mu_{1'}+\theta_1) & 0 \\ -\cos\alpha & 0 & 0 & \cos(\mu_{1'}+\theta_1) & -\cos\phi \\ -\sin\alpha & 0 & 0 & \sin(\mu_{1'}+\theta_1) & \sin\phi \end{pmatrix} \times \begin{pmatrix} \overline{OT}^+ \\ s_*^+ \\ \overline{F'H'}^+ \\ \overline{EF'}^+ \\ \overline{TF'}^+ \end{pmatrix} = \begin{pmatrix} g^+ + \sin\theta_1 \\ g^+ \\ -\cos\theta_1 \\ -\cos\theta_1 \\ -\sin\theta_1 \end{pmatrix} \tag{74}$$

The system is solved for the lengths of the oblique shock wave, the Mach stem, the characteristic wave corresponding to the sonic throat from its intersection with the reflected shock wave to its intersection with the slip line, the characteristic wave corresponding to the sonic throat from the wedge expansion corner to its intersection with the reflected shock wave, and the reflected shock wave from the triple point to its intersection with the characteristic wave corresponding to the sonic throat.

Using algebra and trigonometry, the flow structure can be plotted. Figure 98 shows the Mach stem height variation with the wedge angle. The Mach stem height increases with a larger wedge angle. Figure 99 shows the Mach stem height variation with the wedge separation distance. The Mach stem height decreases with increasing wedge separation distance. For the current study, the wedge angle was $\theta_1 = 35°$ and the nondimensionalized wedge separation distance was $g^+ = 0.85$.

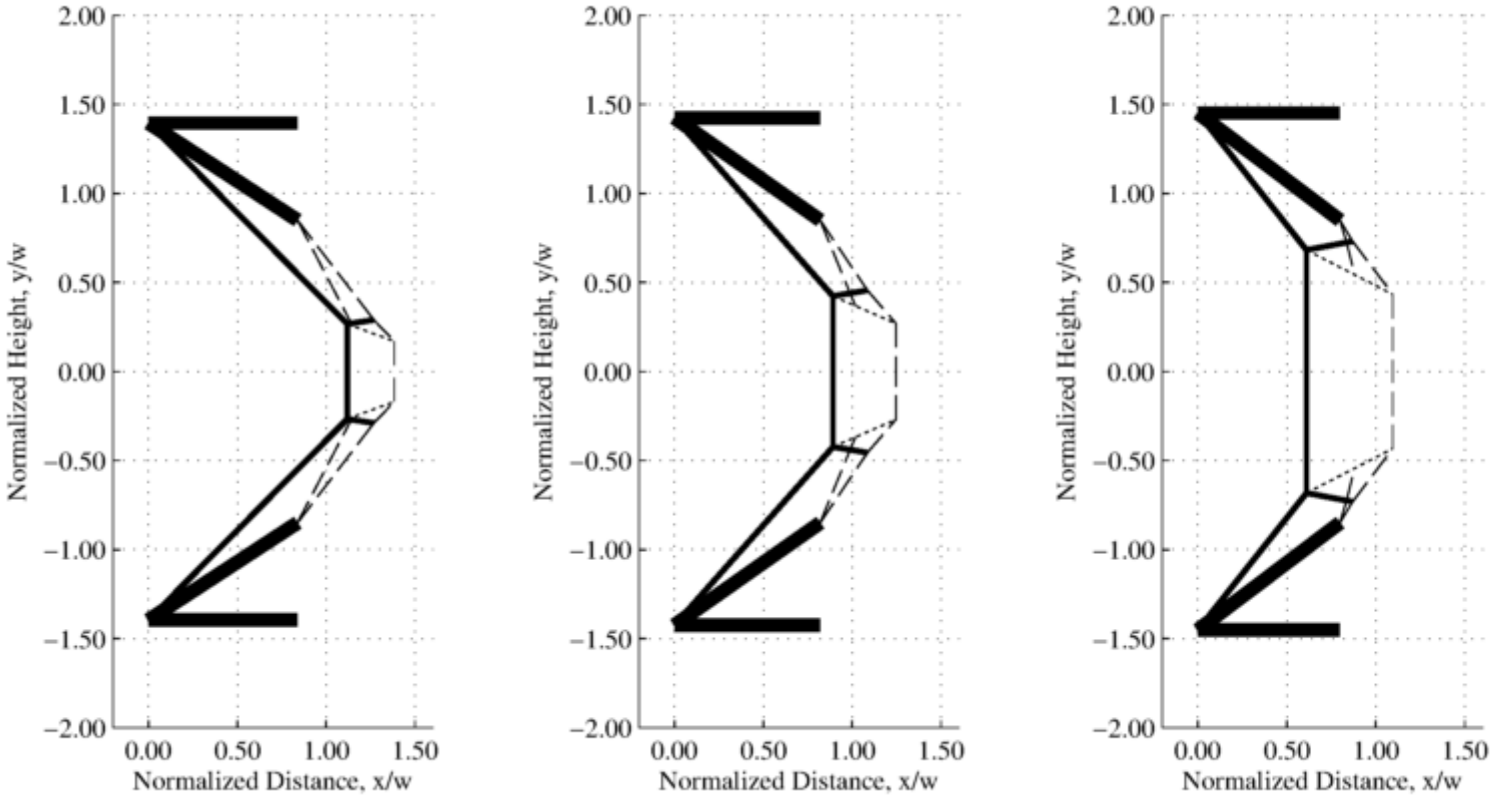

Figure 98. Variation of Mach stem flow structure with wedge angle.

***M* = 5.85. g^+ = 0.85.**

a) θ_1 = 33°. b) θ_1 = 35°. c) θ_1 = 37°.

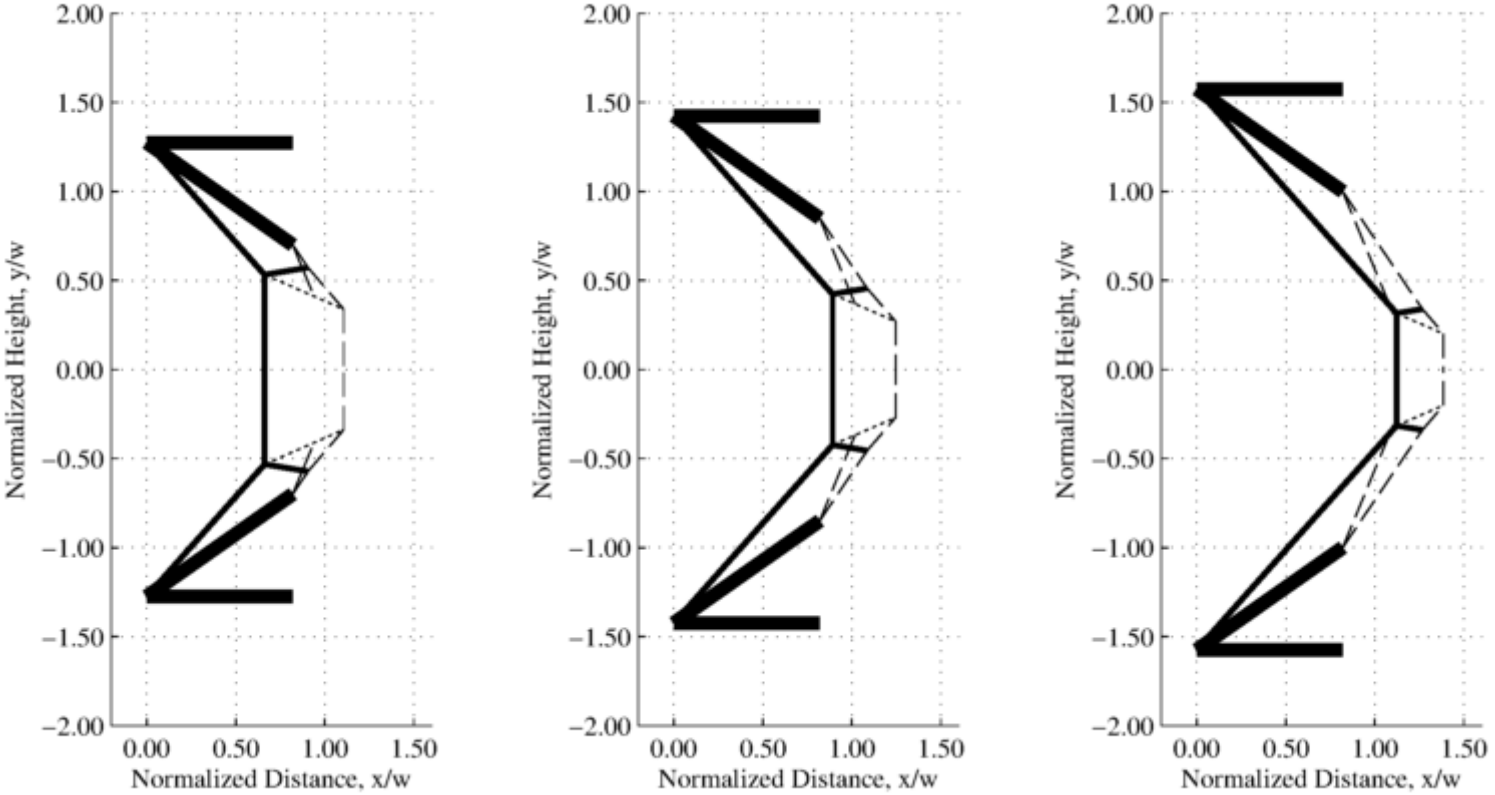

a) **b)** **c)**

Figure 99. Variation of Mach stem flow structure with wedge separation distance.

***M* = 5.85. θ_1 = 35°.**

a) g^+ = 0.70. **b) g^+ = 0.85.** **c) g^+ = 1.00.**

APPENDIX C

MODEL SCHEMATICS

This section provides dimensional drawings of the components that were machined for this study. The drawings are organized into three categories, and the list of drawings is provided below.

- Mach Stem Generator Wedge Struts and Support
  - Figure 100: Window Plug
  - Figure 101: Bottom Outer Strut
  - Figure 102: Left Outer Strut
  - Figure 103: Right Outer Strut
  - Figure 104: Inner Strut
- Mach Stem Generator Wedges
  - Figure 105: Initial Set
  - Figure 106: Wide Set
  - Figure 107: Thick Set
- Traverse
  - Figure 108: Strut
  - Figure 109: Window Plug
  - Figure 110: Sealing Plate – Aluminum
  - Figure 111: Sealing Plate – Silicone
  - Figure 112: Adapter Sleeve

Mach Stem Generator Wedge Struts and Support

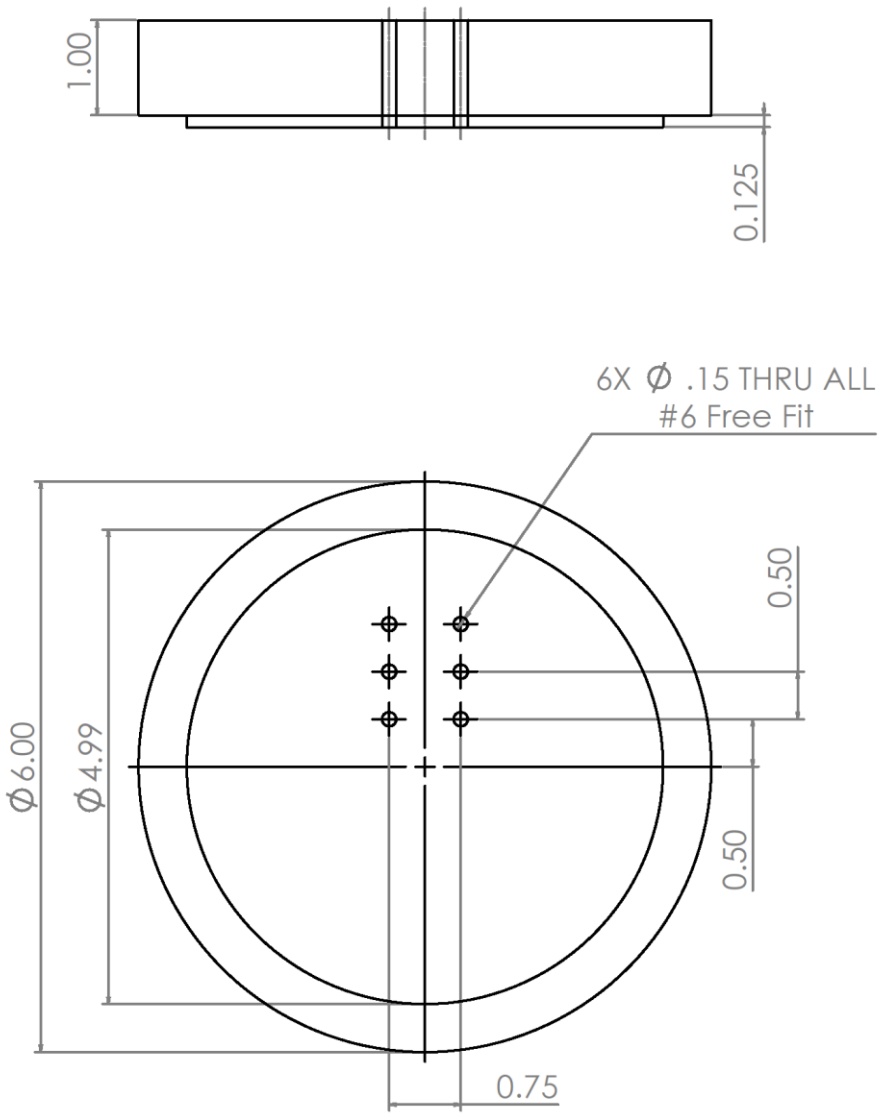

Figure 100. Drawing of Mach stem generator wedge model window plug.

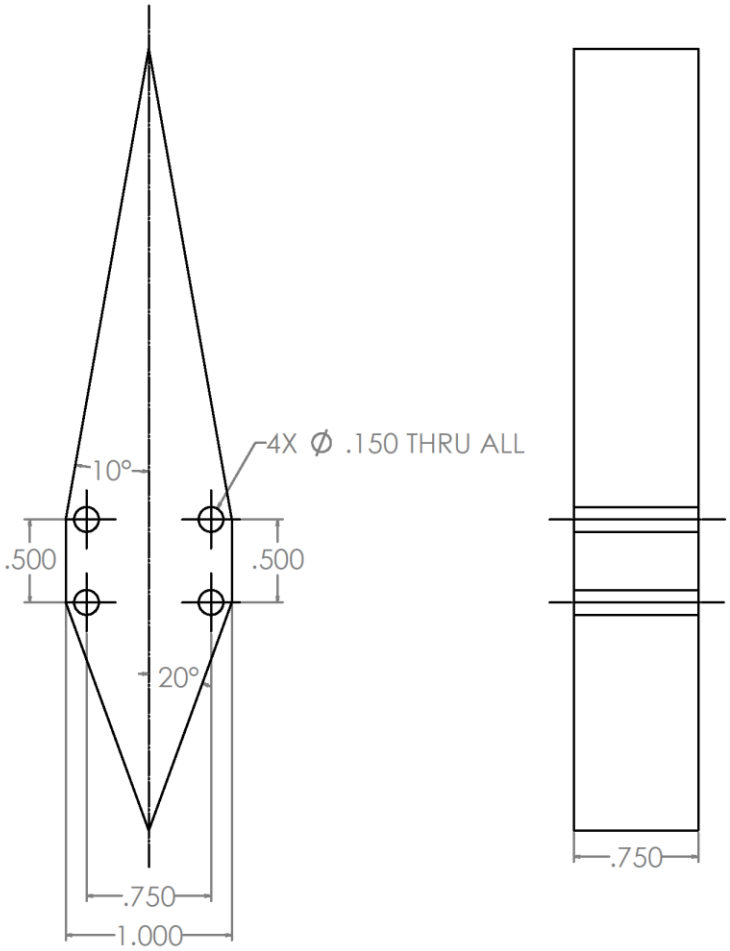

Figure 101. Drawing of Mach stem generator wedge model bottom outer strut.

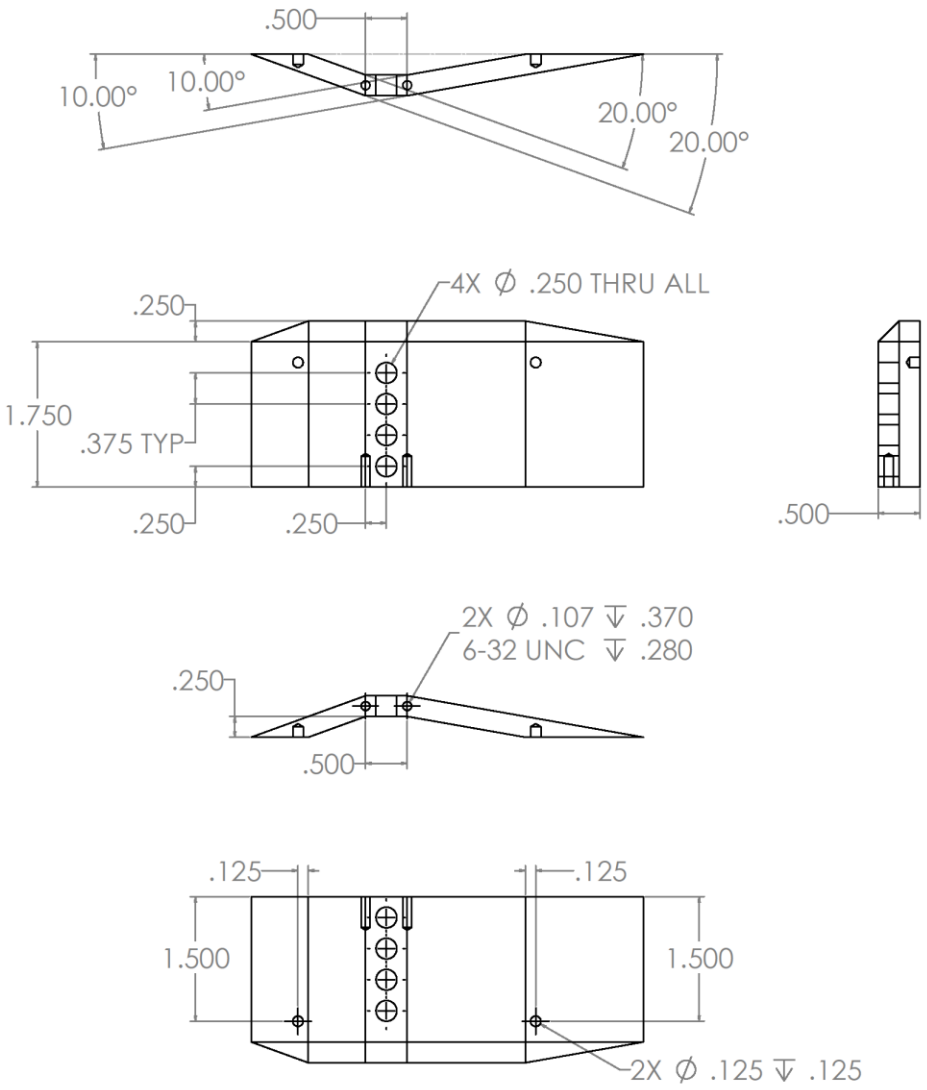

Figure 102. Drawing of Mach stem generator wedge model left outer strut.

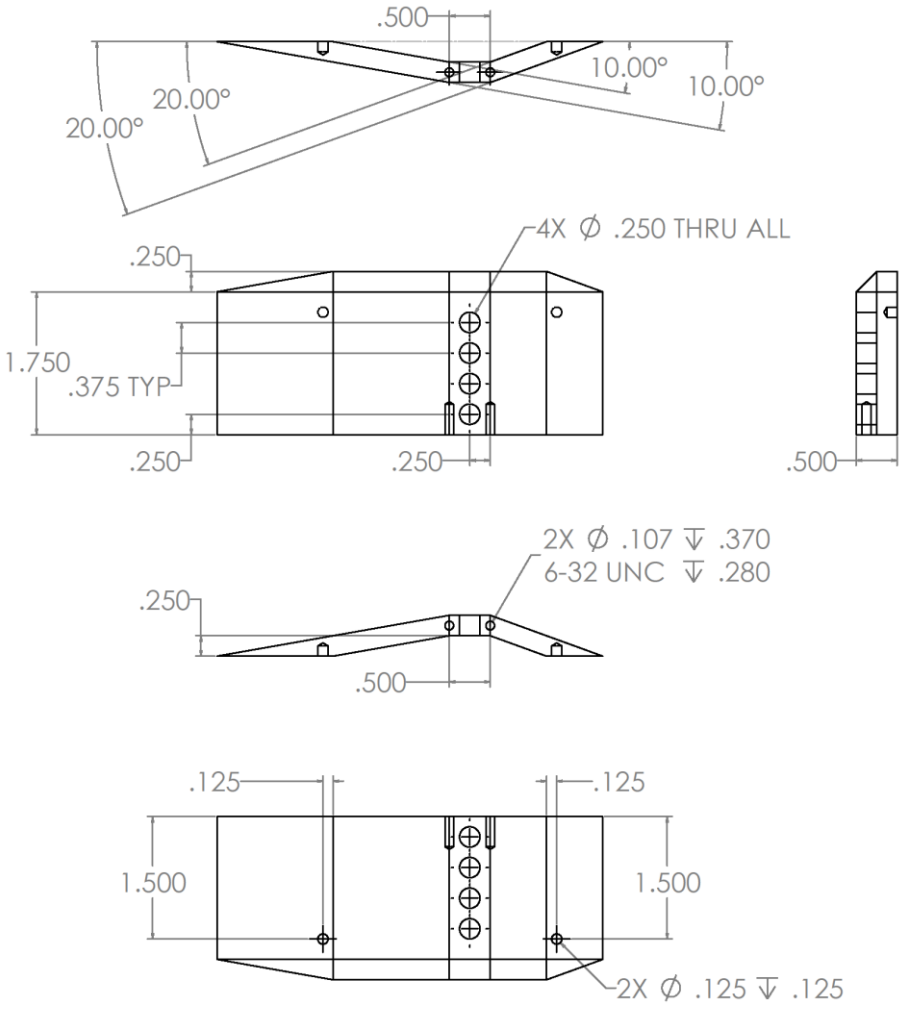

Figure 103. Drawing of Mach stem generator wedge model right outer strut.

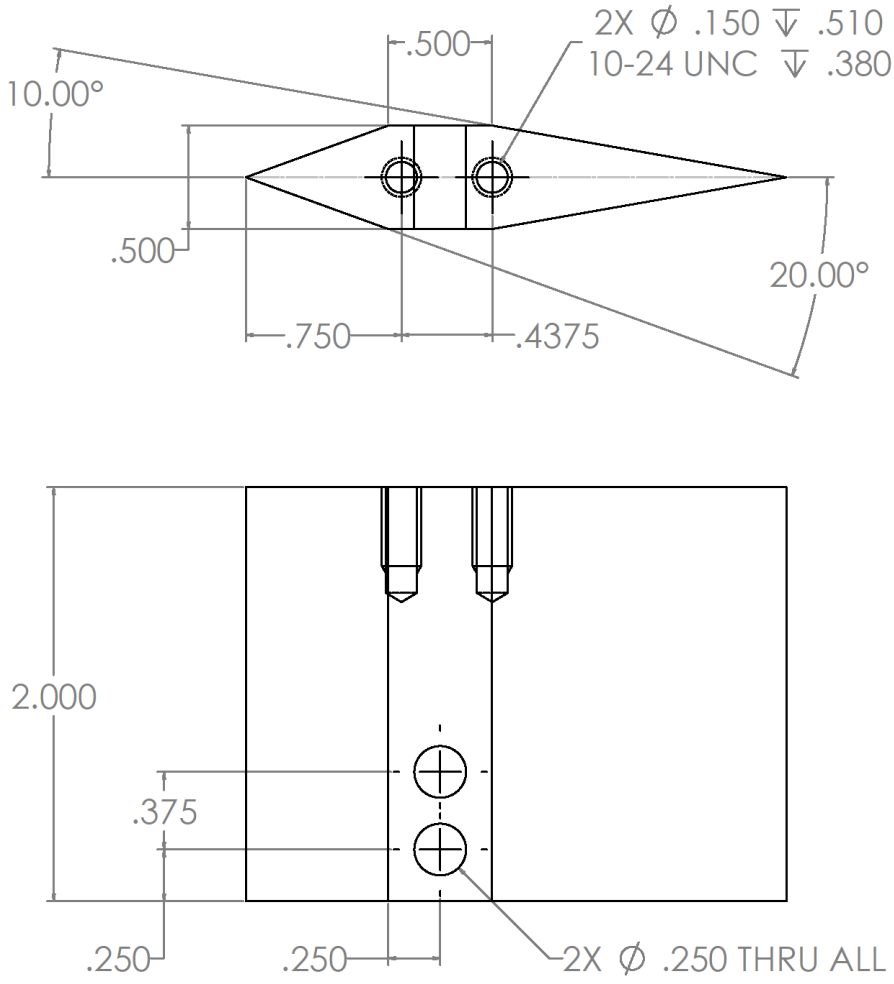

Figure 104. Drawing of Mach stem generator wedge model inner strut.

Mach Stem Generator Wedges

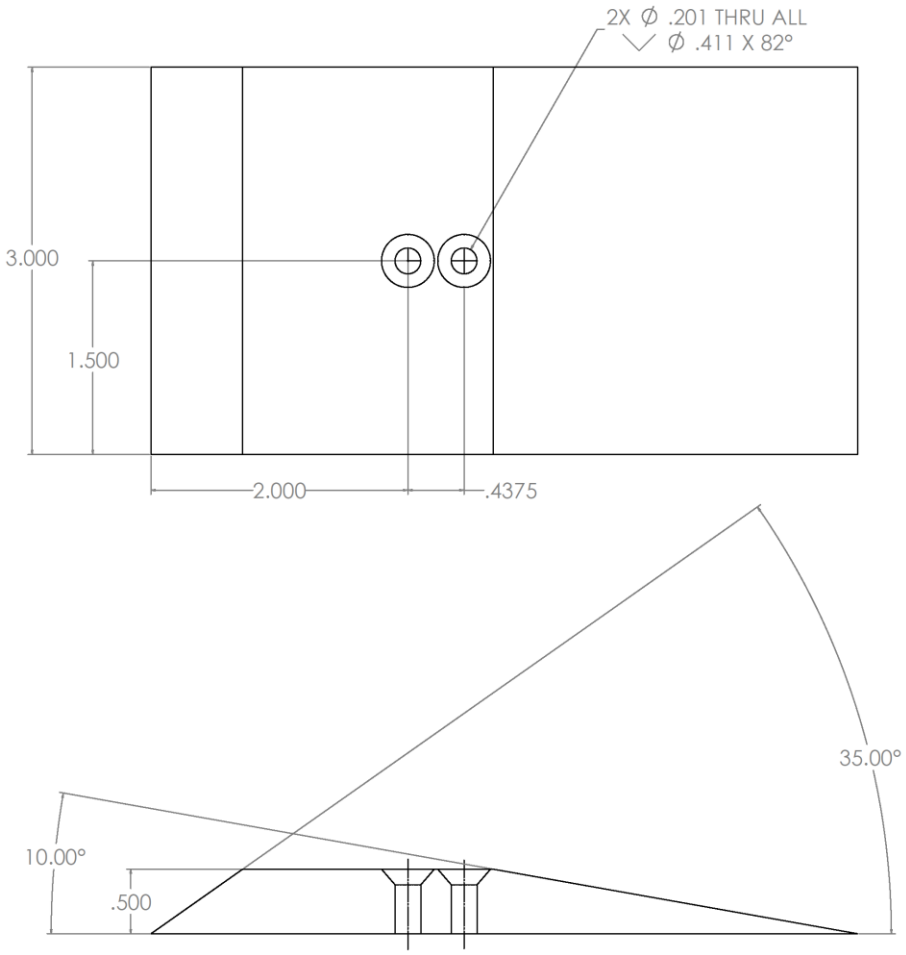

Figure 105. Drawing of initial Mach stem generator wedge model.

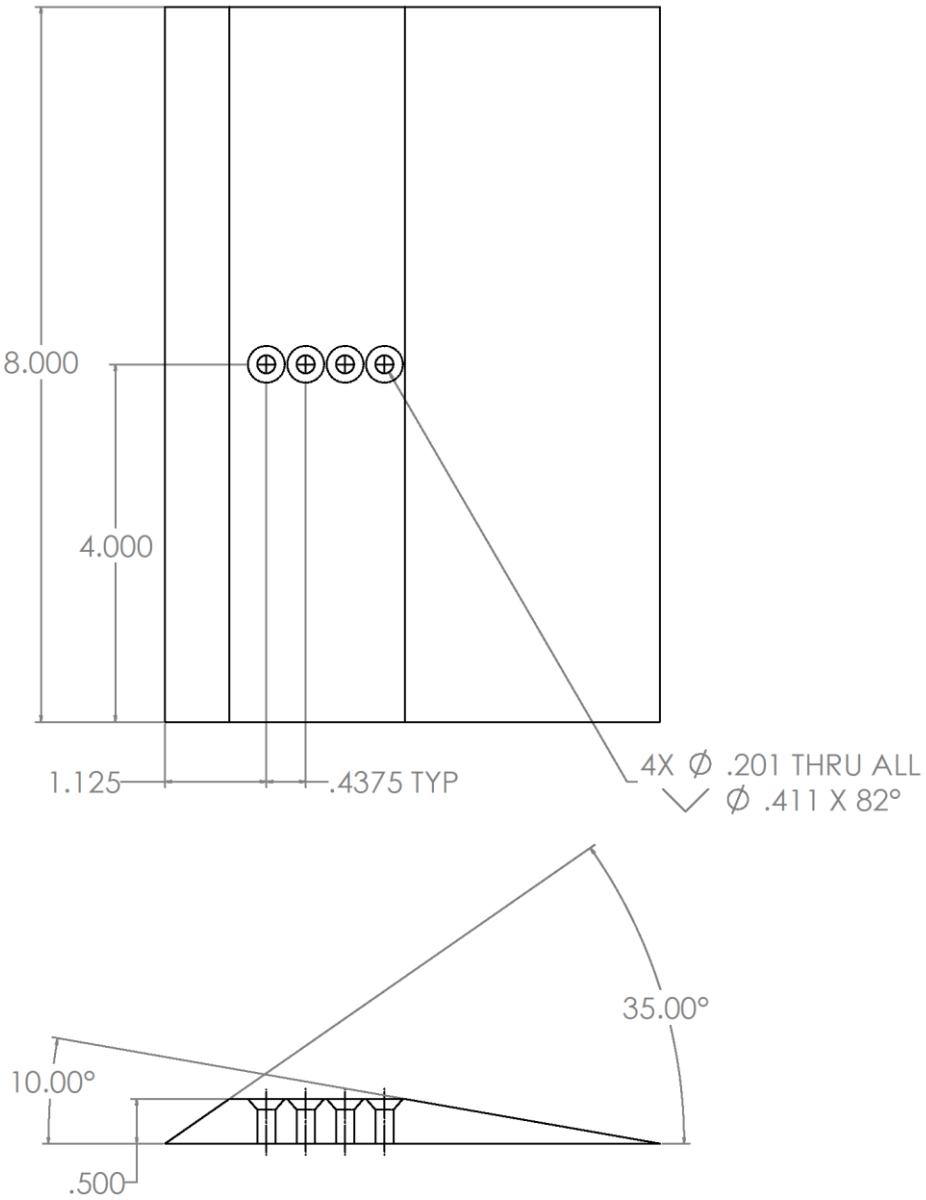

Figure 106. Drawing of wide Mach stem generator wedge model.

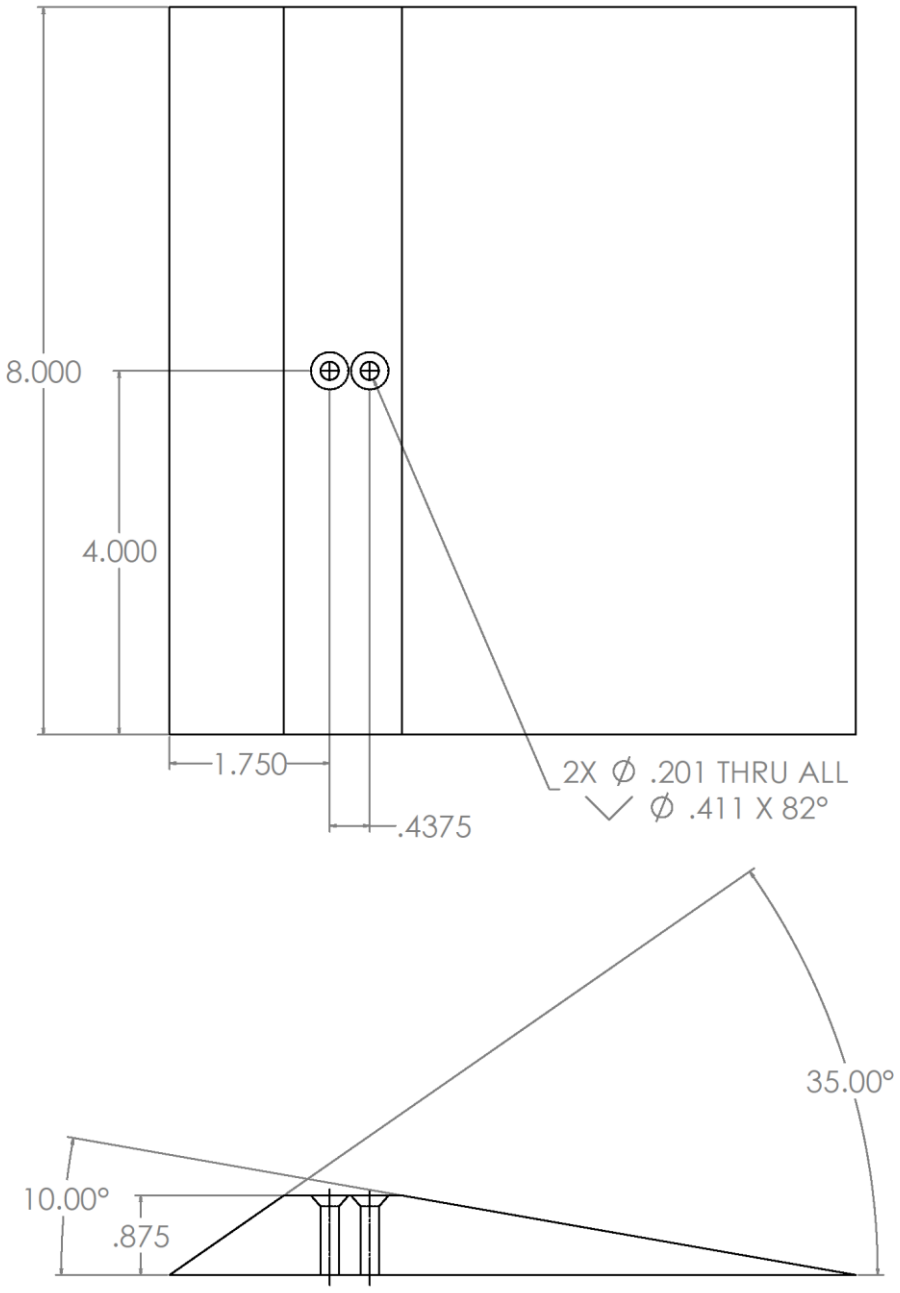

Figure 107. Drawing of thick Mach stem generator wedge model.

Probe Traverse Parts

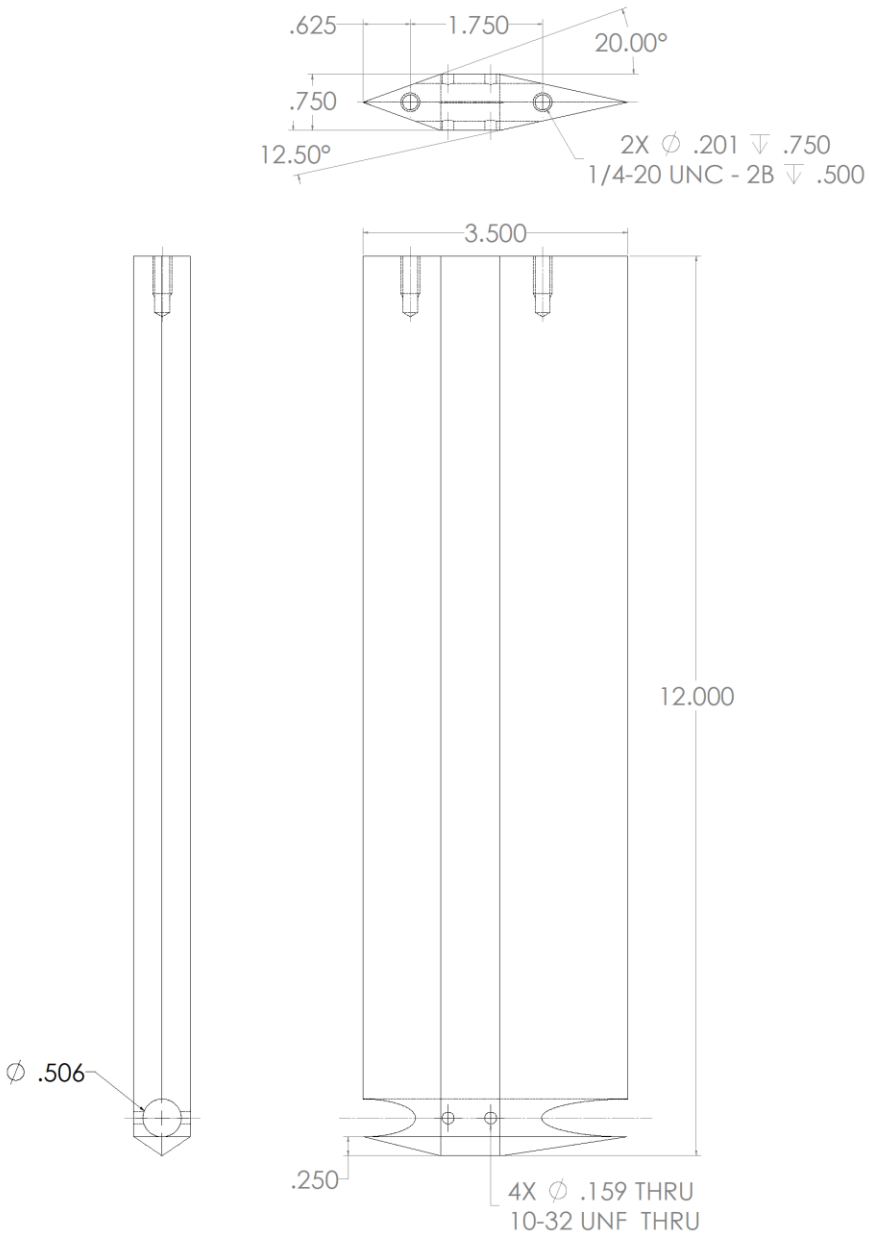

Figure 108. Drawing of traverse strut.

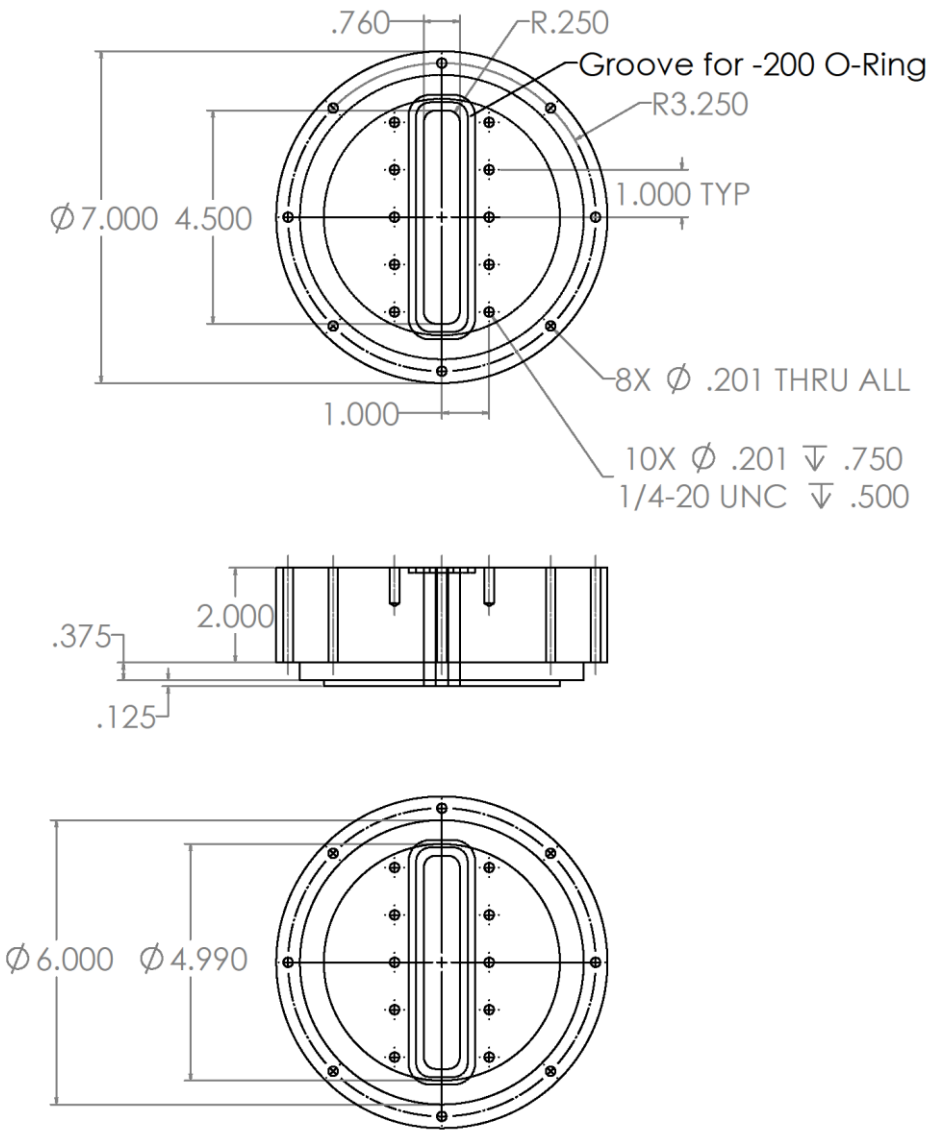

Figure 109. Drawing of traverse window plug.

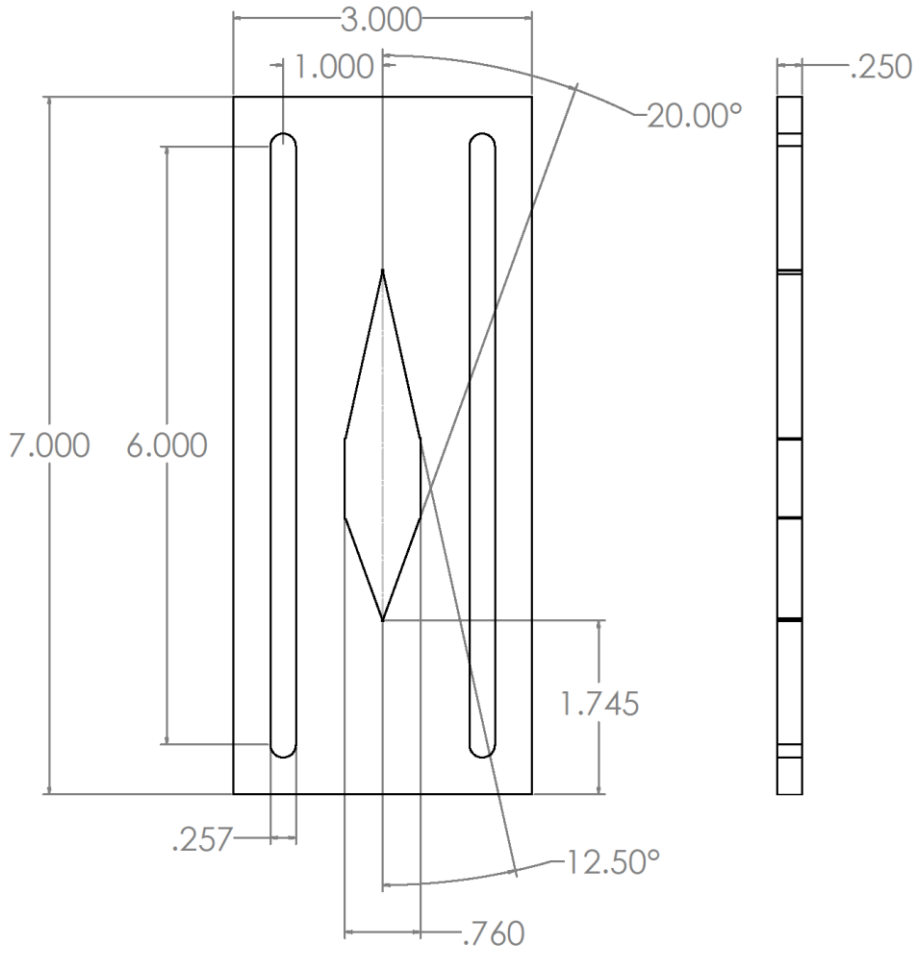

Figure 110. Drawing of traverse sealing plate (aluminum).

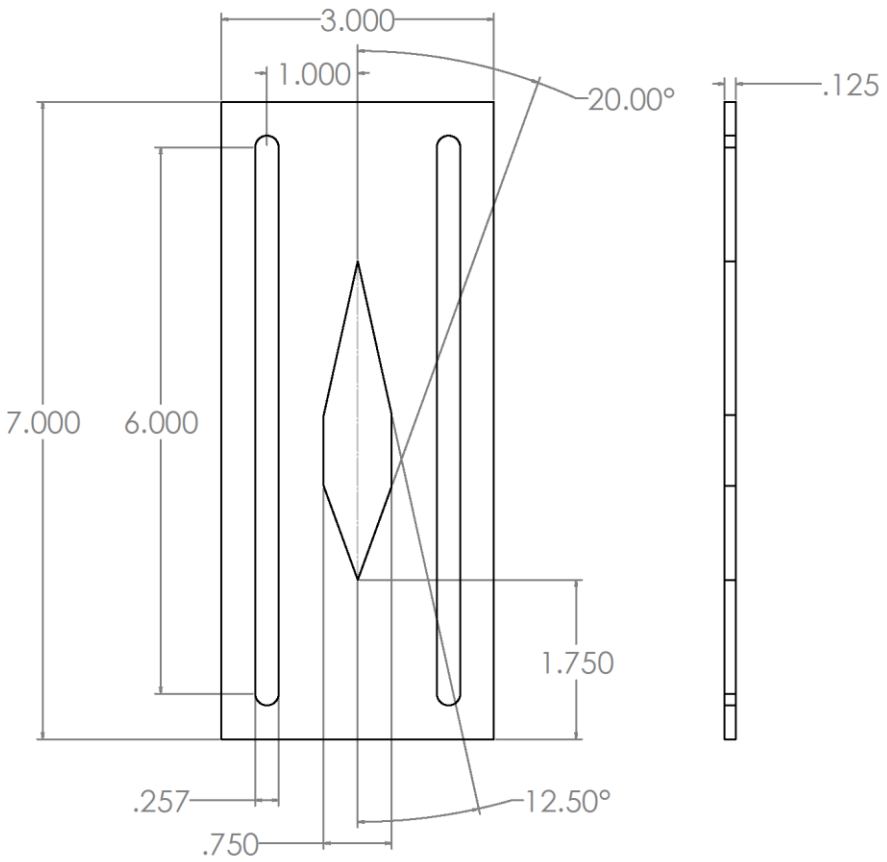

Figure 111. Drawing of traverse sealing plate (silicone).

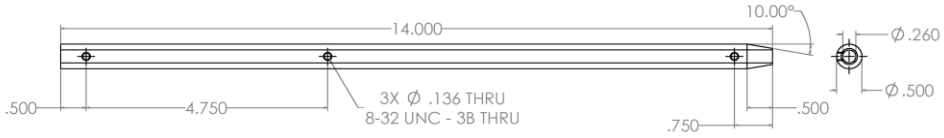

Figure 112. Drawing of traverse adapter sleeve.

APPENDIX D

PITOT PRESSURE PROBE TUBING RESPONSE TIME

The primary measurement instrument, a Pitot pressure probe with a flush-mounted fast-response pressure transducer, was calibrated *in-situ* by comparison to a reference Pitot pressure probe with a capacitance manometer mounted external to the test section. A continuous pressure sweep was performed, and multiple calibration points were obtained. Because the pressure sweep was continuous and not stepped and because there was a relatively significant amount of dead volume in the reference Pitot pressure probe setup, the response time needed to be known to determine if there was a significant time lag between the fast-response pressure transducer reading and the reference transducer reading. A long time lag would affect the accuracy of the calibration.

Volluz [56] provided an equation by Bauer [55] that determined the response time of a pressure-measuring device to obtain a certain pressure, p, given an initial pressure, p_0, and an orifice pressure, p_1. The equation is given below (distances, areas, and volumes are in units derived from feet):

$$t = \frac{128\mu l_e}{\pi d^4} \times \left[\frac{V_1}{p_1} \ln \frac{(p_0 - p_1)(p + p_1)}{(p - p_1)(p_0 + p_1)} + \frac{3V_d}{(p_0 - p_1)} \ln \frac{(p_0 + p_1)}{(p + p_1)} + \frac{V_d}{(p_0 - p_1)} \ln \frac{(p_0 - p_1)}{(p - p_1)} \right] \quad (75)$$

V_d is the displaced volume of manometer fluid or deflection of capsule walls. Since the reference transducer's diaphragm deflection is minimal, V_d is assumed to be zero. The equation then simplifies to:

$$t = \frac{128\mu l_e}{\pi d^4}\left[\frac{V_1}{p_1}\ln\frac{(p_0 - p_1)(p + p_1)}{(p - p_1)(p_0 + p_1)}\right] \tag{76}$$

V_1 is the entire air volume of the pressure measurement system from the orifice to and including the measuring device (in ft.^{3}). μ is the coefficient of dynamic viscosity (in lb-sec/ft^2). d is the common diameter for a set of connected capillaries (in ft.), and l_e is the length of capillary of diameter d, which is equivalent in flow resistance to the total resistance of all series-connected capillaries in the system; these are defined by the equations below:

$$d = d_1 \tag{77}$$

$$l_e = l_1 + l_2\frac{d^4}{d_2^4} + l_3\frac{d^4}{d_3^4} + \ldots + + l_n\frac{d^4}{d_n^4} \tag{78}$$

The subscripts designate a particular capillary/component in the system. For the reference Pitot pressure probe, there were four components: the stainless steel tubing, a KF-type vacuum tee fitting, the dead volume of an MKS Baratron, and the dead volume of an MKS DualTrans (for testing and comparison to the MKS Baratron). Table 19 gives each component's specifications. The effective length of each component i is $l_{eff,i} = l_i\frac{d^4}{d_i^4}$.

Table 19. Reference Pitot pressure probe components.

Subscript	Component	Volume ($ft.^3$)	Diameter (ft.)	Length (ft.)	Effective Length (ft.)
1	Tubing	3.42×10^{-4}	0.0162	1.67	1.67
2	KF Tee	8.50×10^{-4}	0.0525	0.393	0.0035
3	Baratron	2.59×10^{-4}	0.0525	0.120	0.0011
4	DualTrans	9.89×10^{-5}	0.0525	0.046	0.0004

It can be seen that the tubing length dominated the response of the entire pressure measurement system. Table 20 lists the parameters of the reference Pitot pressure probe system. The dynamic viscosity is for air at a temperature of 425 K.

Table 20. Reference Pitot pressure probe system parameters.

Variable	Description	Value	Unit
V_1	Total System Volume	1.55×10^{-3}	$ft.^3$
d	Common Diameter	8.50×10^{-4}	ft.
l_e	Total Effective Length	2.59×10^{-4}	ft.
μ	Dynamic Viscosity	4.99×10^{-7}	$lb.\text{-}s/ft.^2$

Table 21 lists the pressures for both the low Re/m and high Re/m conditions of this study. The difference between the initial pressure and orifice pressure was based on the rate of increase of the settling chamber pressure for a typical, continuous pressure sweep run (~1 psia/sec) and the time of each sampling record (250 ms). In essence, the difference between the pressure at the beginning of a sampling record and at the end of the sampling record is applied, for these calculations, as a step input at the beginning of the sampling record. The target pressure was set to 99.9% of the orifice pressure. The time constant is defined as:

$$t = \frac{128 \mu l_e}{\pi d^4} \frac{V_1}{p_1} \tag{79}$$

Table 21. Reference Pitot pressure probe time response.

Parameter	Description	Low Re/m Condition		High Re/m Condition	
p_0	Initial Pressure	137.5	psfa	251.3	psfa
p_1	Orifice Pressure	138.7	psfa	252.5	psfa
p	Target Pressure (99.9% of orifice pressure)	138.5	psfa	252.2	psfa
t	Time to Reach p	11.9	ms	4.8	ms
τ	System Time Constant	5.6	ms	3.1	ms

The estimated time to reach the target pressure was small compared to the total sampling record time of 250 ms. The estimated time was also a conservative estimate since in actuality, the pressure was continuously increased instead of being a step increase as was assumed here for the calculations. From the definition of the time constant, it was seen that a higher absolute orifice pressure decreased the time constant; thus, the high Re/m condition has a shorter time constant.

Along that same reasoning, the settling chamber pressure tubing response time is less than 1 μs because of the higher absolute pressures in that portion of the tunnel.

APPENDIX E

ANALOG FILTER FREQUENCY RESPONSE

The Krohn-Hite analog filter (50-kHz low-pass, 8-pole Butterworth filter, unity gain) and NI DAQ hardware were checked daily for proper functionality. A function generator directed a known sinusoidal waveform into both the NI DAQ hardware (for the raw signal) and into the Krohn-Hite analog filter whose output was directed into the NI DAQ hardware (for the filtered signal).

A LabVIEW VI [71] was programmed to command the function generator to step through a range of frequencies. Typically, 301 logarithmically-spaced frequencies between 100 Hz and 300 kHz were generated. At each frequency, raw and filtered signal were acquired, and information about each signal's frequency, amplitude, and phase were extracted by LabVIEW's "Extract Single Tone Information" VI. The frequencies of the raw and filtered signals were compared to ensure no frequency distortion was occurring. The amplitudes and phases of the raw and filtered signals were compared to determine the gain and phase response of the filter. The signal time-histories were also displayed to periodically and visually determine the signal integrity during the frequency sweep.

The function generator was a Hewlett-Packard (now Agilent Technologies and eventually Keysight Technologies come November 2014) 33120A 15 MHz function/arbitrary waveform generator. The function generator was connected to the "ACE-DAQ" computer via USB and communicated with the controlling LabVIEW VI via serial communications.

A MATLAB [66] script was written to calculate the theoretical frequency response of the analog filter for comparison to the daily checks. The theoretical gain for a Butterworth filter is:

$$G(\omega) = \frac{1}{\left[1 + \left(\frac{\omega}{\omega_c}\right)^{2n}\right]^{\frac{1}{2}}} \tag{80}$$

Figure 113 shows the comparison between the theoretical gain and the experimental gain of the 50-kHz low-pass, 8-pole Butterworth filter with unity gain. Experimentally, the passband consistently had a gain of 0.997. There was a slight ripple in the passband where the gain would increase to a maximum in the range of 1.000 to 1.003. The experimental rolloff from the passband is not as sharp as the theoretical prediction, but the experimental and theoretical transition band match well. No adjustments were made in the data reduction based on these comparisons.

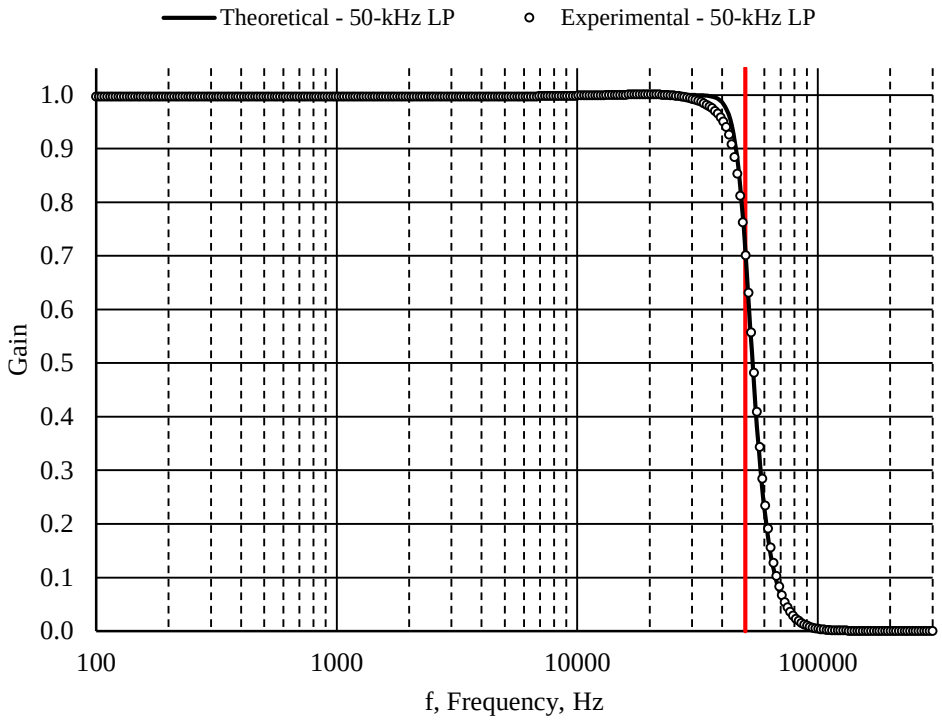

Figure 113. Krohn-Hite 50-kHz low-pass, 8-pole Butterworth analog filter frequency response.

APPENDIX F

FOCUSING SCHLIEREN IMAGING

With conventional schlieren imaging, all details along the coherent beam path are in focus; the conventional schlieren imaging system is said to have an infinite depth of field. Thus, any flow structures at the side of the Mach stem generator wedge models (due to the wedge models not spanning the entire test section width) were as in focus as the flow structures of primary interest at the center of the Mach stem generator wedge models.

To determine the flow structures that exist at the center of the Mach stem generator wedge models, an imaging system with a finite and preferably thin depth of field was desired. Focusing schlieren imaging is one method with this capability. An overview of focusing schlieren imaging is provided by Settles [70], and a practical guide is provided by Weinstein [94]. Focusing schlieren imaging principally is multiple conventional schlieren imaging systems, with multiple source lines and corresponding cutoff lines, imaged together through one lens. The angle subtended by the source and cutoff lines provides the system's focusing capability. The test plane in focus is determined by the location of the image plane from the cutoff grid. In addition to imaging the center plane of the Mach stem generator wedge models, the plane in focus can be set off-centerline to determine spanwise changes to the flow structure and to determine the extent of effects from the sides of the model.

Focusing schlieren has been previously used in the M6QT by Hofferth for deflectometry to observe second-mode instabilities on a flared cone ([89], [95]).

Preliminary focusing schlieren images were obtained in this study by using the same major components (LED array light source, Fresnel lens, and aerial camera lens). The main drawback of focusing schlieren is a limited field of view compared to conventional schlieren. The field of view height was about 43 mm (1.7 in.), which was large enough to see the entire Mach stem, the triple point, the initial shear layer/slip line, and part of the oblique shock. However, the wedge models were not visible. Other problems that had not yet been worked out were the imaging system's relative insensitivity as well as visible banding in recorded videos due to the light source's pulse-width modulated frequency not in synchronization with the rolling shutter of the DSLR camera. Figure 114 is a notional schematic of a focusing schlieren setup.

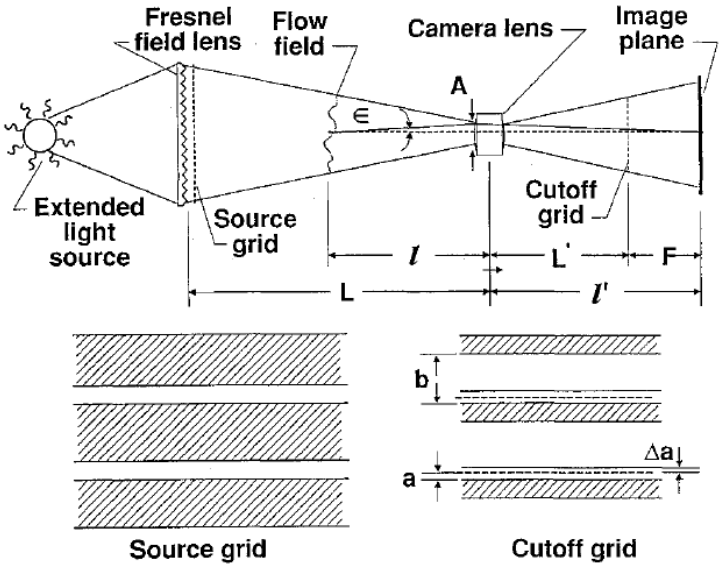

Figure 114. Focusing schlieren imaging setup.
(taken from Weinstein [94])

The parameters of the current setup are shown in Table 22. Equations to calculate the parameters are available in Weinstein [94]. As mentioned before, the imaging (camera) lens was readily available from the M6QT experiments by Hofferth ([89], [95]). The imaging device was primarily a Nikon D800 DSLR camera rental followed by a Nikon D5000 DSLR camera; these were the same cameras used for conventional schlieren. The field of view specifications given below are for the Nikon D800 FX sensor (35.9 mm × 24.0 mm). The sharp and "unsharp" focal depths assumed a flow feature of 3.0 mm (0.12 in.), which was about the size of the Pitot pressure probe diameter.

Table 22. Focusing schlieren imaging system parameters.

Parameter	Description	Value			
ε_{min}	Minimum Sensitivity	16	arcsec	16	arcsec
L	Source Grid to Camera Lens Dist.	1575	mm	62.0	in.
l	Test Plane to Camera Lens Dist.	527	mm	20.8	in.
L'	Camera Lens to Cutoff Grid Dist.	214	mm	8.4	in.
l'	Camera Lens to Image Plane Dist.	294	mm	11.6	in.
A	Imaging Lens Clear Aperture	155	mm	6.1	in.
f	Imaging Lens Focal Length	195	mm	7.7	in.
φ	Pairs of Cutoff Gridlines	10	pairs	10	pairs
2a	Cutoff Grid Opaque Stripe Width	0.221	mm	0.0087	in.
b	Cutoff Grid Clear Strep Width	1.873	mm	0.0738	in.
	Source Grid Opaque Stripe Width	13.8	mm	0.542	in.
	Source Grid Clear Stripe Width	1.63	mm	0.064	in.
m	Image Magnification	0.557		0.557	
	Field of View Width	64.6	mm	2.54	in.
	Field of View Height	43.1	mm	1.70	in.
	Sharp Focal Depth	0.569	mm	0.022	in.
	"Unsharp" Focal Depth	20.4	mm	0.80	in.

Figure 115 is a sample focusing schlieren image obtained in the current study. The initial oblique shock waves and the Mach stem were distinguishable. The slip line/shear layer was noticeable, but the reflected shock wave was not. Comparisons among the Mouton and Hornung theory, the conventional schlieren images, and the focusing schlieren images indicate that there were effects on the flow structure due to the wedge models not spanning the entire test section width, but these effects did not affect the center plane where measurements were made.

Figure 115. Focusing schlieren image sample.
(Run 2110, high Re/m)

Suggested improvements to future focusing schlieren imaging efforts are 1) to increase the field of view height (i.e., decrease the image magnification) to see more of the Mach stem structure and 2) to increase the sensitivity to better detect weaker flow

features. This may require new major components (e.g. imaging lens or camera) since the current setup had required a tradeoff of magnification for increased distance between the cutoff grid and imaging plane to accommodate the camera body dimensions.

APPENDIX G

WEDGE MODEL DATA COMPARISON

This appendix presents results from the wide Mach stem wedge generator models and the thick Mach stem wedge generator models for comparison. Figure 116 shows noise (Pitot pressure fluctuation) values plotted against distance from the Mach stem for the low and high Re/m conditions for both sets of Mach stem generator wedges.

Noise levels for the low Re/m conditions were qualitatively similar between the two sets of wedge models. There was a slight offset in the position, which could be accounted for by the uncertainty of defining when the Pitot pressure probe tip has crossed the Mach stem during a traverse-type run. Across all positions, the noise levels for the wide wedge models were higher than the noise levels for the thick wedge models. This difference can be attributed to the location of the Mach stem relative to the nozzle exit plane for each wedge model. The thick wedge model was installed closer to the nozzle exit plane because of its larger size and the clearance required for the traverse strut situated behind the wedge models. Figure 55 indicates that in the low Re/m range, the noise levels increase with increasing downstream distance from the nozzle exit plane. Thus, it was expected that the noise level for the wide wedge model is higher since it was installed further from the nozzle exit plane. For a more direct comparison between the two sets of wedge models, the noise levels from the wide wedge model were adjusted based on the freestream noise levels at the respective Mach stem locations of each wedge model set. The adjusted wide wedge model noise levels were obtained by dividing the actual wide

wedge model noise levels by the freestream noise level at the wide wedge model Mach stem location and then multiplied by the freestream noise level at the thick wedge model Mach stem location. The discrepancy between the noise levels of the two wedge models decreased, but there were still appreciable discrepancies in the region of interest between x = 2 mm and x = 5 mm.

Noise levels for the high Re/m condition showed very good agreement between the two sets of wedge models if the first millimeter from the Mach stem was ignored due to probe-Mach stem interference effects. Figure 55 shows that the noise levels for high Re/m was insensitive to the distance from the nozzle exit plane, and this was observed in the bottom panel of Figure 116.

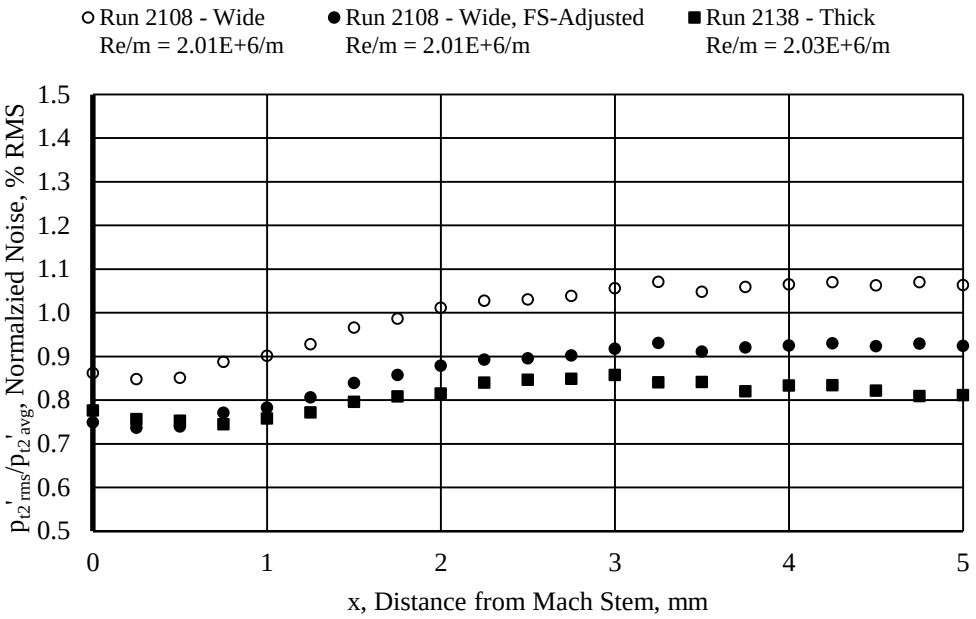

a)

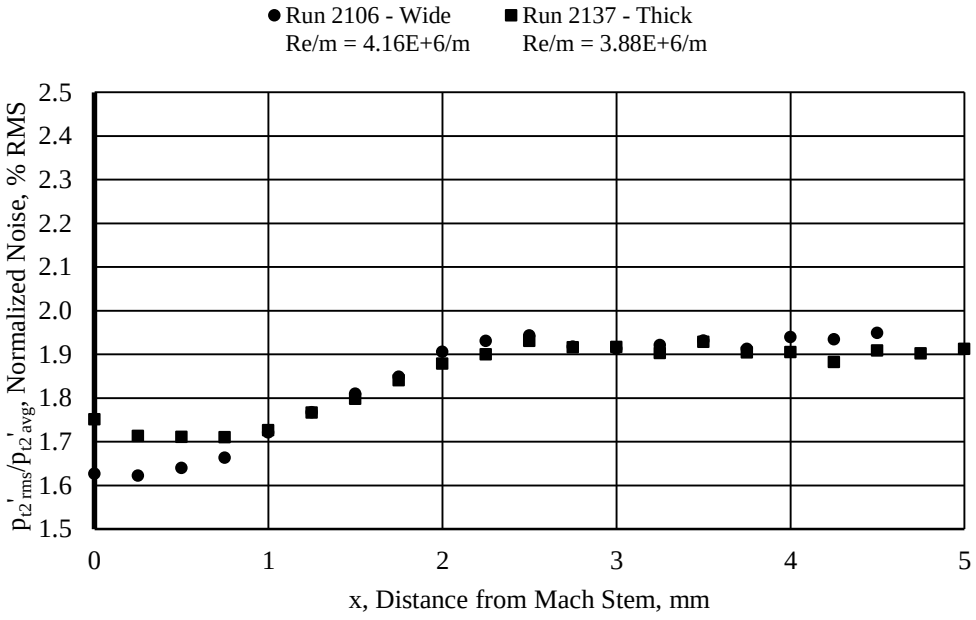

b)

Figure 116. Noise comparisons (traverse runs) between wedge models.

a) Low Re/m condition. b) High Re/m condition.

APPENDIX H

HOT-WIRE ANEMOMETRY

Preliminary hot-wire anemometry has been performed in addition to the Pitot pressure probe data collection of the current study. Freestream fluctuations primarily have been obtained.

Introduction

Hot-wire anemometry is a well-established technique in measuring rapid fluctuations in supersonic flow (see Kovásznay [96] and Smits, Hayakawa, and Muck [97]). Hot-wire anemometry (particularly CTA) is a well-suited technique for turbulent measurements because of the high frequency response of the entire system; acceptable frequency response greater than 100 kHz was obtained in this extended study. In supersonic flow, hot-wires sensors have been shown to be sensitive to mass flux and total temperature. The relative sensitivity of a sensor to mass flux versus total temperature is largely governed by a parameter called the temperature loading factor (similar to the overheat ratio in low-speed flows). The temperature loading factor, following Kovásznay [96] and Bruun [98] is defined as:

$$\tau = \frac{T_w - T_e}{T_o} \tag{81}$$

The equilibrium temperature is defined as:

$$T_e = \eta T_o \tag{82}$$

The hot-wire sensor is sensitive solely to the flow's total temperature at a temperature loading factor of 0 (an unheated wire relative to the flow total temperature). At a high temperature loading factor, such as 0.8 to 1.0, it is often assumed that the hot-wire is primarily sensitive to mass flux. By invoking the so-called strong Reynolds analogy and assuming a constant total temperature and negligible pressure fluctuations, velocity fluctuations are derived from the mass flux fluctuations [97]. By obtaining data at multiple temperature loading factors, however, it is possible to decouple the hot-wire signal's contribution from the mass flux and total temperature ([62], [97], [99]).

The operating principle of a hot-wire sensor in CTA mode is now described. The hot-wire sensor forms one arm of a Wheatstone bridge. The operating resistance (and thus the operating temperature) of the hot-wire sensor is set by adjusting a resistor decade that forms the opposing arm of the Wheatstone bridge. The bridge will then heat the wire to the set resistance and the feedback circuit keeps the bridge in balance. As fluid flows past the wire, heat is carried away by convection, which would cool the wire, decrease the wire resistance, and unbalance the bridge. The feedback circuit inputs a higher voltage to the bridge to keep the wire at a constant temperature. A relationship can be described to relate the bridge voltage to the mass flux/total temperature.

Hardware

The anemometer used in this preliminary hot-wire anemometry campaign was an A.A. Lab Systems AN-1003 CTA.[12] Features of this anemometer include cable resistance

[12] http://www.lab-systems.com/products/flow-mea/an1003/AN-1003%20Brochure.pdf

nulling, resistance decade dials, a square-wave pulse tester, adjustable trimpots for the tuning coil and damping, a low-pass filter (not used since an external filter was used), and adjustable offset and gain to scale the bridge voltage range to a voltage range amenable to a DAQ system.

The hot-wires were TSI single-normal wire (Model 1220) sensors.[13] Also available but not used were TSI cross-wire (Model 1251) sensors and a TSI parallel-wire (Model 1244) sensor. Because of the high-temperature stagnation conditions required of hypersonic flow, the temperatures needed to obtain a sufficient temperature loading factor did not allow the use of tungsten wires. All sensors utilized in this study used platinum-iridium alloy wires. The wire diameters were 6.3 μm (0.00025 in.), and the active sensor lengths were nominally 1.27 mm (0.05 in.); this gave a length-to-diameter ratio of 200.

The recovery factor for the given wire diameters in this study was previously experimentally determined to be η = 1.05 [62]. The Knudsen number based on the wire diameter in conditions behind the shock is 0.16, and it was believed that slip effects result in η greater than 1. In addition, the recovery factor in the slip flow regime is slightly dependent on the Reynolds number.

In practice, a hot-wire sensor probe was connected to a TSI Model 1160-18 high-temperature probe support (45.7 mm/18 in. long). The sensor probe and support were secured together in a TSI Model 1158-18 locking protective shield (45.7 mm/18 in. long).

[13] http://www.tsi.com/Thermal-Anemometry-System/

Tuning and Calibration

To tune the hot-wire sensor, a typical square-wave pulse test was applied to the Wheatstone bridge circuit, and the wire response was measured with two methods (results of both methods are shown in Figure 118). The first method was the typical viewing of the response on an oscilloscope. The response was viewed on a triggered Tektronix TDS 2004B oscilloscope. The optimal response profile is provided by Bruun [98] based on the work by Freymuth [100] in which the damping should be adjusted so that the first undershoot's amplitude is 15% of the main overshoot's amplitude (Figure 117). The wire's cutoff frequency is then calculated by the equation in Figure 117.

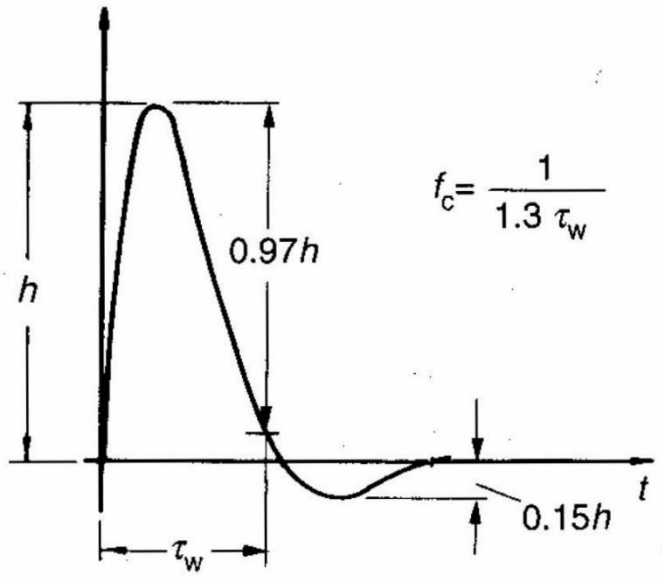

Figure 117. CTA hot-wire square-wave test optimal response.
(taken from Bruun [98])

The second method of measuring wire response was to compare the pulse signal to the response signal and compute the frequency response function using an FFT. An in-house SignalExpress project [101] was created by J. W. Hofferth and recreated by S. A. Craig that read the pulse and response signals from an NI PCI-5122 high-speed digitizer and computed the frequency response function using an FFT.

No dedicated tuning and calibration facility existed at the TAMU NAL at the time of this study. Therefore, hot-wire tuning and calibration were done *in situ* in the tunnels. Tuning a hot-wire required a dedicated tunnel run (or runs). Generally, tuning the hot-wire to an optimal response in a no-flow condition was a good, initial approximation that required minimal to moderate tweaking during the 40-second run time of the tunnel. During a tuning tunnel run, the goal was to obtain a qualitatively good wire response profile on the Tektronix oscilloscope followed by adjustments to flatten the frequency response viewed with the NI digitizer to as high a frequency as reasonably possible. The hot-wires in the freestream characterization study were typically tuned to have acceptable frequency response (-3 dB from the lowest frequencies) to at least 100 kHz. Figure 118 shows a sample wire pulse response and transfer function. At each temperature loading factor for the freestream characterization, a wire tuning tunnel run was performed. The cutoff frequency did not decrease drastically with decreased temperature loading factor.

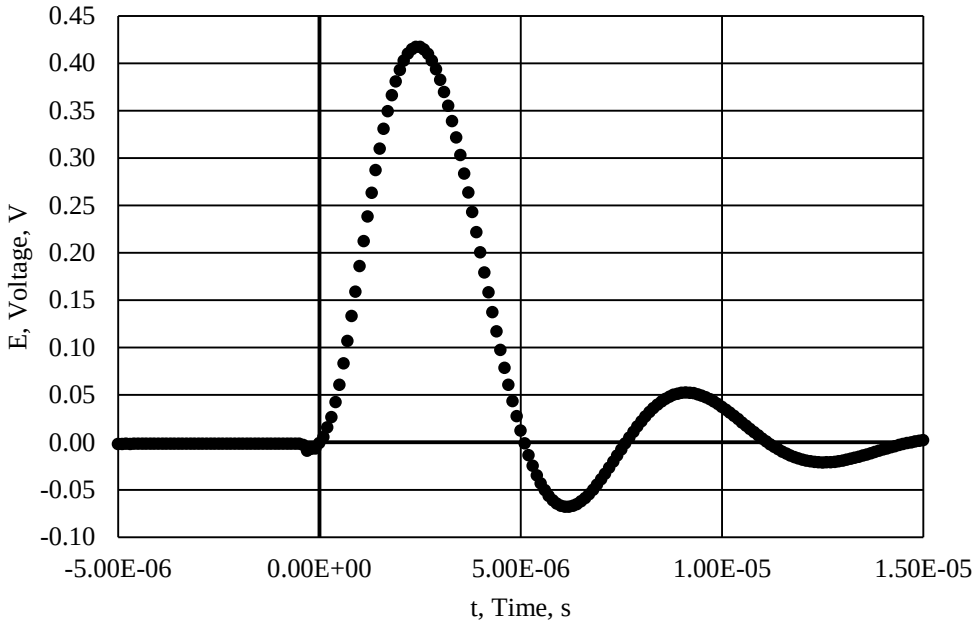

a)

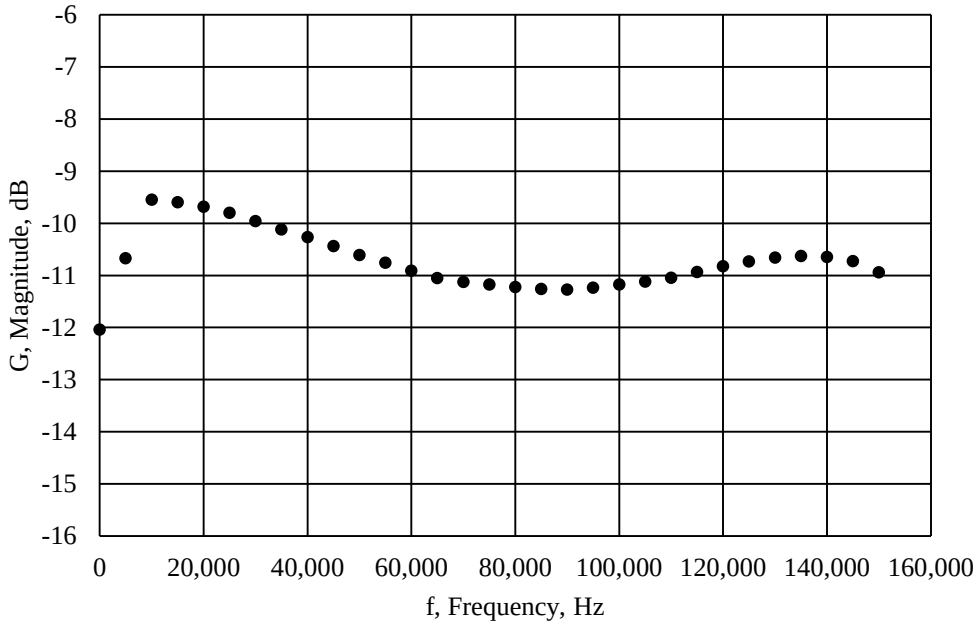

b)

Figure 118. Experimental hot-wire frequency response.

a) Wire pulse response. b) Wire frequency response.

Hot-wire calibration was accomplished by performing another dedicated tunnel run and doing a pressure sweep. Similar to the Pitot pressure probe pressure sweep, the hot-wire calibration pressure sweep had multiple sampling records 250 ms long with a sampling rate of 2 MS/s giving 500,000 sampling points per record. The anemometer voltage was recorded, and knowing the anemometer gain and offset, the bridge voltage could be backed out. For each sampling record, the average bridge voltage was calculated as well as the mean mass flux (derived from the measured settling chamber pressure, settling chamber temperature, and nozzle static pressure as described in the Pitot pressure probe data reduction section). Over all of the sampling records, a linear fit was made between the bridge voltage and the mass flux following a general form of King's law:

$$E^2 = A + B\left(\rho U\right)^n \tag{83}$$

The exponent n was adjusted to maximize the coefficient of determination of the linear fit, but the coefficient did not change appreciably over a wide range of exponents. Exponents in a range of $n = 0.45$ to $n = 0.55$ were used to be near the traditional King's law exponent.

It is important to note for these shock-turbulence interaction experiments that a hot-wire sensor's behavior in supersonic flow is fundamentally different from its behavior in subsonic flow. It was observed in preliminary tests that the tuning did not appreciably change from supersonic flow to subsonic flow. However, the calibrations were different (Figure 119), and thus, it is imperative to perform separate calibrations for supersonic (i.e., freestream characterization) and subsonic (i.e., post-Mach stem characterization) flows.

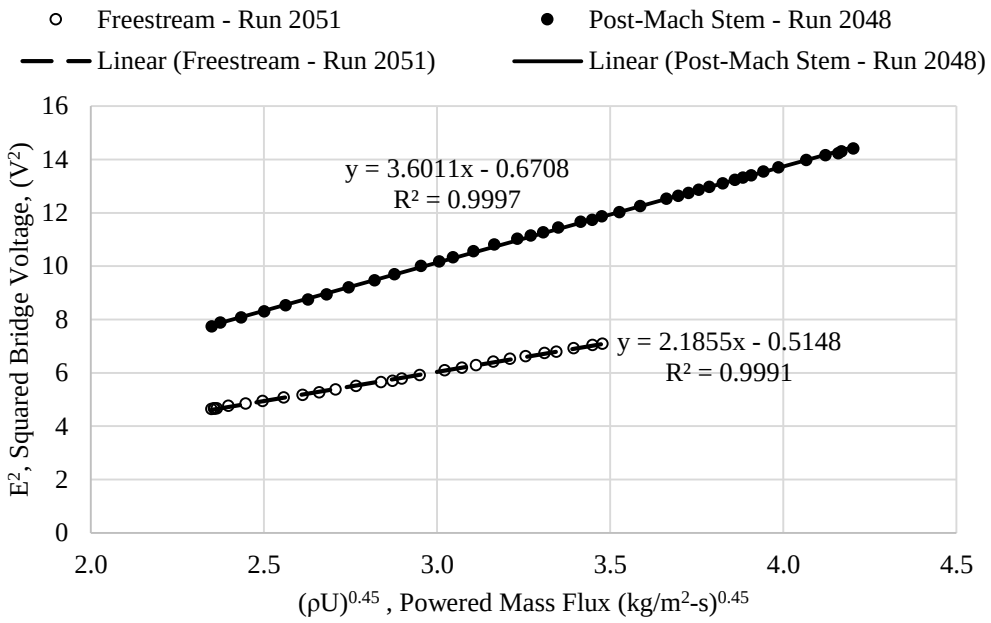

Figure 119. Comparison of hot-wire subsonic and supersonic calibrations.

Data Acquisition and Reduction

Based on the estimated bridge voltage, the anemometer offset and gain were set to use most of the DAQ system's positive voltage range of 0 to 10 V. The anemometer uses the following equation to determine the anemometer voltage output from the bridge voltage:

$$V_{anem} = G\left(V_{TOB} - V_{off}\right) \tag{84}$$

The bridge voltage (V_{TOB}) depends on the set resistance of the wire and flow speed/regime. The bridge voltage values were typically -1 to -3 V, so the offset voltage (V_{off}) was set in a range of -3.0 to -5.0 V and the gain (G) set in a range of 2.0 to 4.0.

The anemometer voltage (V_{anem}) is the raw (DC-coupled) voltage output of the hot-wire system. The AC-coupled signal is obtained by branching off of the raw output and passing it through an 8-pole, Butterworth, 100-kHz low-pass filter with unity gain. Like with the Pitot pressure probe, the filter was a module in a Krohn-Hite FMB3002 chassis. The signal was further conditioned by passing it through a Stanford Research Systems SR560 low-noise preamplifier and filter.[14] The AC-coupling mode was selected on the SR560, which automatically implemented a 0.3 Hz, first-order, high-pass RC filter. However, a higher cutoff frequency of 300 Hz was chosen to closely match the Pitot pressure probe high-pass frequency cutoff of 842 Hz. A first-order, low-pass RC filter was also utilized on the SRS and set to a low-pass frequency cutoff of 1 MHz. A gain factor of 10 or 20 was also applied to the AC-coupled signal by the SR560. Both the raw voltage and the AC-coupled voltage outputs were acquired by the NI USB-6366 DAQ system at 2 MS/s/ch for 250 ms. A schematic of the hot-wire signal conditioning process is shown in Figure 120.

[14] http://www.thinksrs.com/downloads/PDFs/Catalog/SR560c.pdf

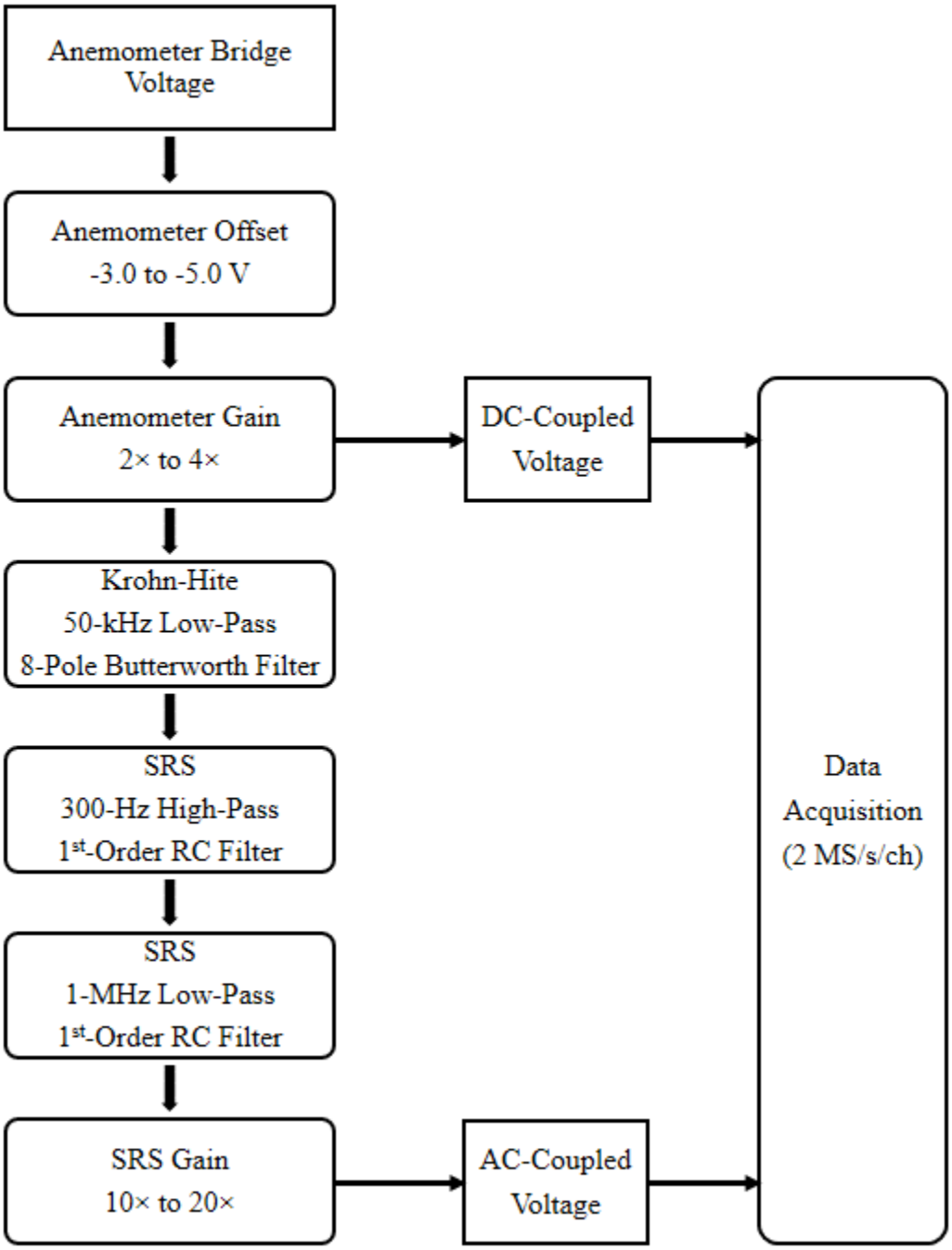

Figure 120. Hot-wire anemometry signal conditioning process.

The data reduction can proceed similarly as the Pitot pressure data reduction with RMS fluctuations, autocorrelation coefficient functions, integral time scales, and PSD estimates. Additional considerations were required since the hot-wire sensor was responsive to both mass flux and total temperature. The hot-wire response equation was derived by Bowersox [99] for a King's law exponent of $n = 0.5$ and again by Semper [62] for an arbitrary exponent. Bowersox also developed a reduction method for data obtained at multiple temperature loading factors.

Hot-wire data have been obtained at multiple temperature loading factors ($\tau = 0.4$ to $\tau = 1.0$) in the freestream of the ACE tunnel. Data reduction (by R. D. W. Bowersox) and results for the highest temperature loading factor ($\tau = 1.0$, in which the hot-wire sensor was primarily sensitive to mass flux) are now presented.

Starting with the general King's law relationship between bridge voltage and mass flux:

$$E^2 = A + B\left(\rho U\right)^n \tag{85}$$

Decompose the voltage and mass flux into its mean and fluctuation components:

$$\left[\bar{E} + E'\right]^2 = A + B\left[\overline{\rho U} + \left(\rho U\right)'\right]^n \tag{86}$$

Apply the binomial expansion theorem and ignore second-order terms and higher:

$$\bar{E}^2 + 2\bar{E}E' + \cancel{E'^2} = A + B\left[\overline{\rho U}^n + n\overline{\rho U}^{n-1}\left(\rho U\right)' + \ldots\right] \tag{87}$$

Take the average of the general King's law relationship, Eq. (85):

$$\bar{E}^2 = A + B\left(\overline{\rho U}\right)^n \tag{88}$$

After removing the self-satisfying terms of Eq. (88) from Eq. (87), the fluctuation relationship is obtained:

$$2\bar{E}E' = Bn\overline{\rho U}^{n-1}\left(\rho U\right)' \tag{89}$$

To obtain the fluctuation relationship in RMS terms, first divide by 2 times the square of the mean voltage:

$$\frac{2\bar{E}E'}{2\bar{E}^2} = \frac{Bn\overline{\rho U}^{n-1}\left(\rho U\right)'}{2\bar{E}^2} = \frac{Bn\overline{\rho U}^{n}}{2\bar{E}^2}\frac{\left(\rho U\right)'}{\overline{\rho U}} \tag{90}$$

$$\frac{E'}{\bar{E}} = \frac{Bn\overline{\rho U}^{n}}{2\bar{E}^2}\frac{\left(\rho U\right)'}{\overline{\rho U}} = f\frac{\left(\rho U\right)'}{\overline{\rho U}} \tag{91}$$

Where f is:

$$f = \frac{Bn\overline{\rho U}^{n}}{2\bar{E}^2} \tag{92}$$

Take the square of Eq. (91):

$$\left(\frac{E'}{\bar{E}}\right)^2 = f^2\left[\frac{\left(\rho U\right)'}{\overline{\rho U}}\right]^2 \tag{93}$$

Followed by the mean:

$$\overline{\left(\frac{E'}{\bar{E}}\right)^2} = \overline{f^2\left[\frac{\left(\rho U\right)'}{\overline{\rho U}}\right]^2} \tag{94}$$

Knowing that *f* is defined entirely by mean components, the right-hand side of Eq. (94) can be decomposed:

$$\overline{\left(\frac{E'}{\bar{E}}\right)^2} = \overline{f^2}\overline{\left[\frac{(\rho U)'}{\overline{\rho U}}\right]^2} \tag{95}$$

Take the root:

$$\left[\overline{\left(\frac{E'}{\bar{E}}\right)^2}\right]^{1/2} = \left[\overline{f^2}\overline{\left[\frac{(\rho U)'}{\overline{\rho U}}\right]^2}\right]^{1/2} = \left[\overline{f^2}\right]^{1/2}\left[\overline{\left[\frac{(\rho U)'}{\overline{\rho U}}\right]^2}\right]^{1/2} \tag{96}$$

Knowing that *f* is defined entirely by multiplicative components, the order of squaring and averaging can be rearranged:

$$\left[\overline{\left(\frac{E'}{\bar{E}}\right)^2}\right]^{1/2} = \left[\overline{f}^2\right]^{1/2}\left[\overline{\left[\frac{(\rho U)'}{\overline{\rho U}}\right]^2}\right]^{1/2} = \overline{f}\left[\overline{\left[\frac{(\rho U)'}{\overline{\rho U}}\right]^2}\right]^{1/2} \tag{97}$$

Expressing the fluctuations in terms of RMS and knowing that $\overline{f} = f$:

$$\left(\frac{E'}{\bar{E}}\right)_{RMS} = f\left[\frac{(\rho U)'}{\overline{\rho U}}\right]_{RMS} \tag{98}$$

Eqs. (92) and (98) were used to calculate the normalized mass flux RMS fluctuations for each sampling record.

Results from a freestream pressure sweep with the TSI Model 1220 high-temperature straight probe (Figure 121) at a temperature loading factor of τ = 1.0 are shown in Figure 122. Similar to the freestream noise pressure sweep (Figure 55), the mass flux fluctuations were relatively low for low Re/m, increased rapidly for Re/m from 2.5×10^6/m to

3.0×10^6/m, and then remained at a relatively high level for Re/m. There was higher variation in the mass flux fluctuation levels for the higher Re/m. Pressure sweep data at lower τ show a similar behavior with local peaks and troughs matching with Re/m. The cause(s) of the variations and the matching variation behavior at high Re/m was unknown at the time.

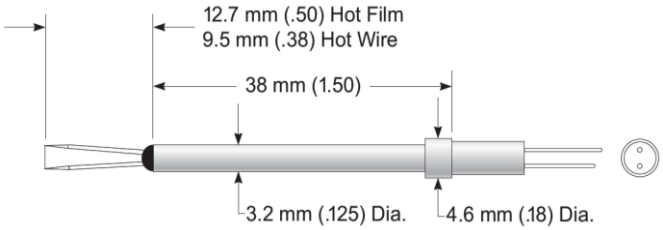

Figure 121. TSI Model 1220 high-temperature straight probe
(taken from TSI thermal anemometry probes catalog)

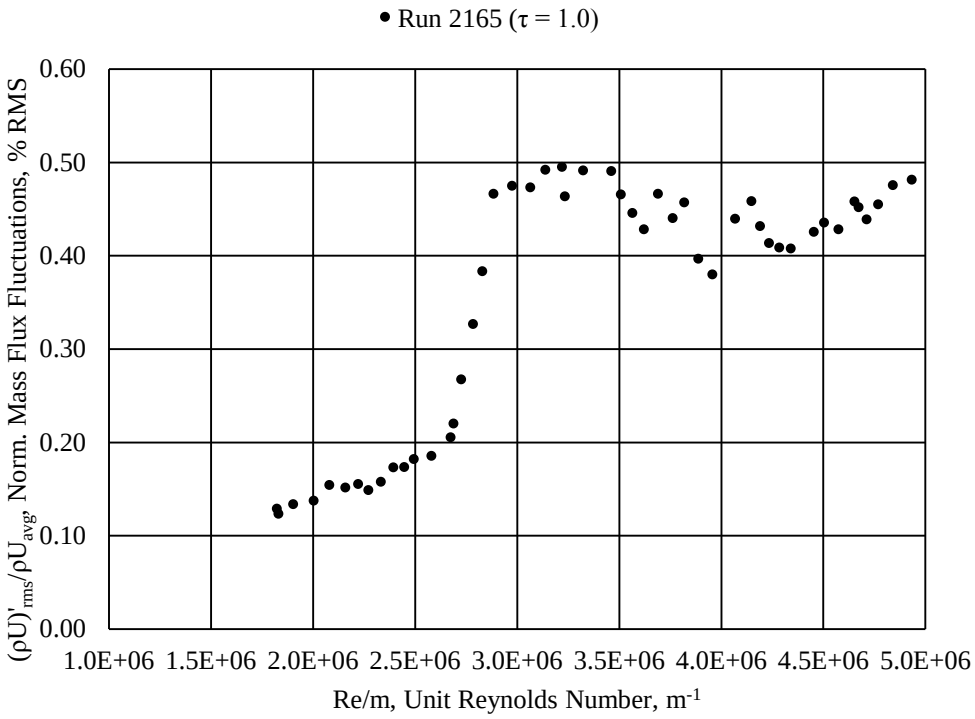

Figure 122. ACE tunnel freestream flow mass flux fluctuations.
Assumption of satisfactorily high *τ*.
104 mm (4.1 in.) downstream of nozzle exit plane.

Ongoing and Future Work

This subsection describes the ongoing and future hot-wire anemometry work to augment the current study's Pitot pressure data.

Decomposition of Hot-Wire Voltage Signals

Freestream characterization data have been obtained for multiple *τ*, but they have not yet been processed to decompose the voltage fluctuations into mass flux fluctuations and total temperature fluctuations.

Post-Mach Stem Characterization

Tunnel runs were attempted to obtain hot-wire data behind the Mach stem, but a few problems were encountered. First, since the tunnel starts and unstarts with a shock wave passing through the test section, the typical hot-wire operation was to not operate the anemometer bridge until the tunnel has started. This was a cautionary measure to prevent the anemometer from attempting to react to the passing of the shock wave, which may shorten the hot-wire sensor's operating life or destroy it outright. It was observed, however, that switching the anemometer to "operate" mode behind the Mach stem after the tunnel started sent a voltage spike that activated the Stanford Research Systems SR560 amplifier's overload protection. Since the overload protection did not deactivate within the tunnel's operating run time, no meaningful output was obtained from the amplifier's output (the AC-coupled signal). Future efforts should remove the SR560 amplifier completely, use another mechanism for AC coupling, and adjust the DAQ range settings accordingly to maximize resolution without any gain applied to the incoming signal.

A second problem was the increased occurrence of the loss of the hot-wire sensor when performing post-Mach stem runs. It is believed that during the tunnel start and unstart processes, the flow behind the Mach stem was more violent compared to the flow upstream of the Mach stem. To accommodate the flow behavior and prolong hot-wire sensor operational life, the operating procedure was adjusted so that:

- the hot-wire sensor started upstream of the Mach stem during tunnel start,
- the hot-wire sensor traversed behind the Mach stem to the desired location,
- the anemometer bridge was switched to "operate" mode and activated,
- the tunnel conditions were adjusted appropriately and data collected,
- the anemometer bridge was switched to "neutral," and

- the hot-wire sensor traversed upstream of the Mach stem followed by tunnel shutdown.

This operating method preserved the hot-wire sensor during a Mach stem run (but would be affected by the SR560 amplifier overload mentioned previously). Tunnel runs in which this sequence of events was not followed (namely going too high on the pressure during a pressure sweep causing an unexpected tunnel unstart) resulted in broken hot-wire sensors. Broken wire sensors were sent to TSI for repair by its after-sales support group.

Multiple Temperature-Loading-Factor Scanning

A custom-built overheat ratio/temperature loading factor scanner was built by J. W. Hofferth and is available for the continuing hot-wire studies. The scanner goes through eight different bridge resistors, which sets the hot-wire resistance to obtain eight different temperature loading factors. A trigger signal built into LabVIEW [71] DAQ software executes a timing scheme programmed into a Berkeley Nucleonics Corporation Model 575 8-channel digit delay/pulse generator with each channel activating relays in the scanner that determines which resistors are used.

The advantage of such a scanner is that it allows data at multiple τ to be obtained during a single tunnel run, which reduces the error associated with varying tunnel conditions run-to-run and the resulting effect on the variable decomposition. The disadvantage, however, is that since the current anemometer does not have a self-tuning capability, the sensor's tuning degrades as the temperature loading factor decreases. A

proposed idea to circumvent this problem is to develop a multiple-τ program to control a TSI IFA 300 CTA (a discontinued product), which has an auto-tuning feature.[15]

Additional Wire Sensors

As mentioned previously, a parallel wire and two cross-wires (Figure 123) are available to use in addition to the single-normal wires. A parallel wire allows data to be collected simultaneously for two values of τ for better mass flux/total temperature correlations. A cross-wire enables the characterization of two mass flux vectors simultaneously. The cross-wires available allow characterization in the freestream direction and a component normal to the freestream direction; the normal component desired can be adjusted by rotating the sensor along the axis in the freestream direction.

[15] ftp://ftp.tsi.com/pub/ThermoPro/5.0.10/Documentation/1990746D-IFA300.pdf

a)

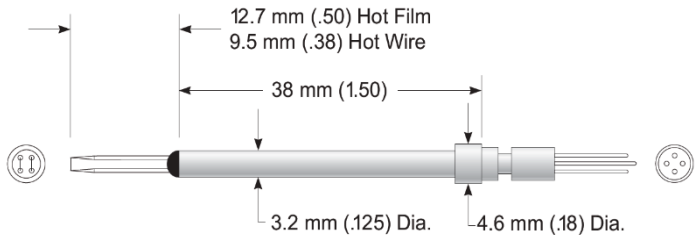

b)

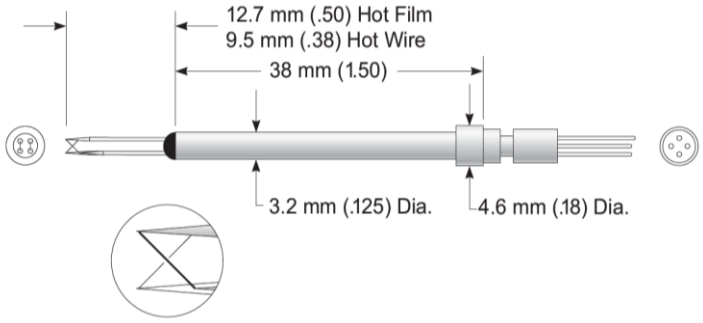

Figure 123. TSI dual-wire sensors.

a) Model 1244 end flow parallel sensor probe. b) Model 1241 end flow "X" probe. (taken from TSI thermal anemometry probes catalog)